

UNIVERSIDADE FEDERAL DE SÃO CARLOS - UFSCAR
GRUPO DE SUPERCONDUTIVIDADE E MAGNETISMO - GSM
PROGRAMA DE PÓS-GRADUAÇÃO EM FÍSICA - PPGFIS
DEPARTAMENTO DE FÍSICA

**Flux avalanches in patterned superconducting thin
films: ac susceptibility, morphology and related
studies**

Avalanches de fluxo em filmes finos supercondutores estruturados:
suscetibilidade ac, morfologia e outros estudos

Maycon Motta

São Carlos, São Paulo, Brasil

2013

MAYCON MOTTA

**Flux avalanches in patterned superconducting thin
films: ac susceptibility, morphology and related
studies**

Avalanches de fluxo em filmes finos supercondutores estruturados:
suscetibilidade ac, morfologia e outros estudos

Tese apresentada ao Programa de
Pós-Graduação em Física da Universidade
Federal de São Carlos como parte dos requisitos
para a obtenção do Título de Doutor em
Ciências com ênfase em Física.

Advisor (Orientador): Prof. Dr. Wilson Aires Ortiz

Co-Advisor (Co-orientador): Prof. Dr. Alejandro Vladimiro Silhanek

São Carlos, São Paulo, Brasil

2013

**Ficha catalográfica elaborada pelo DePT da
Biblioteca Comunitária/UFSCar**

M921af Motta, Maycon.
Avalanches de fluxo em filmes finos supercondutores estruturados : suscetibilidade ac, morfologia e outros estudos / Maycon Motta. -- São Carlos : UFSCar, 2013. 148 p.

Tese (Doutorado) -- Universidade Federal de São Carlos, 2013.

1. Supercondutividade. 2. *Flux jumps*. 3. Instabilidades termomagnéticas. 4. Filmes finos. I. Título.

CDD: 537.623 (20^a)

MAYCON MOTTA

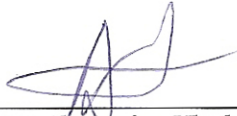
Tese de Doutorado submetida à
Coordenação do Programa de Pós-
Graduação em Física, da Universidade
Federal de São Carlos, como requisito
parcial para a obtenção do título de
Doutor em Ciências.

Aprovado em 12 de Abril de 2013

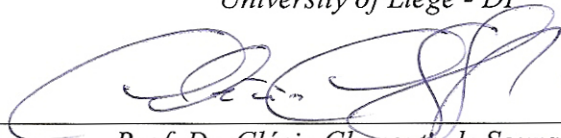
BANCA EXAMINADORA



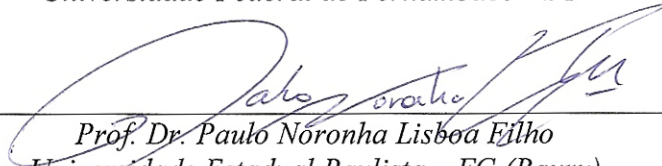
Prof. Dr. Wilson Aires Ortiz
Universidade Federal de São Carlos - DF



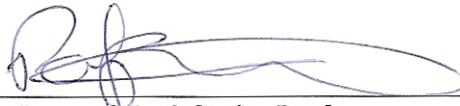
Prof. Dr. Alejandro Vladimiro Silhanek
University of Liège - DP



Prof. Dr. Clécio Clemente de Souza Silva
Universidade Federal de Pernambuco - DF



Prof. Dr. Paulo Noronha Lisboa Filho
Universidade Estadual Paulista – FC (Bauru)



Prof. Dr. Pascoal José Giglio Pagliuso
Universidade Estadual de Campinas- IFGW



Prof. Dr. Tom Henning Johansen
University of Oslo - DP

*Ao meu recém-chegado e amado filho, Victório
e
à minha sempre paciente e amada, Tati.*

Acknowledgements (Agradecimentos)

No fim de um trabalho de doutorado, há muitas pessoas para agradecer, que de alguma forma ajudaram nessa longa jornada. Primeiramente, minha família que conta com um integrante recém-chegado, Victório. Em especial, à Tati por estar sempre ao meu lado. Pela sua paciência, apoio e por entender minha ausência. À minha mãe pela preocupação e apoio. À Fabi, minha irmã, que está conseguindo ultrapassar um momento delicado de sua vida. Ao Rogério, meu cunhado, pela força. À minha sogra, Stella, pelo apoio. À Dona Maria Diagonel e família pela sabedoria, carinho e amizade ao longo desses anos. Mesmo há algum tempo separados, ao meu falecido avô, Victório, cujo incentivo foi crucial no início da minha vida científica. Nos momentos difíceis o apoio e o incentivo de vocês me ajudaram muito.

Ao Prof. Ortiz por acreditar que poderia fazer um bom trabalho. Pelo incentivo quando tudo parecia complicado. Por estar sempre pronto para longas discussões, muitas vezes até altas horas, sobre medidas, resultados e ciência em geral. Por fim, por mostrar via exemplo que é importante se dedicar e se preocupar com a formação do estudante.

I am very grateful to Alejandro V. Silhanek, who kindly allowed me to work with him in Leuven. For teaching me a lot about structured superconductors. Also for helping me in some hard moments. Thanks a lot!

Ao Prof. Fabiano Colauto, pelas discussões que levaram a construir este trabalho. Além disso, pela imprescindível habilidade com as estações experimentais do GSM, principalmente a de Imageamento por Magneto-ótica.

Também ao Prof. Dr. Paulo Noronha Lisboa Filho pelo incentivo nos anos de graduação, mestrado e também no doutorado. Ao Zad (Prof. Rafael Zadorosny) pelas discussões no início do trabalho e também pela amizade ao longo desses anos.

Agradeço profundamente aos amigos e colegas do Grupo de Supercondutividade e Magnetismo: Alexandre J. Gualdi (algoritmo do César), André Varela (É melhor não dizer nada! Shhhh...), César V. Deimling (Zinguem danguem zinguem!), Cláudio (“Waldemá!”), Danusa (Danuzzón!), Driele (ah Dona Dri!), Fernanda (ah DONA Fernanda!), Korllvary (e o lagarto do RU!), Leonardo (sempre bem humorado), Marlon (Pisco!), Jerê (Ricardo!) e Pedro Schio (CGS ou SI!? E o vidraceiro?!). Também aos amigos Rafael R. G. Paranhos (Joe!) e Adriano V. de Carvalho (Zé fofinho!).

I would like to thank Prof. Victor V. Moshchalkov for the opportunity to work in the

INPAC, KU Leuven (Leuven, Belgium). I want to express my gratitude to Jo Cuppens, Weldeslassie Ataklti, Denitza Denkova, and Dorin Cerbu for helping me in the lab and also outside it. Thank you all for the experience that I had in Leuven! I would also like to thank Jørn Inge Vestgården for the simulations using the thermomagnetic model presented in Chapter 8 and for the interesting discussions.

À FAPESP (Fundação de Amparo à Pesquisa do Estado de São Paulo) pelo apoio financeiro durante o desenvolvimento deste trabalho.

Filho é um ser que nos emprestaram para um curso intensivo de como amar alguém além de nós mesmos, de como mudar nossos piores defeitos para darmos os melhores exemplos e de aprendermos a ter coragem. Isso mesmo! Ser pai ou mãe é o maior ato de coragem que alguém pode ter, porque é se expor a todo tipo de dor, principalmente da incerteza de estar agindo corretamente e do medo de perder algo tão amado. Perder? Como?

Não é nosso, recordam-se? Foi apenas um empréstimo!

Autoria desconhecida. Falsamente atribuído ao escritor José Saramago.

Abstract

Avalanches are sudden dramatic phenomena that occur in nature. The technique of magneto-optical imaging (MOI) has allowed us to observe abrupt flux entrances in superconductors, the so-called *flux avalanches*, due to thermomagnetic instabilities in the vortex matter. Their morphology is fascinating, especially in superconducting thin films, where they develop in dendritic patterns. From a practical point of view, the flux avalanches undermine applications of superconducting thin films. In the last years, however, several steps have been reached to fully understand the fundamental physics of the phenomenon and also on how to suppress their occurrence.

The present thesis deals with the study of flux avalanches in structured superconducting thin films. We have studied crystalline Nb and amorphous Mo₇₉Ge₂₁ thin films decorated with arrays of antidots (ADs or holes) produced by electron beam lithography. The magnetic response of these specimens has been investigated by means of MOI, dc magnetization and ac susceptibility. Firstly, we have established a link among those three techniques in the regime dominated by flux avalanches. We have observed that the reentrant behavior in the ac susceptibility at low temperatures occurs as a consequence of flux avalanches. Essentially, there is reuse of the channels created by the first ac cycle in a regime where the signal is weakly dependent on the temperature. Our results show that measurements of ac susceptibility versus ac field amplitude can be used to detect flux avalanches, since the signature of the flux avalanches appears as noisy curves of both ac susceptibility components. As a consequence, the critical current density as a function of temperature [$J_c(T)$] obtained by using the Bean model – whose validity is assured by Cole-Cole plots – is smooth for higher temperatures and, below a certain temperature onset, a non-smooth and noisy behavior takes place due to the avalanches. The temperature dependence of $J_c(T, H)$ was determined for different values of the applied magnetic field. The stability/instability frontier was then identified as the limiting temperature below which the curve $J_c(T, H)$ becomes noisy, indicating the occurrence of avalanches. Associated with this limiting temperature, the threshold critical current density to trigger avalanches is essentially independent of the magnetic field. This frontier corresponds to the upper threshold limit for the occurrence of avalanches.

The effect in a thin film of a graded distribution of ADs which follows nearly the flux profile described by the Bean model has been studied. Compared to the uniform distribution, there is an increase of the critical current density at low fields. Moreover,

the flux avalanches, highly induced by the presence of an array of ADs, have their activity reduced in temperature and magnetic field. For the first time, flux avalanches have been visualized in amorphous $\text{Mo}_{79}\text{Ge}_{21}$ thin film, both in plain and decorated thin films.

Finally, we have investigated the influence of the lattice symmetry and AD geometry on the flux avalanche morphology. We have observed avalanches with the habit of forming trees where the trunk is parallel to the main axis of the square lattice and the branches form angles of 45 degrees. In addition to that, we have found an anisotropic penetration in a Nb thin film decorated with a square lattice of triangular ADs. Besides that, a sample having one half of the ADs in the form of squares, and the other half being circles, has been observed to present avalanches of different morphologies on each of its halves. We have also studied an a-MoGe thin film with a centered rectangular 2D Bravais lattice with square ADs which shows penetrations with different angles depending on the edge. The overall features of the avalanches, and in particular the 45-degree direction of the branches, have been confirmed by numerical simulations using the thermomagnetic model.

Keywords: superconductivity, structured thin films, flux avalanches, magneto-optical imaging

Resumo

Avalanches são eventos repentinos e dramáticos que ocorrem na natureza. A técnica de imageamento por magneto-ótica (MOI) tem permitido visualizar a penetração abrupta de fluxo em supercondutores, as chamadas avalanches de fluxo, que ocorrem devido a instabilidades termomagnéticas na matéria de vórtices. A morfologia dessas avalanches de fluxo em filmes finos supercondutores prístinos é singular e se desenvolve de maneira dendrítica, isto é, com ramificações. Do ponto de vista prático, as avalanches de fluxo são prejudiciais para aplicações dos filmes finos supercondutores. Nos últimos anos, no entanto, tem-se alcançado um bom entendimento da física básica do fenômeno, bem como maneiras para suprimir essas avalanches.

Esta tese trata do estudo de avalanches de fluxo em filmes finos com uma estrutura de defeitos. Para tal, usamos filmes finos cristalinos de Nb e amorfos da liga $\text{Mo}_{79}\text{Ge}_{21}$ decorados com arranjos de *antidots* (ADs), ou buracos, produzidos por litografia por feixe de elétrons. A resposta magnética desses filmes foi investigada através de MOI, magnetização dc e suscetibilidade ac. Na primeira parte dos resultados, uma conexão entre essas técnicas foi estabelecida no regime de avalanches de fluxo. Foi observado que o comportamento reentrante da suscetibilidade ac em baixas temperaturas ocorre devido às avalanches de fluxo. Essencialmente, há o reuso dos caminhos ou canais criados pelo primeiro ciclo ac em um regime em que o sinal é fracamente dependente da temperatura. Esses resultados também mostraram que a suscetibilidade ac pode ser usada para detectar avalanches de fluxo, seja pela construção da curva de corrente crítica dependente da temperatura $J_c(T)$ ou monitorando o ruído nas curvas do tipo Cole-Cole. Assim, a fronteira de instabilidades termomagnéticas/estabilidade foi construída variando-se o campo dc aplicado, tendo sido obtido, um limiar constante de $J_c(T)$ para o disparo das avalanches. Essa observação está de acordo com o modelo termomagnético e refere-se ao limite superior da ocorrência das avalanches de fluxo.

Também foi estudado o efeito da inserção de um arranjo de *antidots* distribuídos de maneira gradiente, que segue aproximadamente a distribuição de fluxo descrita pelo Modelo de Bean. Comparada com uma distribuição uniforme, um aumento da densidade de corrente crítica foi observada para a região de baixos campos. Além disso, as avalanches de fluxo, que são altamente induzidas pela presença de ADs, apresentaram uma redução em sua ocorrência, tanto em magnitude do campo magnético aplicado quanto em temperatura. Pela primeira vez, foram observadas avalanches de fluxo em filmes finos amorfos de $\text{Mo}_{79}\text{Ge}_{21}$ com e sem uma rede de ADs.

Por fim, a influência da simetria da rede e da geometria do antidot na morfologia das avalanches de fluxo foi investigada. Para filmes finos decorados com uma rede quadrada de ADs quadrados, as avalanches têm o tronco paralelo ao eixo principal da rede de ADs, com ramificações em ângulos de 45 graus como em uma árvore de Natal. Além disso, penetrações abruptas anisotrópicas foram vistas em um filme fino de Nb decorado com uma rede quadrada de ADs triangulares. Uma mudança na morfologia das avalanches também foi observada em um filme com metade dos ADs quadrados e a outra metade circular. Também foram observadas penetrações com diferentes ângulos em uma rede retangular centrada de ADs quadrados dependendo da borda. Por fim, as características gerais das avalanches, em particular a de ramificações em 45 graus, foram confirmadas por simulações numéricas usando o modelo termomagnético.

Palavras-chave: supercondutividade, filmes finos estruturados, avalanches de fluxo, imageamento por magneto-ótica

Contents

Acknowledgements (Agradecimientos)	iv
Abstract	vii
Resumo	ix
1 Overview	1
2 Basic aspects of superconductivity	5
2.1 Superconductivity: basic concepts and historical notes	5
2.2 London model	6
2.3 Ginzburg-Landau theory	8
2.3.1 Clean and dirty limits of λ and ξ	11
2.4 Type I and Type II superconductors	12
2.5 Flux quantization, vortex structure, and the Abrikosov lattice	15
2.6 Real superconductors: the pinning centers	19
2.6.1 Intrinsic pinning	20
2.6.2 Artificial pinning	21
2.7 Critical state models: the Bean model	23
2.7.1 Slab/cylinder: parallel configuration	25
2.7.2 Thin film: perpendicular configuration	26
3 Flux avalanches in superconductors	31
3.1 Introduction	31
3.2 Thermally driven avalanches: flux avalanches	32
3.2.1 Flux avalanches in thin films	35

3.2.2	The thermomagnetic model	37
3.3	Dynamic properties of the flux avalanches	39
3.4	Avoiding flux avalanches	44
4	Experimental techniques	47
4.1	Sample preparation	47
4.1.1	Electron beam lithography	47
4.1.2	Pulsed laser deposition	49
4.1.3	Dc-magnetron sputtering	51
4.2	Sample characterization	51
4.2.1	Structural characterizations based on X-ray	52
4.2.2	Atomic force microscopy	53
4.2.3	Scanning electron microscopy	53
4.3	Magnetic measurements	54
4.3.1	Magneto-optical imaging	54
4.3.1.1	MOI workstation at GSM/São Carlos	57
4.3.2	SQUID: dc measurements	59
4.3.3	PPMS: ac measurements	62
4.3.3.1	Ac susceptibility details and Cole-Cole curves	64
5	Visualizing ac susceptibility and ac field effects on flux avalanches*	69
5.1	Introduction	69
5.2	Samples and experimental techniques	70
5.3	Results and discussion	72
5.4	Conclusions	81
6	Threshold of critical current densities to trigger flux avalanches in superconducting thin films	82

6.1	Introduction	82
6.2	Instability region in superconducting thin films	84
6.3	Experimental details	86
6.4	Results and discussions	86
6.5	Conclusions	91
7	Enhancement of pinning properties of superconducting thin films by graded pinning landscapes*	92
7.1	Introduction	92
7.2	Experimental details	94
7.3	Results and discussions	95
7.4	Conclusions	98
8	Guidance and morphology of flux avalanches in superconducting films decorated with lattices of antidots*	99
8.1	Introduction	99
8.2	Samples and experimental techniques	101
8.3	Results and discussions	102
8.4	Conclusions	110
9	Conclusions and perspectives	111
	Appendix A – Shape and profile studies of antidots in decorated thin films	113
	Appendix B – Current crowding effects in superconducting corner-shaped Al microstrips*	117
B.1	Introduction	117
B.2	Samples and experimental techniques	119
B.3	Results and discussion	119
B.4	Conclusions	123

List of Publications	125
-----------------------------	------------

References	127
-------------------	------------

1 *Overview*

Superconductivity is an important area in Condensed Matter Physics. Its mechanisms are not completely understood yet for all superconducting materials, in spite of its discovery more than 100 years ago. Since then, five Nobel prizes in topics directly related to superconductivity have been awarded: Heike Kamerlingh Onnes in 1913, for his studies on the matter in low temperatures; John Bardeen, Leon Neil Cooper, and John Robert Schrieffer (1972) for the microscopic theory of superconductivity; Brian David Josephson, Leo Esaki, and Ivar Giaever because of their studies in tunneling in semiconductors and superconductors (1973); Johannes Georg Bednorz and Karl Alexander Müller for the discovery of High Temperature Superconductors (1987); and Alexei Alexeevich Abrikosov, Vitaly Lazarevich Ginzburg, and Anthony James Leggett in 2003 for their pioneering contributions to the theory of superconductors and superfluids [1].

The work of the last Nobel Prize laureates were especially important for describing the behavior of superconductors immersed in a magnetic field. Abrikosov [2], using the theory developed by Ginzburg and Landau [3], found that the magnetic field penetrates into the so-called type II superconductors as quantized units of flux, forming the mixed state. In pure superconducting materials, these entities organize themselves in a regular hexagonal lattice. However, defects commonly present in real materials act as pinning centers, creating an attractive potential for the vortices inside the superconductors and destroying the long-range order. The term *Vortex Matter* was coined to refer to the vortex system residing in the mixed state of a type II superconductor, which can be organized in different states of aggregation: solid, liquid, and glassy. After the discovery of the High Temperature Superconductors (HTS) in 1986 [4], the liquid and glassy phases have effectively entered the scene, since thermal energies involved made possible the melting of the vortex solid below the critical temperature.

One of the most fascinating issues in the study of Vortex Matter is the occurrence of an abrupt phenomenon of flux entrance. This phenomenon has risen special interest since it has been observed directly by means of Magneto-optical imaging (MOI), revealing an astonishing dendritic morphology in superconducting thin films. From applications point

of view, the importance of detecting and understanding magnetic flux avalanches lies in the fact that it modifies the current-carrying capability of the specimen. Then, it might undermine potential technological applications, such as, for example, superconducting fault current limiters, as pointed out in a Technical Report entitled *Basic research needs for superconductivity* [5] published in 2006 by the U. S. Department of Energy.

This thesis is a natural continuation of some of the last doctorate studies developed at the *Grupo de Supercondutividade e Magnetismo* (GSM) in *Universidade Federal de São Carlos* (UFSCar). Fabiano Colauto [6] made the first investigations on flux avalanches in plain films, as well as the magnetic braking effect of a metal foil on top of them. Besides that he has assembled the magneto-optical imaging setup in the group; Rafael Zadorosny [7] studied the vortex dynamics in decorated thin films, firstly nanoindentated ones and after lithographically patterned with antidots; Ana Augusta M. de Oliveira [8] investigated in depth systems with controlled defects by using the third harmonics of the complex ac susceptibility. Besides those influences above described, the period that I spent in Leuven has also been significant to the development of the present work, because of the exposure to different kinds of techniques and problems.

The aim of this thesis is to clarify the occurrence and the morphology of flux avalanches in superconducting thin films of crystalline Nb and amorphous $\text{Mo}_{79}\text{Ge}_{21}$, with and without an antidot array prepared by electron beam lithography, by means of MOI, dc magnetization and ac susceptibility measurements. We have investigated the signature of the flux avalanches in ac susceptibility and the threshold for its occurrence, showing that the thermomagnetic model picture is perfectly adequate to describe the results. The effects of a graded distribution of antidots on the critical current density and on the occurrence of flux avalanches were also traced, as well as the effects of antidot geometry and lattice symmetry on the morphology of flux avalanches. This thesis is organized as follows:

The theoretical framework for superconductivity is addressed in Chapter 2. It is shown in details the London model and the Ginzburg-Landau theory, as well as the existence of type I and type II superconductors, the flux quantization, the vortex structure and the Abrikosov lattice. The presence of pinning centers in the superconductor is treated, as well as the consequences of introducing artificial pinning centers for the superconducting properties. In the end, the Critical State Models and the effect of thin film geometry on the Bean critical state model are discussed.

Chapter 3 gives a short introduction to avalanches in superconductors. Firstly, it

summarizes the dynamical development of the vortex landscape in the Bean model by non-destructive *vortex avalanches*. Nonetheless, the current understanding of the *flux avalanches* treated in this thesis is based on the occurrence of thermomagnetic instabilities in the superconductors which are explained by the existence of a positive feedback: flux movement \rightarrow heat generation \rightarrow locally temperature increase \rightarrow pinning force decrease \rightarrow more flux movement etc. The chapter is devoted to thorough discussion of the thermomagnetic model, including some important theoretical and experimental results relating to this intriguing phenomenon.

Chapter 4 contains the details of preparation techniques used to fabricate the array of antidots and the deposition techniques as well. The structural characterization of the thin films is also described in this chapter. The measurement platforms PPMS and MPMS are thoroughly described as well the ac susceptibility technique. The evolution of the Faraday-active crystal used to reveal the flux distribution is reviewed and the MOI workstation at GSM/São Carlos is described in detail.

The first results are reported in Chapter 5. MO images were used to prove that the reentrance in ac susceptibility versus temperature measurements is really linked to the occurrence of flux avalanches. We also show the correspondence between MOI, dc magnetization and ac susceptibility to recognize the existence of these abrupt events. An alternative way of determining the threshold critical current density (J_c^{th}) to trigger flux avalanches is discussed in Chapter 6. The existence of J_c^{th} is demonstrated by means of the thermomagnetic model and the frontier of where the avalanches take place, $H^{th}(J_c)$, was determined.

Chapter 7 deals with a comparative analysis among a plain a-Mo₇₉Ge₂₁ film, a second film with a uniformly distributed array of antidots, and a thin film with a graded distribution of antidots. The results have shown that the graded array increases the critical current density and decreases the avalanche activity in comparison with the corresponding results for a uniform array. Moreover, we report the first observation of flux avalanches in a plain a-Mo₇₉Ge₂₁ thin film.

An investigation of the flux avalanche morphology is presented in Chapter 8. The influence of different antidot lattice symmetries and AD geometries on the branching was traced. In thin films of crystalline Nb and a-Mo₇₉Ge₂₁ decorated with a square lattice of square ADs, the secondary branches develop at 45 degrees from the main trunk, in a pattern that remind us of a *Christmas tree*. Simulations using the thermomagnetic model in a film with a square lattice of square ADs have confirmed our observations. Besides

that, a film decorated with a square lattice of triangular ADs have shown anisotropic penetration, depending on the direction relative to the triangle, i.e., if the flux enters facing a tip or an edge of the AD. Branching with 90 degrees appear in a film with a square lattice of circular ADs, whereas in a film with a centered rectangular lattice of square ADs the avalanche morphology is clearly defined by the lattice geometry. In order to explain such branching of the flux avalanches, we have used the idea published in a very recent paper by us, for L-shaped microbridges, where flux penetrates easier into the inner concave angle, due to a crowding effect on the currents. This work is presented as an appendix (Appendix B) to the thesis. Moreover, Appendix A shows an investigation, using AFM and SEM, of the spatial quality of the ADs of the decorated thin films studied here. The Nb film with ADs of $0.4 \mu\text{m}$ and lattice parameter of $1.5 \mu\text{m}$, presented in Chapter 5, has rounded ADs, whereas the a-MoGe thin film with the same AD size and lattice parameter, presented in Chapter 8, has sharp square ADs being this the reason the different avalanche morphologies.

Finally, we show the Conclusions and Perspectives in Chapter 9, discussing some of the results and pointing out some directions for further investigations.

2 *Basic aspects of superconductivity*

This chapter deals with the main characteristics of superconductivity, the phenomenological theories and their implications, such as the discovery of the basic lengths, penetration depth and coherence length, defining the type of superconducting material, the penetration of the magnetic field in the case of type II superconductors, in form of flux vortices, and how these vortices are distributed throughout the material. In the end, the impact of thin film geometry on the magnetic response will be treated.

2.1 Superconductivity: basic concepts and historical notes

At the beginning of the 20th century science underwent an enormous and deep development, especially Physics. The introduction of new ideas and concepts associated with the quantum mechanics led to breakthroughs, resulting in several advances in the comprehension of properties of the matter. In this context, the physicist Heike Kamerling Onnes, who worked in Leiden (The Netherlands) with cryogenic systems, liquefied helium in 1908, allowing him to reach temperatures as low as 4.2 K and thus marked a new chapter in history of low temperature physics. Once this was achieved, the next step was developing controlling apparatus which provided essential tools to study materials at low temperatures. Three years later, in 1911, he and his team were exploring the influence of impurities on the electrical resistance of metals at low temperatures [9], and they observed that the resistivity of pure mercury dropped suddenly more than four orders of magnitude in a narrow temperature range around 4.2 K, which was called the critical temperature (T_c). This property (*perfect conductivity*) was recognized as being of great significance for applications, such as coils to generate high magnetic fields [10]. Moreover, another striking signature of the superconducting materials was observed by Walter Meissner and Robert Ochsenfeld in 1933 [11, 12]. They found out that lead and tin cylinders, immersed in an external field, expelled the magnetic flux below their T_c of 7.2 K and 3.7 K, respectively, independent of their magnetic history, whether they had first been cooled and then subjected to a magnetic

field or vice-versa. This effect was called *perfect diamagnetism* or Meissner-Ochsenfeld effect, but nowadays called only Meissner effect, and could not be explained only considering perfect conductivity, since a hypothetical perfect conductor would not exclude magnetic flux from its interior decreasing the temperature below T_c under an applied field. Thereby, the perfect conductivity and the perfect diamagnetism are two independent and intrinsic features of the superconducting state.

In order to fully understand this phenomenon, the perfect diamagnetism was firstly treated by the London brothers [13], in 1935. Later on, in 1950, V. Ginzburg and L. Landau [3] applied the phase transition theory for the superconducting state and obtained a more complete description of it. Both theories are phenomenological ones and will be treated in details in the following sections using SI units. Nonetheless, the microscopic nature of the superconductivity was proposed by J. Bardeen, L. Cooper and J. Schrieffer in 1957 [14], known as BCS theory. The main idea is the presence of an attractive interaction between two electrons, forming the so-called *Cooper pairs*, which should have opposite momenta and opposite spins. This attractive interaction is intermediated by the lattice vibrations (phonons) and became evident by means of the discovery of the isotope effect in mercury [15, 16], where the critical temperature of the isotopes is proportional to \sqrt{M} , where M represents the mass of the isotope. Although the BCS theory describes the mechanism for superconducting metals, some alloys, intermetallic compounds, and ionic compounds, it does not describe the mechanism for the *High Temperature Superconductors (HTS)*, discovered in 1986 [4], and for other unconventional superconductors such as heavy fermions, organics and iron-based compounds [17, 18, 19]. The HTS materials are ceramics, with Cu-O planes in their crystallographic structures, and exhibit superconductivity above the limit of approximately 30 K implied by the BCS theory. For example, the mechanisms of superconductivity in YBCO ($\text{YBa}_2\text{Cu}_3\text{O}_{7-\delta}$) [20], which was the first superconducting material to exceed the boiling point of liquid nitrogen (77 K), with $T_c = 92$ K cannot be accounted for by the BCS theory. In fact, this theory provides a microscopic explanation for the mechanism in some superconducting materials, but a complete description, including the unconventional superconductors, still lacks in the literature.

2.2 London model

A description of the electrodynamics of superconductivity was proposed by Fritz and Heinz London [13] in 1935. It allowed them to explain the Meissner effect, which was

reported two years earlier. This description was based on the two-fluid model for superconductivity, proposed by Gorter and Casimir [21], in which the average number of conduction electrons per unit of volume, n_t , is composed by the sum of two temperature dependent contributions for $T < T_c$: a normal fluid ($n_n(T)$) and a superfluid ($n_s(T)$). The normal fraction $n_n(T)$ is associated to the density of normal electrons, behaving as in a viscous medium, whereas the superfluidic portion $n_s(T)$ is related to the density of electrons which experience no scattering and are responsible for the impressive properties of the superconductors, called superconducting electrons or superelectrons. When $T \rightarrow T_c$, n_s tends to zero and at $T = 0$ K, all the electrons are taking part in the superconducting state. Applying the equation of motion to the portion n_s , as the Drude model for electrical conductivity in a metal [22], it leads to the first London equation, in SI units:

$$\mathbf{E} = \frac{m^*}{n_s e^{*2}} \frac{\partial \mathbf{J}_s}{\partial t} \quad (2.1)$$

where \mathbf{E} is the electric field, m^* and e^* are the effective mass and charge of the superelectrons and \mathbf{J}_s is the superconducting current density, which is given by:

$$\mathbf{J}_s = n_s e^* \mathbf{v}_s \quad (2.2)$$

where n_s and \mathbf{v}_s are the density and the velocity of the superelectrons. As described by the BCS theory, the superelectrons are composed by electron pairs – or Cooper pairs – and, thus, $m^* = 2m_e$ and $e^* = 2e$, with m_e and e the mass and the charge of the electron, respectively. Eq. (2.1) shows that in the superconducting steady state, the electric field is null, i.e., the voltage across the superconductor is zero (infinite conductivity) and the superconducting current is constant. In order to obtain the second London equation, which enables one to calculate the local field inside the superconductor, one combines Eq. (2.1) and the Maxwell equations to obtain:

$$\frac{\partial}{\partial t} \left(\nabla \times \nabla \times \mathbf{B} + \frac{\mu_0 n_s e^{*2}}{m^*} \mathbf{B} \right) = 0 \quad (2.3)$$

where \mathbf{B} is the magnetic induction and μ_0 is the magnetic permeability of vacuum.

This equation, however, is not compatible with the Meissner effect, since the magnetic field could not change temporally ($\frac{\partial \mathbf{B}}{\partial t} = -\nabla \times \mathbf{E} = 0$). Thus, the London brothers restricted the solutions to those that follow the condition $\nabla \times \nabla \times \mathbf{B} = -\frac{\mu_0 n_s e^{*2}}{m^*} \mathbf{B}$, which leads to the Meissner effect. Therefore, the second London equation is obtained as:

$$\lambda_L^2 \nabla \times \nabla \times \mathbf{B} + \mathbf{B} = 0 \quad (2.4)$$

or

$$\nabla^2 \mathbf{B} = \frac{1}{\lambda_L^2} \mathbf{B} \quad (2.5)$$

where $\lambda_L = \sqrt{\frac{m^*}{\mu_0 n_s e^* 2}}$ is known as the *London penetration depth* and it is one of the fundamental lengths of superconductivity. Besides the trivial solution $\mathbf{B} = 0$, the only possible solution for a semi-infinite superconductor* in the region $x > 0$ occurs when \mathbf{B} vanishes exponentially in the interior of a superconducting bulk, and λ_L provides the characteristic distance along which the field decays from its value at the surface in the Meissner state, where $\mathbf{B} = 0$ [17]. Indeed, the superconducting current can be written as:

$$\nabla^2 \mathbf{J}_s = \frac{1}{\lambda_L^2} \mathbf{J}_s \quad (2.6)$$

The expression above means that the currents responsible for the Meissner effect are superficial currents, also called *shielding currents*, which circulate over the distance λ_L into the superconducting bulk. This shielding currents are responsible for the null induction field ($\mathbf{B} = 0$) inside the superconductor. It means that the current generates a magnetization equals to the opposite of the field strength ($\mathbf{M} = -\mathbf{H}$).

The London approach assumes that the density of Cooper pairs $n_s(T)$ is constant along the whole superconductor, as a consequence of its local character, where the fields and currents are determined at the point \mathbf{r} . When non-local characteristics are taken into account, i.e., $\mathbf{J}_s(\mathbf{r})$ depends on the magnetic vector potential, \mathbf{A} , around the considered point \mathbf{r} , as showed by A. B. Pippard [23], the second fundamental length of the superconductivity emerges, known as coherence length, which will be discussed within the scope of the Ginzburg-Landau (GL) theory.

2.3 Ginzburg-Landau theory

In 1950, V. L. Ginzburg and L. D. Landau proposed their theory for superconductivity [3] based on the Landau theory for second-order phase transitions developed earlier [24]. In zero magnetic field, the transition from the normal to the superconducting state is a second-order phase transition, experimentally supported by the discontinuity on the specific heat at $T = T_c$ [17]. The main idea of the Landau theory is the existence of an order parameter to describe a transition from a disordered to an ordered phase [25]. For the case of a superconductor, a complex order parameter, $\psi(\mathbf{r})$,

*Neglecting demagnetization effects.

is defined as:

$$\psi(\mathbf{r}) = |\psi(\mathbf{r})| e^{-i\varphi(\mathbf{r})} \quad (2.7)$$

where $\varphi(\mathbf{r})$ is a phase factor. This order parameter is employed to describe the phase transition, being null above T_c and nonzero below T_c . Physically, the order parameter is related to the density of superconducting electrons n_s , as following:

$$n_s = |\psi|^2 \quad (2.8)$$

According to the phase transition theory, the free energy is real and should reach a minimum value. As a consequence, it can be expanded in series of $|\psi|^2$ for temperatures near T_c and terms of order larger than two (in this case $|\psi|^4$) can be neglected. The Gibbs free energy per unit volume G_s in the superconducting state, in the presence of an external field, is then:

$$G_s = G_n + \alpha(T) |\psi|^2 + \frac{\beta}{2} |\psi|^4 + \frac{1}{2m^*} |(-i\hbar\nabla + e^* \mathbf{A}) \psi|^2 + \frac{\mathbf{B}^2}{2\mu_0} \quad (2.9)$$

where G_n is the free energy density of the normal state, \hbar is the Planck constant h divided by 2π , $\alpha(T)$ and β are phenomenological parameters of the expansion. The second and third terms on the right side of the equation are related to the expansion, the fourth represents the kinetic energy of the superelectrons, and the fifth refers to the energy density due to the magnetic field. Minimizing the free energy with respect to $|\psi|^2$ and with respect to \mathbf{A} leads to two coupled differential equations, named as the first and the second Ginzburg-Landau equations, respectively:

$$\alpha\psi + \beta |\psi|^2 \psi + \frac{1}{2m^*} (-i\hbar\nabla + e^* \mathbf{A})^2 \psi = 0 \quad (2.10)$$

$$\mathbf{J}_s = -\frac{ie^*\hbar}{2m^*} [\psi^* \nabla \psi - \psi \nabla \psi^*] - \frac{e^{*2}}{m^*} |\psi|^2 \mathbf{A} = \frac{e^{*2}}{m^*} |\psi|^2 \left(\frac{\hbar}{e^*} \nabla \varphi - \mathbf{A} \right) \quad (2.11)$$

Eq. (2.10) allows one to determine the spatial variation of the order parameter, whereas Eq. (2.11) enables one to know the distribution of the supercurrent in a superconducting material. In the absence of field ($\mathbf{A} = 0$) with homogeneous boundary conditions, the equations above show two special solutions: (i) $\psi = 0$, which describes the normal state; (ii) $\psi = \psi_\infty$, with $|\psi_\infty|^2 = \frac{|\alpha|}{\beta}$, where ψ_∞ is the order parameter in the superconductor far away from the surface. This solution describes the superconducting state exhibiting the Meissner effect, neglecting surface effects. In order to obtain a minimum free energy, the values of α and β are $\alpha = \alpha(T) = \alpha_0(T - T_c)$ with $\alpha_0 > 0$, and

$\beta > 0$.

It is possible to determine the second fundamental length of superconductivity from a condition similar to that described above. Considering a boundary condition of being near the surface, for a semi-infinite superconductor at $x > 0$ in the absence of field, Eq. (2.10) can be written by means of a new function f , defined as $f = \psi/\psi_\infty$. In this case, one has

$$\frac{\hbar^2}{2m^* |\alpha(T)|} \nabla^2 f + f(1 - f^2) = 0 \quad (2.12)$$

where

$$\xi^2 = \frac{\hbar^2}{2m^* |\alpha(T)|} \propto \frac{1}{1 - \frac{T}{T_c}} \quad (2.13)$$

has a square length dimension. Thus, the order parameter ψ for $x \sim 0$ is obtained as being:

$$\psi(x) = \psi_\infty \tanh\left(\frac{x}{\sqrt{2}\xi}\right) \quad (2.14)$$

Therefore, ξ determines the scale of distances for spatial variations of the order parameter ψ , called the *coherence length*. It defines the typical size of the Cooper pairs, i.e., the minimum length within which the number of superelectrons varies significantly [2].

The penetration depth λ_L can also be obtained through the GL theory. In a weak field, the order parameter remains almost constant and can be substituted by ψ_∞ in Eq. (2.11),

$$\mathbf{J}_s = -\frac{e^{*2}}{m^*} |\psi_\infty|^2 \mathbf{A} = -\frac{1}{\mu_0 \lambda_L^2} \mathbf{A} \quad (2.15)$$

By applying $\nabla \times \mathbf{J}_s$ and the Maxwell equation $\nabla \times \mathbf{B} = \mu_0 \mathbf{J}$, one has:

$$\nabla^2 \mathbf{B} = \frac{\mu_0 e^{*2} |\psi_\infty|^2}{m^*} \mathbf{B} \quad (2.16)$$

which is similar to the second London equation (Eq. (2.5)) written in other terms, where the penetration length equals to

$$\lambda_L^2 = \frac{m^* \beta}{\mu_0 e^{*2} |\alpha(T)|} \propto \frac{1}{1 - \frac{T}{T_c}} \quad (2.17)$$

Thus, the penetration depth and the coherence length can be obtained from the GL theory, as well as their temperature dependences close to T_c . The temperature range is the main limitation of this theory, since it is valid only for $T \sim T_c$. Although the GL theory is phenomenological, Gor'kov [26] in 1959 demonstrated that it is, in fact, a limiting form

of the microscopic theory, suitable to T near T_c . However, it is also a powerful theory, since it describes the two forms of behavior of the superconductors in the presence of a magnetic field, the flux quantization, the characteristics of the vortex and its interactions in the mixed state.

2.3.1 Clean and dirty limits of λ and ξ

Since the London penetration depth and the coherence length have been described by the GL theory, it is important to take into account the presence of impurities (and defects) and their influence on these lengths [27, 28]. Depending on the *mean free path* l_e of the electron and the *BCS coherence length* ξ_0 introduced by the BCS theory, given by:

$$\xi_0 = 0.18 \frac{\hbar v_F}{k_B T_c} \quad (2.18)$$

where k_B is the Boltzmann constant and v_F is the Fermi velocity ($\sim 10^6$ m/s in metals), there are two limiting cases: (i) the *clean limit* when $l_e \gg \xi_0$, generally for pure metals, and (ii) the *dirty limit* when $l_e \ll \xi_0$, for alloys and metals with defects and impurities.

In the **dirty limit**, the penetration depth $[\lambda(T)]$ and the coherence length $[\xi(T)]$ are

$$\xi(T) = 0.855 \sqrt{\xi_0 l_e} \left(1 - \frac{T}{T_c}\right)^{-\frac{1}{2}} \quad (2.19)$$

$$\lambda(T) = 0.64 \lambda_L(0) \sqrt{\frac{\xi_0}{l_e}} \left(1 - \frac{T}{T_c}\right)^{-\frac{1}{2}} \quad (2.20)$$

where $\lambda_L(0)$ is the penetration depth obtained by the London theory at $T = 0$ K. In the **clean limit**, they are:

$$\xi(T) = 0.74 \xi_0 \left(1 - \frac{T}{T_c}\right)^{-\frac{1}{2}} \quad (2.21)$$

$$\lambda(T) = 0.71 \lambda_L(0) \left(1 - \frac{T}{T_c}\right)^{-\frac{1}{2}} \quad (2.22)$$

An important consequence of the GL theory is the Ginzburg-Landau parameter κ defined as:

$$\kappa = \frac{\lambda(T)}{\xi(T)} \quad (2.23)$$

which is the parameter used to categorize the superconductor as type I or type II. Moreover, the parameter is independent of the temperature, since the temperature dependence is the same both characteristic lengths at $T \sim T_c$.

2.4 Type I and Type II superconductors

The superconducting materials can be distinguished into two kinds, type I and type II, depending on their behavior in the presence of an applied field. Considering a normal-superconductor interface and neglecting any demagnetization effect, the surface energy (σ_{ns}) given by the difference between the Gibbs free energy per unit area of a homogeneous phase (normal or superconducting) and a mixed phase (region where the superconductivity is not completely established, where $\mathbf{B} \neq 0$) can be calculated by the GL theory [17]. Hence, the surface energy is:

$$\sigma_{ns} \approx \frac{\mu_0 H_c^2}{2} (\xi - \lambda) \quad (2.24)$$

where H_c is the critical magnetic field.

From the Eq. (2.24), two different situations arise depending on the sign of σ_{ns} . For superconducting materials with $\xi > \lambda$ or more specifically, for $\kappa < \sqrt{2}/2$, the surface energy is positive, which means that a homogeneous phase is more favored than the mixed phase, where superconductivity can survive with magnetic flux. Consequently, the superconductor will undergo an abrupt transition into the normal state at $H = H_c$. Only two states are possible: the normal state or the superconducting state with total exclusion of the magnetic field (Meissner state), as can be seen in the magnetic field versus temperature (HT) diagram in Fig 2.1a. These materials are known as type-I superconductors.

On the other hand, type II superconductors are materials for which $\lambda > \xi$ or $\kappa > \sqrt{2}/2$. In this case $\sigma_{ns} < 0$, leading to the formation of normal regions with magnetic flux within the superconducting state. However, the free energy is the lowest when maximizing the

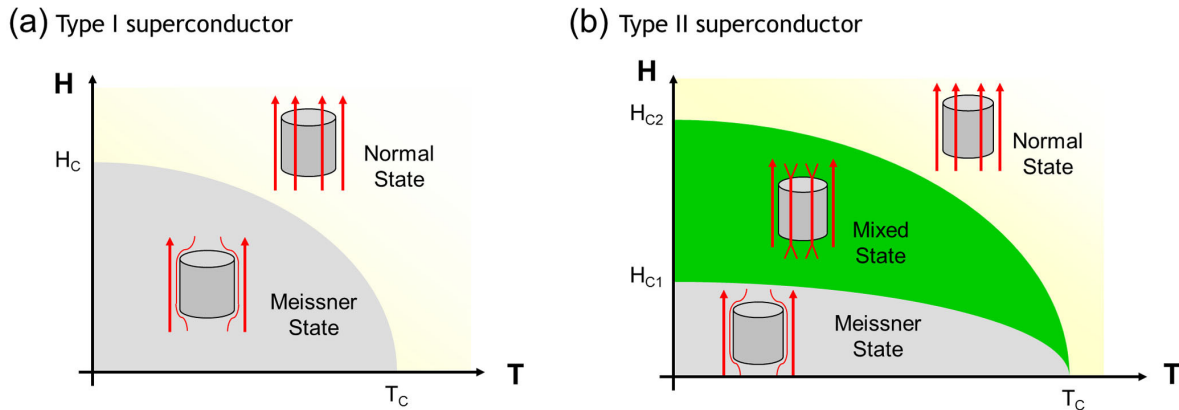


Figure 2.1: Schematic representation of the magnetic field versus temperature (HT) diagram of (a) Type I and (b) Type II. Figure adapted from [29].

surface area between the normal and the superconducting phases. Therefore, the flux penetrates through separated filaments, called *fluxoids* or *vortices*, having radius ξ and carrying one flux quantum (ϕ_0):

$$\phi_0 = \frac{h}{e^*} = \frac{h}{2e} = 2.07 \cdot 10^{-15} \text{ T.m}^2 = 20.7 \text{ G.}\mu\text{m}^2 \quad (2.25)$$

where h is the Planck constant.

From the difference between the Gibbs free energy in the superconducting and the normal states, it is possible to determine the *thermodynamical critical field* $H_c(T)$ for the two kinds of superconductors given as:

$$H_c(T) = \frac{\phi_0}{2\sqrt{2}\pi\mu_0\xi(T)\lambda(T)} \quad (2.26)$$

A type II superconductor has at least two critical fields, the *lower critical field* (H_{c1}) and the *upper critical field* (H_{c2}). The superconductor is in the Meissner state up to H_{c1} , whereas the superconducting state vanishes completely above H_{c2} and the normal state takes place. Between H_{c1} and H_{c2} , it is energetically favorable for vortices to penetrate the superconductor, enabling the *mixed state*, described by A. A. Abrikosov [2]. Fig. 2.1b illustrates these three phases in a schematic HT diagram. The temperature dependence of the lower critical field is given by:

$$H_{c1}(T) = \frac{\phi_0}{4\pi\mu_0\lambda^2(T)} \ln \kappa \quad (2.27)$$

while the upper critical field $H_{c2}(T)$ is

$$H_{c2}(T) = \frac{\phi_0}{2\pi\mu_0\xi^2(T)} \quad (2.28)$$

that is, when the distance between the vortices is the coherence length, the superconducting state is destroyed, as shown in Fig. 2.2c. However, a third critical field (H_{c3}) can appear in finite samples due to surface and interface effects. For the superconductor-vacuum interface of a bulk geometry its value is $H_{c3} = 1.69H_{c2}$.

Fig. 2.2 shows the different phases for the two types of superconductors for $T < T_c$. Panel (a) presents a typical magnetization versus magnetic field ($M(H)$) curve for a type I superconductor[†]. When a specimen is cooled down below T_c in a ZFC (zero field cooling)

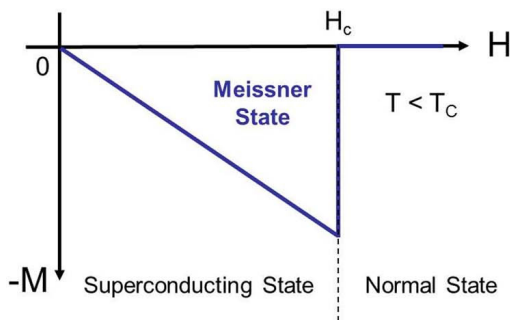
[†]This curve represents $M(H)$ for a slab or a long cylindrical sample in the parallel geometry, i.e., magnetic field parallel to cylinder axis. However, for a different shape the demagnetization factor is nonzero and the effective magnetic field becomes higher than H_c in some regions, creating a domain pattern alternating superconducting and normal regions. This is the so-called intermediate state.

procedure and then an external magnetic field is applied in a particular direction, the Meissner state ($B=0$) takes place. Using the constitutive relation:

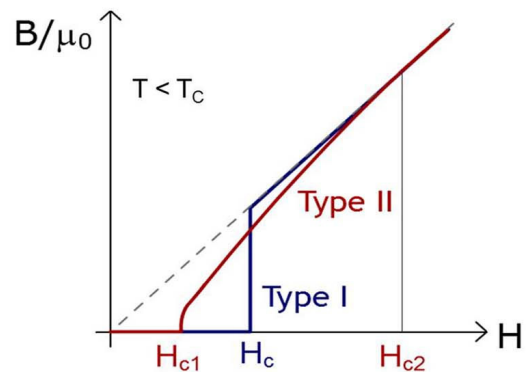
$$\mathbf{B} = \mu_0(\mathbf{H} + \mathbf{M}) \quad (2.29)$$

the magnetization is $-H$ up to the critical field. At $H = H_c$, the specimen undergoes an abrupt transition to the normal state and M becomes zero. Panel (b) shows a B/μ_0 versus H diagram for a type I superconductor with $B = 0$ up to $H = H_c$ and $B = \mu_0 H$ for $H > H_c$. The $M(H)$ curve for a type II superconductor is shown in panel (c), where the Meissner state exists up to H_{c1} . For $H_{c1} < H < H_{c2}$ the mixed state occurs and vortices come into the sample, decreasing the magnitude of the magnetization smoothly. More and more vortices penetrate into the sample up to H_{c2} where the system reaches the normal state. In the panel (b), a type II superconductor undergoes a smooth transition between H_{c1} and H_{c2} due to the progressive penetration in the mixed state. When H is increased, B approaches progressively the straight line $B/\mu_0 = H$ and reaches it at H_{c2} .

(a) Type I superconductor



(b)



(c) Type II superconductor

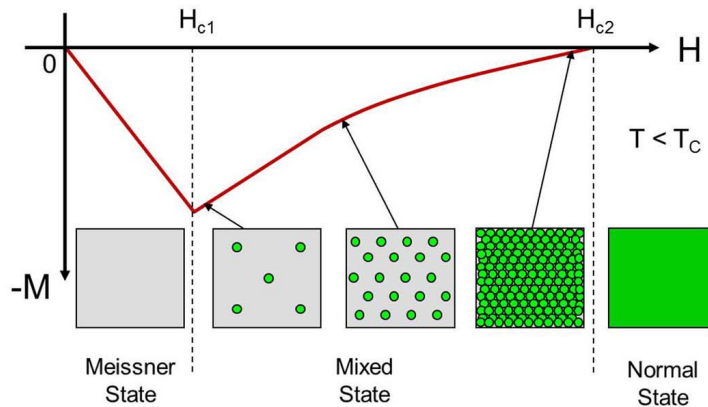


Figure 2.2: Magnetization versus magnetic field for a type I superconductor (a), (b) relation between the induction field and the magnetic field strength ($B/\mu_0(H)$) for the two types and (c) a $M(H)$ curve for a type II superconductor. Figure adapted from [27, 29].

The division of the superconductors into two types is an important triumph of the GL theory. Moreover, this theory provides an overview of the vortex, from the flux quantization to its interaction with neighbor vortices, which leads to the Abrikosov lattice. These issues will be treated in the next section.

2.5 Flux quantization, vortex structure, and the Abrikosov lattice

Before describing the vortex structure, it is important to deduce the flux quantization since the quantum nature of the superconducting state becomes evident [27]. Let us consider a superconducting ring with diameter much larger than 2λ in the Meissner state. Above H_{c1} , the amount of flux that enters into the sample and is trapped inside the hole can be calculated. Assuming a closed contour C around the hole in the superconducting region where the current density $\mathbf{J}_s = 0$ (at a distance greater than λ away from the edge), the path integral around this contour from the second GL equation [Eq. (2.11)] becomes:

$$\oint \mathbf{A} \cdot d\mathbf{l} = \frac{\hbar}{e^*} \oint \nabla\varphi \cdot d\mathbf{l} \quad (2.30)$$

Using the definition of the vector potential and the Stokes' theorem ($\oint_C \mathbf{A} \cdot d\mathbf{l} = \iint_S (\nabla \times \mathbf{A}) \cdot d\mathbf{S} = \iint_S \mathbf{B} \cdot d\mathbf{S} = \phi$) leads to

$$\phi = \frac{\hbar}{e^*} \oint \nabla\varphi \cdot d\mathbf{l} \quad (2.31)$$

The phase φ must change by multiples of 2π , since ψ is a single-valued function. Considering the Cooper pair charge, the quantization condition is

$$\phi = \frac{\hbar}{e^*} 2\pi n = n \frac{h}{2e} = n\phi_0 \quad (2.32)$$

so, the flux inside the superconducting ring must be an integral number (n) of the flux quantum ϕ_0 given by Eq. (2.25). Flux quantization has been experimentally proven in hollow tin cylinders by Deaver *et al.* [30] and independently in lead cylinders by Doll and Näbauer [31] in 1961. When the superconductor is continuous and the contour C passes through the region where $\mathbf{J}_s \neq 0$, the term on the left side of Eq. (2.11), and its integral around C , are also nonzero. Nonetheless, its sum with the term ϕ remains an integral number of ϕ_0 , so that this fluxoid quantization condition is also valid inside a continuous type II superconductor. Since enclosed flux can only take on discrete values in

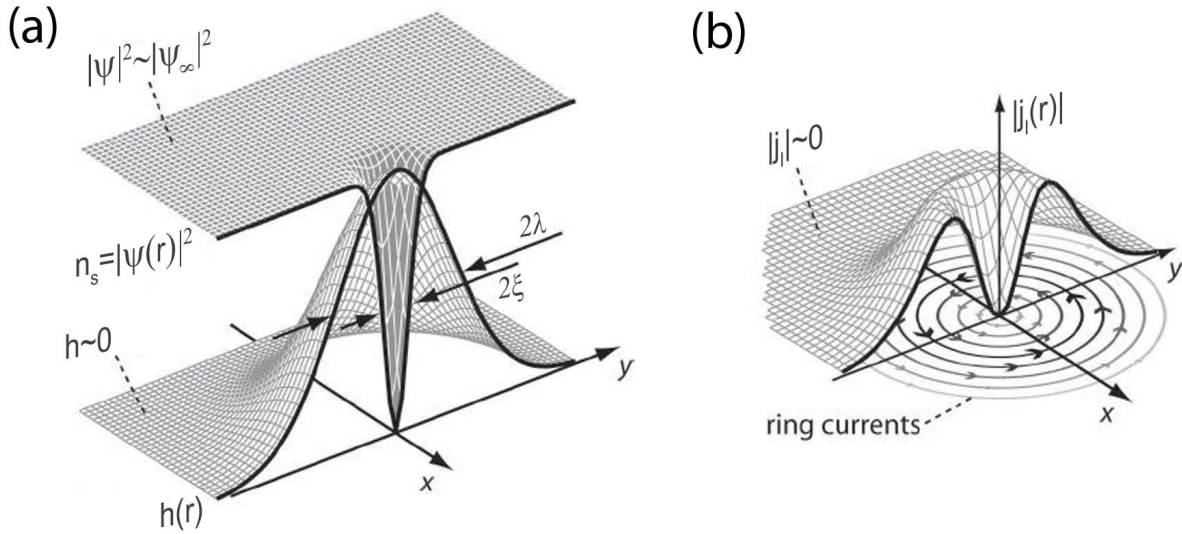


Figure 2.3: Individual vortex structure. (a) Local magnetic field and density of superconducting electrons distributions around the normal core. (b) Local critical current that behaves as current rings around the core with a maximum magnitude at λ . Figure adapted from [32].

type II superconductor in the mixed state, flux nucleates as vortices with density varying monotonously with the magnitude of the external field. Each vortex consists of a normal core with diameter 2ξ where the density of superconducting electrons (n_s) falls, as can be seen in Fig. 2.3a. At the center of the core, $n_s = 0$ and the local or microscopic magnetic field (\mathbf{h})[†] is maximum, decreasing gradually over the distance λ around the core (Fig. 2.3a), surrounded by a local current density (\mathbf{j}_i) which behaves like current rings and screens out the field as depicted in Fig. 2.3b. Therefore, a superconducting vortex is a whirl of supercurrents around a normal filament filled with one quantum of flux.

A vortex can be considered isolated as long as its interactions with other vortices and its environment is negligible. For pairs of vortices, this condition holds for separations much larger than λ . For an extreme type II superconductor with $\lambda \gg \xi$ (or $\kappa \gg 1$), the normal core is treated as a singularity. Therefore, the order parameter can be considered constant ($|\psi|^2 = |\psi_\infty|^2$) except at the normal core. From this description, the London theory can be employed to describe the magnetic field and the current density of an isolated vortex. Adding a term in the Eq. (2.4) due to the existence of the normal core, it becomes:

$$\lambda^2 (\nabla \times \nabla \times \mathbf{h}) + \mathbf{h} = \frac{\phi_0}{\mu_0} \delta_2(\mathbf{r}) \mathbf{z} \quad (2.33)$$

where \mathbf{z} is a unit vector along the vortex and $\delta_2(\mathbf{r})$ is a two-dimensional Dirac delta function at the position of the normal core ($r = 0$). Thus, the behavior of the local field

[†]The local magnetic field is related to the macroscopic induction as $\mathbf{B} = \mu_0 \bar{\mathbf{h}}$.

around the vortex has the form:

$$h(r) = \frac{\phi_0}{2\pi\mu_0\lambda^2} K_0\left(\frac{r}{\lambda}\right) \quad (2.34)$$

where K_0 is a zeroth-order Hankel function[§]. When $r/\lambda \rightarrow \infty$ (large distances), the field \mathbf{h} decreases as $e^{-r/\lambda}$, whereas when $r/\lambda \rightarrow 0$, \mathbf{h} diverges logarithmically as $\ln\left(\frac{\lambda}{r}\right)$. The local current following around the vortex core can be obtained by means of the relation $\nabla \times \mathbf{h} = \mathbf{j}_l$ and becomes:

$$j_l(r) = \frac{\phi_0}{2\pi\mu_0\lambda^3} K_1\left(\frac{r}{\lambda}\right) \quad (2.35)$$

where K_1 is a first-order Hankel function. The $h(r)$ and $j_l(r)$ curves are plotted in Fig. 2.3, as well as $|\psi|^2$, with similar behavior as in Eq (2.14).

The vortex-line energy, or the free energy per unit length (E_l), can be calculated taking into account the kinetic energy of the current and the energy of the magnetic field, regardless the condensation energy lost in the normal core, leading to

$$E_l = \frac{E}{L} \approx \frac{1}{4\pi\mu_0} \left(\frac{\phi_0}{\lambda}\right)^2 \ln(\kappa) \quad (2.36)$$

Note that in a situation where the flux is $2\phi_0$, it is energetically favorable to keep two ϕ_0 -vortices instead of one vortex of $2\phi_0$ because the dependence of the vortex-line energy on ϕ_0 is quadratic. Therefore, a superconducting bulk maintains vortices with one flux quantum ϕ_0 in the mixed state [33]. Nonetheless, superconducting systems with low dimensionality, called mesoscopic superconductors, can show multiquanta vortices under certain conditions [34, 35].

In order to describe the vortex arrangement as a periodic lattice, the magnetic field distribution due to a pair of near vortices located at \mathbf{r}_1 and \mathbf{r}_2 under the $\kappa \gg 1$ approximation is given by:

$$\lambda^2 (\nabla \times \nabla \times \mathbf{h}) + \mathbf{h} = \frac{\phi_0}{\mu_0} (\delta_2(\mathbf{r} - \mathbf{r}_1) + \delta_2(\mathbf{r} - \mathbf{r}_2)) \quad (2.37)$$

The solution \mathbf{h} is the superposition of the fields $\mathbf{h}^{(1)}$, due to the first vortex, and $\mathbf{h}^{(2)}$, due to the second one ($\mathbf{h} = \mathbf{h}^{(1)} + \mathbf{h}^{(2)}$). Thus, the total energy is the sum of each individual vortex and an interaction term between them:

$$E_L^{(12)} = 2E_l + \phi_0 h^{(12)} \quad (2.38)$$

[§]Also known as the Bessel functions of the third kind.

with $h^{(12)} = h^{(1)}(r_2) = h^{(2)}(r_1) = \frac{\phi_0}{2\pi\mu_0\lambda^2} K_0\left(\frac{r_1-r_2}{\lambda}\right)$ is the field at one vortex resulting from the presence of the other. Thus, when the vortices have the same direction, their interaction is repulsive. Taking the derivative of the second term on the right side of Eq. (2.38) and using the Maxwell equations, the Lorentz force per unit length on vortex 2 due to vortex 1, for example, is [27]:

$$\mathbf{f}_2 = \mathbf{J}_1(\mathbf{r}_2) \times \phi_0 \mathbf{z} \quad (2.39)$$

which can be generalized as:

$$\mathbf{f} = \mathbf{J} \times \phi_0 \mathbf{z} \quad (2.40)$$

with \mathbf{J} the total current density, which can be either the current generated by other vortices or the transport current or both, at the normal core of the vortex which has been considered. This is called the Lorentz force per unit length.

Since each vortex has one quantum of flux and the interaction between the vortices is mutually repulsive, there is a more stable arrangement throughout the superconductor to minimize the energy. The most stable configuration is the triangular lattice, since for a given density, B , the distance to the nearest neighbor is then the largest and given by [36]

$$d_{tri} = 1.075 \sqrt{\frac{\phi_0}{B}} \quad (2.41)$$

However, Abrikosov found out that the most stable symmetry would be square, with some possibility to change to a triangular symmetry as the field is varied. For a square lattice, the distance between the vortices is slightly smaller than the triangular one ($d_{sq} = \sqrt{\frac{\phi_0}{B}}$), as discussed by Kleneir and co-authors in 1964 [37]. Nonetheless, the Abrikosov's findings have been very important and the vortex lattice is known as the Abrikosov lattice. As examples, Fig. 2.4 shows the Abrikosov lattice observed by different techniques for several materials. Panel (a) shows the first image of the triangular lattice obtained by Bitter decoration in Pb-4at%In rod at $T = 1.1$ K and $H = 3$ kOe [38], (b) the lattice in a-Mo_{2.7}Ge thin film taken by Scanning-Tunneling Microscopy (STM) at $T = 4.2$ K and $H = 5$ kOe [39], (c) Scanning Hall Probe Microscopy (SHPM) image taken at $T = 81$ K and $H = 12$ Oe in a BSSCO single crystal [40], (d) image obtained from Scanning Tunnel Spectroscopy (STS) for MgB₂ single crystal [41] at $T = 2$ K and $H = 2$ kOe, (e) image from Magnetic force microscopy (MFM) in Nb thin film at $T = 4.3$ K and $H = 40$ Oe [42], and (f) Magneto-optical imaging (MOI) in NbSe₂ single crystal at $T = 4.3$ K and $H = 3$ Oe [43].

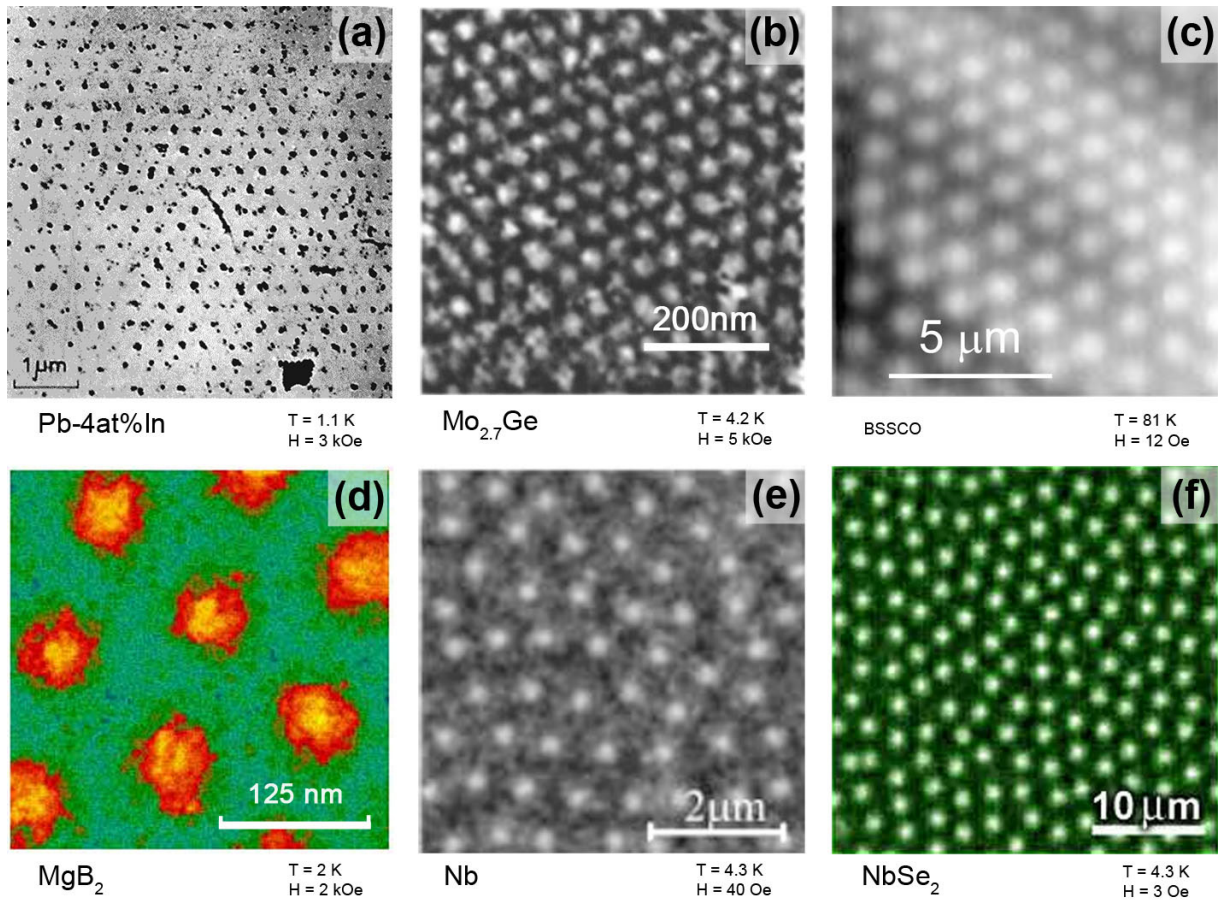


Figure 2.4: Images taken using different techniques to visualize the Abrikosov vortex lattice. (a) Bitter decoration [38], (b) STM [39], (c) SHPM [40], (d) STS [41], (e) MFM [42], and (f) MOI [43], with the conditions and the specimens identified in each panel and also in the text.

As pointed out by Abrikosov, inhomogeneities present in the superconductor influence the overall pattern, as can be seen in Fig. 2.4e and f. Then, the long range order is lost and new vortex phases appear in the mixed state with their own physical properties [36].

2.6 Real superconductors: the pinning centers

The Lorentz force per unit length, Eq.(2.40), acts on an isolated vortex due to the current generated by the other vortices as well as to currents possibly applied to the superconductor. Macroscopically, the lattice starts to move under the action of the Lorentz force density, written as:

$$\mathbf{F}_L = \mathbf{J} \times \mathbf{B} \quad (2.42)$$

since $\mathbf{B} = n\phi_0\mathbf{z}$, where n is the number of vortices and \mathbf{J} is the total current density. In a homogeneous superconductor, the viscous damping force $\mathbf{F}_d = -\eta\mathbf{v}$ and the Magnus force

$\mathbf{F}_m = \alpha_m n_s e (\mathbf{v} \times \mathbf{B})$ acts against the Lorentz force, where η is the friction coefficient, \mathbf{v} is the velocity of the vortex system and α_m is the Magnus coefficient. However, an electric field \mathbf{E} parallel to \mathbf{J} appears due to the velocity $\mathbf{v} \neq 0$, since $\mathbf{E} = \mathbf{B} \times \mathbf{v}$. This electric field gives rise to a power dissipation in the system, a consequence of the extra power needed to drive the normal electrons in the moving core, which can be written as [36]

$$P_d = \frac{1}{\eta} (\mathbf{J} \times \mathbf{B})^2 \quad (2.43)$$

and the superconductors would become useless. In order to make them useful, the vortex velocity should be null in spite of a nonzero \mathbf{F}_L . Thus, the driving Lorentz force should be counteracted by a *pinning force* (F_p). The pinning force defines the maximum critical current density which a real superconductor can bear without resistance, i.e., without depinning of the vortices. This current density is called critical current density (J_c). Hence the macroscopic average of the pinning force density can be estimated by:

$$F_p = J_c B \quad (2.44)$$

There is an upper limit for the critical current density which a superconductor can carry. This maximum value is called *depairing* or *pair-breaking critical current density*, J_c^{depair} or J_{pb} . In the framework of the GL equations, J_c^{depair} can be obtained by considering the free energy written only with the kinetic and magnetic field energy contributions for a superconductor with thickness $d < \xi(T)$. Thus, this ultimate limit is given by:

$$J_c^{depair} = \frac{\phi_0}{3\sqrt{6}\pi\mu_0\lambda^2\xi} \propto \left(1 - \frac{T}{T_c}\right)^{\frac{3}{2}} \quad (2.45)$$

which is written only in terms of intrinsic and fundamental parameters of the superconductor.

In other words, J_c^{depair} can be understood as the necessary current to destroy the Cooper pairs. In real superconductors, however, $J_c < J_c^{depair}$ since other contributions to the free energy, such as the loss associated with the vortex motion and the surface barriers for the vortex penetration, should be taken into account.

2.6.1 Intrinsic pinning

The pinning force is caused by any kind of inhomogeneity or defect distributed throughout the material and incorporated during the preparation process. These inhomogeneities, such as impurities, vacancies, stoichiometric defects, grain boundaries,

dislocations, voids, etc., suppress the superconducting properties (T_c , κ , and consequently, ψ) at that point or region. They reduce the condensation energy related to the nucleation of the normal core of the vortex and act as attractive potential wells holding the vortices and minimizing the free energy. They cause distortions in the Abrikosov lattice due to the landscape of forces acting on the vortex system and destroying the translational long range order, as illustrated in the Fig. 2.4f. This mechanism of pinning, called *core pinning* and first described by P. W. Anderson in 1962 [44], is more effective when the dimensions of the inhomogeneities are approximately the coherence length ξ of the superconducting material.

2.6.2 Artificial pinning

Besides the intrinsic pinning, artificial pinning centers can be introduced in type II superconductors to optimize and trap the vortex lines. It increases the critical current density and consequently, the potential of technological usefulness of the material. One way to insert these defects is by means of irradiating the specimen with high energy heavy ions [45], creating cylinders of non-superconducting material of diameter $\sim \xi$ randomly distributed and with several strengths (or depths). These cylinders are known as columnar defects. These have largely been used in the study of vortex matter in the HTS where ξ is typically of the order of few nanometers, similar to the size of the defects [46]. Columnar defects can be also obtained by mechanical indentations which are distributed as a periodic array of holes with irregular edges, resulting in pinning centers with different strengths [47].

In order to obtain a periodic array of pinning centers almost defect free on the edges, lithographic techniques in thin films have been employed in the last years. The electron beam lithography has allowed one to reach nanometric pinning centers, with controlled size, geometry, and type of defect. There are basically three different types of defects: the antidots[¶] (holes through the material) [48, 49, 50], the blind holes (partially drilled holes) [51, 52] and the magnetic dots (magnetic material on top or below the superconductor) [53, 54]. These defects are sketched in Fig 2.5. The superconducting thin films studied here have arrays of antidots.

For these samples, another mechanism to pin vortices becomes important and appear when the distance between the vortex and the antidot is lower than λ . It is called *electromagnetic pinning*. It takes place due to the perturbation of screening

[¶]The term "antidot" has been taken from similar structured thin films of semiconductors [48].

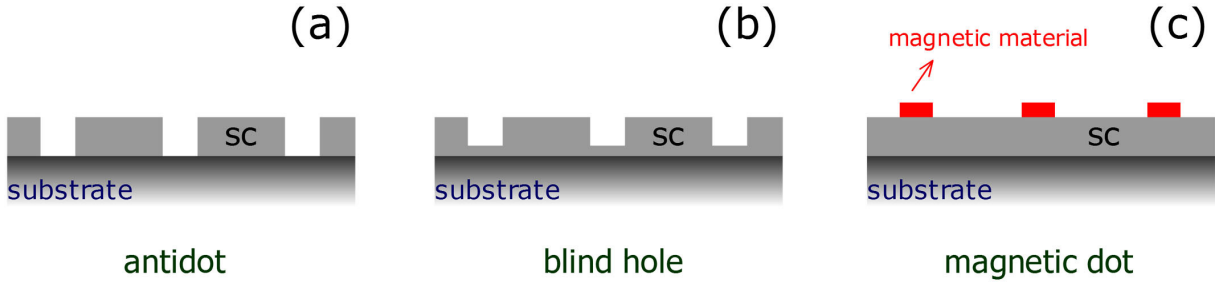


Figure 2.5: Profile representation of a superconducting thin film (SC) with an array of (a) antidots, (b) blind holes and (c) magnetic dots.

currents of the vortex near the edge superconductor/defect which must flow parallel to the hole edge, because of the boundary condition. Buzdin *et al.* [55] have calculated this interaction by the method of image, in which a vortex interacts with its image, an antivortex, located in the hole. Therefore, the antidot acts as an attractive potential for the vortex.

Although a multiquanta vortex is energetically unfavorable as shown before, relatively large artificial pinning centers can favor its appearance. Mkrtchyan and Schmidt [56] have found by using London theory that the saturation number of flux quanta $n_{sat}(T)$ for a cylindrical hole is given by:

$$n_{sat}(T) = \frac{R}{2\xi(T)} \quad (2.46)$$

where R is the radius of the hole. For an empty hole, the incoming vortex is always attracted to the defect. When $1 < n \leq n_{sat}$, n being the number of flux quanta, the flux $n\phi_0$ is captured by the hole and creates a potential barrier for other vortices far from the defect. Increasing the magnetic pressure, for instance, vortices close to the hole can overcome this barrier and enter the hole. When $n > n_{sat}$ the potential becomes repulsive, no more flux is accepted into the hole, and the vortices start to occupy interstitial positions in the superconducting region. It is also important to mention that n_{sat} assumes values of $\approx (R/\xi(T))^2$ in the high-field regime, as recently pointed out by Doria and co-workers [57, 58] using GL theory.

Furthermore, superconductors decorated with artificial pinning centers arranged periodically show commensurability effects between the periodic pinning and the vortex lattice. It means that, when the lattice constants of the pinning centers and of the vortex array are identical, a local maximum in pinning force is reached and consequently, a local maximum in the critical current density occurs. The magnetic

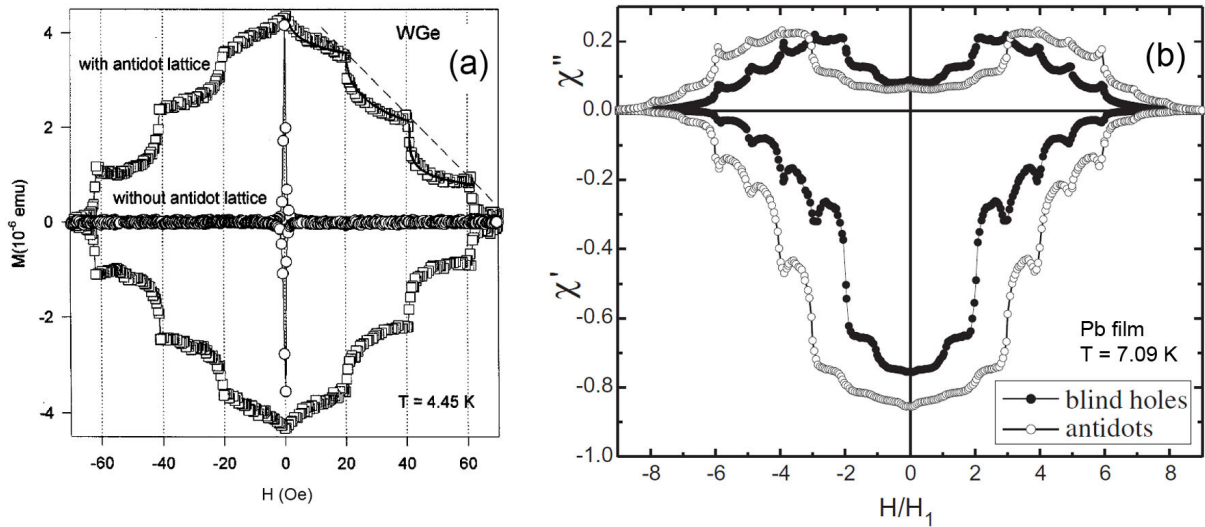


Figure 2.6: Matching fields detected by different techniques. (a) Magnetization versus magnetic field for a decorated $W_{0.77}Ge_{0.33}$ and a plain film [48] and (b) in phase and out-of phase components of the ac susceptibility for Pb thin films with array of holes (open symbols) and blind holes (filled symbol) [51].

fields at which these matching occurs are called matching fields, defined as [59]:

$$H_n = n \frac{\phi_0}{\mu_0 A} \quad (2.47)$$

where A is the unit-cell area of the lattice of defects. At the first matching field H_1 , for instance, the equilibrium configuration is one in which each hole is occupied by a single flux quantum on average. Fig. 2.6 shows the matching fields obtained by magnetization and ac susceptibility techniques. Panel (a) shows $M(H)$ curves for a $W_{0.77}Ge_{0.33}$ thin film with holes of radius $0.22 \mu\text{m}$ in a square lattice of $1 \mu\text{m}$ prepared by electron beam lithography whose matching fields are multiples of 20.7 Oe . In the same graph one can see the absence of matching fields on the magnetic response of the plain film. Panel (b) shows both components of ac susceptibility for a Pb thin film with square holes of $0.8 \mu\text{m}$ in a square lattice of $1.5 \mu\text{m}$ and blind holes with the same characteristic, both with matching fields in multiples of 9.2 Oe .

2.7 Critical state models: the Bean model

In an ideal type II superconductor, its magnetic properties are completely reversible. Nevertheless, real type II superconductors have a large hysteresis in their magnetic behavior, as a consequence of the existence of pinning centers. The critical state models are a useful framework to explain this feature, capable of providing a qualitative and quantitative description of one of the most important properties for applications, the

critical current density (J_c).

In the macroscopic point of view, when a magnetic field H larger than H_{c1} is applied, currents are induced in the region of the sample where the flux penetrates to counteract the change in the internal magnetic field, in accordance to Maxwell's equations (Eq. (2.48)). In this region, the macroscopic current is always the maximum current, or the critical current, which the specimen can carry. Therefore, the sample is in the so-called *critical state* (CS) [60]. From this point of view, it is unnecessary to know any details of the interaction between the vortices and the pinning centers [61]. Nonetheless, the critical state models can be described microscopically. Vortices are nucleated at the edges and penetrate the sample. Since the vortices are captured by the pinning centers, the pinning force acts against the Lorentz force (Eq. 2.42) up to the maximum pinning force (Eq. 2.44). The balance between these two forces (disregarding any other) leads to a local metastable state, where the superconductor employs its maximum current to maintain the flux as close as possible from the edges. Thus, the vortices distribute in such a way that their density decreases from the edge to the center of the specimen. The relation between \mathbf{B} and \mathbf{J}_c can be obtained from the Ampère law:

$$\nabla \times \mathbf{B} = \mu_0 \mathbf{J}_c(\mathbf{B}) \quad (2.48)$$

An important assumption is associated with the relation between \mathbf{B} and \mathbf{H} . The thermodynamic magnetic field \mathbf{H} can be obtained by the Gibbs free energy as $\mathbf{H} = \frac{\partial \mathcal{G}}{\partial \mathbf{B}} \approx \mathbf{B}/\mu_0$, considering a type II superconductor with $\kappa \gg 1$ and $H_{c2} \gg H_{c1}$ [62]. This assumption is related to the region in the Fig 2.2b where \mathbf{B}/μ_0 merges to \mathbf{H} as it approaches H_{c2} .

The idea of the critical state and the most simple model was proposed by Charles Bean in 1962 [63], and better discussed in a *review* published two years later [64]. Bean disregarded the existence of H_{c1} , i.e., there is no Meissner state in the CS models and the penetration depth of the flux front should be greater than λ as well. Thus, Bean considered the critical current density as:

$$J_c(B, T) = J_c(T) \quad \text{Bean model} \quad (2.49)$$

i.e., the value of the critical current density at a specific temperature is constant where the flux is penetrated. Above T_c or for $H > H_{c2}$, the value of J_c is null. Other CS models have been developed to take into account the magnetic field dependence of the critical current density, the most important of which are the Kim model [60] and the Exponential

model [65], represented respectively by:

$$J_c(B, T) = \frac{J_0(T)}{(1 + B/B_0(T))} \quad \text{Kim model} \quad (2.50)$$

$$J_c(B, T) = J_0(T) \exp(-B/B_0(T)) \quad \text{Exponential model} \quad (2.51)$$

Although the field dependence of J_c exists, the Bean model is the simplest but a highly successful tool to determine the critical current density from magnetic and ac susceptibility measurements. In addition to that, the geometric configuration between the field and the specimen affects J_c and the flux distribution inside the sample. Two of the most common configurations will be discussed in terms of the Bean model: parallel and perpendicular.

2.7.1 Slab/cylinder: parallel configuration

The parallel geometry is related to infinitely long slabs with the dimensions in the y and z directions much larger than the dimension $2w$ in the x direction and $2w \gg \lambda$ or infinitely long cylinders with diameter $2R \gg \lambda$. The magnetic field is applied along the z -axis as shown in Fig. 2.7a. In this case, demagnetization effects can be disregarded. Thus, above H_{c1} the gradient of the flux density is given by the Ampère law as follow:

$$J_y = \frac{\partial H_z}{\partial x} - \frac{\partial H_x}{\partial z} \quad (2.52)$$

where the second term on the right side is zero for this configuration. Therefore, the critical current is perpendicular to the magnetic field and given by the slope dH_z/dx . As in the Bean model $J_y = J_c$, the gradient of flux density is constant, with the vortex density B decreasing linearly from the edge to the center of the sample, as illustrated in Fig. 2.7b. By increasing the applied magnetic field from zero upwards, the magnetic induction is given by:

$$B_z(x) = \begin{cases} 0, & |x| < a \\ \mu_0 (|x| - a) J_c, & a \leq |x| \leq w \\ \mu_0 H, & |x| > w \end{cases} \quad (2.53)$$

where a is the distance of the flux front from the center of the specimen. The current density is J_c where the flux is penetrated and null elsewhere:

$$J_y(x) = \begin{cases} J_c, & a < |x| \leq w \\ 0, & |x| \leq a \end{cases} \quad (2.54)$$

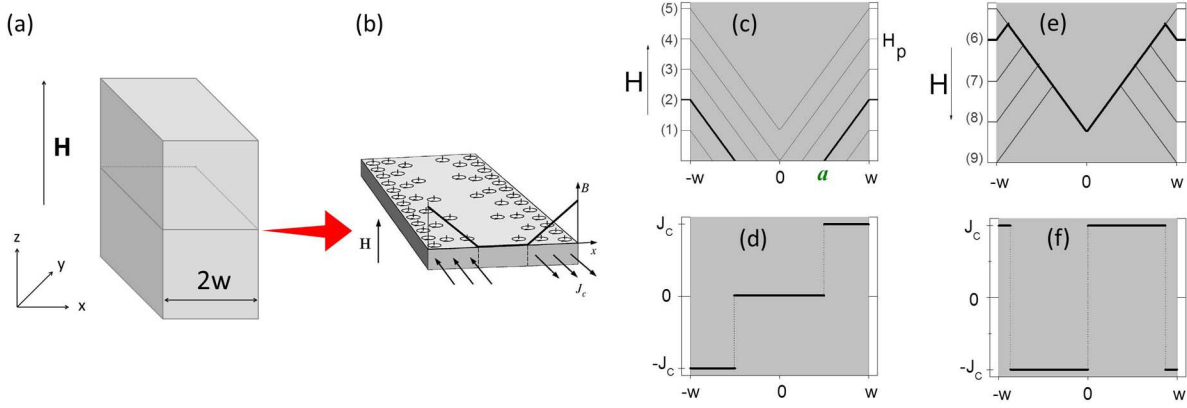


Figure 2.7: Bean model in a slab with width $2w$ in parallel configuration (a). (b) Schematic representation of the microscopic distribution of the vortices in a stripe from the middle of the slab [61]. (c) The magnetic flux profile increasing the field from $H = 0$, with H_p representing the full penetration field and a the position of the field penetration. (d) The profile of the critical current density for the applied field in the bold line of the case (2). (e) Flux profile when the field is decreased from (5) and (f) profile of J_c at the case (6).

Fig. 2.7c and d shows the magnetic flux distribution and the critical current density for the applied field labeled as (2). The magnitude of the critical current density can be evaluated when the full penetration field (H_p) is reached, then

$$J_c = \frac{H_p}{w} \quad (2.55)$$

Once H_p is reached, the vortex density increases and maintains the same constant slope. If the applied field is decreased, the vortex density decreases at the edge of the sample, as illustrated in Fig. 2.7e, with the slope $-dH_z/dx$. The critical current density changes the sign, although its magnitude remains the same in accordance with the assumption of the model (Fig. 2.7f).

2.7.2 Thin film: perpendicular configuration

The reduction of one (or more) dimensions gives rise to different flux and critical current distributions in superconducting systems. For a thin film geometry, considering a small ratio between the thickness and the London penetration depth (d/λ), i. e., $d \ll \lambda$, the structure of the vortices acquires different properties from those of the superconducting bulk, if it is placed in a perpendicular or transverse configuration (the applied field is normal to the specimen surface as in Fig. 2.8a). J. Pearl [66] assumed $\kappa \gg 1$ and established, in this approximation, the current density for this geometry as an infinitesimally thin current sheet ($\mathbf{j}(\mathbf{r}) = \mathbf{J}(x, y)\delta(z)$). Applying this to the second London equation and considering \mathbf{A} as a constant across the thickness, the sheet current

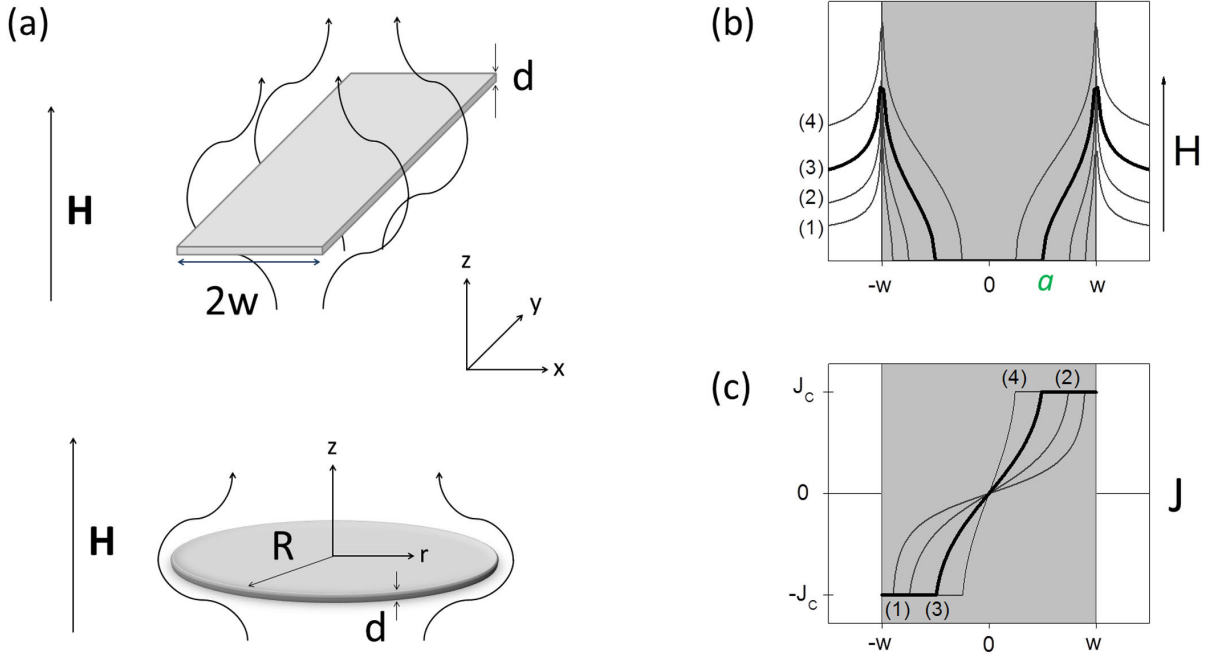


Figure 2.8: Long stripe and thin disk representing a thin film in a perpendicular geometry (a), with w being half of stripe width, R is the disk radius and d is the thickness. Magnetic flux profile (b) and current density (c) in the cases (1) through (4).

can be written as:

$$\mathbf{j} = -\frac{1}{\mu_0\Lambda} \mathbf{A}\delta(z) \quad (2.56)$$

with

$$\Lambda(T) \approx \frac{2[\lambda(T)]^2}{d} \quad (2.57)$$

where $\lambda(T)$ is the bulk penetration depth. As a consequence of the two-dimensional features, a new length scale controls the spatial variation of \mathbf{J} (and \mathbf{A}), named *effective penetration depth*, Λ . It means that the thin-film vortices have an electromagnetic interaction of longer range, compared to the three-dimensional case (Eq. (2.15)), since $\Lambda \gg \lambda$. The radius of the vortex core is the same $\xi(T)$ as in a bulk sample, but the gradual decrease of the current around the vortex is more spread out and consequently, the magnetic field also decays in a longer length [27, 33]. Thus, non-local effects should be taken into account. This becomes clear comparing both geometries: for $r \gg \Lambda$, the current decreases as $1/r^2$, whereas for a bulk, it decreases as $e^{-r/\lambda}$ for $r \gg \lambda$, remembering that the relevant scale for thin films is $\Lambda \gg \lambda$. The local magnetic field and the intervortex force cut-off as $1/r^3$ (for $r \gg \Lambda$) and $1/r^2$ for a thin film, respectively, whereas both cut-off exponentially for a bulk.

In principle, materials which are type I in bulk form, can behave as type II when in thin film geometry, since κ can be bigger than $\sqrt{2}/2$, replacing the penetration depth

by Λ . For instance, tin and lead in bulk shape are type I superconductors, nonetheless in thin film with thickness less than the critical value of around 180 nm and 250 nm, respectively, they behave as type II superconductors [67].

The description of the Bean model for the flux and current profiles for a slab geometry (Fig. 2.7) is no longer valid for a thin film in perpendicular configuration. The superconducting thin films show large demagnetization effects influencing the magnetic response due to magnetic poles appearing on the surface of the thin film. In this case, the internal field is equal to the applied field \mathbf{H} corrected by the demagnetization field \mathbf{H}_d , that is [68]:

$$\mathbf{H}_N = \mathbf{H} + \mathbf{H}_d = \mathbf{H} - \overleftrightarrow{N} \mathbf{M} \quad (2.58)$$

where \overleftrightarrow{N} is the demagnetization tensor and $Tr(\overleftrightarrow{N}) = 1$. Thus, the constitutive relation of the magnetism becomes:

$$\mathbf{B} = \mu_0 \left[\mathbf{H} + \left(1 - \overleftrightarrow{N}\right) \mathbf{M} \right] \quad (2.59)$$

The demagnetization factor depends on the shape of the specimen and of the orientation relative to the magnetic field. For samples in the format of ellipsoids of revolution, the demagnetization tensor can be treated as a scalar demagnetization factor N . For an infinite cylinder with the magnetic field parallel to the main axis, N is null (no demagnetization factor), whereas in a perpendicular geometry, N is $2/3$. For a sphere, the value of $N = 1/3$. For a superconducting thin film in perpendicular configuration, an oblate ellipsoid is used to model N through the ratio between major axis w and the minor axis d , given by $\gamma = d/w$. For small γ , N is:

$$N = 1 - \frac{1}{2}\pi\gamma + 2\gamma^2 \quad (2.60)$$

which results in $N \sim 1$ for the thin films studied here. Consequently, it enables vortices to come into the thin film at applied fields smaller than the bulk lower critical field (H_{c1}^{bulk}), given by:

$$H_{c1}^{film} \approx \sqrt{\frac{d}{w}} H_{c1}^{bulk} \quad (2.61)$$

decreasing the value of H_{c1} for the thin film geometry.

Another consequence of strong demagnetization effects is that magnetic flux lines wrap around the thin film and originate in-plane components of H_x with the opposite sign on the top and bottom surfaces, i.e., $H_x(x, z = -d/2) = -H_x(x, z = d/2)$. It also leads to a larger gradient of $\frac{\partial H_x}{\partial z}$ than the term $\frac{\partial H_x}{\partial x}$ in Eq. (2.52), differently from the slab geometry.

Consequently, the effective magnetic field at the edges is higher than the applied magnetic field, and the screening currents flow everywhere in the sample. There are two geometries where superconducting thin films are depicted: an infinitely long stripe with the width of $2w$ and a thin disk with the radius R , the schematic representation of which are shown in Fig. 2.8a . When the applied field is increased from zero, the magnetic field around the long stripe is [62, 69]:

$$B_z(x) = \begin{cases} 0, & |x| < a \\ \mu_0 H_g \operatorname{arctanh} \left(\frac{w}{|x|} \left(\frac{x^2 - a^2}{w^2 - a^2} \right)^{1/2} \right), & a < |x| < w \\ \mu_0 H_g \operatorname{arctanh} \left(\frac{|x|}{w} \left(\frac{w^2 - a^2}{x^2 - a^2} \right)^{1/2} \right), & |x| > w \end{cases} \quad (2.62)$$

and as the current density is given by:

$$J_y(x) = \begin{cases} J_c \frac{x}{|x|}, & a < |x| < w \\ 2 \frac{J_c}{\pi} \operatorname{arctan} \left(\frac{x}{w} \left(\frac{w^2 - a^2}{a^2 - x^2} \right)^{1/2} \right), & |x| < a \end{cases} \quad (2.63)$$

where a is the position of the flux front written as:

$$a = \frac{w}{\cosh \left(\frac{H}{H_g} \right)} \quad (2.64)$$

and for a long stripe, the characteristic field H_g is

$$H_g = \frac{J_c d}{\pi} \quad \text{long stripe} \quad (2.65)$$

For a thin disk [70], the magnetic flux and the current profiles are approximately the same as shown in Eq. (2.63) and (2.62), except by replacing the following parameters [71]:

$$\begin{aligned} x &\longrightarrow r \\ w &\longrightarrow R \quad \text{thin disk} \\ H_g &= \frac{J_c d}{2} \end{aligned} \quad (2.66)$$

hence both geometries are similar unidimensional problems. Fig. 2.8b shows the magnetic flux profile when the applied field is raised for different values and the panel (c) shows the current density profile. The current is constant and equals to J_c where the field is penetrated, whereas Meissner currents flow in the flux-free region [72].

The kind of configuration based on the alignment between the specimen and the magnetic field is determined by thickness and the penetration depth [73]. For the situation where $d > w \gg \lambda$, the Bean model in the parallel orientation can be employed. For $d \ll \lambda \ll w$, the currents are determined by the curvature of the external field lines and,

therefore, the perpendicular configuration should be considered.

Finally, the Bean model picture fails dramatically when sudden flux bursts develop due to thermomagnetic instabilities. This issue is covered in the next chapter.

3 *Flux avalanches in superconductors*

As discussed earlier, magnetic flux penetrates into the sample in an organized way, drawing a gradient distribution with the maximum on the edge of the specimen when the magnetic field is increased from zero. However, sudden events may occur and flux penetrates with great speed, so that the ordered arrangement is lost. These abrupt flux entrances are called flux avalanches and take place under certain conditions of temperature and magnetic field. From the application point of view, this unpredictable phenomenon is unwelcome since it is related to the device stability. In the following, the circumstances, effects and features under which those events occur are addressed.

3.1 Introduction

In the end of the previous chapter the Bean model was presented for different sample geometries. However, there is no description of vortex structure nor any indication about the dynamics of the magnetic flux inside the sample in the critical state. Thereby, de Gennes [33] proposed in his book an analogy between the critical state models and a *sand pile*. When sand is added to a sand pile and the angle between the horizontal plane and the sloped face reaches the *critical angle* or the *angle of repose* [61], the pile suffers a readjustment, or an avalanche, so that the angle decreases to the critical one. In superconductors, small adjustments of the current to keep it to the critical value, lead to the vortex movement when the applied magnetic field is ramped slowly. As in sand (or snow) avalanches, *vortex avalanches* with a small amount of flux lines moves to reestablish the critical state again. Therefore, from the microscopic point of view, the flux penetration process develops in a discontinuous way through nondestructive small bursts towards the center of the sample.

As pointed out by Altshuler and Johansen in a recent review on this subject [61], this similarity between vortex avalanches and avalanches in a sand pile has been treated as part of a more general physics of complex systems. The mechanism of this kind of avalanche, the so-called dynamically driven avalanche, has been described in the context of *self-organized criticality* (SOC) by several authors [61, 74, 75, 76]. The SOC scenario predicts

that the system is able to organize itself in order to remain at the critical state obeying a power-law distribution of avalanche sizes measured in ϕ_0 units with a universal exponent. Altshuler and co-workers [77] have presented some evidences that vortex avalanches can be described as a SOC system. They have combined magneto-optical images and micro-Hall probe measurements to determine the probability $P(s)$ of detecting an avalanche size with s vortices acting as a power-law behavior ($P(s) \sim s^{-\alpha}$) over two decades. They found $\alpha = 3.1 \pm 0.2$, in a statistics over almost 200,000 avalanches at $T = 4.8$ K in different locations of a $250 \mu\text{m}$ thick Nb foil. Although the value of α is higher than the common value for a complex system ($\alpha = 1$), like in an ideal sand pile, this exponent is the same for each location of the sample, indicating its universality in this system. Therefore, the construction of the critical state by vortex avalanches can be interpreted in the light of SOC systems.

However, in spite of describing the macroscopic smooth evolution of the Bean model when the magnetic field is changed, there is a second type of avalanches in superconductors which is the subject of this thesis. These avalanches occur suddenly during thermal runaways and, consequently, are called thermally driven avalanches [61]. These avalanches locally destroy the critical state, and sometimes they are also catastrophic for the superconducting state. A different mechanism is related to these events and discussed in the following section.

3.2 Thermally driven avalanches: flux avalanches

Since the early 1960s huge jumps have appeared in the magnetization curves of superconducting bulk samples. Kim *et. al.* [60] have named it as *flux jumps* which can destroy completely or partially the superconducting state when the magnetic field is ramped. Fig. 3.1a shows $M(H)$ curves at 1.8 K of Nb disks prepared under different metallurgical conditions, where the red curve displays discontinuities due to flux jumps. The very first observation of these abrupt penetrations had been made earlier by Schawlow [78], in 1956, using the Bitter decoration technique* [79] in vanadium cylinders (a type II superconductor) when he was studying the surface energy of the intermediate state of several pure metals with different geometries. He observed that abrupt jumps take place and from his estimation of the surface energy he found that the

*The Bitter decoration technique consists of spreading out a ferromagnetic or a superconductor powder, e.g. iron or niobium, on the specimen in the state (temperature and magnetic field) that one wants to observe. After that, the images of the powder distribution are generally taken by means of a scanning electronic microscope or optical microscope.

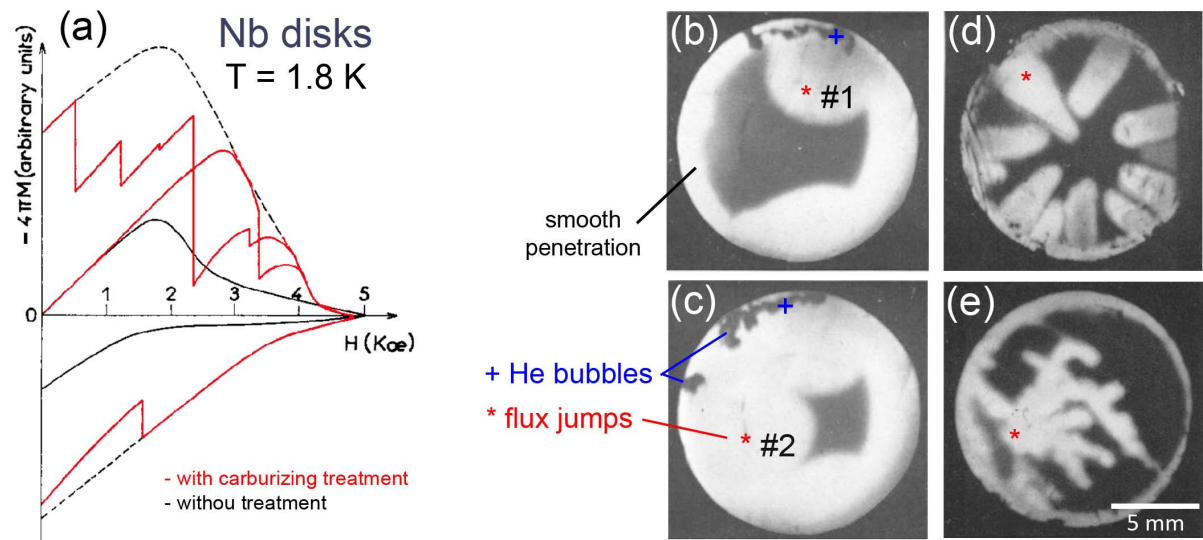


Figure 3.1: Panel (a): Magnetization curves at 1.8 K with discontinuities due to abrupt flux jumps in Nb disks with carburizing treatment (red curve) and a smooth magnetization for the Nb disk without treatment (black curve). The dashed line represents the expected curve without the flux jumps for the treated Nb disk. Panel (b)–(e): MO images taken at 1.8 K where black corresponds to the Meissner region (inside the disk) and white to the penetrated field for disks with diameter of 13 mm. (b) and (c) shows a Nb disk ($d = 0.89$ mm) with uniform and partial flux jump at $H = 2130$ Oe, taken 2.5 ms after the first flux jump (#1), and $H = 2810$ Oe, taken 2 ms after the second flux jump (#2), respectively. The bubbles in the He bath (black regions) on the top of the figures are a strong evidence of the thermal origin of the flux jump. (d) Another Nb disk ($d = 0.1$ mm) which shows a thick finger-like flux jump. (e) Nb52%atZr disks ($d = 0.42$ mm) with “irregular” flux jumps increasing the field. Adapted from [80].

behavior of the vanadium sample was anomalous if compared to the other materials. Just to remember, this observation was carried out before the findings of Abrikosov and Bean.

Another important technique permitting one to obtain a complete and direct view of the macroscopic flux distribution in superconductors is the magneto-optical imaging (MOI). A crucial and exciting feature of the MOI is the possibility to observe the magnetic event in real time. In 1967, Wertheimer and Gilchrist [80] reported images of flux jumps in Nb and NbZr disks using MOI with a high-speed camera (12,000 frames per second), as illustrated in Fig. 3.1b–e. In panels (b) and (c), two large flux jumps are shown with uniform and circular morphologies to increase the magnetic field, different from the regular smooth penetration pictured by the critical state. Panel (d) demonstrates a thick finger-like morphology, where each jump developed at a different field avoiding the already existing one. Panel (e) illustrates “irregular” flux jumps for a NbZr disk for increasing the field. This flux jump morphology is peculiar in bulk geometry and found nowadays in thin film, named *dendritic*[†] morphology and to be discussed later. Furthermore, a strong

[†]The term dendritic comes from the Greek word for tree (“déndron”) and means *having a branching structure similar to a tree or having dendrites* [81].

evidence of the thermal origin of the flux jumps is shown in this paper. Few milliseconds after the jumps, bubbles in the helium bath were observed as black spots on the edge of the disk, as can be seen in the images (b) and (c). Thus, a significant amount of heat was released during the abrupt penetration of magnetic flux. More recently, J. I. Vestgård and co-authors [82, 83] have found by numerical simulations that the temperature during the avalanche evolution can be higher than T_c in thin films. Therefore, it suggests that the term *flux avalanches* for the avalanches thermally driven or flux jumps in this geometry is more appropriated than vortex avalanches. More details about the flux avalanche dynamics in superconducting thin films are treated ahead.

The hypothesis about the thermal origin of the flux jumps had already been addressed by Kim and others [60]. However, a long treatment of the flux jump problem has been carried out by Swartz and Bean [84], by Mintz and Rakhmanov [85] and by Wipf [86], all of them considering the stability conditions in type II superconductors. The mechanism for occurrence of the flux jumps is based on the fact that the heat generated by a small flux movement in a small region of the superconductor can result in a *thermomagnetic (TM) instability*. Then large regions of the superconductor can become normal because of this unstable process, which takes place depending on the relative importance between the magnetic flux diffusion (D_m) and the heat diffusion (D_t) [85]. Thus, the dimensionless parameter τ can be defined as:

$$\tau = \frac{D_t}{D_m} = \mu_0 \frac{\kappa_0 \sigma}{c} \quad (3.1)$$

where κ_0 is the thermal conductivity, σ is the electrical conductivity, and c is the specific heat of the bulk superconductor.

When $\tau \gg 1$, the heat diffusion is faster than the flux magnetic diffusion which means that the specimen has enough time to assimilate the heat generated by the vortex motion. Then the superconductor keeps stable and a smooth penetration takes place. Microscopically speaking, dynamically driven avalanches build the gradient profile flux as in the critical state-like. However, if $\tau \ll 1$, the magnetic flux diffusion is faster than the thermal diffusion, the sample has no time to assimilate the heat generated by the flux motion (adiabatic process). As a consequence, thermomagnetic instabilities can trigger a flux jump due to the positive feedback illustrated in Fig. 3.2. Then the Joule heating increases the local temperature T of the sample by a small perturbation δT , resulting in a reduction of the critical current density by $\delta \mathbf{J}_c$, since $\mathbf{J}_c(T)$ is a decreasing function of the temperature, and reduces the pinning force locally by $\delta \mathbf{F}_p$ as well. More flux comes into the sample in that region due to the decrease of the screening current and the Faraday

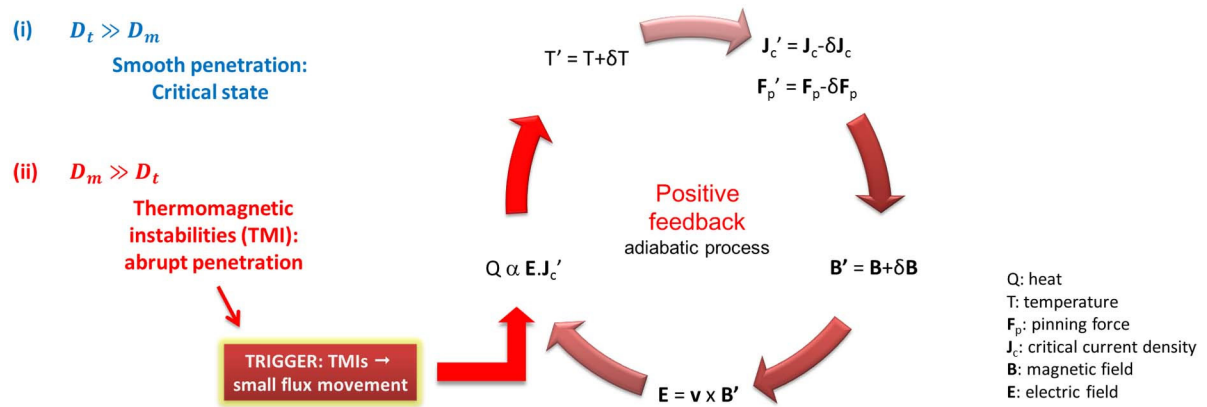


Figure 3.2: Schematic diagram for the flux jumps/flux avalanches occurrence. When $D_t \gg D_m$, a smooth penetration takes place, whereas when $D_m \gg D_t$ abrupt penetrations occur due to thermomagnetic instabilities. Then a small vortex motion generates heat and the positive feedback (adiabatic process) actuates as a mechanism for the flux avalanches. Adapted from [86].

law assures that an electric field \mathbf{E} is induced. So more heat is generated, leading to an additional temperature increase and a further reduction of the critical current density and so on. This is an adiabatic process which, depending on the conditions, can lead to a local flux jump or a jump in the entire volume of the sample. These sudden events occur at low temperatures, since the local temperature rise occasioned by the flux motion is high because the specific heat is low.

It is also worth remarking that the SOC concepts do not contain the thermal effects and neither the positive feedback which is found in the flux jumps and flux avalanches.

3.2.1 Flux avalanches in thin films

Whereas bulk superconductors have limited morphologies for the flux jumps, thin films have received renewed attention due to the unusual and impressive dendritic morphologies developed by flux avalanches. Moreover, studies of these branched characteristics [87, 88] have been promoted in order to identify the main parameters leading to these distinct and impressive images. In this sense, MOI has given us the opportunity to investigate from the flux avalanche morphology up to the dynamics of such catastrophic events.

Using MOI, Leiderer *et al.* [89] observed dendritic flux avalanches in a superconducting thin film of $\text{YBa}_2\text{Cu}_3\text{O}_{7-\delta}$ in 1993. In their findings, the TM instabilities were artificially triggered by a hot spot caused by a laser pulse at the edge of the specimen and striking pattern shapes grew inside the 300 nm thickness film under a fixed dc field of 206 Oe. Fig. 3.3a shows a flux avalanche in a YBCO thin film with a branched tree-like aspect

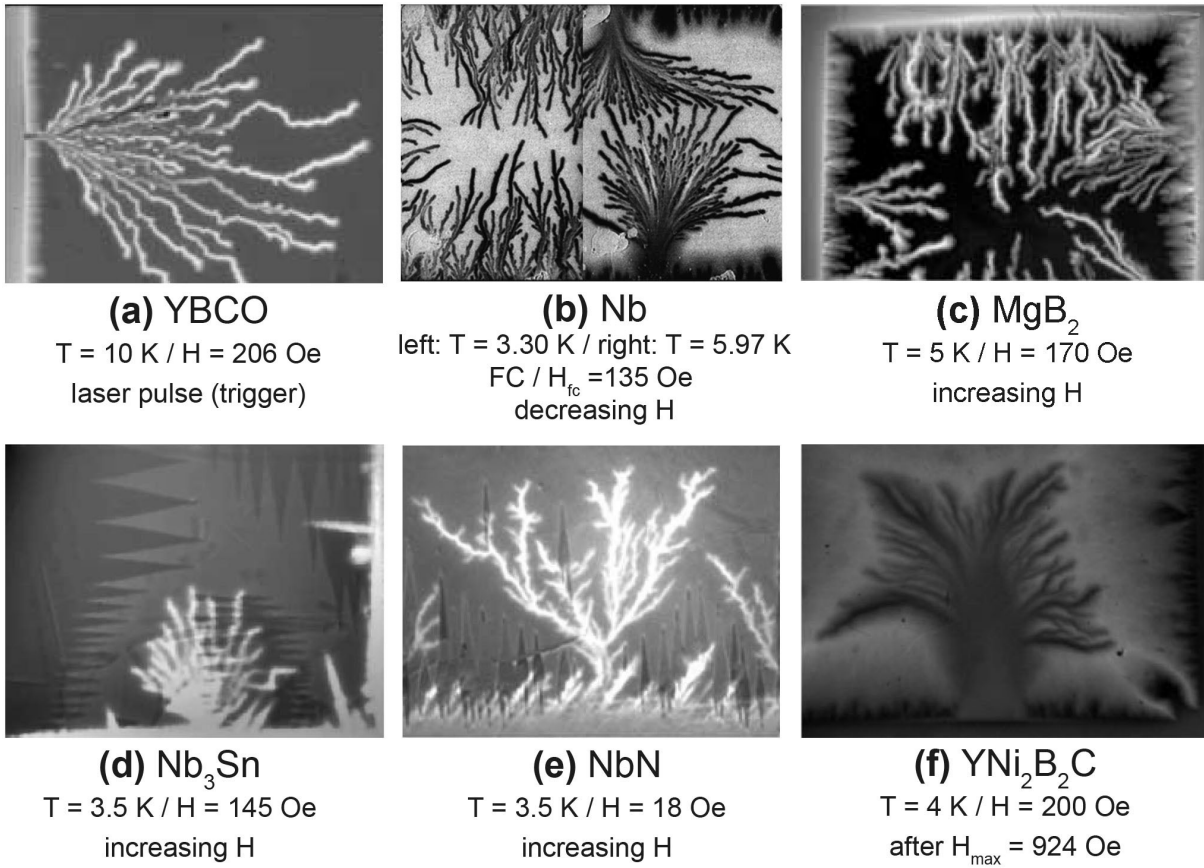


Figure 3.3: Dendritic morphology of the avalanches in thin films visualized by MOI: (a) YBCO after a laser pulse [89, 90]; (b) Nb decreasing the field after a field cooled procedure at $H = 135$ Oe [91]; (c) MgB_2 increasing the magnetic field [92, 93]; Nb_3Sn increasing the field [94]; YNi_2B_2C decreasing the field after an maximum field (H_{max}) [95]; and NbN increasing the field [96].

(bright region) with the darker region in the Meissner state. Indeed, it is interesting to mention that *spontaneous* flux avalanches still have not been observed in any HTS superconductor. Durán and others have reported dendritic avalanches in a Nb thin film with a thickness of 500 nm, displayed in the panel (b) of Fig. 3.3. They used the field cooled (FC) procedure where a magnetic field of 135 Oe was applied above T_c and then the sample was cooled down below T_c and the initial field was subsequently removed down to the remnant state ($H=0$), shown in the picture. The left panel shows the flux avalanches with a finger-like shape or dendrites with quasi-one dimension structures at 3.30 K, whereas the right panel shows enormous branched structures at higher temperatures ($T = 5.97$ K). Above a certain threshold temperature, the dendritic structures were suppressed and a smooth penetration took place. In those images, the bright region corresponds to more intense local fields and the dark areas represent lower local fields.

The first paper to show spontaneous dendritic avalanches when the magnetic field is ramped up was published by T. H. Johansen's group [92], in 2001. They reported dendritic

avalanches when the field was applied starting from zero in a MgB_2 thin film below 10 K. Fig. 3.3c shows one of their observations at $T = 5$ K and $H = 170$ Oe with several dendrites which were triggered in different fields. Once the flux avalanche is formed, the entire dendritic structure remains frozen even if the applied magnetic field continues to increase [93, 97]. When the next avalanche is formed in a higher magnetic field, a new pattern appears with a similar branched structure and tends to avoid overlapping the existing dendrites, changing its growth direction if necessary [92] because of the long-range character of the repulsive interactions in a superconducting thin film [66, 98]. If the field is decreased, the exit of flux also presents a dendritic pattern. Other superconducting thin films have also shown dendritic flux avalanches during the invasion or exit of magnetic flux into the samples, as the images presented in Fig. 3.3d–f. Branched structures are shown for Nb_3Sn and NbN thin films when the magnetic field is increased, and for $\text{YNi}_2\text{B}_2\text{C}$ film in the panel (f) which shows an enormous tree-like shape when the field is decreased. In Chapter 7, we report, for the first time, flux avalanches in a plain film of molybdenum-germanium alloy.

The observation of this unusual flux avalanche morphology in several superconducting thin films have aroused great interest, mainly for a theoretical description which could describe and also predict properties of this fascinating phenomenon.

3.2.2 The thermomagnetic model

The thermal origin of the abrupt penetration of magnetic flux inside the superconductors is a well-established idea. Several theoretical studies have been developed in order to map the dynamics of the flux avalanches. Among them, there are three descriptive models: the boundary layer model [99], the shock wave model [100, 101], and the thermomagnetic model [87, 102]. The boundary layer model is described in terms of the local temperature at a sharp layer between a Meissner domain and a uniformly penetrated flux domain. The shock wave model describes all the parameters, such as temperature, magnetic field and electric field, as a wave inside the sample. These first two models have described finger-like morphology, whereas the TM model has shown the most consistent information about the flux avalanches regime including the dendritic patterns and their dependence on the temperature [93, 82], as illustrated in Fig. 3.4, since the flux pattern is a long finger at low temperatures, whereas it becomes more branched at higher temperatures. Comparisons between the experimental data and numerical simulations, as presented in this figure, can be made

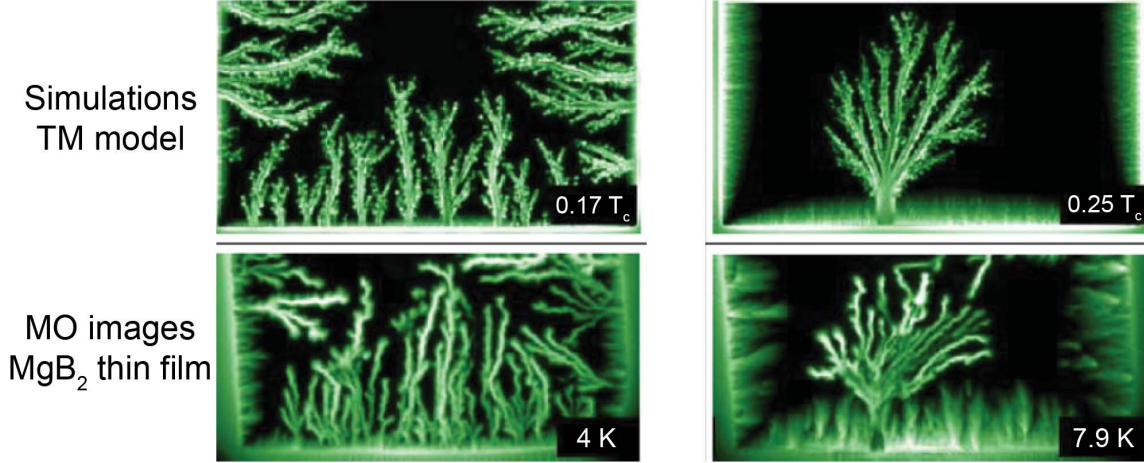


Figure 3.4: Comparison of the morphology of the flux avalanches between MO images taken of a MgB₂ thin film at 4 K and 7.9 K and simulations by using the TM model for two reduced temperatures ($0.17 T_c$ and $0.25 T_c$), showing a remarkable correspondence. Adapted from [82].

with a high degree of correspondence. One of these agreements between the experimental and theoretical results is addressed in Chapter 8, where flux avalanche morphologies in thin films with different antidot shapes are debated.

Considering a more general description, which includes a superconducting thin film subjected to a magnetic field transverse to film plane, the TM model is written using the Ampère law ($\nabla \times \mathbf{B} = \mu_0 \mathbf{J}$), Faraday law ($\nabla \times \mathbf{E} = -\frac{\partial \mathbf{B}}{\partial t}$) and the heat diffusion equation:

$$c\dot{T} = \kappa_0 \nabla^2 T - d^{-1} h_0 (T - T_0) + d^{-1} \mathbf{j} \cdot \mathbf{E} \quad (3.2)$$

where h_0 is the coefficient for heat transfer to the substrate held at the temperature T_0 , d is the thin film thickness, \mathbf{E} is the electric field, and \mathbf{j} is the sheet current related to the current density \mathbf{J} by $\mathbf{j} = \mathbf{J}d$. This equation provides the temperature distribution of the specimen and the second term on the right side refers to the contact between the superconducting thin film and the substrate. In addition, the nonlinear current-voltage relation of type II superconductors, which is conventionally approximated by a power law, should be considered:

$$\mathbf{E} = \frac{\rho_0}{d} \left(\frac{\mathbf{j}}{j_c} \right)^{n-1} \mathbf{j} \quad (3.3)$$

where $j = |\mathbf{j}|$, n is the creep exponent and ρ_0 is a resistivity constant. So the heat diffusion equation is solved together with the Eq. 3.3 and the Maxwell's equations. The time evolution of the magnetic properties inside the sample is obtained by inverting the Biot-Savart law [82]. From this description, the heat capacity, the thermal conductivity, the thickness, the critical current density and the heat transfer to the substrate strongly influence the existence of thermomagnetic instabilities.

3.3 Dynamic properties of the flux avalanches

In order to shed light on the dynamics of flux avalanches, some of the findings provided by the TM model are presented in this section. Moreover, experimental results are also shown to reveal the remarkable properties of the flux avalanches in thin films. First of all, the key prediction of the TM model is the existence of a threshold flux penetration depth (l^*) where a thin superconducting stripe with a width of $2w$ experiences the onset of dendritic flux avalanches, i.e., a condition for the instability onset, obtained by stability analysis, which is given by [88]:

$$l^* = \frac{\pi}{2} \sqrt{\frac{\kappa T^*}{E J_c}} \left(1 - \sqrt{\frac{2h_0 T^*}{ndEJ_c}} \right)^{-1} \quad (3.4)$$

where κ and h_0 are proportional to T^3 , n is proportional to the inverse of T and $T^* = -\left(\frac{d \ln J_c}{dT}\right)^{-1}$. As can be observed in the equation above (Eq. (3.4)), l^* depends only on the thermal and electromagnetic parameters of the superconductor and heat transfer coefficient to the substrate.

This critical flux penetration depth means that if the flux penetration depth (l) from the edge of the sample is smaller than l^* when magnetic field is applied starting from zero, the sample is stable and a critical state penetration takes place. However, when $l = l^*$ there exists the minimum flux penetration depth for the sample to become unstable, and TMIs trigger flux avalanches [88, 103]. As a consequence of the existence of l^* , it is possible to identify an onset field to trigger flux avalanches, the so-called threshold magnetic field (H^{th}), by considering the field profile of a long stripe with the width of $2w$ in the Bean model written in Eq. 2.64 resulting in the following:

$$H^{th} = \frac{J_c d}{\pi} \operatorname{arccosh} \left(\frac{w}{w - l^*} \right) \quad (3.5)$$

where $w - l^* = a$, which is the position of the flux front measured from the center of the sample. Fig. 3.5 proves the existence of l^* and also the dependence of H^{th} with this critical depth to cause the flux avalanches. Panel (a) shows magneto-optical images from a set of MgB₂ stripes with $d = 300$ nm and width ranging from 0.2 mm to 1.6 mm in steps of 0.2 mm taken at 4 K and 150 Oe, to illustrate the reduction of the avalanche activity depending on the width of the sample. Whereas for the widest stripe several dendritic avalanches can be observed, the narrowest stripe shows no sign of dendritic avalanches under this temperature and magnetic field. As the set of stripes were co-prepared on the same substrate and under the same conditions, l^* is assumed to be equal

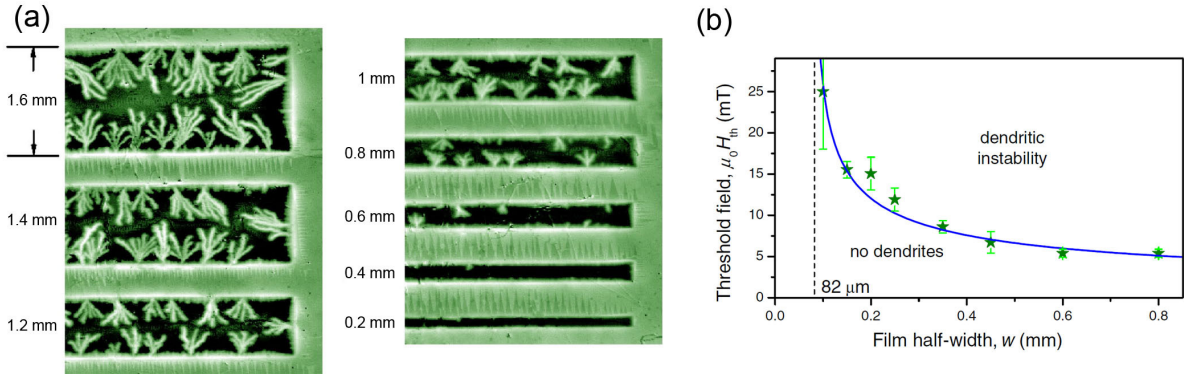


Figure 3.5: (a) MO images taken at 4 K and 150 Oe of MgB₂ stripes with widths ranging from 0.2 mm to 1.6 mm in steps of 0.2 mm, illustrating the decrease of avalanches activity. (b) Threshold field versus half width which shows the increase of stability decreasing the width and the minimum half width to cause flux avalanches. Adapted from [88].

for all samples. Therefore, the dependence of the onset field with half of the width is illustrated in Fig. 3.5b, showing that the stability of the thin film increases when the width is reduced. It is possible to identify a minimum half width of $82 \mu\text{m}$, below which thermomagnetic instabilities do not occur.

As H^{th} and l^* depend on the critical current density, a curve $H^{th}(J_c)$ can be built. This graph is shown in Fig. 6.1a and elucidates the existence of the onset field to trigger flux avalanches, as shown above when $l = l^*$, and of the upper limit, which is the cut-off field for the flux avalanches taking place when $l^* = w$ [104]. In other words, the region of the H - J_c diagram where $l^* \leq l \leq w$ delimits the area where the sample becomes unstable. This issue is treated in details in Chapter 6, where we build this border between stability and instability regions by measuring the ac susceptibility in order to obtain the critical current density. A very good agreement with this description of the TM model was obtained. Therefore, the existence of l^* taken analytically from the TM model shed light on several features of the dendritic flux avalanches in thin films.

The velocity with which the dendritic flux avalanches propagate in thin films is a remarkable feature. Whereas in superconducting bulks, the flux jumps take place in $10^{-3} - 10^{-5}$ s [80], in thin films this occurs in the range of nanoseconds. Leiderer and co-authors [89] have measured the propagation velocity of the flux avalanches induced by a short laser pulse in a YBCO thin film. They found a non-ballistic propagation when the dendritic avalanches penetrate the Meissner state with one initial regime where the velocity can reach more than 10^2 km/s, higher than the velocity of sound in the materials [61], decreasing for dozens of km/s in a second regime as can be seen in Fig. 3.6a. By means of simulations, Vestgård *et al.* [82] have found similar values and behavior of the propagation velocity of the flux avalanches which are displayed in Fig. 3.6b.

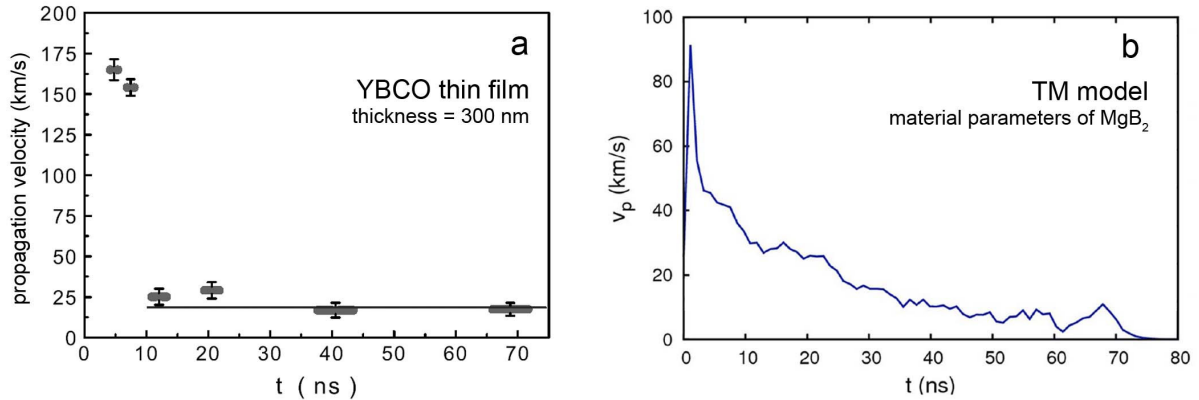


Figure 3.6: Propagation velocity in flux avalanches. (a) Experimental data for an YBCO thin film at $T = 10$ K and $H = 206$ Oe. (b) Simulations obtained from TM model using the material parameter of the MgB_2 . Adapted from [90] for (a) and [83] for (b).

Besides the propagation velocity, the numerical simulations based on the TM model also make it possible to obtain more information about the dynamics of the abrupt flux propagation inside the sample. Fig. 3.7 illustrates the temporal evolution of the distribution of magnetic flux (B_z), sheet current streamlines (j), reduced temperature (T/T_c) and induced electric field (E) for a dendritic flux avalanche occurring in an MgB_2 thin disk. Panel (a) reveals the flux pattern at 1 ns, 22 ns and 86 ns after nucleation of the thermomagnetic instability. A small dendrite emerges on the edge of the sample at first in the critical state, branching at 5 ns (not shown). At 86 ns the complex structure is completely formed and frozen. The sheet current streamlines in each stage of the evolution are displayed in Fig. 3.7b, which illustrates the critical state-like current at 1 ns and a non-homogeneous distribution after that with a higher current around the dendrites and a decreasing one inside them, already demonstrated experimentally by Laviano *et. al.* [105]. One of the most striking results is the temperature map of the flux avalanches. The local temperature in some regions inside the dendritic pattern during its propagation rises above the critical temperature destroying superconductivity in the main trunks, whereas the small branches show temperatures below T_c (Fig. 3.7c). The maximum temperature (T_{max}) versus time plotted in panel (e) shows the superconducting thin film at the same substrate temperature when a sharp increase of the temperature occurs due to the beginning of the process ($t = 0$ ns), decreasing smoothly after some nanoseconds. It shows that at least in the main trunks these avalanches do not contain quantized magnetic flux (vortices). Fig. 3.7d shows the behavior of the electric field reaching a plateau with values as high as 10^4 V/m during the propagation, much higher than the value predicted for the Bean model, of around 0.01–1 V/m. The model also predicts jumps in E before the dendritic avalanche, as

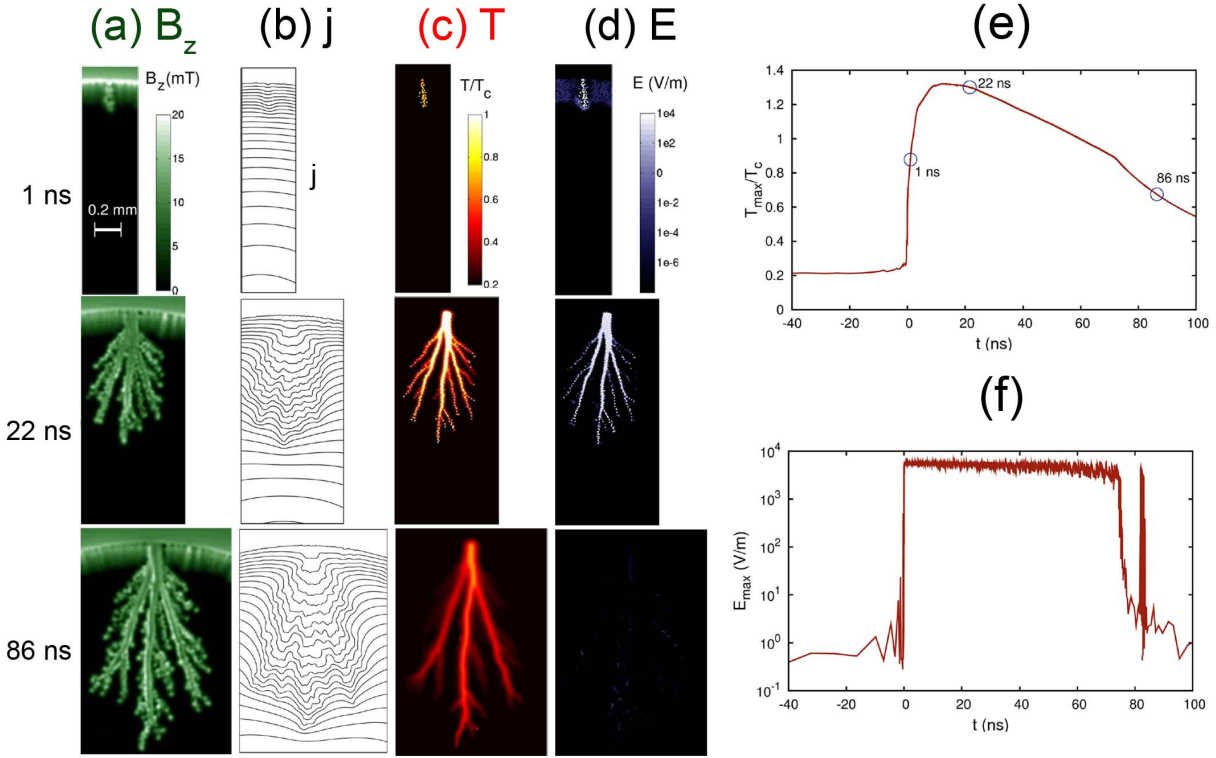


Figure 3.7: Theoretical predictions for the avalanche evolution for the (a) flux distribution (B_z), (b) induced sheet current (j), (c) reduced temperature (T/T_c) and (d) electric field (E) for 1 ns, 22 ns and 86 ns after the avalanche triggering in an MgB₂ disk. (e) Maximum temperature versus time which shows that $T > T_c$ and (f) Maximum electric field in the flux avalanche. Adapted from [90] and [83].

illustrated in the $E_{max}(t)$ curve below $t = 0$ s [panel (f)], which shows an initial perturbation of the vortices that will culminate in the abrupt event. It is important to mention that there are strong evidences that the temperature rise above T_c [89, 106], estimated from the laser pulse energy which nucleates flux avalanches in YBCO (Fig. 3.3a), and that the electric field has this order of magnitude during the flux avalanche [107], discussed briefly in the next section.

As already pointed out in the end of Chapter 2, the critical current density flows in the whole thin film perpendicularly to the applied magnetic field due to the demagnetization effect. The main consequence of it is related to the stability, which is lower for a thin film than for a bulk. Furthermore, the avalanche morphology is also influenced by the non-local electrodynamics. Denisov and others [102] have demonstrated that the dendritic avalanches are more probable in thin films than in bulks as a consequence of the demagnetization effects. For bulks, the flux jump shape depends on the electric field background, where above a certain threshold value (E_c) it transforms from a uniform to a fingering jump. This value is higher for bulks, however, Fig. 3.1d–e shows finger-like structures for thick disks, where the electric field is

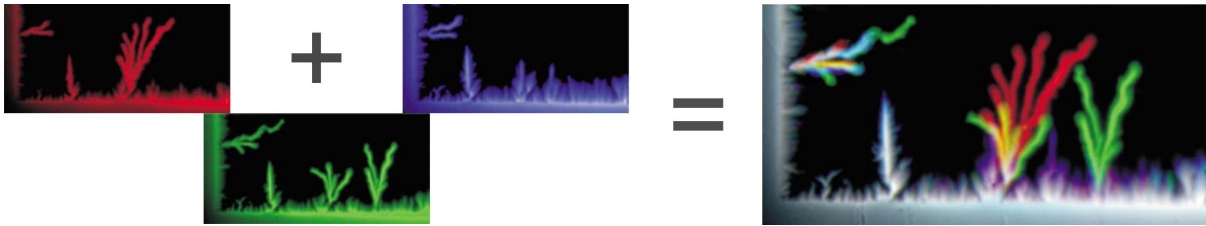


Figure 3.8: Left: Three images taken at $T = 9.2$ K and $H = 200$ Oe in identical runs in a MgB_2 thin film named and colored in red (R), green (G), and blue (B). Right: the large image shows the overlapping of the RGB images which shows the irreproducibility of the flux avalanches inside the specimen. Gray represents the superposition of three colors. Adapted from [88].

probably above E_c . In the case of thin films, the heat transfer coefficient between the superconducting film and the substrate also plays an important role, which above a certain critical value results in dendritic patterns independent of E . Therefore, the occurrence of avalanches with dendritic morphology is more likely in thin films than in bulks.

The flux avalanche morphology is never completely reproduced even at the same conditions which suggests it is a stochastic process. Fig. 3.8 shows three MO images colored with red (R), green (G) and blue (B) where the field is penetrated for three repeated identical runs carried out in a MgB_2 thin film [88]. As a result of adding the RGB images, an overlapped image is formed and the behavior of reproducibility can be visualized. In this figure, the color areas represent none or partial superposition whereas gray regions mean the sum of all colors and corresponds to a repeated flux distribution. As can be observed in the dendrite roots, the nucleation sites are reasonably reproducible. Mints and Brandt [108] have pointed out that a defect on the edge changes the critical current lines and consequently increases the electric field during the flux penetration. For this reason, the flux avalanches are more likely to occur at this point. However, other dendrites can appear as the green one on the bottom edge in Fig. 3.8 due to the stochastic feature of such event. Furthermore, the branching pattern inside the sample is different at each run, which means that the dendritic flux avalanches are not a result of a macroscopic pattern of quenched disorder in the thin film.

After the avalanche ceases – i.e., when the heat exchange with the substrate balances with the generated heat – the induced electric field rapidly decays and the temperature decreases (see Fig. 3.7) in the thin film. When $T < T_c$, the magnetic flux turns into vortices immersed in the superconducting sea. From the microscopic point of view, the vortices are distributed in a complex, non-uniform manner inside the dendrites as can be seen in Fig. 3.9a obtained by the Bitter decoration technique. The bright intensity is directly related to the vortex concentration and it is possible to observe that the center of the

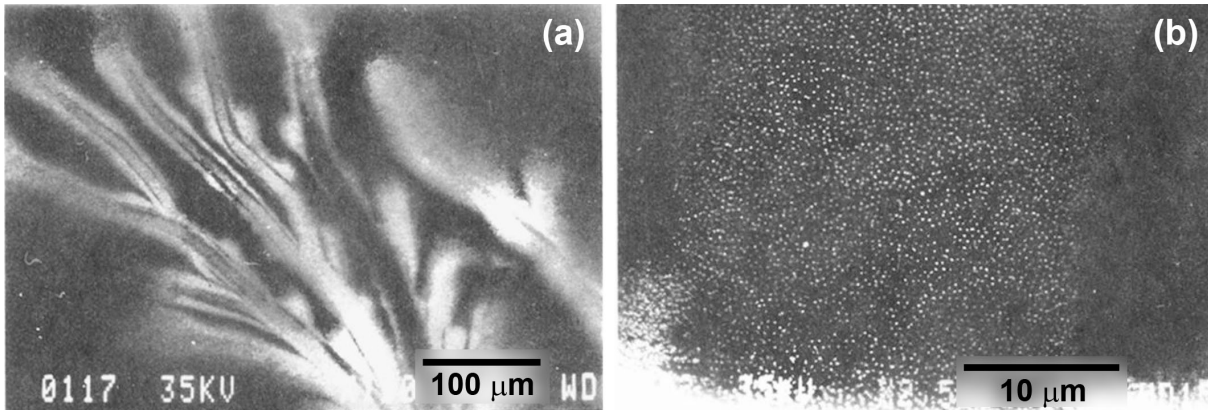


Figure 3.9: Bitter decoration image taken from the Nb thin film at 4.2 K already shown in Fig. 3.3b. (a) Flux distribution inside the flux avalanche after the event ceases. (b) Individual vortices which form a dendrite. Adapted from [91].

dendrites show a path, where the temperature is higher [93]. This feature is also addressed in the simulations presented earlier in Fig. 3.7a at 86 ns. Fig. 3.9b shows the vortices inside a dendrite of the pattern where it can be seen that they are highly disordered like in a vortex liquid state [91]. After Vestgård's simulations, which show that $T > T_c$ for a short time, this absence of order seems to be occasioned by the abrupt quench of the penetrating magnetic flux.

The introduction of artificial defects has shown interesting results for the morphology and for the occurrence of the flux avalanches as well [109, 110, 111]. Vlasko-Vlasov *et al.* [112] have shown that in a film with a lattice of ADs, flux avalanches are guided along the antidot rows. Moreover, the existence of the antidot lattice increases the instability region in the magnetic field versus temperature (HT) diagram. Therefore, arrays of antidots are inducers of flux avalanches [109, 110], as discussed in Chapter 7. The guidance and morphology of flux avalanches, as well as interesting aspects of avalanche are discussed in more details in Chapter 8.

3.4 Avoiding flux avalanches

Flux jumps in the past and flux avalanches nowadays have gotten a lot of attention as they can have impact on the performance of materials considered relevant for the technological applications of superconductors. Stability is essential for the reliability in the operation of many devices, such as superconductor magnets [86] and microwave resonators [113]. Obviously, the simplest way to avoid the abrupt flux jump is to employ the material outside the avalanches region in the HT diagram [114]. Actually, flux avalanches in thin films also can be prevented by designing devices where the width is

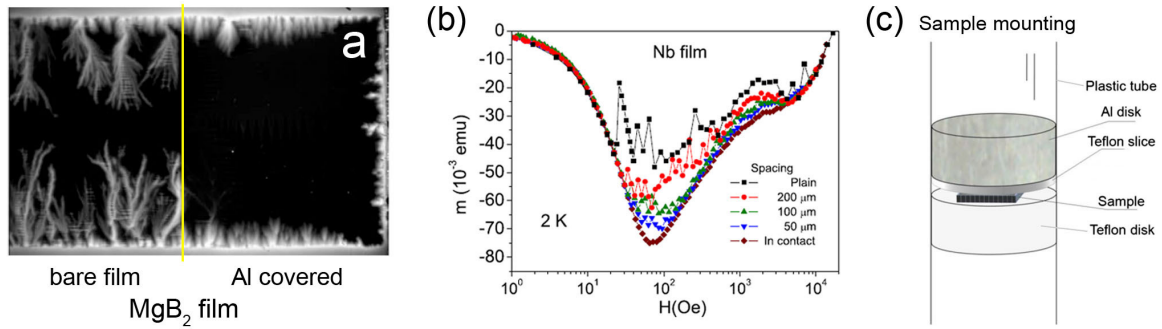


Figure 3.10: (a) MO image taken at 3.5 K with $H = 85$ Oe of a MgB_2 thin film partly covered with an Al foil (on the right half) with the suppression of the avalanches. (b) Dc magnetization (virgin curve) of an Nb film at 2 K with an aluminum disk separated by different distances by Teflon spacers showing that while the distance is reduced the suppression of the avalanches activities increases. (c) Sample mounting with the Teflon spacers and Al disk on top to suppress the avalanches. Adapted from [115] (a) and [116] (b,c).

smaller than l^* , as pointed out by Denisov and co-authors [88] and shown in Fig. 3.5. In superconducting magnets, flux jumps have been prevented by producing wires with a multifilamentary profile in a copper matrix [86]. Nonetheless, in some cases these options can be unfeasible choices, and other alternatives may be necessary.

Baziljevich *et al.* [115] have shown that a metallic layer on top of the superconducting thin film can suppress the activity of the flux avalanches. Fig. 3.10a shows an MO image of a MgB_2 thin film with the left half bare, where dendritic avalanches occur, and the other part covered with an aluminum foil, where gradual penetration takes place, despite of a certain roughness due to defects spread out in the film. The authors claimed that this metallic foil provides an efficient heat sink for the superconductor, which means, there would have been enough time for the covered region to assimilate the heat generated by vortex motion, and the TMI would not have been initiated. Nonetheless, Colauto and co-workers [116] have demonstrated that the suppression is inversely proportional to distance between an Al disk and the superconducting thin film, as illustrated in Fig. 3.10b by dc magnetization curves. The distance is altered thanks to Teflon slices with different thicknesses, which are used as spacers, placed between the Al disk and the film, as displayed in (c). These data show that the thermal surroundings virtually do not change, but the avalanche activity decreases with the reduction of the distance between the metallic disk and the superconducting specimen. Thus, they concluded that the eddy currents induced in the metallic cover act as a magnetic brake, partially inhibiting the abrupt flux entrance. Very recently, Mikheenko and co-authors [107] have measured the voltage induced in a coated metallic layer during the occurrence of flux avalanches, allowing them to estimate an electric field of around 10^4 V/m, as predicted by Vestgård's simulations [83].

The aim of this thesis is not to describe a way to suppress the flux avalanches, after all, arrays of ADs in decorated samples induce avalanches in a larger window of temperatures and magnetic fields. However, we investigated the effects of the flux avalanches in ac susceptibility measurements, the existence of a threshold critical current density to trigger flux avalanches, and the influence of the landscape of nanoengineered antidots on the dynamics of flux avalanches. We have also studied the influence of the shape of ADs and of different types of lattices on the avalanche morphology.

4 *Experimental techniques*

This chapter introduces the main experimental techniques used for sample preparation and characterization. The electron beam lithography was used to obtain patterned thin films, deposited by pulsed laser deposition and dc-magnetron sputtering. Structural characterizations were performed by X-ray diffraction, X-ray fluorescence, atomic force and scanning electron microscopies. The superconducting properties were studied by means of magneto-optical imaging, dc magnetization and ac susceptibility.

4.1 Sample preparation

The samples investigated in the present work are superconducting thin films of either Nb or a-MoGe, prepared on Si/SiO₂ substrates, with a periodic array of holes (antidots). These periodic microstructures were fabricated by the electron beam lithography technique described in Section 4.1.1. The PLD and dc-magnetron sputtering techniques used to deposit the thin films are discussed in Sections 4.1.2 and 4.1.3, respectively.

4.1.1 Electron beam lithography

The fabrication of micro- and nano-scale features by lithographic techniques is well established. Lithography is a general term for several nearly related processes which includes coating, exposure, and development of resists. Among several techniques, the Electron Beam Lithography (EBL) is an essential tool for obtaining ultrasmall structures with high quality and a reasonable writing speed [117, 118].

The EBL is based on the interaction between high-energy electrons and organic materials. In the polymeric materials, an electron beam (e-beam) interacts predominantly via inelastic scattering and may lead to permanent modifications of the polymeric chains. The sensitive polymers specially optimized for EBL are known as *e-beam resists*, the function of which is therefore to act as a resist mask, i.e., to generate structures and, afterward, transfer them to the sample or the device. There are two types of e-beam resists: *positive* and *negative* [118]. When a positive resist is used, the

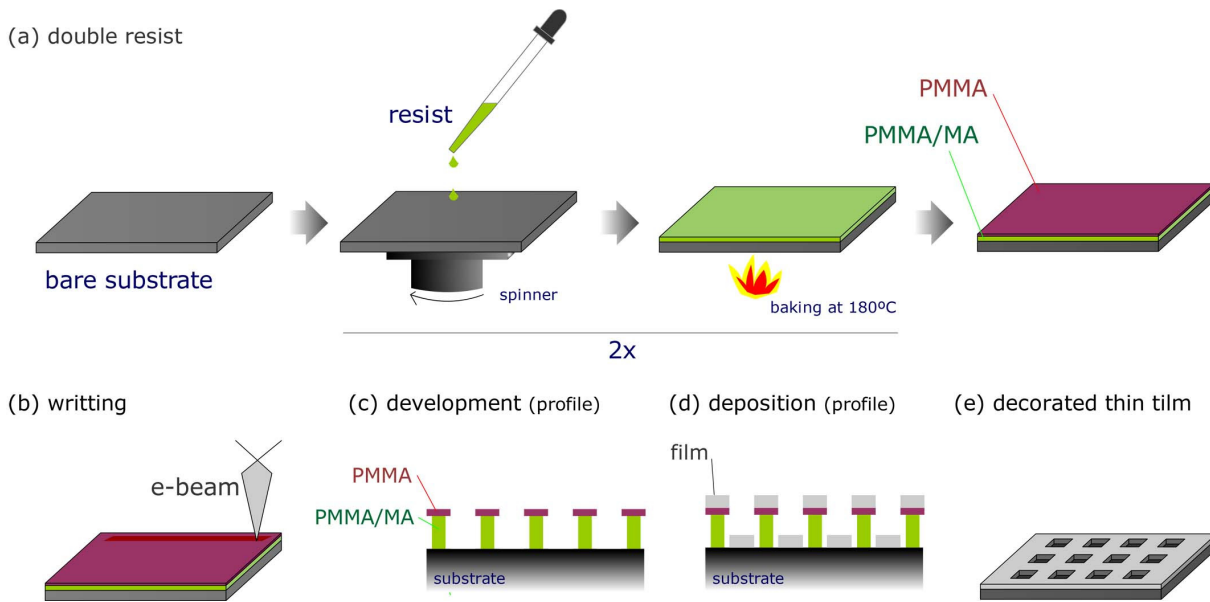


Figure 4.1: Schematic representation of the e-beam lithographic process: (a) a double resist layer is spun on the substrate; (b) the scanning electron beam breaks the positive resist and changes the physical properties of the exposed area; (c) profile of the resists after the development; (d) deposition of the material onto the resist mask; (e) after a lift-off procedure, the final patterned film is reached.

e-beam leads to a permanent breakage of chemical bonds, decomposing it into their unbound monomers. After that, an organic solvent, so-called *developer*, is used to remove the resist exposed to the e-beam in a process named *development*. On the other hand, when a negative resist is employed, the polymer becomes cross-linked due to the interaction with the energetic electrons. In this situation, the unexposed resist is removed by the developer. In other words, the e-beam modifies the original structure of the polymer in both cases and, consequently, the exposed parts have different properties compared to the unexposed polymer [118, 119].

For the samples in the present thesis, the patterns were designed by using positive double resist layers. A bare Si/SiO₂ substrate was coated by copolymer methyl metacrylate (PMMA/MA) and polymethyl metacrylate (PMMA) using a spinner with a vacuum pump, over 40 seconds using speeds of 3500 rpm for PMMA/MA and 6700 rpm for PMMA. After that the resists were baked out at 180 °C for 120 s on a hot plate after each spinning, resulting in a total resist thickness of about 200 nm. A schematic representation of the coating process of the double resist is shown in Fig. 4.1a. The resists were then exposed to an e-beam from a dedicated or an adapted scanning electron microscope in order to write the structure (Fig. 4.1b). After the exposure, the developer 4-Methyl-2-Pentanon-1-Propanol was used to the development for 105 s at room temperature and then the film was immersed in Propanol for 30 s, followed by baking out during 90 s at 95 °C on a hot plate [120].

The double resist procedure was chosen in order to eliminate interfacial problems between the resist and the deposited film. For this, the sensitivity of the e-beam resists should be taken into account. This property is related to the dose (flux of electrons per area unit) needed to decompose the e-beam resists. In this configuration, PMMA and PMMA/MA have the nominal sensitivity of $100 \mu\text{C}/\text{cm}^2$ and $20 \mu\text{C}/\text{cm}^2$, respectively, which means that under the same dose, PMMA/MA breaks in its monomers more than PMMA [120]. Due to this, the overhanging resist profile can be observed in the panel (c) of Fig. 4.1. After that, a continuous film is deposited on top of the resist mask (Fig. 4.1d). The thin film should be deposited at temperatures lower than 200°C in order to avoid the melting of the mask and the film thickness should have $1/3$ of the resist thickness as well. Finally, the double layer resist was removed in a lift-off procedure, facilitated by the resist profile, in acetone at 65°C for a few minutes and agitated in an ultrasonic bath in order to remove the resists completely and, consequently, the material above the resist, resulting in the thin film decorated with a pattern as illustrated in Fig. 4.1e.

The electron beam lithography has been done at IMEC (Interuniversity Microelectronic Center) in Leuven or in a JEOL-5600 scanning electron microscope equipped with a Raith GmbH controller, including a software, for electron beam writing at the Institute for Nanoscale Physics and Chemistry (INPAC), Katholieke Universiteit Leuven, also in Leuven, Belgium.

4.1.2 Pulsed laser deposition

Pulsed Laser Deposition (PLD) is a versatile growth technique where a material from the surface of a target is evaporated by using high-power laser pulses. The principle of PLD is illustrated in Fig. 4.2. It consists of an ultra-high vacuum (UHV) chamber where a target holder and substrate heater are kept under controlled conditions of temperature, gas environment and pressure. Outside the chamber, a set of optics including optical windows, lenses, mirrors, and apertures are responsible to focus the laser beam – the specifications of which are in the figure – onto the target inside the chamber [121].

The intensity and duration of the incoming pulsed laser are crucial factors in the PLD deposition. In general, the intensity is of the order of $10^8 \text{ W}/\text{cm}^2$ with a pulse duration ranging from femtoseconds to nanoseconds. When the pulse achieves the target several processes take place. In the initial part of the pulse, electromagnetic energy is converted into electronic excitation and after that into thermal, chemical and mechanical energy, which results in evaporation and ablation of the target. Then there is a plasma formation

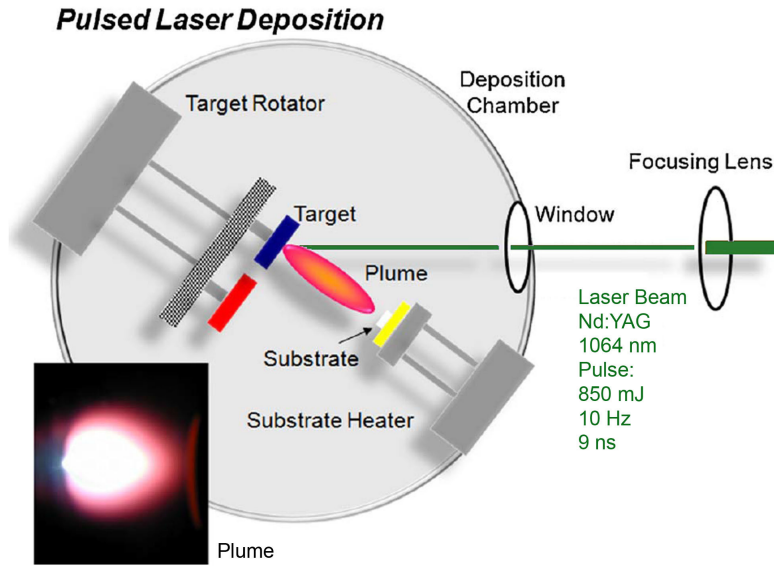


Figure 4.2: Scheme of deposition with pulsed laser deposition. The inset shows a plume picture. Figure adapted from [121].

which also interacts with the incoming pulse, increasing the plasma temperature. This plasma, also known as *plume* (for instance, the inset of Fig. 4.2), is formed by ions, electrons, molecules, atoms, clusters, and micron-sized particulates with high energy. The plume has a dense shape and expands because of thermal and repulsive effects, creating a jet of material towards the substrate where it recondensates and forms a thin film [122, 121].

Although already described in the 1960s, the research interest in PLD increased drastically with the advent of high temperature superconductors in 1987. PLD was the first successful technique employed to grow high-quality thin films of YBCO [123, 124]. Nowadays, PLD is a suitable technique to deposit thin films with a complex composition, especially oxides, since it is possible to keep the same target stoichiometry because the growth occurs far from the equilibrium. On the other hand, ejection of large particles, small homogeneous area of deposition ($\sim 1 \text{ cm}^2$), and low evaporation rates ($\sim 1 \text{ \AA}$) are the disadvantages and have hampered the scalability of PLD.

A better crystallinity is reached by increasing the substrate temperature. Nonetheless, in our case, amorphous thin films of Mo-Ge alloy (a-MoGe) were desirable since its superconducting properties improve with its amorphicity [125]. Therefore, these thin films were prepared at room temperature. The source material with composition $\text{Mo}_{78}\text{Ge}_{22}$ and purity of 99.95% was evaporated in Leuven/Belgium at INPAC. In that setup, a neodymium-doped yttrium aluminum garnet (Nd:YAG) laser (Quanta-Ray GCR-3) with a fundamental wavelength of 1064 nm and pulse with energy, duration and

frequency of 850 mJ/pulse, 9 ns, and 10 Hz, respectively, was used as the ablation source. The deposition was performed with base pressure of the order 10^{-7} Torr and the evaporation rate of approximately 0.3 Å/s.

4.1.3 Dc-magnetron sputtering

Sputtering is a widely used technique for the deposition of thin films for several applications. This technique consists of momentum transfer from an incident beam with enough energy to a target, resulting in an ejection of particles from the source material. The dc-magnetron sputtering is a suitable technique to produce thin films of conductor materials, since it is an alternative low-cost option compared to MBE (Molecular Beam Epitaxy) [126], whereas rf-magnetron sputtering is suitable to deposit insulating materials.

In a UHV chamber, argon gas is inserted with a pressure of the order of 10^{-3} Torr. After that, a dc voltage of some kV is applied between the target (cathode) and the substrate holder (anode). Under the right conditions of gas pressure and voltage, the gas will breakdown into a plasma discharge. Then Ar^+ ions are accelerated and bombard the target, which after the collision cascades, eject secondary electrons and atoms from the source material. These electrons are accelerated and collide with Ar atoms to form more ions in order to sustain the plasma. Consequently, ejected atoms during this process condensate on the substrate and form the thin film [121, 126]. In the present work, dc-magnetron sputtering systems were used. In this configuration, permanent magnets are placed behind the target. The local magnetic field traps the secondary electrons close to the cathode, increasing the number of collisions with Ar atoms and consequently, the plasma intensity. As a result, it raises significantly ($\sim 10x$) the evaporation rate [126].

The main advantages of the dc-magnetron sputtering are its scalability, as well as large homogeneous area of deposition and reproducibility. The niobium thin films studied in this work were deposited at the University of Cambridge/UK (Prof. M. G. Blamire's Group), at the Università degli Studi di Salerno/Italy (Prof. C. Attanasio's Group), and at the Chalmers University of Technology in Göteborg/Sweden (Prof. J. Fritzsche's Group).

4.2 Sample characterization

The thin films studied in this thesis were characterized by X-ray diffraction (XRD) and X-ray fluorescence (XRF), atomic force microscopy (AFM), and scanning electron

microscopy (SEM). A brief description of each technique will be presented in the following.

4.2.1 Structural characterizations based on X-ray

Two techniques based on X-rays have been used to structural studies. First, X-ray diffraction (XRD) was used to determine the crystallinity and lattice structure of the thin films studied here. Second, X-ray fluorescence (XRF) studies were conducted to analyze the final composition of the samples.

The working principle of XRD is probing elastic scattering of high energy photons (≈ 40 kV) on a periodic lattice, whose typical interatomic distances are of the order of the photon wavelength [127]. The source of these photons is a copper anode from which a CuK_α radiation was selected with $\lambda = 1.541 \text{ \AA}$. The condition for a peak in the measured intensity is found when the reflected rays from successive atomic planes interfere constructively. This is the case when the Bragg condition is satisfied, with $2d \sin \theta = n\lambda$, where d is the crystal lattice plane spacing, n is an integer, and θ is the angle of the incident beam with respect to the planes. The model of the diffractometer used at *Grupo de Materiais Avançados* at the *Universidade Estadual Paulista/Bauru* was a ACF-7 from Rigaku performed in a small angle θ - 2θ scan.

XRF is widely employed for the quantitative and qualitative elemental analysis. When photons of sufficiently high energy from an X-ray source hit the sample, ionization of its constituents may take place. The ionization induced by X-ray photons occurs in the inner shell electrons by photoelectric effect and creates vacancies. Then, electrons from the outer shell undergo an allowed transition and will occupy these vacancies, releasing a well-defined photon in the X-ray range corresponding to the energy difference between the atomic shells involved. Therefore, detecting the energy of the X-ray photons emitted from the sample and its intensity provides the identification of the elements and the determination of their concentration, respectively [128]. The spectra were carried out in a Shimadzu EDX 720 at LCE (*Laboratório de Caracterização Estrutural*), DEMa (*Departamento de Engenharia de Materiais*) at UFSCar (*Universidade Federal de São Carlos*).

The Nb thin films have shown a body centered cubic (bcc) structure, whereas the a-MoGe thin films have not shown any sign of crystallinity. Its composition was determined to be $\text{Mo}_{79}\text{Ge}_{21}$.

4.2.2 Atomic force microscopy

The atomic force microscopy (AFM) was developed by Binnig, Quate and Gerber in 1986 [129] and provides a topographic characterization of the specimen surface. It is based on scanning-probe microscopy, where some local property is monitored by a sharp tip (probe) scanned in close proximity to the sample surface. In the case of AFM, the interatomic force between the tip and the surface which is being monitored allows one to obtain an image with the superficial roughness of the sample.

The principle of operation of an AFM is schematically represented in Fig. 4.3. The tip is attached to a flexible cantilever. To perform the scan on the surface, the sample is mounted on piezoelectric drives and the cantilever is raster-scanned across the specimen in the xy -plane. The z -motion of the cantilever is related to the interatomic van der Waals forces between the tip and the specimen surface. This motion deviation is recorded by the angular deflection of a reflected laser beam, whereas a feedback mechanism maintains the force on the tip constant by controlling the z -direction of the piezoelectric drive in order to compensate the changes in force. Therefore, the morphology and thickness of the surface structures down to micrometer scale are determined.

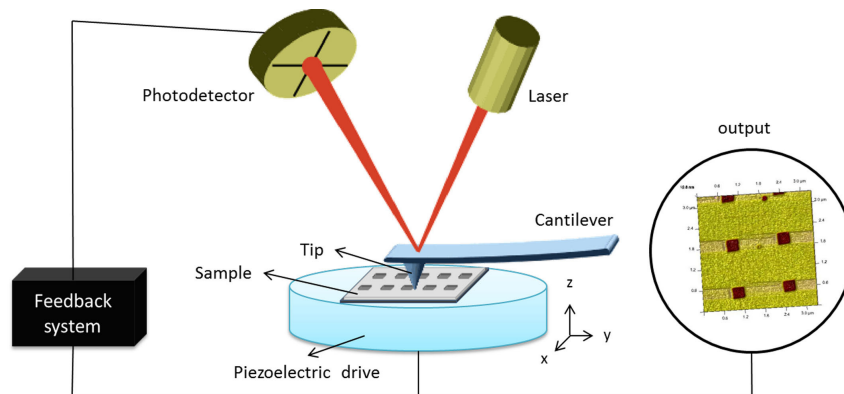


Figure 4.3: Schematic representation of the atomic force microscope. Adapted from [130].

The images, taken at LCE/DEMa-UFSCar, with a Nanoscope V microscope manufactured by Digital Instruments, were obtained in the contact mode, where the tip is kept in contact with the sample surface.

4.2.3 Scanning electron microscopy

In order to obtain complementary information about the antidot morphology, as well as the thin film surface, the specimens were studied by Scanning Electron Microscopy (SEM). This technique consists of a gun that emits an electron beam accelerated due to

a potential difference of some dozens of kilovolts. This beam is focused by electromagnetic lenses and scans the sample surface with the aid of deflecting coils [131]. The primary electrons interact with atoms close to or at the surface and atomic electrons may be ejected. If those electrons have energy lower than 50 eV, they are so-called secondary electrons, and result from the inelastic interactions between the incoming electrons with electrons of the conduction band in metals or electrons of the valence band in semiconductors and in insulators. An image can be built by collecting secondary electrons from each small scanned area on the specimen. The intensity of each point will depend on the quantity of electrons that arrives at the detector [119].

The measurements were carried out in a Phillips XL-30 FEG microscope, with a Schottky-type field emission gun, also at LCE/DEMa at UFSCar.

4.3 Magnetic measurements

The thin films were studied by dc and ac magnetometry in the experimental setups PPMS-6000 (Physical Property Measurement System) and MPMS-5S (Magnetic Properties Measurement System), both fabricated by Quantum Design. The images were taken in the magneto-optical imaging (MOI) setup. All these experimental apparatus are installed in São Carlos/São Paulo/Brazil at GSM/UFSCar.

4.3.1 Magneto-optical imaging

Several imaging techniques of low temperature have been developed and refined to visualize the magnetic flux distribution of superconductors [132], one of which has been demonstrated to be very efficient and versatile – the Magneto-Optical Imaging (MOI). This technique is based on the magneto-optical Faraday effect in which the polarization plane of a linearly polarized beam of light is rotated when it passes through a Faraday active material under a magnetic field applied parallel to the incident beam [133], as illustrated in Fig. 4.4a, where the beam of light crosses the crystal twice. The rotation angle θ_F varies with the magnitude of the magnetic field component H_z parallel to the incident beam, the length of the optical layer d in the indicator material and a material-specific and frequency-dependent parameter $V(\omega)$, so-called Verdet constant:

$$\theta_F = V(\omega)dH_z \quad (4.1)$$

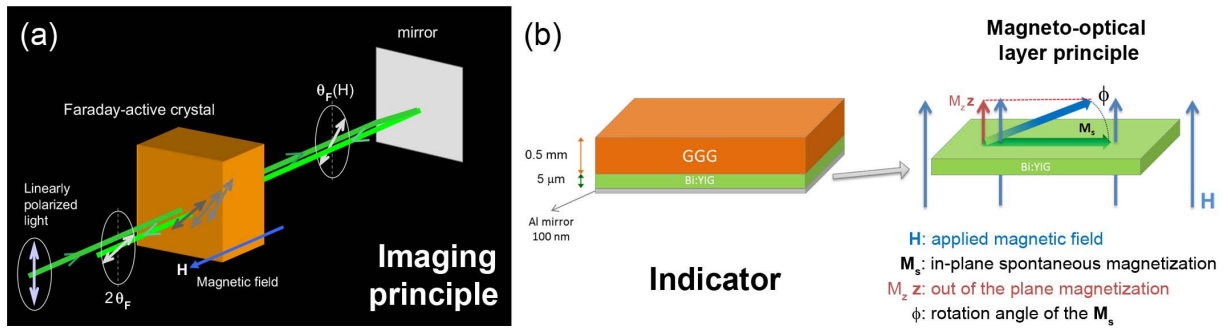


Figure 4.4: (a) Linearly polarized light goes through a Faraday-active crystal under an applied magnetic field. (b) Schematic representation of the indicator and the MOL with spontaneous magnetization in plane. A component out-of-plane (M_z) arises under influence of the perpendicular magnetic field. Adapted from [139].

Since the superconducting materials have not shown a significant Faraday effect, a magneto-optical layer (MOL) with a large Verdet constant has been used as a sensor to reveal the landscape of magnetic flux inside the superconductor. The first observations by employing this phenomenon was done by Alers [134] and De Sorbo [135] in 1957 and 1960, respectively. They imaged the intermediate state in type I superconductors by using a MOL of transparent paramagnetic cerium-based glass compounds with $V(\omega)$ of about $5 \cdot 10^{-4} \text{ }^\circ/\text{Oe} \cdot \mu\text{m}$, reaching a spatial resolution better than $200 \mu\text{m}$. In 1968, Kirchner [136] developed a new family of MOLs based on the thin film coating of paramagnetic europium compounds EuS , EuF_2 , and EuSe , with a Verdet constant of $0.1\text{--}1^\circ/\text{Oe} \cdot \mu\text{m}$, obtaining spatial resolution of $2 \mu\text{m}$. These materials, as well as their mixtures, were used with great success to study type II superconductors [137] until the HTS were discovered in 1986. The studies with HTS were rather limited since the sensors lost their Faraday effect above around 15 K [138], making a rush to find MOLs which exhibit the Faraday effect within a larger range of temperatures.

In 1989, Polyanskii and co-authors [140, 141] employed another class of Faraday-active crystals to visualize the flux distribution in superconducting materials. These new indicators are ferrimagnetic films with anisotropic spontaneous magnetization and a complex structure, the so-called garnet* which shows a large Faraday effect from cryogenic temperatures up to 400 K and nearly temperature-independent below 150 K [133]. Since 1980s, the most used MOI sensor is the bismuth-substituted yttrium iron garnets (Bi-doped YIG) with a thickness between 2 and $5 \mu\text{m}$ (in our case $5 \mu\text{m}$), grown by liquid phase epitaxy on gadolinium gallium garnet ($\text{Gd}_3\text{Ga}_5\text{O}_{12}$, GGG) substrates with [100] growing direction. These indicators show an in-plane spontaneous magnetization (\mathbf{M}_s) which tilts out of the plane by an angle ϕ due to the normal magnetic field, for instance,

*The general formula of the garnets is $\text{X}_3\text{Y}_2(\text{ZO}_4)_3$.

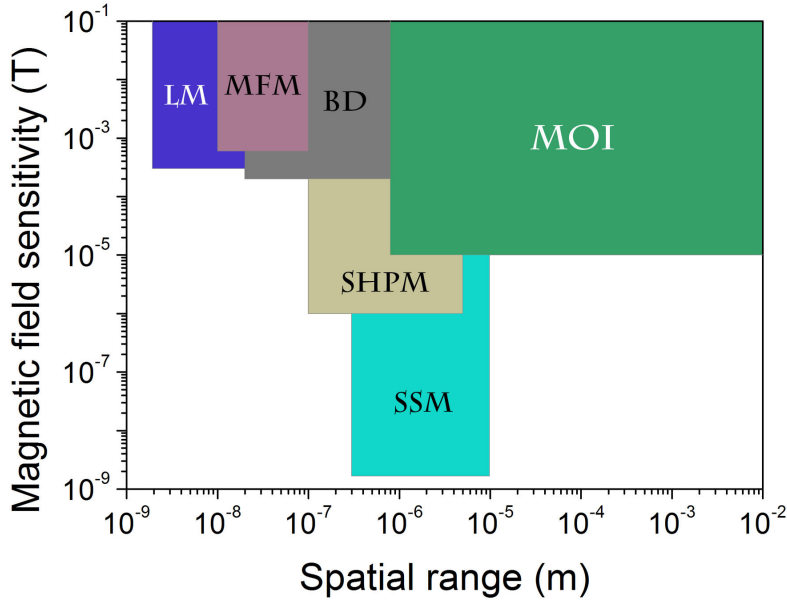


Figure 4.5: Magnetic field sensitivity versus spatial range of several techniques: MOI, Scanning SQUID microscopy (SSM), Scanning Hall-probe microscopy (SHPM), Bitter Decoration (BD), Magnetic Force Microscopy (MFM), and Lorentz microscopy (LM). The data for MOI were taken from [133]; for MFM, SSM and SHPM from [142]; for BD from [38, 79, 143]; for LM from [144]. Figure adapted from [132, 145, 146].

due to the stray field of the superconductor, where the Faraday rotation is proportional to the out-of-plane component (M_z). A schematic representation of the indicator film is shown in Fig. 4.4b as well as the stack of layers and their thickness for the Bi:YIG films used in the present thesis.

Fig. 4.5 shows a comparison among MOI and other imaging techniques: Scanning SQUID Microscopy (SSM), Scanning Hall-probe Microscopy (SHPM), Bitter Decoration (BD), Magnetic Force Microscopy (MFM), and Lorentz Microscopy (LM). It can be seen that the magnetic field sensitivity and spatial resolution of MOI is around 10^{-5} T and $0.8 \mu\text{m}$ [43] with the largest field of view, ranging from microns to centimeters. Physically, the spatial resolution is limited by the wavelength of the light source (~ 500 nm), however, the distance between the superconducting thin film and the Faraday-active layer also influences the spatial resolution enormously. This problem can be overcome by means of the deposition of the MOL directly on top of the superconductor, which allowed Goa *et al.* [43] to observe single vortices in NbSe₂ single crystal. Moreover, the temporal resolution is a powerful characteristic of the MOI technique, which reaches 10 ns and, for instance, allowed Bolz and co-authors [90] to measure the flux avalanche velocity of about 100 km/s in YBCO thin films.

In conclusion, dynamical processes can be investigated in wealth of details by means of MOI, since it is possible to obtain images with a resolution of a few microns in a short

time, allowing one to observe the magnetic processes in real-time in the superconducting materials.

4.3.1.1 MOI workstation at GSM/São Carlos

A magneto-optical setup is essentially composed by a polarized light microscope, a cryostat with optical window, electromagnetic coils to apply a magnetic field and a camera to record the images, as illustrated in Fig. 4.6a. A light source emits a visible light beam of high intensity that passes through a polarization filter (polarizer). Then, the polarized beam is deflected by a beam splitter, reaching the indicator film. The light passes through the GGG substrate, which has a low light absorption coefficient, and passes through the MOL, rotating θ_F where the MOL has a nonzero M_z component. After that, the mirror layer reflects back the light which returns to the MOL, rotating θ_F again. Thus, the total rotation angle of the polarization plane is $2\theta_F$, as presented schematically in Fig. 4.6a. Then, the beam passes again through the beam splitter and reaches the analyzer filter. This analyzer is set at 90° relative to the polarizer, allowing only rotated light to go through. A coupled charged device (CCD) camera captures the intensity of the rotated light, producing a map of light intensities proportional to the rotation angle, forming an image of the flux distribution landscape of the superconductor [61, 133].

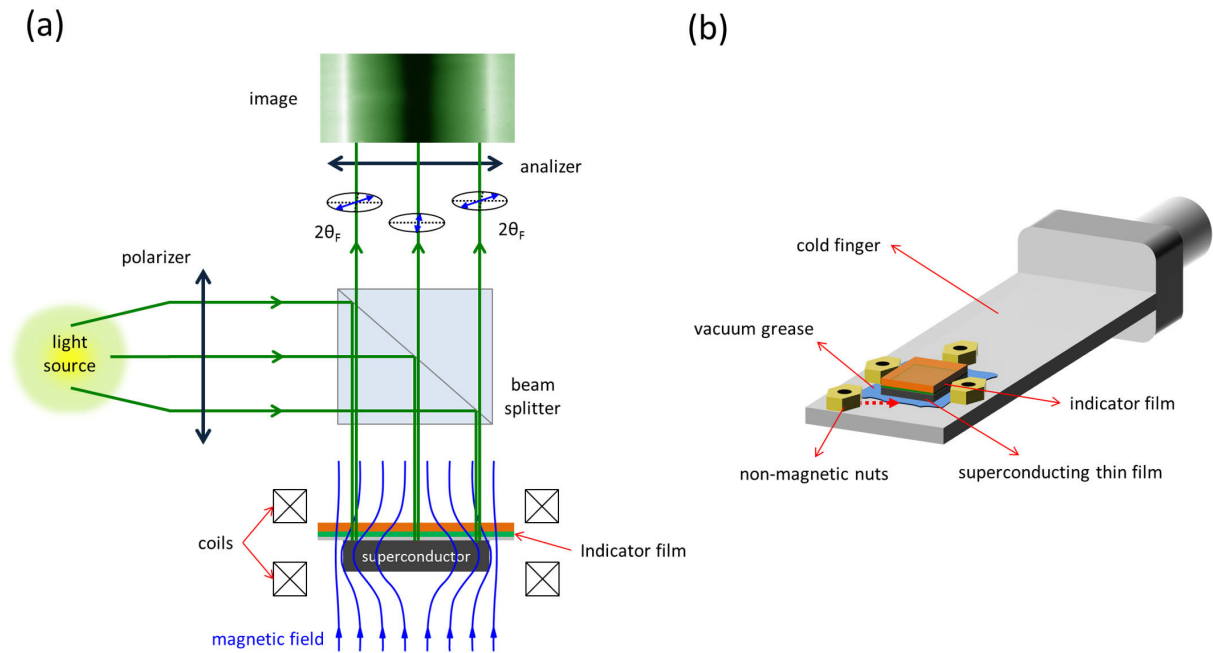


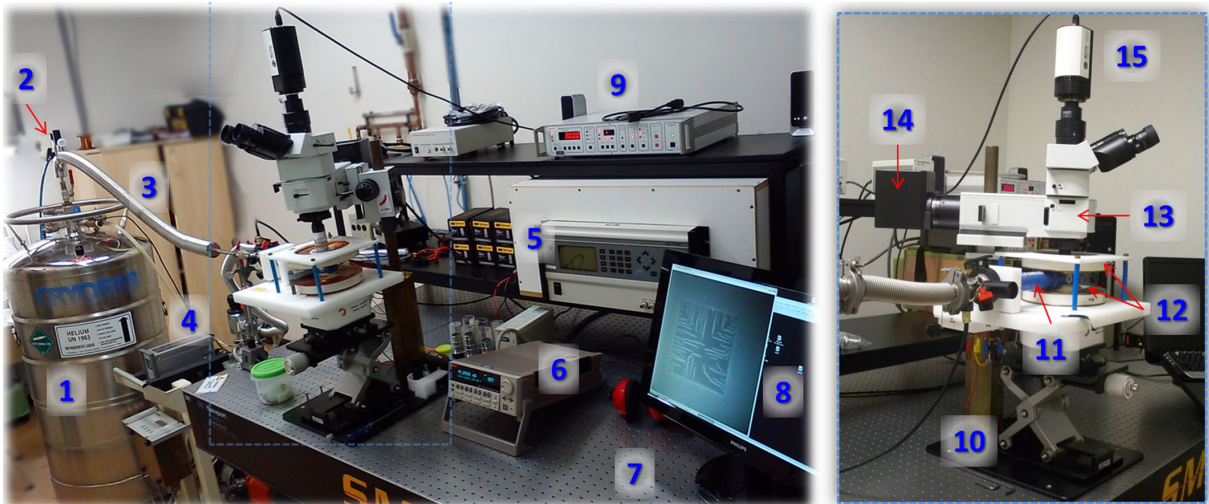
Figure 4.6: (a) Schematic representation of the magneto-optical setup and (b) of the grease-superconducting thin film-indicator assembly on the cold finger. Figures adapted from [139] and from [6], respectively.

In order to run the experiment, the superconducting thin film and the indicator film are cleaned up by using toluol in an ultrasound bath for about 5 seconds. After that, the films are immersed in acetone and isopropanol to remove any dirt, ensuring a flawless contact with the MOI sensor to improve the spatial resolution. Then the superconducting thin film is carefully positioned on the copper cold finger with a small amount of Dow Corning vacuum grease to assure a good thermal contact between them. The indicator film is directly placed on top of the superconducting thin film to reveal the magnetic flux distribution. A scheme of the experimental assembly is illustrated in Fig. 4.6b. Non-magnetic nuts are added around the assembly to avoid any undesired movement of the indicator film.

The next step is achieved by inserting the cold finger into the chamber cryostat. The film indicator should be horizontally positioned in order to obtain the maximum intensity of the reflected light. Then the chamber cryostat is pumped out by an Alcatel vacuum pump set with a mechanical and a turbo pump to reach a pressure of $2 \cdot 10^{-5}$ Torr. In our system, a continuous flow cryostat model MicrostatHe with optical windows, manufactured by Oxford instruments, is used. The liquid helium (LHe) supply is provided by a suitable transfer tube put into the cryostat and connected to an external Dewar vessel. LHe is collected from the Dewar vessel, passes through the transfer tube and exchanges heat with the cold finger while pumped with a Sogevac SV40B pump. In order to achieve temperatures as low as 2.5 K, a needle valve controls the LHe flow to maintain it at low pressure and reach temperatures lower than the boiling point of helium. A heater is installed in the cold finger and the temperature control is provided by an Oxford ITC 503S temperature controller.

The magnetic field is generated perpendicular to the superconducting film plane by a split-pair of copper coils. Two current sources can be used to obtain the magnetic field: a Keithley model 6221 and an Elgar model SW1750A, which allows one to reach fields up to 48 Oe and above 1 kOe, respectively. It is important to mention that the MOL saturates around 1000 Oe, that is, at that field the MOL magnetization is completely rotated in the z direction and no contrast is detected.

The experimental setup is served by a reflected beam polarization microscope model BX-RLA2 equipped with a 100 W mercury lamp (U-LH100H-3), a polarizer (U-PO3), an analyzer (U-AN360-3), and an ultraviolet cut filter (U-25L42), all manufactured by Olympus. The cryostat and the copper coil set are mounted on an x - y - z micrometer stage to focus the sample. The images are acquired by a digital camera model Retiga-4000R



- | | | |
|--------------------------|-----------------------------|------------------------------|
| 1 – dewar vessel | 6 – Keithley current supply | 11 – cryostat |
| 2 – needle valve | 7 – optical table | 12 – cooper coils |
| 3 – transfer tube | 8 – PC | 13 – polarization microscope |
| 4 – pump set | 9 – temperature controller | 14 – light source |
| 5 – Elgar current supply | 10 – xyz stage | 15 – CCD camera |

Figure 4.7: Magneto-optical imaging workstation in São Carlos with the microscope set in detail. The parts are identified in the caption on the bottom.

Fast 1394 Mono Cooled from QImaging with 4.19 megapixel (2048 x 2048 pixels) in a 12-bit digital output connected to a software developed at LabView, allowing one to control the temperature, the magnetic field and the camera. The images are processed with the software ImageJ [147].

The MOI apparatus at the GSM/São Carlos is illustrated in Fig. 4.7. The microscope and the 3D positioner stage, including the cryostat and the coils, are mounted on a Newport optical table model RT equipped with active pneumatic suspension system in order to minimize noise from mechanical sources. The typical acquiring time used in our experiments was of the order of 100 ms (due to the camera) and the nominal spatial resolution was $2.24 \mu\text{m}$ with a 5X lens.

4.3.2 SQUID: dc measurements

The Magnetic Measurement Property System model 5S (MPMS-5S), manufactured by Quantum Design [148], is a powerful tool to investigate the magnetism in matter over a long range of temperatures and magnetic fields. The MPMS-5S is an extraction magnetometer equipped with a very sensitive detector of magnetic flux based on a Superconducting QUantum Interference Device (SQUID) and operates over the temperature range of 1.8 K to 400 K with dc magnetic fields up to ± 50 kOe.

The MPMS-5S system comprises a LHe Dewar vessel for 56 liters, a console with the controlling modules and a computer to control the system and serve as the interface with the user. The temperature control inside the vessel permits one to obtain a thermal accuracy of 0.01 K in the experimental region at low temperatures. Indeed, the temperature control is divided in two regimes: below and above 4.4 K. For $T > 4.4$ K, the heat flow is controlled by combining helium gas flow and heaters. At lower temperatures, a sophisticated set of impedances constrains the gas flow from the liquid helium bath, enabling the temperature control by regulating the pressure over the gas flow using a mechanical vacuum pump in the CLTC (Continuous Low Temperature Control) mode. The magnetic field is provided by a superconducting solenoid made of multifilamentary NbTi alloy embedded in a copper matrix, to avoid flux jumps [86], with field steps as small as 0.1 Oe and field resolution of 0.1 Oe up to 5 kOe, and 1 Oe for larger fields. The electric current is charged into the magnet by a power supply coupled to a small heater, the so-called persistent switch, which drives a region of the magnet to the normal state and allows charging of the magnet. Thus, the magnet can be operated in two modes: the persistent and the driven mode. In the driven mode, the current source and the magnet are connected all the time, what introduces noise from the source, and the heater is always on, causing extra evaporation of helium. On the other hand, in the persistent mode, the connection between the power supply and the magnet is switched on only when the magnetic field is charging. After the requested field is reached, the heater is turned off and the field is maintained by the persistent current in the magnet. Since the field is more stable in this mode, all the measurements in the following were carried out by using it.

The detection system consists of a primary circuit with a superconducting detection coil and a secondary circuit with basically a rf current supply, a resonant LC circuit and a control electronic, as depicted schematically in Fig. 4.8a. The superconducting detection coil consists of superconducting loops in a second-order gradiometer configuration with an optimized geometry to eliminate the signal from the superconducting magnet, with which is concentric. Coupled to it, an rf SQUID sensor is formed by a superconducting loop with one Josephson junction (JJ) [149, 150]. The bias current is provided by an rf source tuned to set the JJ close to its the critical current in the operation region on the current-voltage curve. When the sample moves through the gradiometer, a signal is induced due to the Faraday law and it is transferred to the SQUID ring, which operates as a flux-to-voltage converter. Then the screening current due to these both components increases above the critical value, one flux quantum ϕ_0 penetrates the ring through the junction, and a

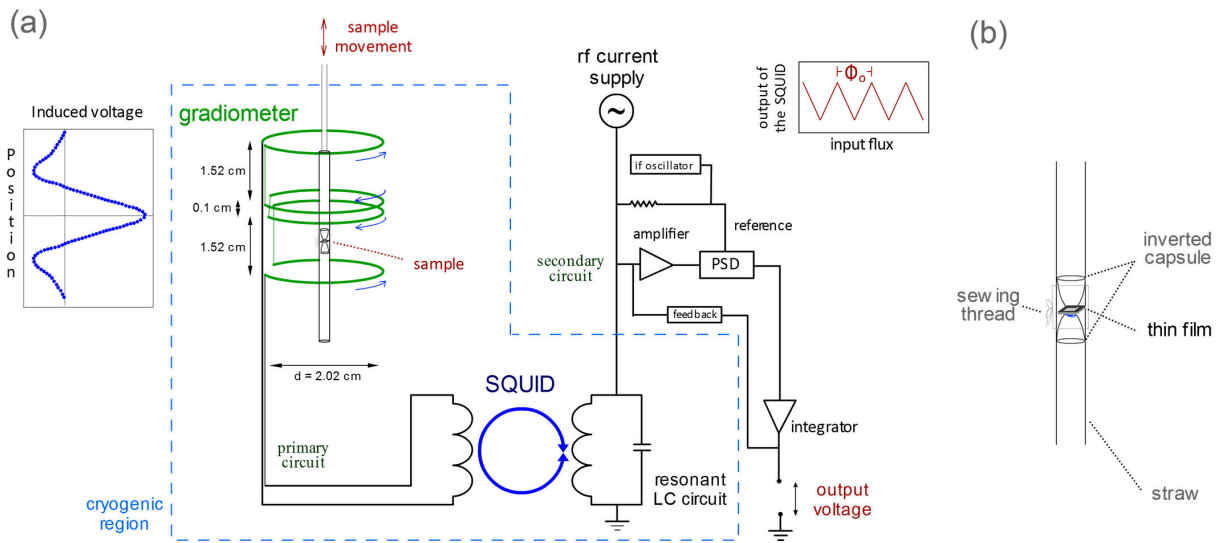


Figure 4.8: Simplified schematic diagram of the detection system in the MPMS-5S. The primary circuit is composed by the superconducting detection coil which consists of a second-order gradiometer and superconducting wires connecting the signal to an rf SQUID sensor. The secondary circuit comprises a resonant LC circuit, an rf power supply, and an electronic system. Top right graph: output voltage from the SQUID sensor as a periodic function of the input flux. Left inset: induced voltage versus position curve after a complete extraction of the sample through the gradiometer. Adapted from [151]. In (b), sample mounting with an inverted organic capsule in a straw fixed by sewing thread.

transition to a new quantum state in the SQUID takes place. After that, the amplitude of the rf signal is reduced and the superconducting state is again reestablished in the junction. The rf amplitude increases again after some cycles by the resonant LC circuit. Thus, the detected voltage is a function with a period ϕ_0 of the input flux, as shown in the top right graph of Fig. 4.8a. Counting the number of periods through the electronics for locked-loop operation (feedback and phase-sensitive detection) it is possible to determine the signal that comes from the sample moving in the gradiometer [151].

The thin films were mounted in a transparent plastic straw with low susceptibility, 19 cm long and diameter of 5.5 mm by using a transparent organic capsule for medicine positioned inverted, as shown in Fig. 4.8b. A small amount of vacuum grease was used in the lower part to maintain the film centered. Under a low field (< 1000 Oe) and at 2 K, this sample set has a diamagnetic signal lower than 10^{-5} emu. Then this assembly is fixed at the end of a long rod attached to a stepper motor on the other side, enabling the rod to scan the sample through the gradiometer. The used scan length was 4 cm divided in 25 positions to acquire points in the region of the magnet where the magnetic field is highly homogeneous in our system [7]. During the scan, the SQUID output voltage is monitored at each position and a voltage-position curve is obtained, as shown in the left inset of Fig. 4.8a. Then, the magnetic moment value is obtained by fitting a point magnetic dipole to this curve. This scan length was chosen to monitor carefully the signal

obtained during the measurement as well as the fitting process of the magnetic dipole.

In order to minimize the remnant field in the experimental region, two procedures were performed before each measurement: the *degauss shield* and the *magnet reset*. In the former one, a magnetic field of 1 T is applied and then reduced to zero by oscillating the field with gradually decreasing amplitude (oscillate mode), in order to demagnetize the shield; in the latter one, a small region of the magnet is heated above T_c and becomes resistive, generating more heat and driving the whole magnet to the normal state. Thus, the persistent current is reduced to zero, releasing the flux trapped in the superconducting windings [152]. After both procedures, the remnant field in our magnet is reduced from some units of Oersted down to 0.5 Oe.

All the dc magnetization (magnetic moment over the sample volume) and dc magnetic moment curves showed in the present work were carried out in this platform which can detect a magnetic moment as small as 10^{-6} emu. This system is also equipped with an AC module, allowing one to apply an oscillating field with a maximum magnitude of 3.8 Oe over a frequency range of 0.001 Hz to 1000 Hz and a resolution of 10^{-9} emu. More details about ac susceptibility is going to be discussed in Section 4.3.3.1.

4.3.3 PPMS: ac measurements

The Quantum Design Physical Property Measurement System (PPMS) model 6000 [153] is an experimental setup based on open architecture, making it rather versatile. This system allows one to connect different modules such as dc/ac magnetometry, electrical transport, heat capacity, as well as homemade instrumentation. The temperature range is 1.9 K to 400 K with thermal stability and accuracy of 0.2% and 5 mK, respectively, for temperatures used in the present study (below 10 K). The maximum magnetic field is ± 90 kOe, the smaller step is 0.1 Oe and the field uniformity is 0.01% over a 5.5 cm region inside the sample space. The temperature control and the magnet control are similar to the MPMS-5S described earlier. This workstation is also formed by a liquid helium Dewar vessel (68 liters) isolated by a nitrogen-jacketed Dewar of 48 liters, a control console, and a personal computer.

In order to measure dc magnetization and ac susceptibility in the PPMS, the ACMS (AC Measurement System) module should be installed. Fig. 4.9a shows the ACMS insert, where a thermometer, electrical connections, and the coil set wound on sapphire (for a good thermal contact) are placed, showed in details in the inset. The coil set comprises an ac drive, a detection and a compensation coil made of copper. The drive

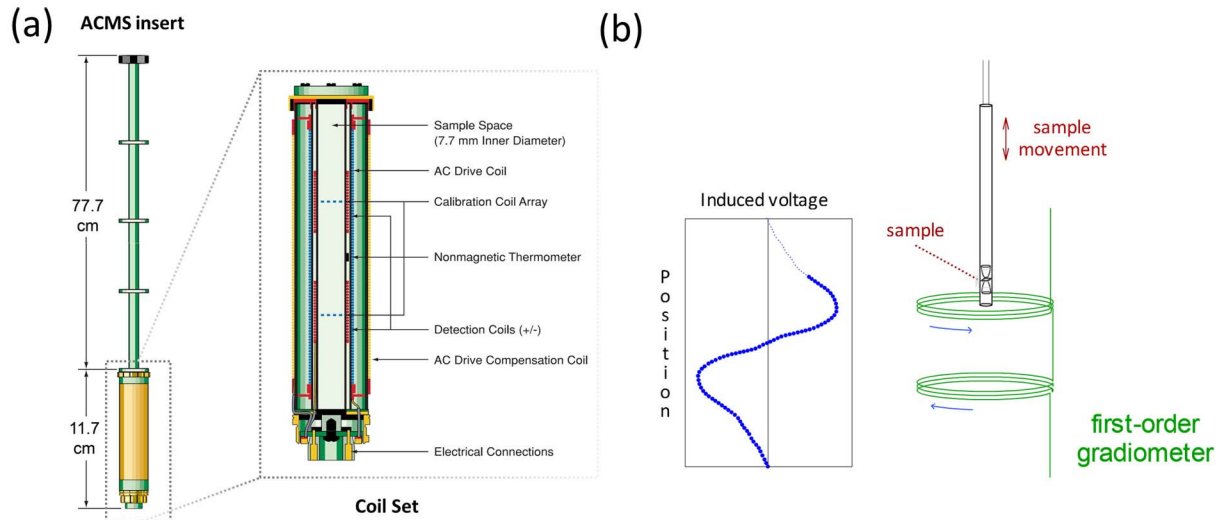


Figure 4.9: (a) ACMS insert which is placed inside the PPMS Dewar vessel concentric to the magnet. The inset shows details of the coil set. Adapted from [154]. (b) A schematic representation of the first-order gradiometer and a position-voltage curve during the sample extraction.

coil generates an oscillating field with an amplitude (h) ranging from 2 mOe up to 15 Oe over a frequency range of 10 Hz to 10 kHz superimposed to the applied field generated by the superconducting dc magnet, both applied perpendicularly to the thin film plane in our experiments. The detection coil is wound around the drive coil and is composed by two sets of counter-wound coils arranged in a first order gradiometer configuration, as illustrated in Fig. 4.9b, to eliminate spurious signals. In order to reduce noise from the interaction of the ac field with conductive materials of the system, a compensation coil is placed around the detection coil to cancel the excitation field outside the sample chamber.

For dc measurements, the servo motor coupled to the sample holder extracts the sample through the detection coil at speeds of about 100 cm/s. It induces a signal in the gradiometer and an output voltage versus position curve (inset in Fig. 4.9b) can be measured in order to obtain the magnetic moment. The PPMS allows one to determine a magnetic moment ranging from 5 emu to 10^{-5} emu. On the contrary to the dc magnetization, which measures the magnetic moment of the sample, the ac susceptibility measurement determines the variation in the magnetic moment due to the ac drive field. Thus, two signals are detected: an in-phase (m') and an out-of-phase (m'') with the ac applied field. Nevertheless, the real and the imaginary ac susceptibility components are obtained normalizing m' and m'' by the ac field amplitude (h), respectively. In order to measure those components, the PPMS is equipped with a powerful Digital Signal Processor (DSP) which acts as a Lock-in Amplifier and identifies a phase shift by comparing the response of the sample with the drive signal. Besides,

the DSP eliminates any instrumental phase shift and reports the first ten harmonics of each component of the ac susceptibility.

In this system the thin films were mounted as in the MPMS-5S and illustrated in Fig. 4.8b. However, the straw size should be near 14 cm long and the position of the sample inside should be 13.6 ± 0.4 cm as well. After inserting the sample/sample holder set into the ACMS module, the sample should be located by a centering method, in our case the AC one, where the servo motor adjusts the sample position to the center of the detection coil. Once it is localized, the measurement set can be started. To obtain the ac susceptibility response, the PPMS utilizes a five point measurement procedure. Firstly, the sample is positioned in the center of the bottom coil of the gradiometer then an ac wave train is applied over the sample and the amplified and filtered response is stored. After that, two more measurements are carried out one in the top coil and the other in the bottom coil. The ac susceptibility components χ' (in-phase) and χ'' (out-of-phase) are obtained from these three measurements. To reduce the instrumental (coil set) signal and to improve the system sensitivity (10^{-8} emu at 10 kHz), two more measurements are executed to calibrate the system. In these measurements, the sample is positioned at the center of the gradiometer and two counter-wound single loops, which operate as calibration coils located in the center of each detection coil of the gradiometer, are connected to the detection circuit one at a time. Then the signal of these two measurements is subtracted to eliminate the sample contribution, resulting in a calibration vector in the complex plane. This vector is taken off the first three measurements. In the end, the final sample response is provided as in-phase and out-of-phase components of the ac susceptibility.

4.3.3.1 Ac susceptibility details and Cole-Cole curves

The ac susceptibility is a robust technique which has been widely used for characterizing properties of type II superconductors, such as their critical temperature and critical current density [155]. In response to an oscillating field, shielding currents are induced to exclude it from the interior of the sample. So the global magnetization can be written as:

$$\mathbf{M}(t) = \frac{1}{2V} \int_V \mathbf{r} \times \mathbf{J}(\mathbf{r}, t) d^3r = \chi_t \mathbf{H}(t) \quad (4.2)$$

where $\mathbf{J}(\mathbf{r}, t)$ is the time-dependent current density inside the sample of volume V and χ_t is the magnetic susceptibility [156, 157].

As pointed out earlier, this technique consists of applying an ac excitation field $\mathbf{h}_{ac}(t)$ which oscillates between h and $-h$ with a period T (or frequency $f = 1/T$) described as

$\mathbf{h}_{ac}(t) = \mathbf{h} \cos(\omega t)$ with $\omega = 2\pi/T = 2\pi f$, on top of a dc magnetic field (\mathbf{H}_{dc}). Considering both fields parallel and in the z -direction, the total field is then

$$H(t) = H_{dc} + h_{ac}(t) = H_{dc} + h \cos(\omega t) \quad (4.3)$$

Thus, the magnetization $M(t)$ in this direction is a waveform deformed response with a shift in the phase (θ) compared to the ac applied field, which means that an out-of-phase component (χ'') proportional to $\sin(\omega t)$ is also present:

$$M(t) = \chi_{dc} H_{dc} + \tilde{\chi} h \cos(\omega t - \theta) = \chi_{dc} H_{dc} + h[\tilde{\chi} \cos(\theta) \cos(\omega t) + \tilde{\chi} \sin(\theta) \sin(\omega t)] \quad (4.4)$$

where χ_{dc} is the dc susceptibility, $\chi' = \tilde{\chi} \cos(\theta)$ and $\chi'' = \tilde{\chi} \sin(\theta)$. As the magnetization also varies periodically, it can be written as a Fourier series expansion covering the entire harmonic spectrum [157], one finds:

$$M(t) = \chi_{dc} H_{dc} + h \sum_{n=1}^{\infty} [\chi'_n \cos(n\omega t) + \chi''_n \sin(n\omega t)] \quad (4.5)$$

with the ac susceptibility components χ'_n and χ''_n expressed by:

$$\chi'_n = \frac{\omega}{\pi h} \int_0^{2\pi} M(t) \cos(n\omega t) dt \quad (4.6)$$

and

$$\chi''_n = \frac{\omega}{\pi h} \int_0^{2\pi} M(t) \sin(n\omega t) dt \quad (4.7)$$

respectively. In our experiments, only the response of the fundamental frequency ($n=1$) was analyzed, that is, $\chi' = \chi'_1$ and $\chi'' = \chi''_1$ which represents the real and imaginary parts of the ac complex susceptibility, $\chi = \chi' + i\chi''$, respectively.

Physically, the ac field describes a minor magnetic hysteresis loop superimposed to a larger one due to the dc applied field. The real component χ' (in-phase) is associated with the inductive response, i.e., the diamagnetic shielding of the superconductor to screen out the ac excitation field ($\chi' < 0$). On the other hand, the imaginary component χ'' (out-of-phase) is related to the resistive response of the superconductor [70, 155, 156, 157, 158]. This resistive signal leads to the energy losses occurring mainly due to flux flow loss and hysteretic loss mechanisms, the first of which is associated with viscous flux movement in the absence of pinning and the latter with the bulk and surface pinning centers that prevent the vortex motion [159]. Then the energy dissipation per unit volume per cycle can be calculated as the area A enclosed by the $M(h)$ loop:

$$W_d = \mu_0 \oint h dM = \mu_0 \oint M dh = \mu_0 A \quad (4.8)$$

Nevertheless, this energy per unit volume of the sample is provided by power supply of ac coil, and can be found by considering Eq. (4.5), as being:

$$W_d = \mu_0 \int_0^T h_{ac}(t) \frac{dM(t)}{dt} dt = \mu_0 \chi'' \pi h^2 \quad (4.9)$$

Substituting Eq. (4.8) into Eq. (4.9), the imaginary ac susceptibility component is:

$$\chi'' = \frac{A}{\pi h^2} \quad (4.10)$$

where A is the area of the magnetization hysteresis loop. Geometrically, the component χ'' is the loop area divided by the circle area whose radius is the ac excitation amplitude and, consequently, χ'' is always positive.

Fig 4.10 shows an example of an ac susceptibility curve measured as a function of the ac excitation field h [$\chi(h)$] with its two components. The measurement was performed in a niobium thin film with thickness 50 nm at temperature of 2 K and frequency of 100 Hz in the remnant dc field of the superconducting magnet (H_{rem}). The real part (blue) is negative at low ac fields and shows a plateau while the sample is in the Meissner state, so-called χ_0 . Its absolute value is used to normalize both components to obtain a dimensionless susceptibility. At higher ac field amplitudes, the field starts to penetrate in the sample and χ' increases, however, the superconductivity is not lost up to $h = 15$ Oe. The imaginary component (red) shows no dissipation in the Meissner state and increases as long as the field starts to enter the specimen, reaching a maximum value. The field with the maximum dissipation is called h_p and, depending on the geometry of

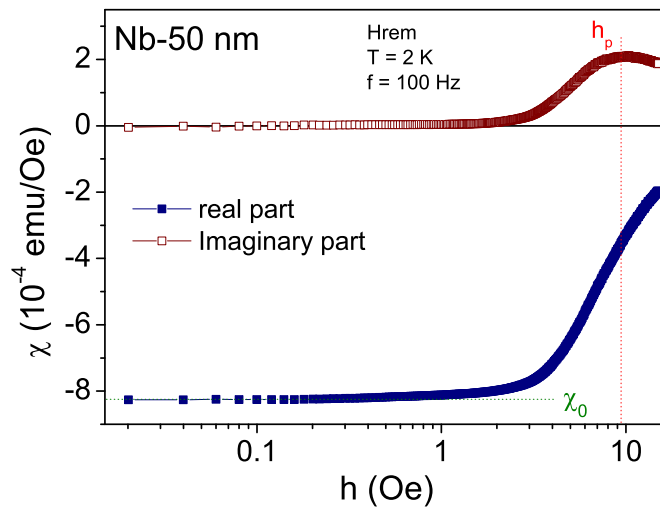


Figure 4.10: Ac susceptibility plotted against ac excitation field at 2 K with null dc field for a Nb thin film. Both components of the ac susceptibility are identified as well as the magnitude of the smallest value of the real part χ_0 and the peak position of χ'' component (h_p).

the sample, allows one to estimate the critical current density using expressions derived in the framework of the Bean model. We will return to this issue in the Chapters 5 and 6.

Another important information that ac susceptibility measurements can provide is the identification of the field dependence of the critical current density of the specimen and its dynamical regime as well [160, 161, 162, 163]. In general, the ac susceptibility is measured as a function of the ac field or temperature, however, parametrizing the normalized components as a $[\chi''(\chi')]$ curve, i.e, plotting the ac susceptibility in the complex plane, certain features of the system under study can be recognized at once. This kind of plot is called a Cole-Cole plot and originated in studies of complex dielectric constant [164].

Cole-Cole curves for a theoretical superconducting thin disk in different regimes are illustrated in Fig. 4.11a. The maximum value of χ''/χ_0 is located at $(-0.38, 0.24)$ for the Bean model [70]. If the critical current density shows any dependence on the magnetic field, the maximum shifts to smaller values of $-\chi'/\chi_0$ and higher values of χ''/χ_0 . In the region of low temperatures or low ac fields, a critical state model with $J_c(H)$ is similar to the Bean model, whereas for high temperatures or high ac fields it decays more abruptly. Nonetheless, if a flux creep regime takes place, the peak position changes to higher values of $-\chi'/\chi_0$ and also increases in magnitude compared to the Bean model. On the contrary, for low temperatures or low ac fields this curves are steeper and in the other extreme, they are similar to the Bean model. Therefore, the curves are characteristic for each

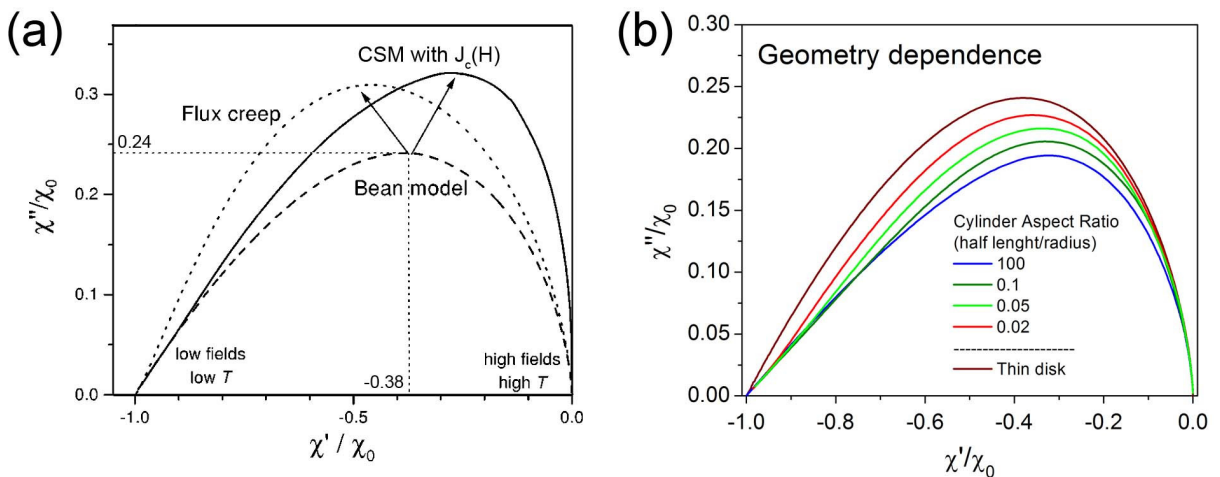


Figure 4.11: (a) Cole-cole plot showing different regimes. The dashed line represents the Bean model for a thin disk with the maximum at $\chi'/\chi_0 = -0.38$ and $\chi''/\chi_0 = 0.24$. Flux creep shifts the maximum in the Cole-cole curve to the left, whereas field dependence of J_c shifts the maximum to the right and both to higher values of χ'' . Figure modified from [160]. (b) Theoretical Cole-Cole plots for a thin disk (red line) [70] and cylinders with aspect ratio half length/radius 0.02, 0.05, 0.1 and 100 [165] obeying the Bean model.

regime for a specific geometry [160]. Chen and co-workers [166] have shown that a square or stripe thin film can be scaled by using the Cole-Cole plot for a thin disk with error below 1%. Panel (b) of Fig. 4.11 depicts the influence of the geometry on the normalized $\chi''(\chi')$ curve, showing this for a thin disk and cylinders with several aspect ratios (half-length/diameter) [165] in the Bean model where the curves tend towards that of a thin disk as the aspect ratio decreases.

Finally, these plots are a very useful tool to analyze ac susceptibility data, since they allow one to compare specimens under different conditions of temperature and magnetic field with theoretical curves in different regimes. In this thesis, the Cole-Cole plots have been used as a figure of merit to validate the use of the critical state expressions on our studies of plain and patterned thin films.

5

*Visualizing ac susceptibility and ac field effects on flux avalanches**

We have established a link between the global ac response and the local flux distribution of superconducting films by combining magnetic ac susceptibility, dc magnetization and magneto-optical measurements. The investigated samples are three Nb films: a plain specimen, used as a reference sample, and other two films patterned with square arrays of antidots (ADs). At low temperatures and small ac amplitudes of the excitation field, the Meissner screening prevents penetration of flux into the sample. Above a certain ac drive threshold, flux avalanches are triggered during the first cycle of the ac excitation. The subsequent periodic removal, inversion and rise of flux occurs essentially through the already created dendrites, giving rise to an ac susceptibility signal weakly dependent on the applied field. The intra-dendrite flux oscillation is followed, at higher values of the excitation field, by a more drastic process consisting of creation of new dendrites and antidendrites. In this more invasive regime, the ac susceptibility shows a clear field dependence. At higher temperatures a smooth penetration occurs, and the flux profile is characteristic of a critical state. We have also shown that the regime dominated by flux avalanches can be reliably identified by ac susceptibility measurements.

5.1 Introduction

Superconductivity is a state of matter characterized by a diamagnetic response caused by the exclusion of magnetic flux from its interior. In type II superconductors, the resulting field dependent magnetic moment can be linked to the internal distribution of the quantum units of flux, so-called vortices. Indeed, a picture of the flux distribution at microscopic scales can be indirectly achieved from integrated response techniques, via the assumption of certain predetermined models. Arguably, the most successful and popular mapping between the microscopic and macroscopic superconducting worlds is the Bean critical state model [63, 64]. This model allows one to estimate, from magnetization and susceptibility measurements, the maximum current a superconductor can bear before dissipating, i.e., its critical current. The basic

*This chapter is based on M. Motta, F. Colauto, R. Zadorosny, T. H. Johansen, R. Dinner, M. G. Blamire, G. Ataklti, V. V. Moshchalkov, A. V. Silhanek, and W. A. Ortiz, Visualizing the ac magnetic susceptibility of superconducting films via magneto-optical imaging, Phys. Rev. B 84, 214529 (2011).

assumptions validating the Bean model are the existence of a continuous flux distribution throughout the specimen and a field-independent critical current. Clearly, such restrictive conditions do not account for all possible scenarios of flux distribution. Attempts for adjusting to more realistic situations included the decrement of critical current with magnetic field [60], the presence of edge barriers [167, 168], and the existence of a finite lower critical field [169, 170]. In most cases, these improvements result in marginal corrections to the simpler Bean approximation.

A situation in which the Bean critical state model fails dramatically occurs when sudden flux bursts develop as a consequence of a thermomagnetic instability [88]. Under these circumstances, any estimation of the critical current based on global response techniques is futile and local magnetic probes become imperative. An unambiguous identification of the field range dominated by avalanches can be obtained through the field dependence of the magnetization, which exhibits clear jumps within the instability region [114, 171, 172]. However, signatures of the avalanche regime in the ac susceptibility are not easy to recognize, most specially for values of the ac drive, h , sufficiently small to avoid disturbance on the flux distribution which one intends to probe. For larger values of h , however, both components of the ac susceptibility, $\chi = \chi' + i\chi''$, are reentrant in temperature and in applied field; i.e., shielding becomes stronger and dissipation decreases upon increase of either of those two variables. This reentrant behavior has also been observed in Pb films and ascribed to the occurrence of flux avalanches [109, 110]. The present work reveals the cause for such change of the diamagnetic response through investigations of the early stages of flux penetration in Nb films. In our approach we performed magnetic measurements employing global techniques – namely, susceptibility and magnetization – as well as magneto-optical imaging (MOI). Our experiments revealed that the first avalanches, while serving as a track for flux entrance, do also guide flux exit, thus suggesting why the initial ac response of the superconducting film is nearly constant for variations of the dc applied field (H) or temperature (T). Upon increase on H or T , the ac response reenters, i.e., becomes more diamagnetic as the avalanches cease.

5.2 Samples and experimental techniques

The samples investigated consist of Nb films of approximately rectangular shape, with thickness $d = 50$ nm. Their lateral dimensions appear on Table 5.1. Two of them have a square array of antidots (ADs) fabricated by electron beam lithography. The Nb

Table 5.1: Superconducting critical temperature, T_c ; coherence length, $\xi(0)$; penetration depth, $\lambda(0)$; lateral dimensions, l , w ; for the three samples investigated.

Sample	T_c (K)	$\xi(0)$ (nm)	$\lambda(0)$ (nm)	l (mm)	w (mm)
Plain	7.91	9.4	168.0	3.0	2.5
AD04	7.40	9.1	170.0	2.7	2.6
AD08	6.42	9.1	173.0	2.7	2.5

was deposited via dc sputtering on top of a SiO_2 insulating substrate. Our preliminary investigations included a variety of similar samples, all of them leading to comparable results. The present report, however, is restricted to results on only three samples, one of each type. Thus, the sample investigated through magnetic measurements is the very same which was imaged using the MOI technique. The patterned samples – named AD04 and AD08 – have antidots with sides $0.4 \mu\text{m}$ and $0.8 \mu\text{m}$, respectively. The third specimen – the reference sample – is a plain film of Nb. The period of the patterns is $\alpha = 1.5 \mu\text{m}$, which corresponds to a commensurability field* $H_1 = \frac{\Phi_0}{\alpha^2} = 9.2 \text{ Oe}$ at which the densities of vortices and antidots match each other. Using the expression for the upper critical field (Eq. (2.28)) and for the dirty limit (Eqs. (2.19) and (2.20)), the zero temperature superconducting coherence length, $\xi(0)$, and the penetration depth, $\lambda(0)$, were estimated. The obtained values are shown in Table 5.1, as well as the superconducting transition temperature at zero field, T_c . Noticeably, a drop in T_c results from the insertion of antidots.

Measurements were made for temperatures ranging from 2 K up to T_c , and the ac sinusoidal drive was simulated, in MOI experiments, by cycling the dc field in complete loops made up of 0.1 Oe steps. Ac susceptibility and dc magnetization measurements were carried out in commercial Quantum Design equipments (MPMS and PPMS). The susceptibility measurements were recorded using a fixed frequency of 1 kHz, for values of the ac field amplitude ranging from 0.02 Oe to 15 Oe. Prior to fixing the value of the excitation frequency, we have verified that the ac susceptibility response is independent of frequency within 5 orders of magnitude, up to values above 1 kHz, as can be seen for the three thin films in Fig. 5.1. After each measurement, the previous magnetic history was erased by increasing T to values above T_c . In all cases, the excitation field h and the external magnetic field H were applied perpendicular to the film plane. The magneto-optical imaging technique employed relies on the occurrence of the Faraday effect [173]

*Matching effects are less pronounced at the temperature interval reported here (i.e., not very close to T_c). The commensurability field, characteristic of the lattice of ADs, is a reference for the window of magnetic fields at which the events treated here take place.

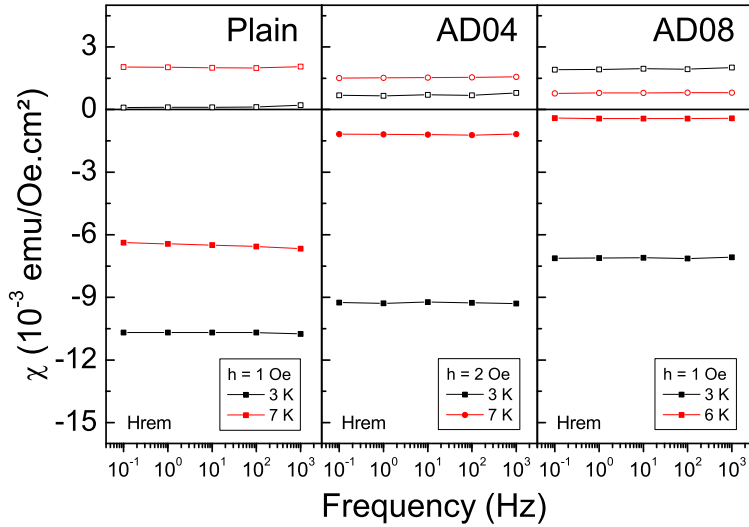


Figure 5.1: Susceptibility versus frequency ranging from 10^{-1} Hz to 10^3 Hz for the Plain, AD04 and AD08 samples at different temperatures and applied ac field amplitudes. After each point, the magnetic history was erased by increasing the temperature above T_c .

on an indicator film placed on top of the superconducting specimen. The indicators used in the present work are Bi-substituted yttrium iron garnet films (Bi:YIG) with in-plane magnetization. Data for the so-called Cole-Cole plots of the susceptibility, i.e., its imaginary part, χ'' , as a function of the real part, χ' , were taken isothermally, varying the amplitude of the ac drive. Data normalization of the ac susceptibility was performed using the reference value χ_0 of its real component, which represents the Meissner plateau, as presented in Fig. 4.10, measured in the PPMS at $T = 2$ K with an ac amplitude $h = 20$ mOe, in the remnant magnetic field.

5.3 Results and discussion

It is well-known that thin films of most superconducting materials exhibit flux avalanches within specific intervals of temperature and applied field [89, 91, 93, 94, 95, 96, 102, 114, 171, 172, 174]. Such behavior is intimately correlated to thermomagnetic instabilities experienced by the material when heat generated by a sudden displacement of vortices cannot be dissipated, creating thus an increase in the local temperature. This warmer region, in turn, has its pinning capability reduced, being thus likely to host even more vortex motion, reinforcing the process [115, 116]. There is a threshold temperature, T_{th} , above which no avalanches occur, and a rather smooth penetration of the magnetic flux is observed. It has been shown that T_{th} can be substantially increased if antidots are introduced into the specimen [109, 110, 112, 175, 171]. In this case, the most relevant difference, compared

to plain films, is that flux is guided preferentially along the rows of ADs [112, 110]. This aspect will be further discussed later. Above T_{th} , flux invades the sample gradually, and the system appears to obey a critical state regime. Assuming the simplest of such critical state regimes, i.e., the Bean model, one can obtain the superconducting critical current density, J_c , by measuring the field h at which the magnetic flux front reaches a characteristic geometry-dependent penetration distance [63, 64]. If one considers a thin disk of thickness d and diameter $2R \gg d$, the two-dimensional effective penetration depth in the perpendicular geometry is $\Lambda = \frac{2\lambda^2}{d}$. For $\Lambda \ll 2R$, J_c can be related to the field amplitude at which χ'' peaks, h_p , corresponds to 72% of the full penetration field and can be related to the critical current density by the expression $J_c = \frac{1.03h_p}{d}$ [70]. On the other hand, an approximate expression for J_c has been recently developed by Chen and co-authors [166] for films of rectangular shape. We have employed Eq. (20) of the Ref. [166] to calculate J_c of our rectangular samples:

$$J_c = \frac{4.85\Upsilon_0(\gamma)}{(3 - \gamma^{-1})w} h_p \quad (5.1)$$

where $\gamma = l/w$ ($l \geq w$), $\tau = d/w$, and

$$\Upsilon_0(\gamma) = \frac{\arctan(1 - 0.7223\gamma^{-0.954} + 0.3522\gamma^{-2.57} - 0.141\gamma^{-3.66})}{\tau} \quad (5.2)$$

Fig. 5.2 compiles results obtained from isothermal ac susceptibility measurements on the three films, taken with the PPMS in remnant field, using the excitation amplitude $h \leq 15$ Oe as the external variable. Panel (a) shows $J_c(\frac{T}{T_c})$ obtained as discussed in the previous paragraph, with h_p determined from the peak in $\chi''(h)$ curves. We have used the reduced variable $t = \frac{T}{T_c}$ to unify the superconducting domain of all studied samples. Curves for the plain film and sample AD04 have two distinct regions: at higher temperatures, $J_c(t)$ is smooth, with upward curvature; below a certain limiting temperature, however, it deviates from this canonical behavior, a change that is intimately connected to the appearance of avalanches in both specimens, as explained later in this chapter. The equivalent curve for sample AD08 is quite different: a downward curvature is maintained throughout the whole interval, as a consequence of avalanches being present within the entire temperature domain. As a matter of fact, values of J_c shown for temperatures below the avalanche threshold should not be interpreted as representative of the critical current density, since they were obtained under the erroneous assumption that the system is in a critical state regime. In the avalanche regime, the actual critical current is a local, extremely inhomogeneous

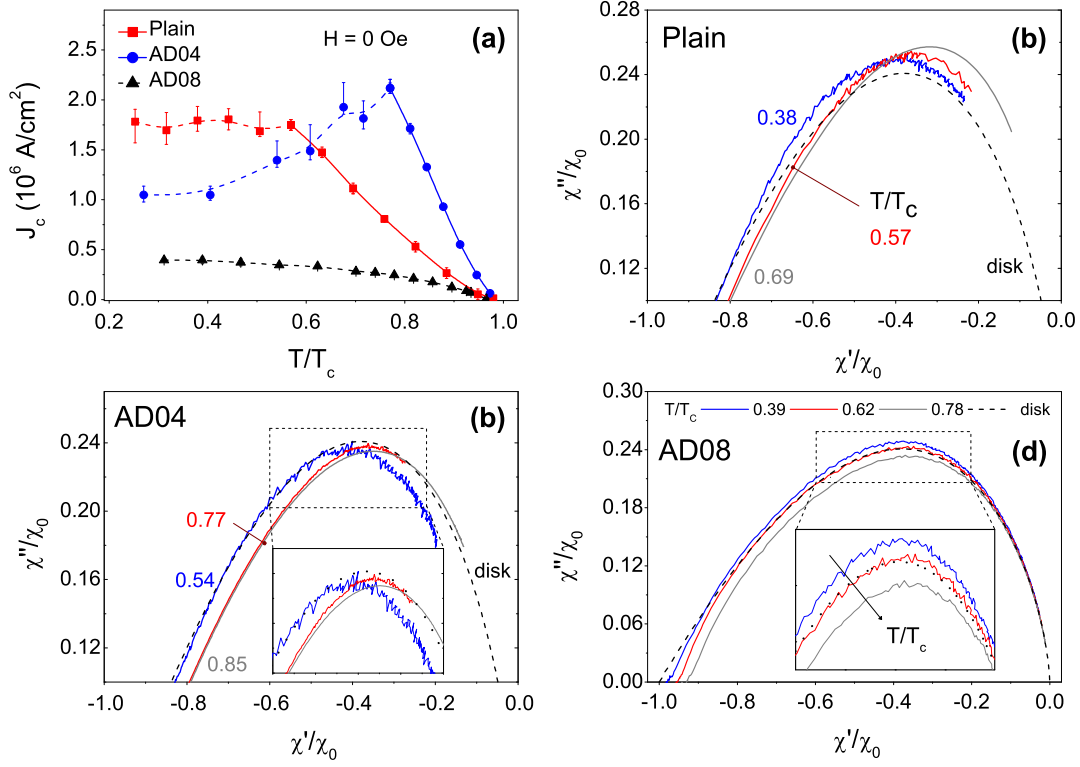


Figure 5.2: (a) Temperature dependence of the critical current in the absence of a dc field (see main text), as determined from the peak on the imaginary part of the susceptibility measured as a function of the excitation amplitude. Cole-Cole plots, at different temperatures, for the studied samples: plain (b), AD04 (c) and AD08 (d). The theoretical plot for a thin circular disk is also shown. Smoothness/noisiness of the Cole-Cole plots emphasize different regimes (critical state/avalanches) of flux penetration.

variable, which cannot be properly described by a unique global value. Nonetheless, displaying all points in a single picture stresses the idea that a frontier between both regimes can be reliably obtained from ac susceptibility measurements. It should be noticed that the curves in Fig. 5.2a confirm that the inclusion of ADs of moderate size promotes an increase in J_c [176] and T_{th} [110, 171]. Comparing the high- T portions of $J_c(t)$ for the plain film and sample AD04, one clearly sees this improvement, as well as the relative enlargement of the area where avalanches occur. For sample AD08, however, this comparison does not apply, since avalanches take place in the whole temperature window.

A second important signature of the occurrence of avalanches that can be drawn from ac susceptibility measurements is depicted in panels (b) through (d) of Fig. 5.2, which show Cole-Cole plots of the susceptibility. Displaying data in such a manner can be quite advantageous to emphasize the occurrence of different regimes of vortex matter. For example, all Cole-Cole plots for a system obeying a critical state dynamics should collapse into one single universal plot, irrespective of the values of applied field, temperature, frequency and amplitude of the ac drive. Panel (b) shows results around the peak for the

plain film, taken at three different values of T : for temperatures below the threshold limit for avalanches ($t = 0.38$ and 0.57), $\chi''(\chi')$ is very noisy, contrasting with the behavior observed at higher temperatures ($t = 0.69$), for which the curves are noticeably smooth. A similar set of curves is shown on panel (c) for sample AD04, which exhibits avalanches for $t = 0.54$ and $t = 0.77$, but not for $t = 0.85$. Complete Cole-Cole plots for sample AD08 are shown on panel (d) for $t = 0.39$, $t = 0.62$ and $t = 0.78$. The inset features the central portion of the curves, emphasizing the noisy behavior which, for this sample, is present over the entire range of temperatures. It should be noticed that, at the left lower part of Fig. 5.2d, χ'' goes to zero while χ' is not -1 for larger values of T . The reason for this behavior is that the initial screening on curves $\chi'(h)$ remains flat but imperfect (see main panel of Fig. 5.5a), while there is essentially no dissipation [$\chi''(h) \sim 0$]. This means that some flux enters but remains pinned by the ADs. Since this behavior is also exhibited by sample AD08 and the plain film, one is led to associate it with the intrinsic pinning of Nb. We will return to this point further ahead.

It is also worth comparing the experimental results with those expected theoretically. Chen *et al.* [166] have shown that the ac susceptibility of rectangular films can be adequately treated using the same expression derived by Clem and Sanchez for a thin circular disk [70]. This result, also included in all Cole-Cole plots of Fig. 5.2, indicates that, at all temperatures, the plain-film response [panel (b)] is different from that obtained for the Bean approximation, a result that is possibly due to the fact that J_c is not field-independent, as assumed in that simple model. As a matter of fact, the Bean model predicts a peak at $\chi'_{max} = -0.38$, whereas the assumption of a field dependence on J_c shifts the peak to right and up (illustrated in Fig. 4.11a) [160], just as observed for the plain film. On the other hand, the Cole-Cole plots for the patterned samples deviate from the one predicted by Bean's model in a nonsystematic manner, so that the difference cannot be ascribed to a specific mechanism - e.g., the introduction of creep or of a field-dependent J_c [160, 177, 178].

We turn now the discussion to the MOI results of flux penetration and exit at relatively small fields. Such images were taken after cyclic field excursions, as in the case of those performed during susceptibility measurements. To emulate the magnetic history imprinted by the ac excitation, the external field was ramped up and down in steps of 0.1 Oe. However, given the time needed to acquire images, on the order of 100 ms, the cycles were not sinusoidal, but step-like, as roughly indicated at the bottom of Fig. 5.3. The similarity among this procedure and that taking place during a sinusoidal cycle in a susceptibility measurement is ensured by the frequency independence of the ac

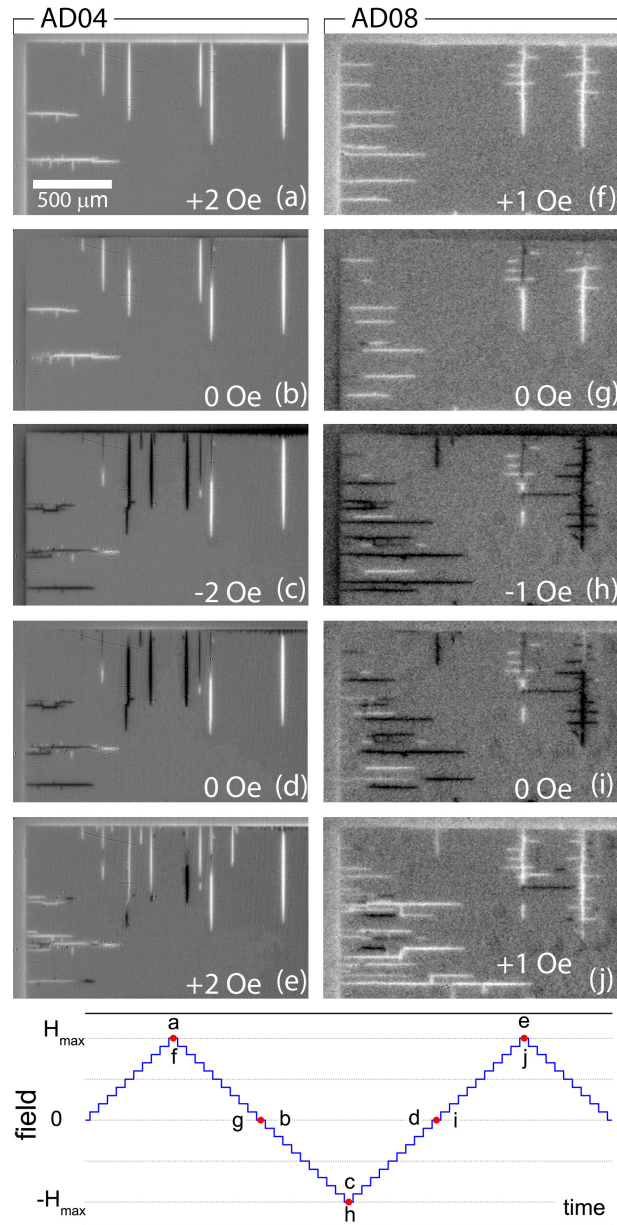


Figure 5.3: MO images taken at 3 K. White indicates positive flux, dark negative, medium gray stands for zero flux (screened). Panels (a) to (e) are for sample AD04: after zero field cooling, field increased to 2 Oe (a), decreased to zero (b) and -2 Oe (c), increased back to zero (d) and 2 Oe (e). Same protocol followed for sample AD08, panels (f) to (j), with field extremes of ± 1 Oe. Bottom panel: sketch of time evolution of the applied field during data collection. The total time to complete an ac emulated cycle with amplitudes of 2 Oe and 1 Oe was 8.4 s and 4.2 s, respectively.

measurements. Fig. 5.3 and 5.4 present some selected MO images for the three samples studied here. All pictures were taken for $T = 3$ K. White regions correspond to positive penetrated flux, dark areas represent negative flux (antiflux), while medium gray stands for unpenetrated portions of the sample (zero flux). Panels (a) to (e) in Fig. 5.3 are for sample AD04: after a zero field cooling procedure, the field was increased to 2 Oe (a), decreased back to zero (b) and to -2 Oe (c), and then increased again to zero (d) and

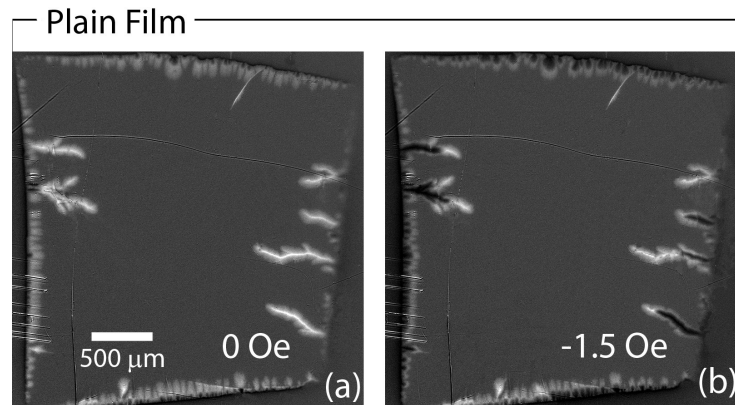


Figure 5.4: MO images of the plain film, taken at 3 K, following the same protocol depicted in Fig. 5.3: after zero field cooling, field was cycled between ± 4 Oe. Panel (a) was taken at 0 Oe after the first half cycle of the field; panel (b) is for -1.5 Oe. The time to complete this ac emulated cycle was 16.8 s.

finally to 2 Oe (e). All steps were performed with a ramp rate of 20 Oe/s. We find that near 1.4 Oe, abrupt avalanches suddenly invade the sample from the edge, in the form of fingertype dendrites, clearly guided by the rows of ADs[†] (a). Upon decrease of the field, reversed flux penetrates the sample through the same tracks [(b) and (c)], transforming them progressively into antidendrites. When the field is increased again [(d) and (e)], the tracks are penetrated once more by positive flux, so that the original dendrites are gradually restored. The same behavior is seen in panels (f) to (j) for sample AD08, for which the field protocol is just the same as for AD04, with field extremes of ± 1 Oe. This feature is also presented by the plain sample, as exemplified in panels (a) and (b) of Fig. 5.4, taken respectively at fields zero and -1.5 Oe, after a field excursion to 4 Oe.

It is worth mentioning that all samples studied here exhibit dendritic penetration at certain values of dc field and temperature. However, for experiments repeated under the same conditions, flux dendrites follow different tracks during each run. This further emphasizes that the onset of flux avalanches is governed by an instability condition. The lattice of antidots is nevertheless causing some degree of guidance for the full avalanche, in contrast to the dendritic penetration in unpatterned samples.

We have also used magnetic measurements and MO imaging to investigate the reentrant behavior of ac susceptibility curves. The inset of Fig. 5.5a shows the temperature dependence of χ' and χ'' , measured with ac amplitudes of 1.0, 2.5 and 3.8 Oe, for sample AD04. For the lower value of h , one sees the ordinary ac response of a superconductor; at larger amplitudes, however, the reentrant behavior appears, as

[†]The flux avalanche morphology in decorated thin films is extensively discussed in Chapter 8 and also in Appendix A for the AD04 and AD08 samples.

already seen earlier in Pb films [109]: upon increase of the temperature, the real part first decreases, to a more diamagnetic level, and then increases towards zero at the transition. The imaginary part is also odd, starting at a relevant dissipation level and then decreasing before peaking as the transition is approached. One can also follow the evolution of both susceptibility components with the excitation field at fixed temperatures. The main graph of Fig. 5.5a shows isothermal $\chi(h)$ measurements at 3, 5 and 6.5 K. It is rather intriguing that the loss of diamagnetism starts earlier for 3 K than for 5 K, a feature that is also matched by the peaks on χ'' . Further increasing T , however, restores the ordinary behavior, i.e., the transition is broaden and starts at lower amplitudes h . The vertical dashed lines on the main panel are guiding lines to connect both experiments: for $h = 1$ Oe, the real part χ' increases monotonically as the temperature changes from 3 to 5, and then to 6.5 K. The imaginary part is also monotonous: negligible for 3 and 5 K, and nonzero at 6.5 K. On the other hand, for $h = 2.5$ Oe both components have an initial decrease as T is switched from 3 to 5 K, followed by an increase, for T growing from 5 to 6.5 K. This feature is even more pronounced at large h . One can notice that, for small values of h , $\chi'(h) \sim -1$ at low temperatures (e.g. 3 K), but is less negative for larger values of T , whereas the corresponding $\chi''(h) \sim 0$ in all temperatures. As discussed earlier, this is due to efficient pinning: flux enters the sample but is prevented from moving. For this reason, the left-lower parts of the Cole-Cole plots for all samples studied here do not collapse, as seen, for example, in Fig. 5.2d for sample AD08. This reentrant behavior, discussed here for sample AD04, is also presented by the plain film, as illustrate in Fig. 5.5b for the temperature dependence of χ' and χ'' for a variety of values of the excitation amplitude. However, as sample AD08 exhibits avalanches in the whole temperature interval, there is no transition between different regimes, and therefore no reentrance could occur, as is actually the case.

Invoking frequency-independence of the ac susceptibility, one can emulate an ac measurement by cycling the dc field and capturing MO images of the penetration profile of the sample at adequate values of H . Panels (a)-(c) on Fig. 5.6 show magnetization hysteresis loops for sample AD04 at temperatures 3 K, 5 K and 6.5 K, respectively. At 3 K one sees a hysteretic loop whose nonvanishing area is due to the viscous motion of entering and exiting flux within the AD-guided dendrites [panel (d)]. As shown on panel (c), at 6.5 K the loop is wide open, as could be expected for temperatures approaching T_c . The corresponding image is shown on panel (f), with a critical-state-like envelope and a certain “microtexture”. Flux entrance is not abrupt, as in an avalanche,

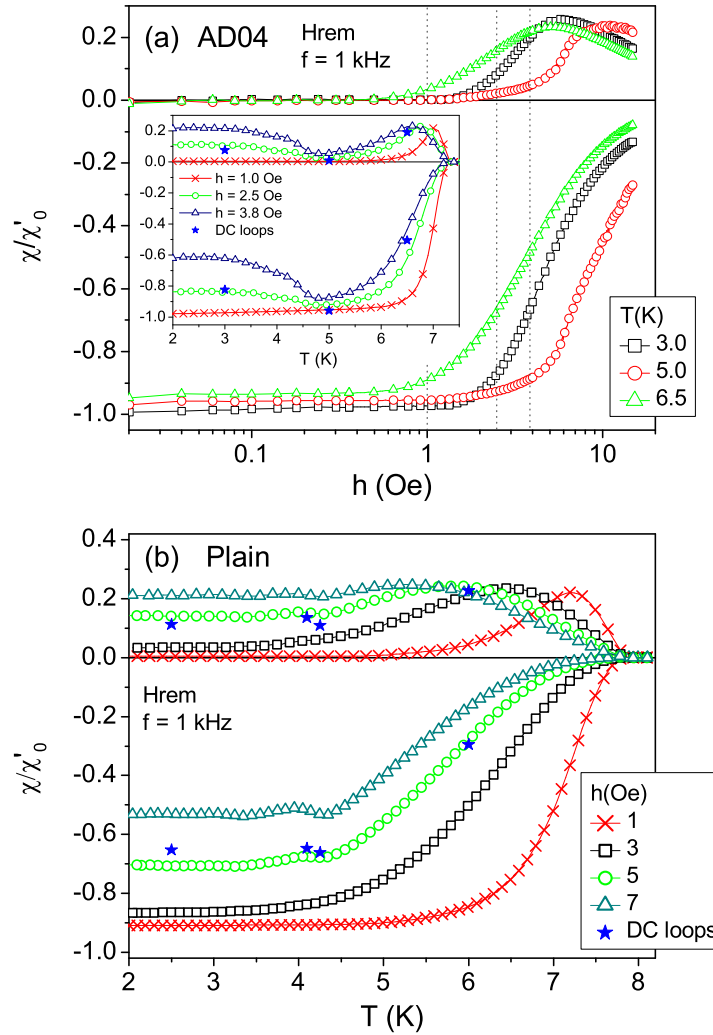


Figure 5.5: (a): Real and imaginary parts of χ as a function of the ac amplitude, taken at $T = 3, 5$ and 6.5 K. The inset shows the temperature dependence of the same quantities, measured with $h = 1, 2.5$ and 3.8 Oe. Stars represent values of both components, at $3, 5$ and 6.5 K, calculated from magnetization loops (see text). (b): Similar to inset in (a) for the plain film.

exhibiting a filamentary though smooth penetration. Mostly interesting, however, is the fact that the magnetic response at 5 K is nonhysteretic[‡], which means that, upon increase of the temperature, the loop first closes down and then opens up again, originating a reentrant behavior of the hysteretic loop. The MO image, represented on panel (e), shows quite clearly that the heart of the sample is not penetrated by magnetic flux at 5 K and 2.5 Oe. We have also compared hysteresis loops and MO images for the plain film, obtaining similar results. The collapse of the loop, however, does not occur for sample AD08 which, as already discussed, always exhibits avalanches. We take this as an additional evidence that the closing down of the loop is a feature intimately

[‡]Notice that the same scale is used for the 3 magnetic loops shown. Further amplification of the 5 K loop would evidence some amount of hysteresis, due to smooth penetration at the edges.

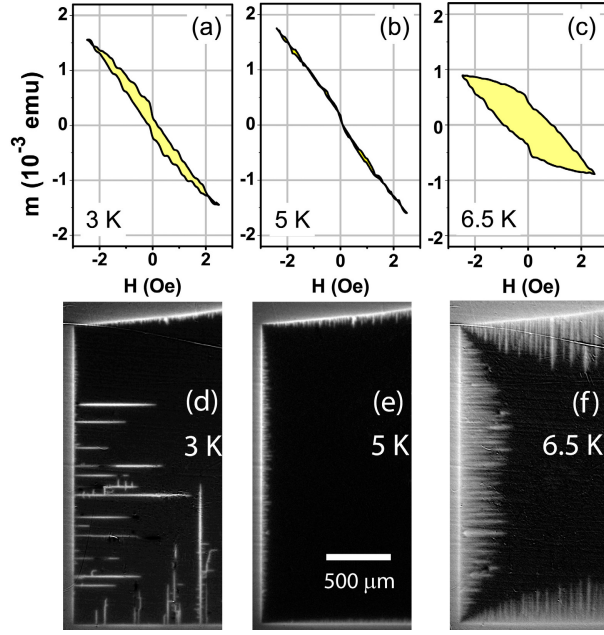


Figure 5.6: Hysteresis loops for sample AD04 at temperatures 3 K (a), 5 K (b) and 6.5 K (c). The area of the loop, which is nonzero at 3 K, closes down at 5 K and reopens at 6.5 K. Panels (d)-(f) are the corresponding images at the maximum field (2.5 Oe), taken immediately after the virgin curve. The total time to complete this ac emulated cycle in the MPMS magnetometer was 2h13min.

related to the suppression of avalanches in samples AD04 and Plain.

One further evidence that ac measurements can be emulated using dc magnetization loops arises from the argument that χ' is the average slope of the magnetization loop (throughout one full cycle), whereas χ'' is related to the energy losses per sample volume per cycle (W_d) by the Eq. (4.10) ($\chi'' = \frac{A}{\pi h^2}$) [70, 179]. Employing this reasoning, we calculated both components of χ using data from the dc loops. As an illustration we have included, on the inset of Fig. 5.5a, blue stars representing such results as obtained from the ± 2.5 Oe loops measured at 3, 5 and 6.5 K. A similar procedure for the Plain film, taken with $H_{max} = 5$ Oe, leads to the set of stars on Fig. 5.5b. One can thus conclude that the reentrant behavior of χ' – i.e., a reinforced diamagnetism – is related to the temperature limit for the occurrence of avalanches [114, 172].

As a final remark, we comment on the filamentary structure of the penetrated flux on sample AD04 at high temperatures. Panel (f) in Fig. 5.6 shows this clearly: while the penetration front has the typical format of a critical state regime, it is in fact an envelope for a filamentary fingertype structure. Noticeably, however, no thermomagnetic avalanches take place at that temperature, and the filamentary inner structure develops smoothly. From time to time, the smooth penetration is perturbed by small amounts of flux entering the film. Minor fluctuations seen on $M(H)$ at 6.5 K (Fig. 5.6c) are the

corresponding signatures of those tiny perturbations. This interesting feature, which is in straight connection with the existence of the array of ADs, can be compared with another occurrence of a filamentary structure, observed by Welling *et al.* in a YBCO film with an array of ADs [180]. Flux penetration in the form of thin filaments was also observed in YBCO films deposited on vicinal cut substrates [111, 181, 182, 183].

5.4 Conclusions

Combining magneto-optical visualization of penetrated flux with magnetic ac susceptibility and dc magnetization measurements, we have investigated the early stages of flux penetration on Nb films with and without arrays of antidots. Our results show that ac susceptibility measurements can be used to detect flux avalanches, either by constructing $J_c(T)$ curves or by monitoring the occurrence of a noisy behavior in Cole-Cole plots. We have also shown that, in the low-field regime, the roots of most dendrites are reused during the process of entrance and exit of flux, although some new dendrites and antidendrites might also be created at different points along the sample edges. From hysteresis loops measured at different temperatures, we were able to calculate both components of the ac susceptibility. MO images taken at several points of those loops enabled us to establish a reliable link among those three experimental techniques and, through this correspondence, visualize the flux distribution throughout the sample after an ac field cycle.

6 *Threshold of critical current densities to trigger flux avalanches in superconducting thin films*

Flux avalanches develop in superconducting thin films as a consequence of thermomagnetic instabilities. These branched patterns are well-described by the thermomagnetic model, which predicts the stability/instability frontier in a magnetic field-critical current density (H - J_c) diagram. By using ac susceptibility measurements, the critical current density of a 50 nm thick Nb thin film was determined as a function of temperature and applied magnetic field. The experimental data confirms the existence of a threshold value of the critical current density below which no avalanches are triggered, regardless of the values of T and H . This finding is in strict agreement with the predictions of the thermomagnetic model for the occurrence of instabilities in a superconducting film.

6.1 Introduction

It is well-known that, in type II superconductors, vortices organize [2] in a non-uniform profile. This characteristic is a consequence of the simultaneous action of the magnetic pressure exerted by the external applied field, the protective role of the screening currents, and the existence of pinning centers, building up a vortex landscape that can be suitably described by critical state models. In the simplest approach, C. P. Bean [63, 64] considered that in the region where the flux is penetrated, the screening current density is field-independent, being everywhere equal to maximum value that a superconductor can carry without dissipation, i.e., its critical current density ($J_c(H) = J_c$). Bean's critical state model has also allowed evaluating efficiently J_c of superconducting thin films [62] by using different techniques, such as magneto-optical imaging (MOI) [133], dc magnetization [160] and ac susceptibility [70, 166].

Nonetheless, a totally different scenario may appear when, for field and temperature values limited to certain sample-characteristic intervals, magnetic flux can suddenly penetrate the specimen as a flux avalanche, destroying the smooth critical state

penetration. These abrupt events are most commonly detected as jumps in the magnetization versus applied magnetic field [93, 184, 114, 172] and dendritic patterns in thin films using the MOI [89, 91, 93]. In ac susceptibility, an increase in shielding and a reduction in dissipation, i.e., a reentrance upon the increase of the temperature T , and a noisy response varying the ac field (h) [109, 185, 186] are the signatures of the occurrence of flux avalanches, as shown in the panels (b)-(d) of Fig. 5.2 and in Fig. 5.5.

This catastrophic flux penetration happens as a result of thermomagnetic instabilities (TMI) at low temperatures when the magnetic diffusion is faster than the thermal diffusion. Thus, the motion of flux lines releases heat, leading to a local temperature rise in a nearly adiabatic process which, in turn, reduces the pinning force and facilitates further vortex motion. Then a positive feedback loop is established, facilitating flux invasion in the form of avalanches [85, 86]. Considering the stability analysis for a thin superconducting stripe thermally coupled to a substrate [88, 187], the thermomagnetic (TM) description has successfully described the experimental results. Some examples of this correspondence between numerical simulations and actual observations are the conditions for the appearance of instabilities [102, 103, 104, 188], the avalanche morphology, its dynamics and the time evolution of the dendritic pattern [82, 83, 186].

The most remarkable prediction of the TM model is the need of a minimum flux penetration depth (l^*) inside the specimen in order for the TMIs take place [102]. Apart from the thermal properties, l^* also depends on J_c and, implicitly, on the half-width of the sample, which are more easily controlled. Thus, by varying the width of MgB₂ stripes, Denisov *et al.* [102] and Choi *et al.* [188] have found a quantitative agreement with the TM model for the lower (H_1^{th}) and the upper (H_2^{th}) threshold fields with respect to the width and the temperature (T). On the other hand, J_c also plays a crucial role in the instability regime. In a H - J_c diagram, below a certain threshold value of J_c , named here as J_c^{th} , no flux avalanches take place whatever the field applied. Albrecht and co-workers [103] have found that a slight anisotropy in J_c in a square MgB₂ thin film leads to a dramatic anisotropy in avalanche activities close to this threshold. The stability/instability limit in a H - J_c diagram has also been studied by Yurchenko and co-workers [104] via MOI, where the value of J_c was controlled by the value of the applied magnetic field in a field-cooled procedure under isothermal conditions.

This chapter presents a different approach to obtain the stability/instability limit in the $H(J_c)$ diagram by investigating the field dependence of the critical current density

using magnetic measurements. We use ac susceptibility measurements to obtain $J_c(T)$ for different values of H . Our results confirm the existence of a threshold value of the critical current, J_c^{th} , below which no avalanches occur, regardless of the values of H and T . The complete boundary of the instability region in the H - J_c diagram was determined and fitted using the corresponding expression derived from the TM model. Experimental data and results from the model are in excellent agreement.

The chapter is organized as follows: Section 6.2 briefly shows the instability region in $H(J_c)$ and $H(T)$ diagrams, as well as the equations which provide the instability/stability limit. Section 6.3 reports the properties of the thin film used in this study and the experimental details, whereas the results are summarized in Section 6.4.

6.2 Instability region in superconducting thin films

Before presenting the experimental details we discuss in detail the stability limit in the H - J_c diagram for a thin superconducting stripe. As discussed earlier (Section 3.3), the TM model predicts the existence of a threshold length which the magnetic flux has to penetrate before a dendritic avalanche is triggered. This means that the stripe develops the critical state until it becomes unstable, what occurs when the penetration depth l^* is reached [88, 102]. The threshold length, already shown in Eq. (3.4), depends on the electromagnetic and thermal properties of the sample which, in turn, vary with temperature, according to:

$$l^* = \frac{\pi}{2} \sqrt{\frac{\kappa T^*}{E J_c}} \left(1 - \sqrt{\frac{2 h_0 T^*}{n d E J_c}} \right)^{-1} \quad (6.1)$$

where E is the electric field; κ is the thermal conductivity, depending on the temperature as $\kappa(T) = \kappa_0(T/T_c)^3$; T_c is the critical temperature; h_0 is the temperature-dependent heat transfer coefficient between the superconducting film and its substrate $h_0(T) = \tilde{h}_0(T/T_c)^3$; d is the film thickness, n is the power-law exponent of the current-field relationship, $E = \gamma J^n$ and $1/T^*$ is the logarithmic temperature derivative of the critical current density, $1/T^* = -d \ln J_c / dT$.

Considering a long thin stripe with width $2w$ in a perpendicular applied field, the model allows one to evaluate the frontier above which the sample becomes unstable and flux avalanches start to take place. In the framework of the Bean model, the magnetic

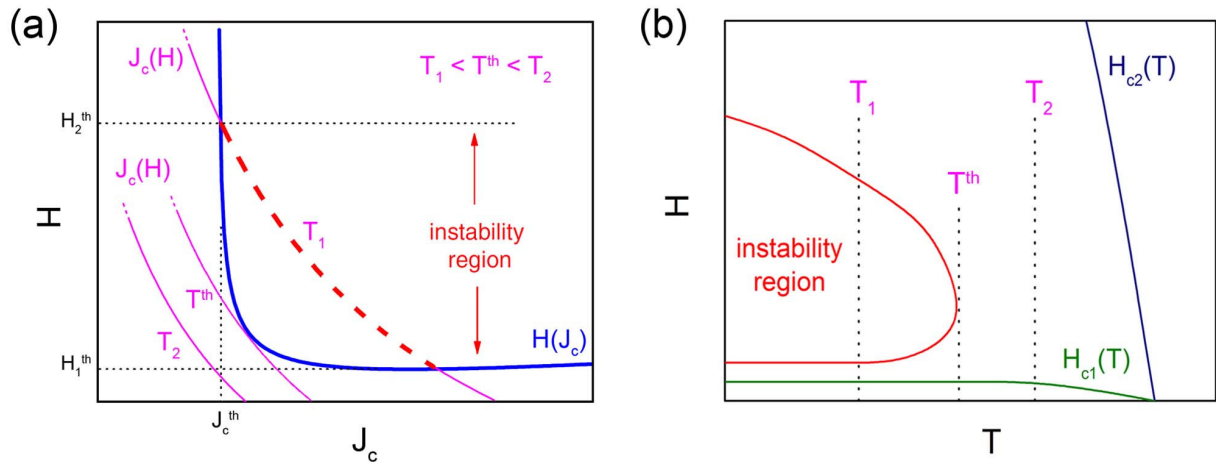


Figure 6.1: Scheme of the region of flux avalanches diagrams $H(J_c)$ [panel (a)] and $H(T)$ [panel (b)]. For a lower and fixed temperature T_1 , when the flux penetration reaches l^* (or $H = H_1^{th}$) flux avalanches are triggered. The increasing of the magnetic field decreases the critical current density and when it reaches H_2^{th} (or $l^* = w$), the sample recovers the stability and Bean penetration takes place again. However, for higher temperatures, the isothermal curve J_c does not cross the instability threshold and instabilities do not occur [104]. When the isothermal line is scanned in an H - T diagram [114] below T^{th} , two limits of the field are reached. Above T^{th} , no avalanches take place. The panel (a) is based on [104] and (b) on [114].

field profile in a superconducting thin film is known [62, 70] to obey:

$$a = \frac{w}{\cosh\left(\frac{H\pi}{J_c d}\right)} \quad (6.2)$$

where a is the flux front position measured from the center of the sample. Since there is a minimum value of the penetration depth for an avalanche to be triggered, a threshold field (H^{th}) can be defined between the stable and unstable regions in a $H(J_c)$ diagram. Equation (6.3) (same as Eq. (3.5)) earlier show the expression for such a threshold field.

$$H^{th} = \frac{J_c d}{\pi} \operatorname{arccosh}\left(\frac{w}{w - l^*}\right) \quad (6.3)$$

The panel (a) in Fig. 6.1 is a magnetic field versus critical current diagram showing the threshold line (blue), $H^{th}(J_c)$, and three isothermal curves, $J_c(H)$, representing the field dependence on the critical current at different temperatures. At lower values of T (e.g., T_1), $J_c(H)$ crosses the threshold curve twice, defining a lower and an upper limit for the occurrence of avalanches, H_1^{th} and H_2^{th} , respectively. As T increases, the difference between these threshold fields decreases, there being a limiting temperature, T^{th} , above which $J_c(H)$ and $H^{th}(J_c)$ do not cross each other (T_2), so that no avalanches can occur. One can then envisage that the portion of the H - T phase diagram where thermomagnetic instabilities occur, consists of an enclosed region, as depicted in the panel (b) of Fig. 6.1: at small enough values of T (e.g., T_1), as the field H is increased from zero in an isothermal

process, avalanches start to occur when the threshold penetration depth is achieved; however, l^* increases with H and, eventually exceeds the lateral dimensions of the film so that avalanches become unviable in this upper limit, at which $l^* = w$, H^{th} diverges [104] and $J_c = J_c^{th}$. The upper limiting temperature on the instability region, T^{th} , represents the case when $H^{th}(J_c)$ and $J_c(H)$ are tangent to each other.

6.3 Experimental details

The investigated sample consists of a Nb thin film with thickness $d = 50$ nm, deposited by dc sputtering on top of a SiO₂ substrate. The sample dimensions are 2.5 x 3.0 mm² and its critical temperature (T_c) is 7.9 K. The values of coherence length and penetration depth at 0 K are 9.4 nm and 168.0 nm, respectively, estimated from the temperature derivative of $H_{c2}(T)$ near T_c and the dirty limit expressions [Sec. 2.3.1]. This sample corresponds to the pristine thin film studied in the previous chapter.

Ac-susceptibility and dc-magnetization measurements were carried out in commercial Quantum Design PPMS and MPMS instruments. The ac susceptibility measurements were recorded for the ac field h ranging from 20 mOe to 15 Oe, with a fixed frequency of 1 kHz. In all cases, both components of χ were normalized using the lowest value of the real component χ'_0 , which represents the Meissner plateau, taken at $T = 2$ K with a drive amplitude $h = 20$ mOe in a null dc field, which was very close to the theoretical value for a thin disk with the same superconducting area [70]. Both h and H were applied perpendicular to the plane of the film.

6.4 Results and discussions

In order to measure $J_c(T)$, ac susceptibility measurements as a function of the ac excitation field, $\chi(h)$, for several values of T and H , were conducted. From these data, Cole-Cole plots [$\chi'(\chi'')$] were built and used to indicate if the film response can be treated as following Bean model [160, 161, 177], from which one can extract numerical values for J_c . For fields of 10 Oe and above, the sample does indeed behave according to Bean model, a conclusion that can be withdrawn comparing its Cole-Cole plots with the corresponding curve for a circular/rectangular thin film [70, 166]. Fig. 6.2 shows Cole-Cole plots taken at several temperatures and $H = 35$ Oe (a) and 100 Oe (b) to emphasize the smoothness and noisiness indicating different regimes of vortex penetration. The curves measured at

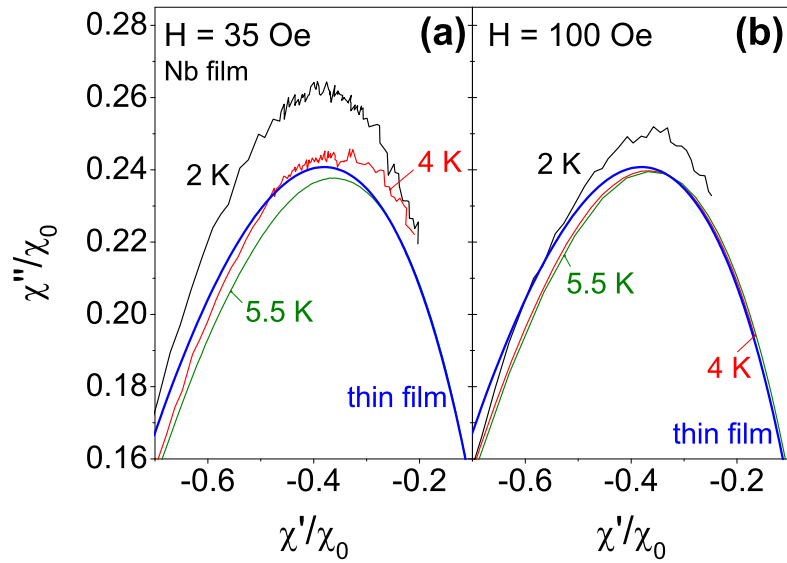


Figure 6.2: Cole-Cole plots for the Nb thin film at 2 K, 4 K, and 5.5 K for $H = 35$ Oe and 100 Oe, as well as the theoretical curve for a thin circular disk/rectangular thin film [70, 166]. The noisy response refers to flux avalanche activity.

2 K and 4 K in panel (a), and at 2 K in panel (b), show a noisy behavior, indicating the occurrence of flux avalanches at those temperatures and applied fields [185]. However, the curves taken at 5.5 K for both fields, and at 4 K for 100 Oe, show a Bean-like behavior, comparable to the theoretical curves for circular/rectangular thin films (blue line), what assures smooth flux penetration and also critical current densities independent of H . Therefore, J_c was then obtained inserting the value of the field amplitude at which χ'' peaks (h_p) into the expression derived by Chen *et al.* [166] for rectangular thin films and given by Eqs. (5.1) and (5.2).

Fig. 6.3 shows $J_c(T)$ curves for fixed values of H . The curves corresponding to applied fields of 35 Oe, 100 Oe and 280 Oe have two distinct behaviors, being smooth for higher temperatures and noisy below a certain value of T (vertical arrows), which is precisely the threshold temperature, T^{th} , at this field. A power law expressed by

$$J_c(T) = J_{c0} \left(1 - \frac{T}{T_c}\right)^\beta \quad (6.4)$$

where J_{c0} and β depend on H , was used to fit the higher- T portion of the curves, allowing us to identify this limiting temperature, below which thermomagnetic instabilities dominate. The values of the exponent β ranges from 1.68 to 1.91. At 1000 Oe, the curve is smooth and the power law expression provides a good fitting along the entire temperature interval accessible to experiments. One can observe that the onset temperature (T^{on}) depends on the applied field, diminishing for increasing H . Although we have attributed values to J_c for temperatures and fields at which avalanches take

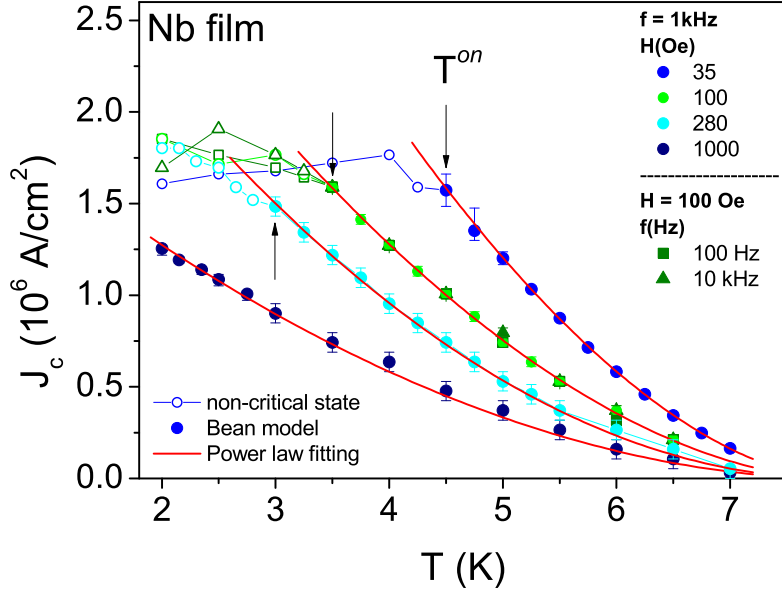


Figure 6.3: Critical current density versus temperature for the isofield lines at 35 Oe, 100 Oe (for three different frequencies), 280 Oe, and 1 kOe. The closed and open symbols designate where the Bean model is valid, showing no presence of flux avalanches, and invalid, respectively. A power law fitting (Eq. (6.4)) has been used to find the threshold value of J_c at the onset temperature (T^{on}) below which the instabilities take place, indicated by the black arrows for $H = 35, 100$ and 280 Oe. At 1 kOe, there is no signal of avalanche occurrence.

place, these points are not representative of the critical current density, since the sample is not obeying the critical state picture for $T < T^{on}$. Nonetheless one can benefit from the visual aspect of the curve, which emphasizes a clear change in the flux penetration regime. Repeating the same procedure for a variety of H values, a complete map of the critical current density was determined for this sample. To verify the possible influence of the frequency on our results, the ac susceptibility measurements have been carried out at 100 Hz, 1 kHz, and 10 kHz, with no significant difference of T^{on} and J_c for the studied Nb thin film. Fig. 6.3 includes curves at different frequencies, where one can see that the values are essentially equal within experimental error. This nearly inexistent effect of excitation audio-frequencies on the appearance of flux avalanches has been observed earlier [109, 185, 189], although a strong dependence has been reported in experiments conducted in the microwave range [190].

Fig. 6.4 shows the experimental results for the threshold critical current, $J_c^{th}(H)$, above which avalanches are triggered in the sample. This seemingly constant response represents the upper threshold for the avalanches, expressed by Eq. (6.3), and depicted in Fig. 6.1a as a nearly vertical branch. The threshold critical current is independent of H and T , having, for the sample studied here, the value $J_c^{th} = (1.54 \pm 0.05) \cdot 10^6$ A/cm². An H - J_c diagram, similar to the schematics shown in Fig. 6.1a, can now be built, and

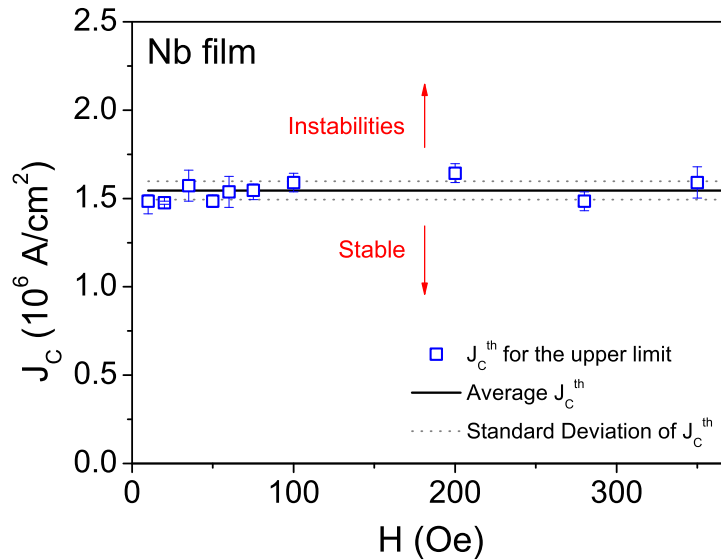


Figure 6.4: Threshold critical current density to trigger avalanches obtained by the power law fittings for $H \geq 10$ Oe, which separates the stable region (below the line) from the instability region (above).

appears in Fig. 6.5, along with the experimental points for $J_c(H)$ determined at different temperatures. The vertical line $H(J_c^{th})$ defines the limit between the regime of smooth penetration (lower values of J_c) and the thermomagnetically unstable region, where avalanches take place. The low-field portion of the diagram is amplified on the right panel, Fig. 6.5(b), where one can now distinguish the lower threshold line which, in fact, is horizontal, since the lower field to trigger avalanches is nearly independent of T . In the present study, this line representing the lower limit of the avalanche regime, cannot be accessed using ac susceptibility measurements, for a reason easy to grasp: in the small applied field limit, J_c is comparatively large, meaning that the ac field amplitude for maximum dissipation (i.e., peak in χ'') is also large*. In the present case, the value of h corresponding to the lower limit is larger than the field corresponding to l^* , so that the first signs of avalanches cannot be obtained by calculating J_c from ac measurements.

To circumvent this technical limitation, the lower limit was determined from the first jump in the virgin curve of the sample [$m(H)$] [114], from which we extracted the nearly constant value of 3 Oe. To find the corresponding values of J_c in this lower limit, we verified that each isothermal $J_c(H)$ curve obeys the so-called Extended Kim Model [191], expressed by:

$$J_c(H) = \frac{J_0}{H_0 + H} + J_1 \quad (6.5)$$

where J_0 , J_1 and H_0 are temperature-dependent constants. We have then extrapolated the curves down to $H = 0$, so that the crossing of each extrapolation with the horizontal

*For thin films obeying the Bean Model, the amplitude of the ac field needed to achieve maximum dissipation (h_p) is 72% of the full penetration field.

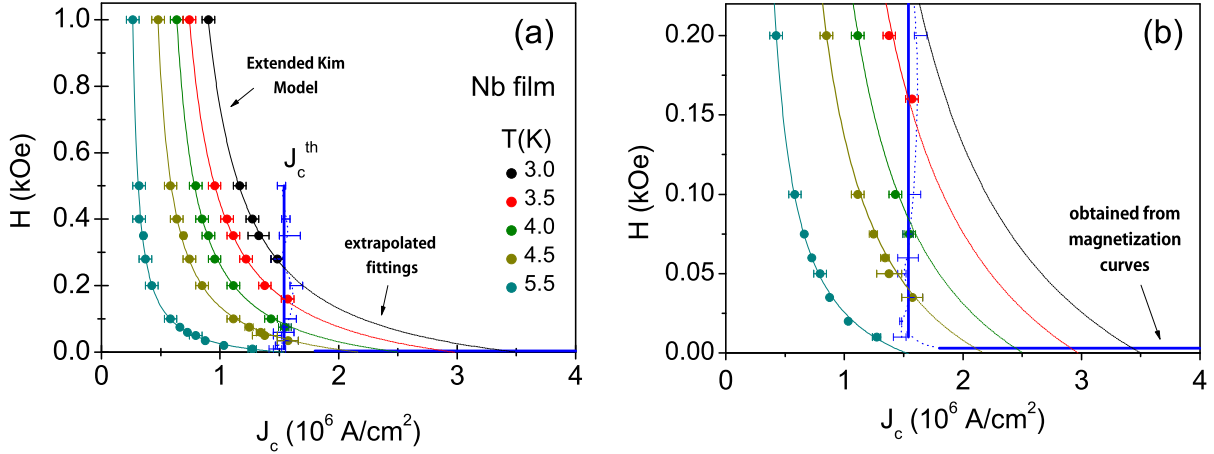


Figure 6.5: Plot $H(J_c)$ for the Nb film that shows the threshold critical current to trigger avalanches obtained by ac susceptibility (a). The lower limit was obtained from magnetization curves and the isothermal fittings were calculated by the Extended Kim Model [191]. (b) Zoomup from the low field region with the lower limit taken from the first jump in the virgin part of the magnetization curves.

line H_1^{th} , allowed us to calibrate the abscissa J_c of each point in the lower limit frontier, as seen on panel (b) of Fig. 6.5. For temperatures higher than T^{th} , there is no crossing between J_c^{th} and $J_c(H)$, as illustrated by the 5.5 K curve: the thin film is stable for any value of the applied field, and no avalanches occur in this temperature.

The complete set of points defining the limits of instability for the sample studied here is collected in the panel (a) of Fig. 6.6. The frontier is composed of two subsets: the upper limit, a nearly vertical line for which $J_c = J_c^{th} \approx constant$, and the lower limit, characterized by a virtually horizontal line, with $H = H_1^{th} \approx constant$. Using Eqs. (6.1) and (6.3) – since H^{th} depends on J_c and l^* , and the latter, in turn, also depends on J_c – we have fitted the experimental data with two adjustable parameters, namely, $\kappa T^*/E = 8.18$ A and $h_0 T^*/nE = 366.63$ A/m, which are independent of the temperature and the applied magnetic field. Assuming an electric field of 5 kV/m, a value that matches those obtained from numerical simulations [82, 83] and from measurements of the voltage induced in a metallic layer [82, 83, 107], the value of the thermal conductivity constant κ_0 corresponding to our data would be $3 \cdot 10^6$ W/Km. This value is rather different (four orders of magnitude) from that of 120 W/Km employed by Denisov *et al.* [88] for bulk Nb. However, in that case the estimated electric field was 0.3 V/m much smaller than the above-mentioned values published more recently. Besides, since above the threshold point in the upper limit the sample obeys the Bean model, the value of n in the non-linear relation between J and E , should be $n \gg 1$, and one is tempted to choose the typical value of $n = 51$, frequently adopted by E. H. Brandt [161]. Following this assumptions we obtained $\tilde{h}_0 \approx 6.7 \cdot 10^9$ W/Km² for the Nb thin film studied here. It is also worth to

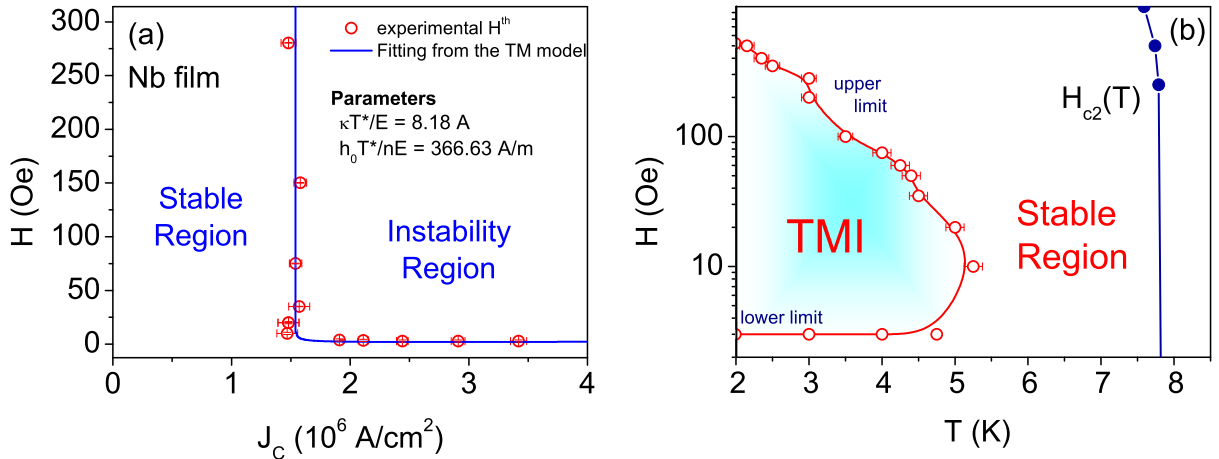


Figure 6.6: Frontier between the stable and instability regions taking from the limiting points to trigger flux avalanches. (a) $H(J_c)$ graph where the parameters were obtained by fitting the TM model from Eqs. (6.1) and (6.3). Panel (b) shows the region where TMIs in a H - T diagram obtained from the T^{on} and from the first jump in the $m(H)$ curves.

mention that, the set of values of $T^{on}(H)$ and of $H_1^{th}(T)$ allows one to obtain the upper and lower limits for the regime of flux avalanches, respectively, in the H - T diagram, which is shown in Fig. 6.6b. The upper border of the TMI region corresponds to the threshold at which the critical current density is constant.

6.5 Conclusions

We have employed ac susceptibility measurements to determine the temperature and applied field dependence of the critical current density of a Nb thin film. A threshold value of the critical current density of $(1.54 \pm 0.05) \cdot 10^6$ A/cm² was identified for this film, below which no thermomagnetic instabilities take place, regardless of the values of T and H . The existence of this limit corresponds to the description of the thermomagnetic model for the upper limit of occurrence of instabilities in a superconducting film. Fitting our experimental data with the expression for the threshold border of the instability region, $H(J_c)$, predicted by the model, we were able to estimate typical values of the local electric field associated with the borders of the instability regime.

7

*Enhancement of pinning properties of superconducting thin films by graded pinning landscapes**

A graded distribution of pinning centers (antidots) in superconducting MoGe thin films has been investigated by magnetization and magneto-optical imaging. The pinning landscape has maximum density at the border, decreasing progressively towards the center. At high temperatures and low fields, where this landscape mimics the vortex distribution predicted by the Bean model, an increase of the critical current is observed. At low temperatures and fields, the superconducting performance of the non-uniform sample is also improved due to suppression of thermomagnetic avalanches. These findings emphasize the relevance of non-uniform pinning landscapes, so far experimentally unexplored, on the enhancement of pinning efficiency.

7.1 Introduction

In the mixed state of type II superconductors, magnetic flux is admitted into the sample in the form of quantized vortices [2]. When superconducting currents are present, vortices undergo a viscous motion, generating a local temperature rise. This unwanted consequence of vortex motion should be prevented, in order to avoid the weakening of the superconducting properties of the material, what would constitute a threat to its potential use in real applications. For this reason, the task of understanding vortex dynamics in the presence of pinning centers (PCs) has maintained, throughout the years, its status of a timely and relevant research problem [36, 192] for fundamental science and applications [49, 54, 193, 194, 195, 196, 197, 198, 199, 200, 201]. A natural strategy in this attempt to anchor vortices is to spread, at random, small clusters of normal material, an approach adopted since long for superconducting alloys [192, 202, 203] and reproduced more recently for high-temperature superconductors [198, 204] and MgB₂ [205,

*This chapter is based on M. Motta, F. Colauto, W. A. Ortiz, J. Fritzsche, J. Cuppens, W. Gillijns, V. V. Moshchalkov, T. H. Johansen, A. Sanchez, and A. V. Silhanek, Enhanced pinning in superconducting thin films with graded pinning landscapes, *App. Phys. Lett.* 102, 212601 (2013); and deposited at arXiv:1301.6283.

206]. Other commonly employed methods are the placement of arrays of magnetic dots on the surface of superconducting films [54, 199, 207]; and the creation of lattices of antidots (ADs) in films [49, 48, 176, 208, 209, 210].

It has been demonstrated [176, 185] that the insertion of arrays of ADs in a superconducting film can lead, at high temperatures, to an increase of the critical current, via enhancement of the pinning efficiency, as can be seen in Fig. 5.2a. Unfortunately, at low temperatures, such PCs facilitate the proliferation of flux channeling [109, 110, 112, 185, 211, 212] leading to unwanted instabilities of thermomagnetic origin [85, 88, 104] which render the superconductor impractical.

One major issue regarding the efficiency of vortex anchorage is to adapt the PC landscape in order to match the actual distribution of vortices. In this regard, a considerable effort has been done to investigate the case where artificial pinning sites reproduce the regular (periodic) vortex distribution, typically obtained under field cooling conditions. However, in order to create a distribution of PCs compatible with flux distribution builds up from the zero-field cooling procedure, one should then distribute them with a density gradient, decreasing from the edges toward the center of the sample, as expected for the vortex distribution of a partially penetrated sample in the mixed state according to the well-established Bean model illustrated in Fig. 2.7c and Fig. 2.8b. Such an inhomogeneous distribution, should provide nearly optimum pinning only for a small interval of values of the magnetic field and temperature, within which local matching conditions between the density of PCs and the density of vortices, would be achieved. Determining the optimum gradient parameters is a non trivial problem needing to extend the standard Bean model, which assumes a constant critical current density J_c , in order to account for the Meissner currents and also to take into account the spatial dependence of demagnetizing fields. However, even a non-optimized version of a gradient density of ADs, decreasing from the edges to the center, constitute a seemingly promising alternative way of using arrays of PCs in order to increase the critical current of the specimen.

In this chapter we demonstrate that an array of ADs with a spatially decreasing density of pinning sites (the gradient sample) promotes an increase of the critical current which is even better than the enhancement obtained when a homogeneous array of ADs (the uniform sample) is used. Furthermore, although flux avalanches on the gradient sample are induced - as expected - by the presence of the array of pinning sites, this effect is comparatively less important than for the uniform sample. This is evidenced by the

substantially smaller thermomagnetic instability region on the magnetic phase diagram for the gradient sample compared to the corresponding region for the uniform sample. Thus, the presence of a grid of ADs with density gradient not only generates the desired increase in critical current, but also promotes an additional protection against the early occurrence of flux avalanches, as compared to the case of a film with a uniform distribution of ADs.

7.2 Experimental details

The samples investigated consist of amorphous $\text{Mo}_{79}\text{Ge}_{21}$ ($\text{a-Mo}_{79}\text{Ge}_{21}$) thin films with thickness $d = 25$ nm, deposited by pulsed laser deposition on top of a Si/SiO_2 substrate. The pinning centers on both the gradient and the uniform sample consist of square holes of $0.5 \mu\text{m}$ side, prepared by standard electron beam lithography. The lattice parameter of the uniform film (UNI) is $1 \mu\text{m}$ and the lattice symmetry is square. At the edges of the gradient sample (GRAD) the separation between the centers of neighboring holes is also $1 \mu\text{m}$, and its density varies inwards (but not laterally) with a constant increase on the row separation of 10 nm/row. Fig. 7.1a and Fig. 7.1b left panel sketch the scheme of the spatial dependence of the density of ADs on the three films studied here. The right panels of Fig. 7.1b show a zoomed up view obtained via atomic force microscopy of the edges and the center of sample GRAD, illustrating its density gradient. A third film (Plain), without ADs, was used as a reference sample.

The samples have a lithographically defined square shape with lateral dimensions of

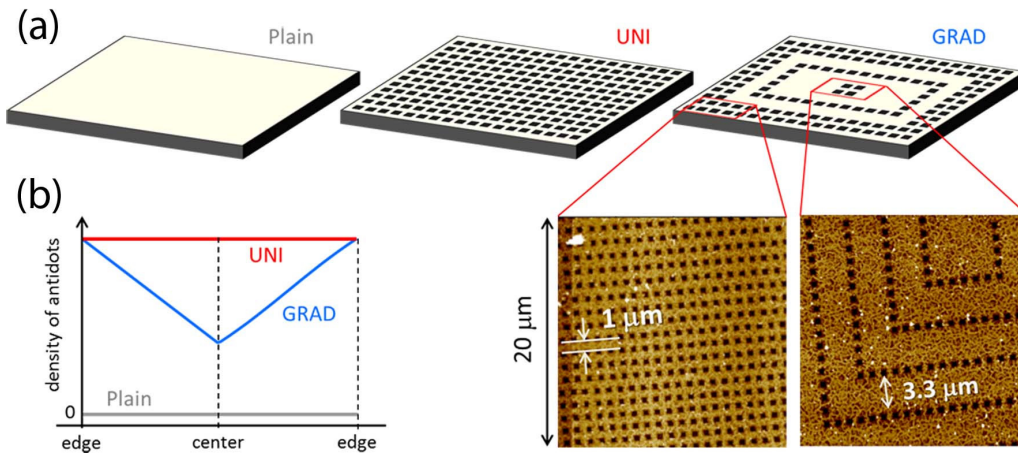


Figure 7.1: (a) Scheme of the density of ADs for samples Plain, UNI, and GRAD (not to scale); (b) left panel: average areal density of antidots as a function of position for the three cases of pinning distribution considered in this work; (b) right panels: atomic force microscopy image showing the distribution of antidots at the border and at the center of the GRAD sample.

1x1 mm² and the critical temperatures, T_c , are 6.73 K, 6.65 K and 7.10 K, for samples Plain, UNI and GRAD, respectively. Using the temperature derivative of the upper critical field, the normal state resistivity and the dirty limit expressions [213], the zero-temperature superconducting coherence length ($\xi_{GL}(0)$) and penetration depth ($\lambda_{GL}(0)$) were estimated to be 5 nm and 500 nm, respectively. Dc magnetization measurements were carried out in a commercial Quantum Design MPMS instrument. The magneto-optical technique employed to image the flux penetration morphology is based on the Faraday effect [173] in an indicator film placed on top of the superconducting specimen. The indicators used in the present work are Bi-substituted yttrium iron garnet films (Bi:YIG) with in-plane magnetization.

7.3 Results and discussions

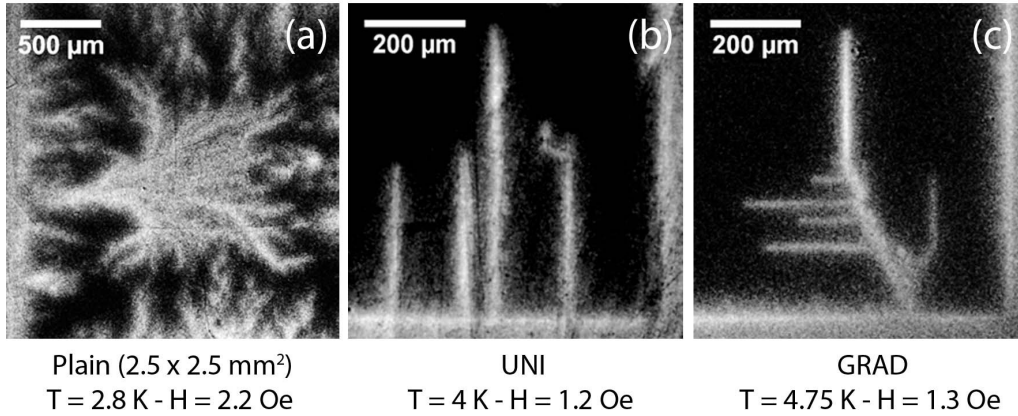
Within a limited interval of values of the applied field and temperature, flux avalanches originating from thermomagnetic instabilities are likely to develop in thin films of a variety of superconducting materials [89, 91, 92, 94, 95, 96, 171]. To our knowledge, however, amorphous films of MoGe were not reported thus far as members of this list. The panels (a) through (c) of Fig. 7.2 are representative examples of such avalanches in three MoGe films: panel (a) show freely expanding dendritic structures, typical of plain films*, whereas panels (b) and (c) exhibit straight tracks, guided by the rows of ADs[†] [110, 112, 185], in the specimens UNI and GRAD, respectively. In order to verify the flux penetration depth, which is related to the magnitude of the critical current density, images were taken at the same temperature (5 K) and applied field (1 Oe) out of the region where flux avalanches occur for all samples. The panels (d)-(f) of Fig. 7.2 show the flux penetration for the Plain, UNI and GRAD specimens, respectively. It is possible to observe that the smooth Bean envelope develops in each film and the penetration depth is the deepest in the plain film, as expected, with the UNI sample deeper than the GRAD specimen, indicating an increase of the critical current density when an array of ADs is present and being higher in the thin film with a graded pinning landscape at this applied field.

Fig. 7.3 depicts the effects on the critical current of a film of a-Mo₇₉Ge₂₁, caused

*Flux avalanches in superconducting films develop only below an upper threshold temperature, which is characteristic of each sample. For the sample named Plain in this work, this threshold temperature is 2.6 K, as determined by magnetic measurements, a value that we cannot achieve in the cold-finger type cryostat of the magneto-optical imaging setup. We present instead an avalanche observed on a sister plain film of larger dimensions (2.5 mm x 2.5 mm), at $T = 2.8$ K and $H = 2.2$ Oe.

[†]The flux avalanche morphology in decorated thin films is extensively discussed in Chapter 8 and also in Appendix A for the UNI sample.

Flux avalanches



Smooth flux penetration

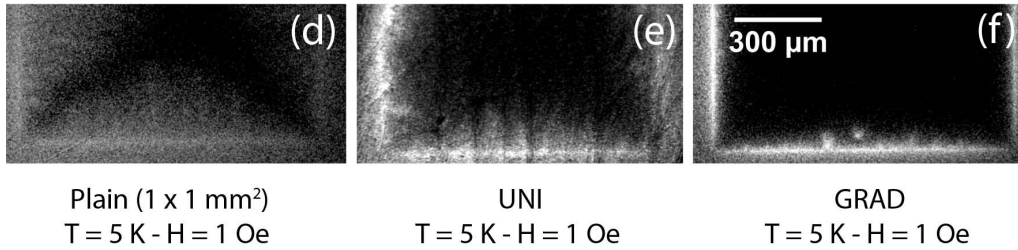


Figure 7.2: (a) Magneto-optical image, taken at $T = 2.8$ K and $H = 2.2$ Oe, for a sister plain sample; (b) same as (a) for sample UNI, at $T = 4$ K and $H = 1.2$ Oe; (c) sample GRAD at $T = 4.75$ K and $H = 1.3$ Oe. The panels (d), (e), and (f) refer to the specimens Plain, UNI, and GRAD, respectively, taken at $T = 5$ K and $H = 1$ Oe.

by the insertion of different arrays of ADs. Panel (a) comprises magnetization loops for the three samples studied, taken at the reduced temperature $t = T/T_c = 0.75$. At such temperatures, the loops for the samples with ADs are clearly wider and taller than that for the Plain film, confirming the enhanced pinning capability of the patterned samples, which implies larger critical currents for those specimens. It is particularly interesting to notice that, at large enough magnetic fields, sample UNI performs somewhat better than sample GRAD due to the fact that sample UNI has more ADs than sample GRAD, so that its pinning capability is better at larger fields. At fields below 60 Oe, however, the magnetic response of sample GRAD represents an enormous enhancement of the critical current, as compared with the uniform sample. At fields around zero, its increased pinning capability leads roughly to a factor of 2 on the critical current. We have obtained similar results in Pb samples with much smaller λ/ξ ratio (not shown). The fact that no much difference is seen in the magnetization loop for increasing and decreasing field, indicates that the graded distribution is equally efficient as a vortex dam preventing vortex entrance and exit and leading to a huge flux trapping at zero field. It is worth mentioning here

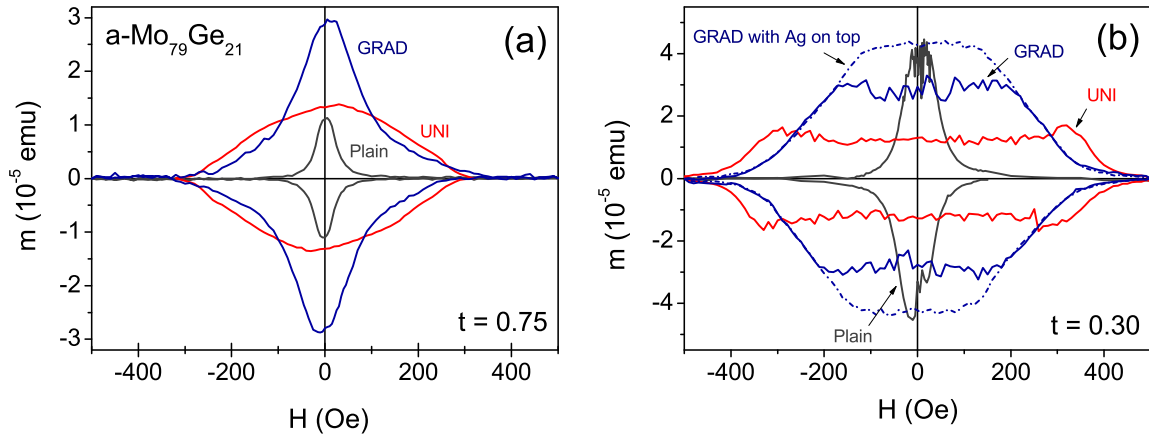


Figure 7.3: (a) Dc magnetization versus magnetic field taken at the reduced temperature $t = 0.75$ for samples Plain, UNI and GRAD. (b) Magnetization loops for the three samples in the avalanche region ($t = 0.3$); a fourth loop is also shown for sample GRAD covered with a thick disk of Ag, an artifact employed to substantially suppress flux avalanches.

that similar results were recently predicted theoretically from simulations of the critical current of superconducting specimens with somewhat more complicated landscapes of graded pinning centers [214, 215].

The panel (b) in Fig. 7.3 shows a similar set of hysteresis loops at the reduced temperature $t = T/T_c = 0.30$. The noisy response at the central portion of the loops is the typical signature [93, 172] of the flux avalanches mentioned above. Alternative means to suppress such flux bursts have been already discussed in the literature [115, 116, 216, 217] and in Section 3.4, the simplest of which we have applied here by placing a metallic disk (Ag) with height of 0.1 mm directly on top of sample GRAD, as shown in Fig 3.10c, one manages to inhibit, via magnetic breaking [116], the thermomagnetic instabilities that trigger avalanches. The dot-dashed curve in Fig. 7.3b shows the hysteresis loop of sample GRAD with the Ag disk, indicating that flux avalanches are mostly suppressed in this configuration. One can thus conclude that the strategy of patterning a superconducting film with a gradient distribution of ADs is clearly more efficient in increasing the critical current than using a uniformly distributed array of ADs.

By repeating experiments as those depicted in Fig. 7.3 for different values of the temperature, one can construct a HT -diagram containing the boundaries of the instability region for the samples studied. These frontiers are shown in Fig. 7.4, from which one can clearly see that the inclusion of ADs enlarges the instability region, as compared to the Plain film. The region for sample GRAD is, however, substantially smaller than for sample UNI (notice the logarithmic scale on the lower portion of the vertical axis).

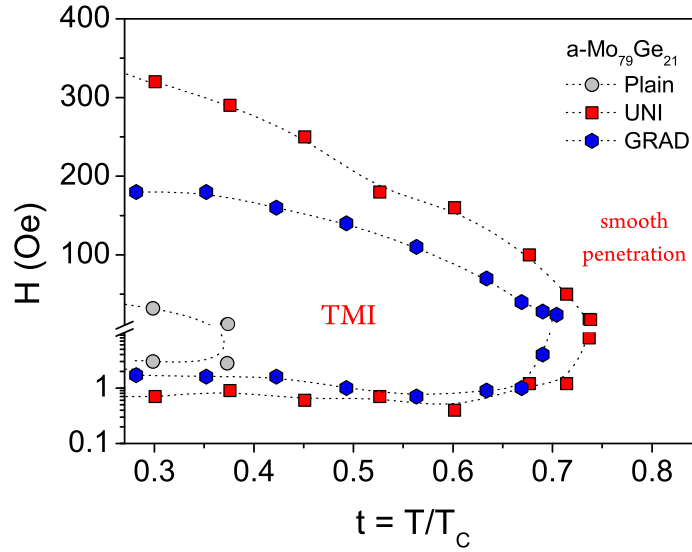


Figure 7.4: Boundaries of the instability region of the studied a-MoGe thin films. Notice the logarithmic scale on the lower portion of the vertical axis.

Since these avalanches can be efficiently suppressed by depositing a metallic layer on top of the film of interest, one can fully appreciate the reach of the present results, from which we conclude that the strategy of inserting a graded pinning landscape represents an increased protection of the film against flux avalanches, a substantial advantage in terms of practical use of superconducting films in the presence of perpendicular magnetic fields. At the moment it remains unclear whether this improved performance – better pinning at low fields and narrower TMI area in Fig. 7.4 – of the sample GRAD arises from the lack of perfect periodicity in the antidot lattice or from the gradient itself.

7.4 Conclusions

In summary, we have demonstrated that, for low fields, a graded pinning landscape introduced in a superconducting film of a-Mo₇₉Ge₂₁ increases the critical current, as compared to a uniform distribution of ADs. In addition, flux avalanche activity, typically induced by the presence of arrays of ADs, is less prejudicial for the sample with gradient distribution of antidots than for the uniformly distributed pinning centers. This work focus on a particular gradient geometry following a very smooth linear decrease of areal density of pinning centers from the border of the sample towards its center. Further investigations in other gradient geometries including non-linear areal-density dependence or inverted gradients will be necessary to identify the main mechanisms and geometrical parameters responsible for the striking improvement of the pinning properties of this sort of pinning landscape.

8 *Guidance and morphology of flux avalanches in superconducting films decorated with lattices of antidots**

We have employed magneto-optical imaging to visualize the occurrence of flux avalanches in superconducting films of crystalline Nb and amorphous $\text{Mo}_{79}\text{Ge}_{21}$. For specimens decorated with square antidots arranged in a square lattice, avalanches were observed with the systematic habit of forming trees having the main trunk perpendicular to the sample edge, running along one of the main axis of the square lattice, with branches making angles of 45 degrees with the trunk, as in a Christmas tree. For films with a square lattice of triangular antidots and of circular antidots, avalanches exhibit a different morphology, anisotropic depending on the relative direction with the triangular hole and with branches orthogonal to the main trunk, respectively, emphasizing the role of the antidot geometry on the paths followed by the penetration profiles in these films. Samples of a fourth kind, with square holes displayed in a centered rectangular lattice, were also investigated, for which the avalanches follow the lattice symmetry. The overall features of the avalanches and, in particular, of the angles followed by the penetrating flux, were confirmed by numerical simulations. Since the present results were obtained for films of superconductors so diverse as Nb and a-MoGe, it seems perfectly conceivable that the features reported here derive from lattice symmetry and antidot geometry, rather than from any crucial material-related characteristics.

8.1 Introduction

One century after its discovery by Heike Kamerlingh Onnes [9, 10], superconductivity is widely recognized by its most appealing feature of allowing the transport of electrical currents without dissipation. However, as was soon verified by Onnes [10], clean specimens are useless for this kind of application. The widespread employment of superconducting wires as, for example, in large volume electromagnets designed to produce high magnetic fields [218, 219], was made possible by use of certain type II superconductors – like NbTi and Nb_3Sn – combining a high upper critical field

*This chapter is an extended version from the manuscript: M. Motta, F. Colauto, W. A. Ortiz, J. I. Vestgård, T. H. Johansen, J. Cuppens, V. V. Moshchalkov, and A. V. Silhanek, Anomalous flux avalanche morphology in an a-MoGe superconducting film with a square antidot lattice - experiment and simulation, arXiv:1109.2532 (2011). This study will soon be submitted for publication.

with a significantly large amount of pinning centers (PCs). These, in turn, anchor vortices – entities carrying magnetic flux quanta – preventing their viscous motion in the presence of transport currents, what otherwise would cause energy dissipation. For this reason, the task of understanding vortex dynamics in the presence of PCs has maintained, throughout the years, its status of a timely and relevant research problem [36, 192] for fundamental science and applications [49, 54, 193, 194, 195, 196, 197, 198, 199, 200, 201].

A natural strategy in this attempt to anchor vortices is to spread, at random, small clusters of normal material, an approach adopted since long for superconducting alloys [192, 202, 203] and reproduced more recently for high-temperature superconductors [198, 204] and MgB_2 [205, 206]. Other commonly employed tactics are the insertion of columnar defects through the sample, produced by irradiation of highly energetic particles [45, 220]; the placement of arrays of magnetic dots at the surface of superconducting films [54, 199, 207]; or the creation of arrays of holes (antidots) in films [49, 48, 176, 208, 209, 210].

The effectiveness of vortex anchorage by lattices of ADs has been clearly demonstrated [176], appearing as a substantial enhancement on the critical current at higher temperatures. Below a certain threshold temperature, however, the occurrence of instabilities of thermomagnetic origin [85, 88, 104] give rise to flux avalanches, as reported in the literature for a variety of superconducting films, both with [109, 110, 112, 185, 211, 212] and without [89, 91, 92, 93, 94, 96, 95, 221] ADs. As revealed by magneto-optical imaging (MOI) experiments, flux avalanches in plain films develop freely in format, creating bush-looking regions of penetrated flux [91, 92, 93]. For superconducting films decorated with a lattice of ADs, however, flux channeling is facilitated: entrance and exit are guided, and the avalanches appear in geometrical arrangements of straight lines. The interaction between moving flux and the rows of ADs seems to be of central relevance to define the patterns followed by the avalanches.

It becomes clear that the strategy of introducing antidots works positively to enhance pinning – and thus, the critical current – but might be deleterious to the usability of superconducting films, since it induces the occurrence of stronger and more abundant flux avalanches. This fundamental problem, of potential impact to applications of superconducting films, has been so far unexplored in depth in the literature, deserving a methodical study. The present chapter reports a systematic investigation on the influence of lattice symmetry and antidot geometry on the

morphology of flux avalanches in films decorated with ADs. We have studied films of crystalline Nb and amorphous a-MoGe decorated with either square or centered rectangular lattices of ADs which, in turn, were shaped in the format of squares, circles or triangles. The results indicate that within the limits of our study, the avalanche morphology is strongly dependent on the lattice symmetry and antidot geometry, but not on the superconducting material of the film.

8.2 Samples and experimental techniques

The study involved a large collection of films of amorphous $\text{Mo}_{79}\text{Ge}_{21}$ (a-MoGe) and crystalline Nb, with and without lattices of ADs. In order to present here the most representative results, we have selected five samples, whose names and main features appear in Table 8.1. A scheme of the lattice symmetry and AD geometry of the specimens is shown in each MO image presented in the next section. Sample MoGe-I is an amorphous film, approximately rectangular in shape, with thickness $d = 25$ nm and lateral dimensions 2.0 mm x 2.6 mm. A square lattice of square ADs was fabricated by electron beam lithography using a double resist layer covering the Si/SiO₂ substrate. After the thin film deposition, the resist was removed in a lift-off procedure in warm acetone in order to obtain the sample with an array of ADs. The a-MoGe was deposited via pulsed laser deposition on top of the patterned substrate. The antidots have sides $\beta = 0.4$ μm , lattice parameter $\alpha = 1.5$ μm . This sample has critical temperature $T_c = 6.7$ K. Using the temperature derivative of the upper critical field near T_c obtained by ac susceptibility measurements (temperature derivative of Eq. (2.28)) and the dirty limit expressions (Section 2.3.1 and [33]), the zero temperature superconducting coherence length, $\xi_{GL}(0)$, and penetration depth, $\lambda_{GL}(0)$, were determined, as shown in Table 8.1, which compiles the characteristic parameters of all superconducting films reported in this study. In sample MoGe-II, prepared using the same method, the square ADs form a centered rectangular 2D Bravais lattice, obtained by displacing every row by one half of the repetition length in its own direction and by a full length in the orthogonal direction. The side of the square antidots is $\beta = 2$ μm , and the lattice parameters of the pattern is $\alpha_1 = 3$ μm and $\alpha_2 = 6$ μm .

Samples Nb-I and Nb-II are thin films grown at room temperature by dc-magnetron sputtering on Si/SiO₂ substrate, with a base pressure in the low 10^{-8} mbar regime and sputtering Argon pressure of $1 \cdot 10^{-3}$ mbar. Both have square lattices ($\alpha = 4$ μm) of ADs, with edges of 1.5 μm for the squares in Nb-I as well as for the triangles in Nb-II. The sample Nb-III, with thickness of 50 nm, was deposited also by dc-magnetron sputtering

Table 8.1: Description of the investigated samples, where α is the lattice parameter; β is the antidot size; d is the thickness; l and w are the length and width of the thin film; $\xi_{GL}(0)$ is the coherence length; and $\lambda_{GL}(0)$ is the penetration depth, both at $T = 0$ K.

Parameters \ Material		a-MoGe		Nb		
		I	II	I	II	III
Lattice	Symmetry	□	▣	□	□	□
	α (μm)	1.5	3.0/6.0	4.0	4.0	4.0
AD	Shape	□	□	□	△	□○
	β (μm)	0.4	2.0	1.5	1.5	1.5
External dimensions	d (nm)	25	25	50	50	50
	l (mm)	2.6	1.0	5.0	5.0	2.5
	w (mm)	2.0	1.0	5.0	5.0	2.5
Characteristic parameters	T_c (K)	6.7	6.2	6.8	6.7	8.3
	$\xi_{GL}(0)$ (nm)	6	5	8	8	12
	$\lambda_{GL}(0)$ (nm)	517 ^a	517 ^a	132	132	92

^a Using Eq. A13 of Ref. [213], $\lambda_{GL}(0) = 517$ nm was obtained from transport measurements in a thin film without ADs.

on top of a 400 nm SiO₂ substrate also at room temperature. For this specimen, the square lattice with one half of square ADs and the other half of circular ADs was defined by electron beam lithography and subsequent reactive ion etching.

Characterization measurements were carried out in a Quantum Design MPMS-5S. The MOI technique employed relies on the Faraday effect [173] occurring in an indicator film placed on top of the superconducting specimen. The indicator used in the present work was a Bi-substituted yttrium iron garnet film (Bi:YIG) with in-plane magnetization. In all experiments, the dc magnetic field was applied perpendicular to the film plane.

Two important features influencing our choice for films of Nb and a-MoGe are the difference between the values of κ , larger for a-MoGe than for Nb, and the intrinsic pinning characteristics of each of these materials. In fact, the studied samples of a-MoGe have critical currents smaller than the corresponding values for our Nb films (e.g., $J_c \sim 2 \times 10^6$ A/cm² for Nb and $J_c \sim 0.7 \times 10^6$ A/cm² for a-MoGe at the reduced temperature $T/T_c = 0.77$ and zero applied field). Using materials with such a different properties allowed us to verify that these parameters are virtually of no relevance for our morphological studies of avalanches in films with lattices of ADs.

8.3 Results and discussions

Fig. 8.1a shows a magneto-optical image taken at $T = 4.5$ K for sample MoGe-I and then submitted to an applied dc field $H = 1$ Oe. One of the principal axes of the

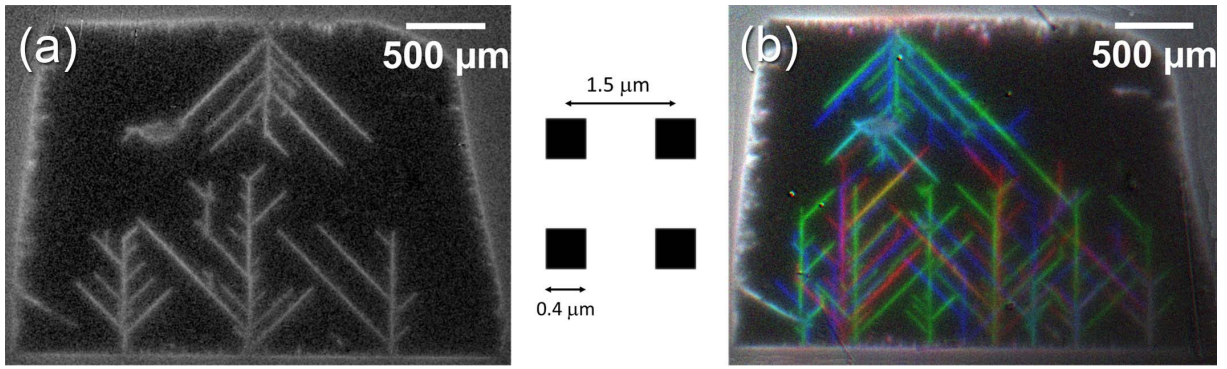


Figure 8.1: Magneto-optical images of flux penetration in MoGe-I for (a) $T = 4.5$ K and $H = 1$ Oe, applied perpendicular to the film. The image brightness is proportional to the magnitude of the local flux density. (b) Overlay of 3 repeated identical MOI experiments showing the flux penetration into the a-MoGe film, carried out at $T = 3$ K with $H = 1.4$ Oe. Each experiment is color coded in red, green and blue, thus the presence of these colors in the overlay shows that the penetration is non-reproducible.

AD lattice is aligned with the nearly parallel edges of the film. Noticeably, the main trunk of the tree-like avalanches are perpendicular to such edges, i.e., parallel to the other principal axis of the lattice, with secondary branches forming angles of 45 degrees relative to the main trunk, resembling a Christmas tree. In order to rule out the possibility of specific defects or inhomogeneities being the reason for the guided avalanches, we have routinely repeated the same experiment under identical conditions. Fig. 8.1b is an overlay of the results obtained in three different experiments, all of them carried out at $T = 3$ K with $H = 1.4$ Oe. The images are colored red, green and blue, so that overlapping penetrations in all three experiments appear as shades of gray, whereas non-repetitive flux patterns combine in color, as already shown in Fig. 3.8. Evidently, there is essentially no overlap in the dendritic flux patterns formed in the three experiments. The background flux penetration, however, is fully reproducible. Thus, we conclude that the 45-degree branches are due to the whole pinning landscape distributed in the specimen.

In order to gain more insight, we have simulated such a superconducting thin film with a square array of square ADs by using the TM model. The origin of dendritic avalanches in superconducting films is a thermomagnetic instability mechanism between the Joule heating created by vortex motion and the reduction of the critical current density as the temperature increases, as pointed out in Section 3.2.2. The instability is also a consequence of the nonlinear material characteristics of type II superconductors, which is conventionally approximated by a power law

$$\mathbf{E} = \frac{\rho_0}{d} \left(\frac{j}{j_c} \right)^{n-1} \mathbf{j}, \quad (8.1)$$

where \mathbf{E} is the electric field, \mathbf{j} is the sheet current, $j = |\mathbf{j}|$, ρ_0 is a constant with dimension

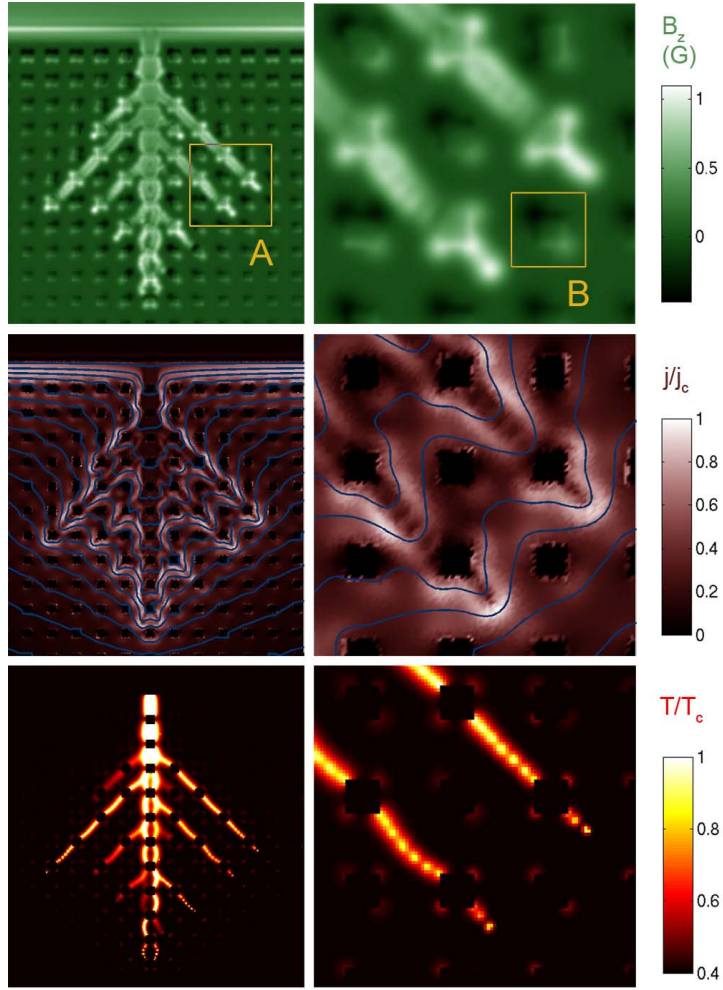


Figure 8.2: Flux avalanche in an square array of square antidots reproducing the 45 degree avalanches at $T/T_c = 0.4$ and $H = 1.1$ Oe with the typical parameters of the a-MoGe thin film. (a) Distribution of the magnetic flux density B_z , (b) the induced sheet current j/j_c , and (c) the map of reduced temperature. The numerical simulations have been done by Jørn Inge Vestgård from University of Oslo.

of resistivity, d is the sample thickness, j_c is the critical sheet current, and n is the creep exponent. In the simulations, the temperature dependencies are taken as

$$j_c = j_{c0}(1 - T/T_c), \quad n = n_1/T, \quad (8.2)$$

where T_c is the critical temperature, and j_{c0} and n_1 are constants. The electrostatics must be supplemented by the heat diffusion equation

$$c\dot{T} = \kappa_0 \nabla^2 T - \frac{h_0}{d}(T - T_0) + \frac{1}{d}jE, \quad (8.3)$$

where c is the specific heat, κ_0 is the thermal conductivity, h_0 is the coefficient for heat removal to the substrate, and T_0 is the substrate temperature. Equation (8.3) must be solved together with Maxwell's equations and the material law, Eq. (8.1). The description of the simulation method is found in Ref. [82].

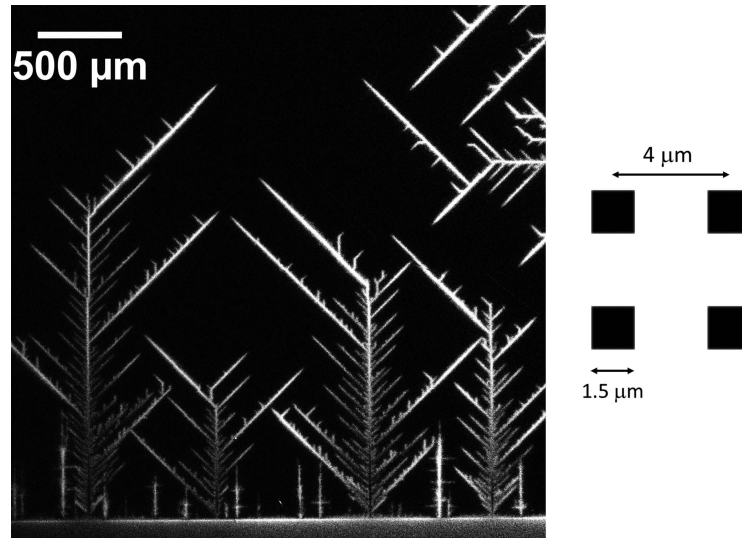


Figure 8.3: Magneto-optical image of magnetic flux penetrating into a superconducting film patterned with a square lattice of antidots (Nb-I) taken at 5 K and 2.1 Oe.

Fig. 8.2 illustrates the results of such a simulation in a film with a square array of square ADs, using material parameters typical (ρ_n , κ_0 , J_c , and T_c) of a-MoGe. The left panels (a) through (c) show a Christmas tree-like avalanche with 45-degree branches as captured by the space distribution of the magnetic field, sheet current and relative temperature. The right panels are zoomed up views of the square labeled ‘A’ in Fig. 8.2a. It is worth noticing how flux penetrates mainly in the direction along to the diagonal of the ADs. The AD marked ‘B’ on the right panel of Fig. 8.2a (not hit by the avalanche) shows that flux is pushed away from the tip, clearly delineating the 45-degree propagation tendency. The actual difference between the AD at ‘B’ and its top and left nearest neighbors is the overlay of an intense bright tone for those which lie along the avalanche path. The same trend was captured by the current streamlines in Fig. 8.2b, whose paths around the AD indicate the sources of flux/antiflux in that neighborhood and, thus, the preferential direction of the Lorentz force pushing flux along the direction parallel to the diagonal of the ADs.

A similar morphology – i.e., 45-degree branches emerging from the main trunk – was obtained for a Nb film with a square lattice of square ADs (Nb-I). Although the sizes of lattice parameters and ADs were different from those in sample MoGe-I, the overall shape of the avalanches is repeated, as shown in Fig. 8.3*. In reality, this similarity is intimately related to the shape of the ADs and the geometry of the lattice, as one can infer not only from the reasoning presented when we discussed details of Fig. 8.2. An

*This image was awarded the 1st Prize of the *Photography – Science and Arts Award* (2011) in the category *Photomicrography – special lenses, microscopes* of the Brazilian National Research Council (CNPq).

samples, positioned in such a way as to form a closed superconducting loop. The case of an AD surrounded by superconducting material is sketched in Fig. 8.4b, where four 90-degree bridges – one in each quadrant – were juxtaposed. The streamlines are closed loops of screening currents around the AD (disregarding the screening current component around the sample). The red dashed line represents the middle current streamline and shows clearly the current crowding near the corners. If magnetic flux reaches such a central portion of the sample coming from an edge (not shown in the sketch), entering the AD as a consequence of the local magnetic pressure, it will leave the AD as in the current crowding effect experiment reported in Ref. [223], i.e., entering the superconducting microstrip

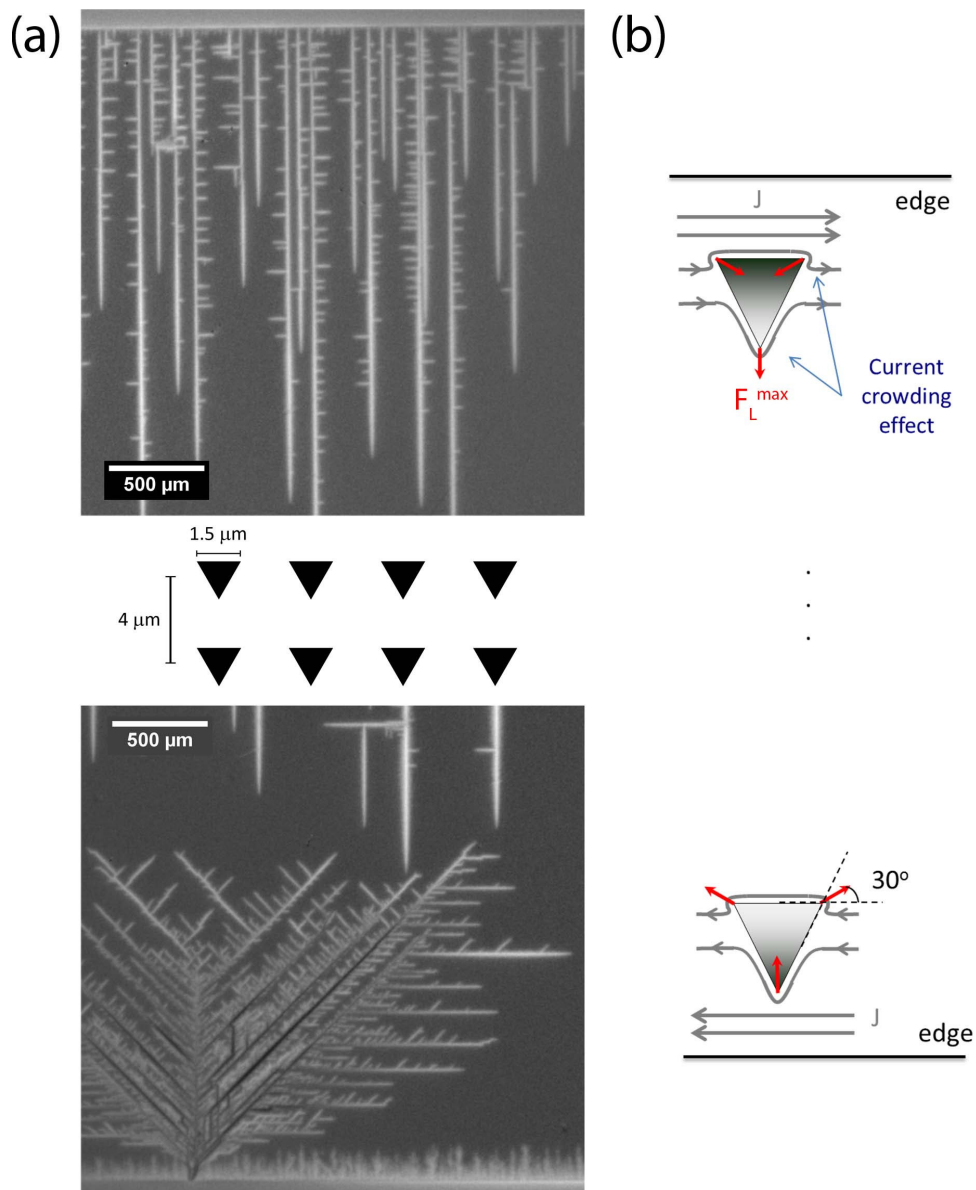


Figure 8.5: (a) MO image taken from the thin film Nb-II at $T = 3$ K and $H = 3$ Oe which shows the anisotropic penetration of the flux avalanches in a sample with a lattice of triangular ADs, arranged as shown between the MO images. (b) Total screening current around a triangular AD in the top and the bottom edges. The red arrows indicate where the Lorentz force is maximum.

preferentially through the inner concave angle. Moreover, in a superconducting film with an array of ADs, the total current flow splits around the AD, leading to current crowding effects on the AD corners. Then a maximum Lorentz force (F_L^{max}) occurs on them with the direction depicted by the red arrows in Fig. 8.4c. Regarding the avalanche evolution, Fig. 8.4d represents the evolution of the main trunk and 45-degree ramifications in a sample with a square array of square ADs, as a consequence of the current crowding effects which results in a maximum Lorentz force at the corners of the square AD. In addition, the main trunk develops mainly due to screening currents parallel to the sample edge which circulate throughout the film and push the flux toward the center of the sample.

To emphasize the role of the lattice symmetry and antidot geometry on the path followed by the avalanches, Fig. 8.5 presents MO images of avalanches in a film with a square lattice of triangular ADs (Nb-II). Since the lateral dimensions of this film is too large to be seen in full on the field of view of the microscope, we show two pieces of a single image: when facing directly the tip of the triangular ADs (bottom edge of the figure), avalanches entered the film in the form of Christmas tree (like in Fig. 8.3 for square ADs); however, they look very different – i.e., straight finger-like trunks with 90-degree secondary branches – when invading the film from the opposite edge, i.e., flowing against the edge of the triangular ADs. The tip of the triangular AD induces this finger pattern due to the current crowding effect, as illustrated in Fig. 8.5b and discussed above for the

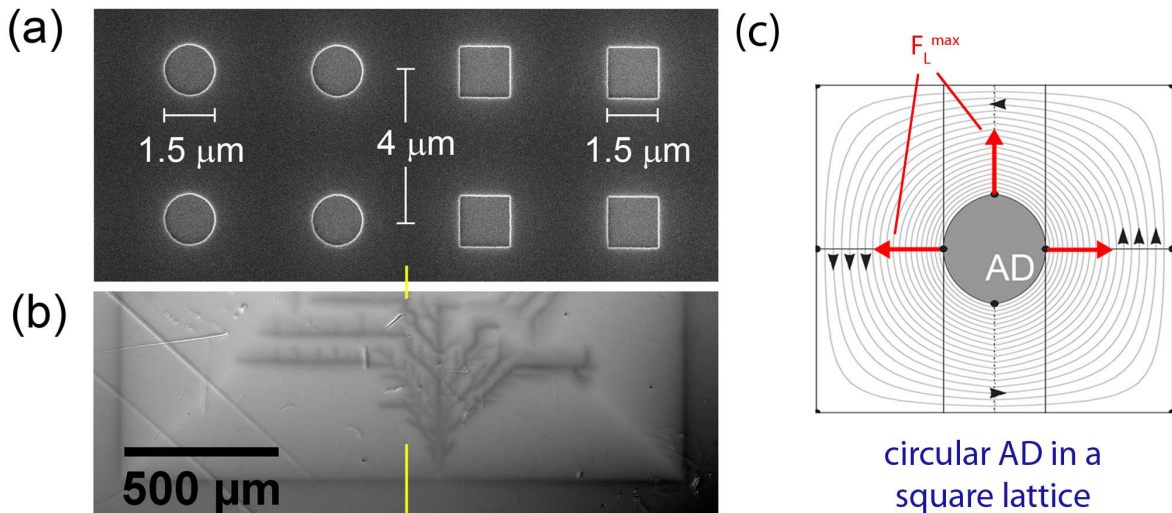


Figure 8.6: (a) Scanning electron microscope image from the sample Nb-III which shows half square ADs and half round ADs. (b) Image taken at $T = 6$ K and $H = 14$ Oe after increasing up the magnetic field to 48 Oe. The yellow lines are guides to the eye and indicate the boundary between the square and circular antidots. (c) Circular AD and its screening current in a square lattice. The red arrows indicate where the Lorentz force is maximum.

square AD. Nonetheless, the effect of the lattice symmetry on the avalanche morphology appears in the 45-degree secondary branches on the bottom edge. After entering the AD, flux has the tendency of initially leaving it from the triangle base at 30 degrees from the sample edge (maximum Lorentz force), propagating to the next triangle tip located diagonally to it and, consequently, creating the 45-degree branches. Thus, there is an interplay between the AD shape and the lattice symmetry.

Another very suggestive observation which also emphasizes the role of AD geometry on the morphology of avalanches is shown in Fig. 8.6a, taken on sample Nb-III when the applied field was decreasing. The sample has circular ADs on the left side and square ADs on the right, as illustrated in panel (a). Panel (b) shows a flux avalanche triggered on the square AD half of the sample, with 45 degree branches. When branches on the left side of the main trunk reach the circular ADs, the ramifications modify their directions (due to the new AD geometry) and follow a finger-like pattern (on the left of the yellow line), with some small 90-degree branches. Fig. 8.6b shows the screening currents around a circular AD. In principle, there is no preferential direction, however, due to the symmetry of the square lattice the current streamlines at 45 degrees becomes farther than the vertical and horizontal directions, privileging these directions to be followed by flux during an avalanche.

As a final example of how symmetry and geometry combine to form the avalanche morphology, Fig. 8.7 presents avalanches occurring on sample MoGe-II, for which the AD lattice consists of a centered rectangular 2D Bravais lattice, constructed by displacing

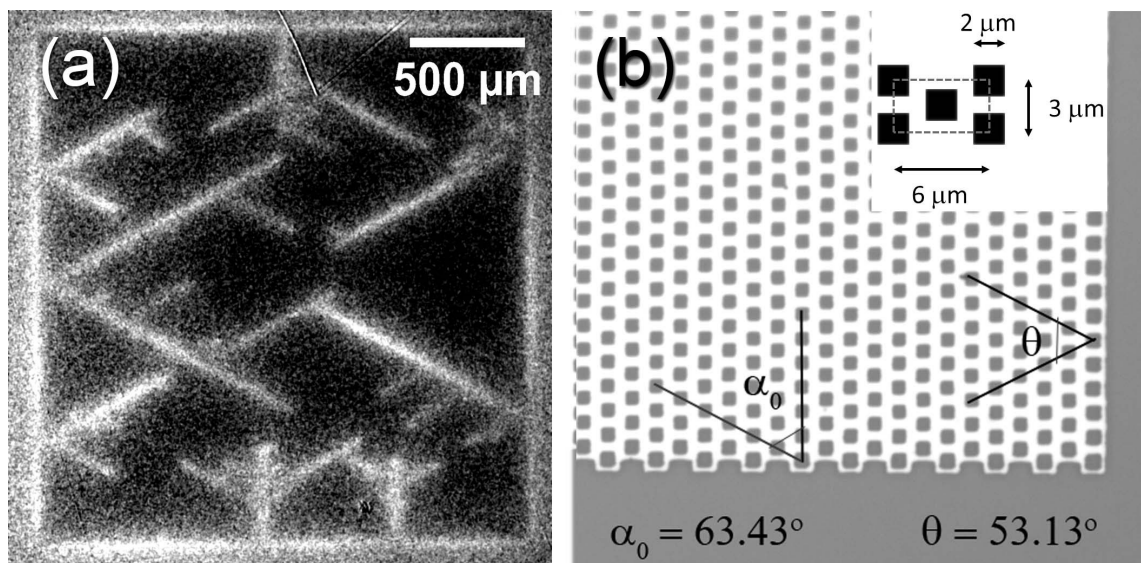


Figure 8.7: (a) MO image taken at 3 K and 1 Oe for the MoGe-II thin film. (b) Optical image shown the centered rectangular lattice and the nominal angles of 63.43° and 53.13°.

every row by one half of the repetition length in its own direction and by a full length in the orthogonal direction. Shown in Fig. 8.7b are two edges of the sample, the lower one evidencing the effect of the shift needed to create the centered rectangular lattice. In view of the knowledge acquired with the systems already discussed, one would expect the avalanches to follow the angles α_0 and θ , which is actually the case: taking 20 branches following angle α_0 and 14 following θ , the average values obtained were $\alpha_0 = (62 \pm 2)^\circ$ and $\theta = (54.0 \pm 1.3)^\circ$, both comparable, within experimental error, with the nominal values of 63.43° and 53.13° , respectively.

8.4 Conclusions

In summing up, we have employed MOI to visualize the occurrence of flux avalanches in superconducting films of crystalline Nb and amorphous a-MoGe. For specimens decorated with square antidots arranged in a square lattice, avalanches have the form of trees where the main trunk is perpendicular to the sample edge, with branches forming an angle of 45 degrees with the main axes of the antidot lattice. The overall features of the avalanches, and in particular the 45-degree direction of the branches, were confirmed by numerical simulations using the TM model. Besides, the habit of growing like a tree with inclined branches can be explained as a consequence of the so-called current crowding effect in superconducting corner-shaped microstrips, which makes flux penetration easier from the concave (inner) than from the convex (outer) angle. By choosing to study films of Nb and a-MoGe, we were able to conclude that, although strongly dependent on the lattice symmetry and antidot geometry, the avalanche morphology is not sensitive to specific characteristics of the superconducting material, such as κ or the intrinsic pinning capability.

9 *Conclusions and perspectives*

In the present thesis we have studied instabilities of thermomagnetic origin in the vortex matter of type II superconductors. Several Nb and a-Mo₇₉Ge₂₁ superconducting thin films with arrays of antidots were prepared by means of electron beam lithography. A detailed investigation of the flux avalanches and their morphology in this structured thin films have been investigated by magneto-optical imaging, dc magnetization and ac susceptibility.

In the first chapter of results, the signature of flux avalanches in both components of the ac susceptibility is explored. Magneto-optical images have confirmed the reentrant behavior in χ as an effect of the flux avalanche activity, as well as the reuse of the channels created by the ac field in a nearly constant response that occurs before the reentrance. The signature of the flux avalanche in ac susceptibility versus ac field amplitude curves has been identified as a noisy behavior of such curves. As a consequence, the critical current density versus temperature obtained from these curves shows two behaviors: a smooth power law, compatible with the Bean model and, below a certain temperature a noisy response. By employing these criteria for determining the border of the regime where flux avalanches occur, we could map the onset temperature for a range of dc applied magnetic fields. Thus, we could identify the threshold value of J_c to trigger the flux avalanches, which surprisingly at a first sight, is constant. This striking behavior of the threshold J_c to trigger flux avalanches is related to the existence of an upper limit described by the thermomagnetic model. Above J_c^{th} , the critical flux penetration depth is larger than the half-width of the sample, and the superconductor is stable. When $l^* = w$, at this limit, thermomagnetic instabilities trigger flux avalanches.

The effect of modifying the geometric parameters of the landscape of arrays and of ADs was addressed in the second half of the results. The introduction of these arrays enhances the critical current density, but also increases the flux avalanche activity for higher temperatures and applied magnetic fields. However, only random distribution and uniform distribution of pinning centers have been described in literature. We have found that a graded distribution of ADs shows an enhancement of the properties compared to

a uniform one. An increase of the critical current density is verified in the region of low fields and the flux avalanche activity is reduced for lower temperatures and magnetic fields. Furthermore, the landscape of pinning centers also produces interesting morphology in the flux avalanches. A thin film with a square array of square antidots have shown avalanches with a main trunk perpendicular to the edge and branches at 45 degrees, like a Christmas tree, for superconducting thin films so diverse as crystalline Nb and amorphous $\text{Mo}_{79}\text{Ge}_{21}$. The overall characteristics of the avalanches were reproduced by numerical simulations using the TM model. These rich and geometry-dependent morphologies of the flux avalanches are a consequence of current crowding effects in the corners of the antidots, as shown in detail in the Appendix B for aluminum L-shaped stripes.

Further work would be useful in order to expand our knowledge about the effects of ac fields on the occurrence of flux avalanches. The ac susceptibility response where the flux avalanche signature takes place should be explored further, especially the region where the diamagnetism is reinforced. In addition, the effect of an ac excitation field superimposed to a dc field in the avalanche regime can be investigated by MOI. Moreover, the mechanism responsible for increasing the critical current in samples with a graded array of ADs still lacks in the literature. Thus, more samples and more gradients types should be explored in order to understand those effects. Finally, the role of the superconducting lengths such as the penetration length – or, more likely, the effective penetration length – should be established in order to shed more light on the current understanding of flux avalanche morphologies.

APPENDIX A – Shape and profile studies of antidots in decorated thin films

The shape and the profile of the antidots have been performed in the decorated thin films studied here, using optical microscopy, SEM and AFM. In this appendix, images of the samples of crystalline Nb and amorphous MoGe, both with ADs of $0.4 \mu\text{m}$ in a square lattice of $1.5 \mu\text{m}$ are shown in an attempt to determine the role of the AD geometry in the avalanche morphology. The antidots in the a-MoGe film are squares with sharp edges, whereas in the Nb film they are rounded. Besides, the AD shape of the specimens Nb-AD08 and a-MoGe-UNI are also discussed. These findings represent important information to be taken into account in our discussions regarding avalanche morphology in the main chapters of this thesis.

Before our observation of the Christmas-tree morphology of the flux avalanches in the a-MoGe film with ADs of $0.4 \mu\text{m}$ in a square lattice of $1.5 \mu\text{m}$, shown in Chapter 8 and in the right inset in Figure A.1, Vlasko-Vlasov *et al.* [112] and Menghini *et al.* [110] have reported that the flux avalanches in thin films with arrays of ADs develops with 90-degree branching. They concluded that there is a strong interaction between the flux avalanche and the underlying antidots lattice. In this thesis, this morphology has been also observed in the decorated Nb films presented in Chapter 5. In order to shed light on the aspects which lead to the 45-degree branching of the flux avalanches in the a-MoGe film, an extensive study using optical microscopy, AFM and SEM was carried out firstly on the edges of the samples and then on the shape and the profile of the antidots.

The edges of the samples were imaged by using optical microscopy (not shown). No relation could be established between the spatial quality of the edges and the avalanche morphology, since both, sharp and broken edges, show avalanches with the same shape (see, for instance, the top (broken) and bottom edges of the sample shown in Fig. 8.1a). The only difference from edge to edge is related to the field value to trigger avalanches, which depends on the existence of defects near or at the sample edge [108]. One can then

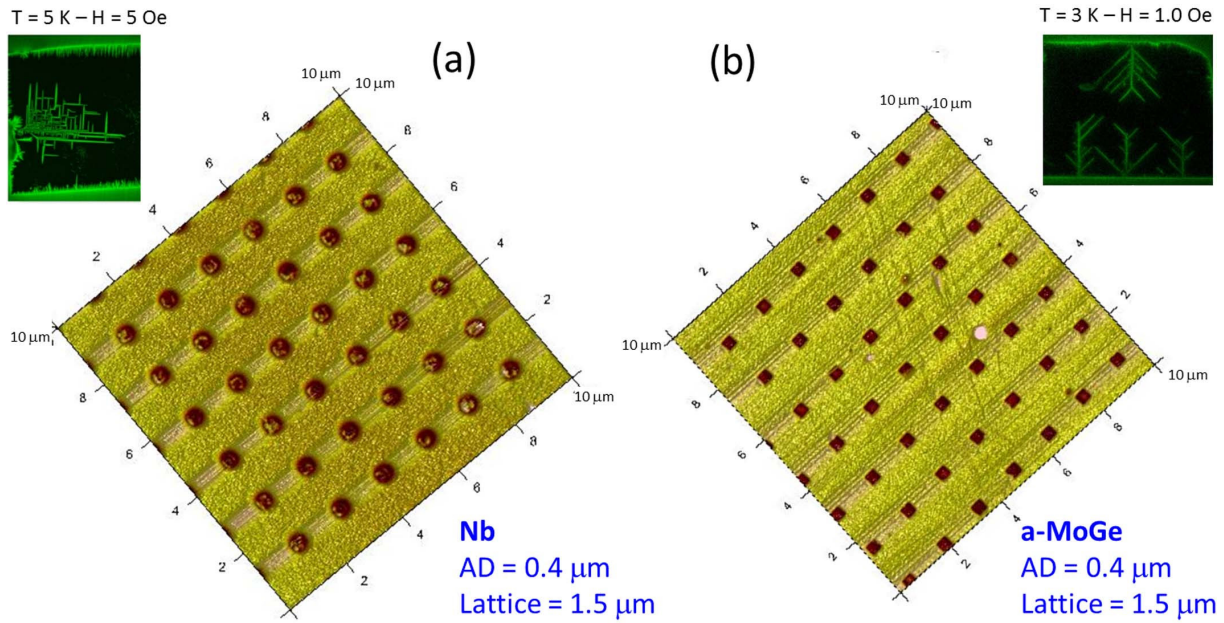


Figure A.1: Atomic force microscopy images of the two decorated thin films with AD of $0.4 \mu\text{m}$ in a square lattice of $1.5 \mu\text{m}$: (a) Nb and (b) a-MoGe. The left inset shows an MO image taken at $T = 5 \text{ K}$ and $H = 5 \text{ Oe}$ of the Nb-AD04 sample and the right inset shows an MO image taken at $T = 3 \text{ K}$ and $H = 1 \text{ Oe}$ of the a-MoGe film.

infer that the avalanche morphology is strongly influenced by the geometric aspects of the mesh of ADs in the sample, namely, the lattice symmetry and the AD shape.

Thus, a careful investigation of the lattice and AD geometry was carried out. The images were taken, at least, in five different regions of each sample: four in the center of each edge, where the avalanches are most likely to occur, and one in the center of the sample. The goal was to obtain a comprehensive map of the AD shape and lattice symmetry throughout the film. Figure A.1 illustrates AFM representative images for both samples, Nb in main panel (a) and a-MoGe in main panel (b). The ADs in sample Nb-AD04 are rounded, in clear contrast with those in the a-MoGe sample. Although the ADs in Nb-AD04 are nominally squares, in reality they are clearly rounded.

In order to complete the picture, we have also made SEM images of the films. Since the polymeric resist is sensitive to an electron beam, we have also used this technique to image the region inside the ADs, including the interface between AD and superconductor. Figure A.2 shows images for both samples: panel (a) shows the antidot landscape for the Nb-AD04 film, whereas panel (b) depicts the profile of the same three rows of ADs shown on the left panel, which one can observe that the interface between the AD and the superconductor is gradual. Figure A.2c shows square ADs for the decorated a-MoGe sample, whereas the profile shown in panel (d) indicates a sharp interface at the AD edges. Both the SEM and the AFM images furnish a consistent picture indicating that

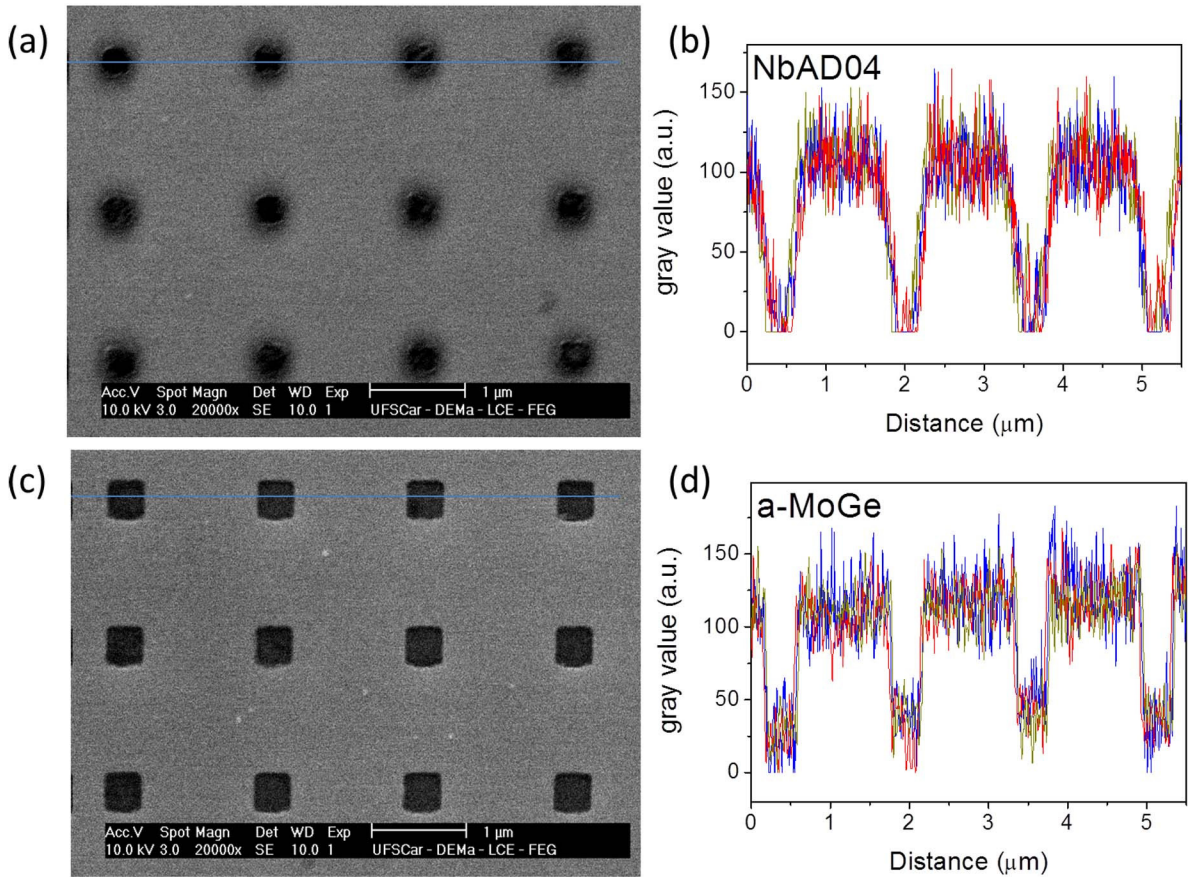


Figure A.2: Scanning electron microscopy images of the two decorated thin films with AD of $0.4 \mu\text{m}$ in a square lattice of $1.5 \mu\text{m}$: (a) Nb and (c) a-MoGe. The profiles of the three rows of ADs of the decorated Nb sample is shown in (b) and of the a-MoGe specimen in (d).

the Christmas tree avalanches are induced by the sharp corners of the ADs in the decorated a-MoGe, whereas the Nb-AD04 film present 90-degree branched avalanches due to round ADs. These findings were the main motivation for the discussions addressed in Chapter 8.

Furthermore, the specimens Nb-AD08 and a-MoGe-UNI presented in Chapter 5 and in Chapter 7, respectively, do not show a well-defined AD profile. Fig. A.3 shows AFM images and profiles for both samples. Panel (a) shows the gradual profile for Nb-AD08, which results in gradual corners. The antidots of the sample a-MoGe-UNI show a peak in one of the edges, as depicted in panel (b). This peak also appears at the same edge by rotating the sample (not shown), indicating that it is not a simple mere experimental artifact of the measurement. Both AD profiles lead to 90-degree branching in the avalanche morphology observed in these samples. Since the studies presented in Chapters 5 and 7 were not related to avalanche morphology in these samples, the fact that these samples have imperfect ADs has no impact on the results, nor on the corresponding interpretation.

In summary, these observations reinforce the notion that the avalanche morphology is

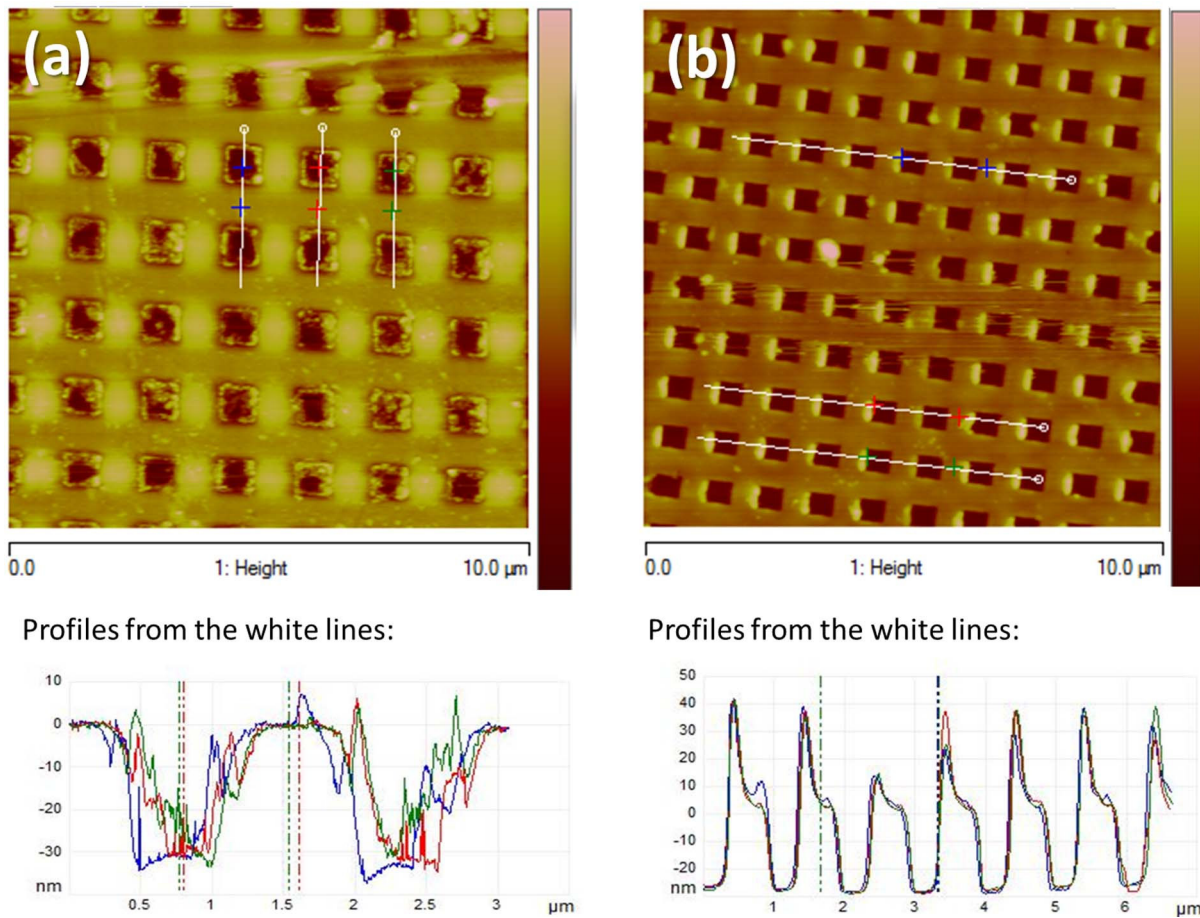


Figure A.3: Atomic force microscopy images of the samples (a) Nb-AD08 and (b) a-MoGe-UNI. The AD profiles from the white lines are shown on the bottom.

intimately dependent on the AD geometry, to an extent that the Christmas-tree pattern occurs only if the square ADs on a square lattice have well defined tips and sharp edges.

*APPENDIX B – Current crowding effects in superconducting corner-shaped Al microstrips**

The superconducting critical current of corner-shaped Al superconducting microstrips, has been investigated. We demonstrate that the sharp turns lead to asymmetric vortex dynamics, allowing for easier penetration from the inner concave angle than from the outer convex angle. This effect is evidenced by a rectification of the voltage signal otherwise absent in straight superconducting strips. At low magnetic fields, an enhancement of the critical current with increasing magnetic field is observed for a particular combination of field and current polarity, confirming a theoretically predicted competing interplay of superconducting screening currents and applied currents at the inner side of the turn.

B.1 Introduction

The ability of superconductors to carry electricity without resistance holds in a restricted current density range $J < J_{max}$. Several physical mechanisms can be identified as responsible for determining J_{max} such as the presence of pinning centers, the edge or surface barriers for vortex penetration or eventually when the pair-breaking current, J_{pb} , is reached.

In principle, it is possible to attain the ultimate limit $J_{max}=J_{pb}$ by properly choosing the dimensions of the superconducting strip. Indeed, if the width w of the strip is such that $w < 4.4\xi$, where ξ is the coherence length, vortices cannot fit into the sample [224] and therefore J_{max} cannot be limited by a vortex depinning process. In 1980 Kupriyanov and Lukichev [225] were able to determine theoretically J_{pb} for all temperatures, by solving

*Appendix based on: O.-A. Adami, D. Cerbu, D. Cabosart, M. Motta, J. Cuppens, W. A. Ortiz, V. V. Moshchalkov, B. Hackens, R. Delamare, J. Van de Vondel, A. V. Silhanek. Current crowding effects in superconducting corner-shaped Al microstrips, Appl. Phys. Lett. 102, 052603 (2013).

the Eilenberger equations, and only two years later their predictions were experimentally confirmed by Romijn *et al.* [226] using *straight* Al strips. These works focused on the case where $w \ll \Lambda$, with $\Lambda = 2\lambda^2/d$ the Pearl length [66], λ the London penetration depth, and d the thickness of the superconductor.

Recently a renewed interest for understanding the limiting factors of J_{max} in *non-straight* strips has arisen, partially motivated by the ubiquitous presence of sharp turns in more realistic architectures as those used in the superconducting meanders for single photon and single electron detectors [227, 228, 229].

Early theoretical calculations by Hagerdorn and Hall [230] showed that a sharp bend in a superconducting wire leads to current crowding effects at the inner corner of the the bend, which in turn reduces the total critical current when compared to a straight wire. Not only sharp angles along the superconducting bridge, but any sudden change in the cross section of the wire, can lead to a reduction of the critical current. For instance, it has been pointed out in Ref. [231] that a sudden increase in the cross section of a transport bridge leads to severe modifications of the voltage-current characteristics rendering unreliable those measurements performed in cross-shaped geometries. More recently, Clem and Berggren [222] have theoretically demonstrated that sudden increases in the cross section of a transport bridge, as those caused by voltage leads, also produce current crowding effects and the consequent detriment of the critical current, similarly to right-angle bends. These predictions have been independently confirmed experimentally by Hortensius *et al.* [232] and by Henrich *et al.* [233] in submicron scale samples of NbTiN and NbN, respectively, and found to be also relevant in larger samples [234].

The effect of a magnetic field applied perpendicularly to the plane containing the superconducting wire with a sharp turn has been discussed in Ref. [232] and Ref. [235]. Strikingly, in Ref. [235] it is theoretically predicted that due to compensation effects between the field induced stream-lines and the externally applied current at the current crowding point, the critical current of thin and narrow superconducting bridges ($\xi \ll w \ll \Lambda$) should *increase* with field for small fields values and for a particular polarity of the applied field.

In this work we provide experimental confirmation of the theoretical predictions of Ref. [235] and show that current crowding leads also to a clearly distinct superconducting response for positive and negative fields (or currents), making these asymmetric superconducting nanocircuits potentially voltage rectifiers.

B.2 Samples and experimental techniques

The samples investigated were all co-fabricated on the same chip and consist of electron-beam lithographically defined Al structures of thickness $d = 67 \pm 2$ nm, deposited by rf sputtering on top of a Si/SiO₂ substrate. We focus on two different geometries. Sample S90 consist of a 3.3 μm wide transport bridge with a 90° corner equidistant from two voltage probes separated 9.6 μm from the inner angle of the sharp bend. Similarly, S180 is a conventional straight transport bridge 3.7 μm wide and with voltage probes separated by 20.9 μm . These dimensions depart from the nominal values and were obtained via atomic force microscopy as shown in Fig. B.1a-b. For all samples we found a residual resistivity ratio, $\rho(2\text{ K})/\rho(300\text{ K})$, between 2.2 and 2.5.

The field dependence of the superconducting-to-normal metal transitions, $T_c(H)$, determined as $0.95R_N$, where R_N is the normal state resistance, and using an ac-current* of 1 μA , is basically the same for the two samples studied (see Fig. B.1c). This similarity of the phase boundaries allows us to make reliable and direct comparisons between the two samples without the necessity to work with reduced temperatures or field units. The critical temperature at zero field is $T_{c0} = 1.320 \pm 0.008$ K and the superconducting coherence length obtained from the Ginzburg-Landau approximation is $\xi(0) = 121 \pm 3$ nm. The BCS coherence length for Al of similar characteristics [226] (T_{c0} and d) as the one used here is $\xi_0 = 1320$ nm, indicating that our Al falls in the dirty limit $\ell \ll \xi_0$, with ℓ the electronic mean free path. Using the relation $\xi(0) = 0.855\sqrt{\xi_0\ell}$ we deduce $\ell \sim 15$ nm. An independent estimation of $\ell \sim 17$ nm can be obtained from the normal state resistivity $\rho = 2.0 \pm 0.1 \cdot 10^{-8}$ Ωm , and taking [226] $\rho\ell = 4 \cdot 10^{-16}$ Ωm^2 . In the dirty limit the magnetic penetration depth is given by $\lambda(0) = \lambda_L(0)\sqrt{\xi_0/\ell} \approx 145$ nm, where $\lambda_L(0) = 16$ nm is the London penetration depth. For thin film geometry with a perpendicular external field we need to use the Pearl length [66] $\Lambda = 2\lambda^2/d$. In the considered samples $\Lambda > 2w$ for $T > 1.19$ K.

B.3 Results and discussion

Let us now concentrate on the current-voltage characteristics, $V(I)$, of the considered systems. At zero external field, the $V(I)$ curves and, in particular the critical current, I_c , should be uniquely defined, irrespective of the direction of the applied current. This

*The transport measurements have been done with the sample immersed in superfluid ⁴He for minimizing heating effects. Special care has been taken to avoid the high frequency noise signal (above ~ 1 MHz) by using a pi-filter.

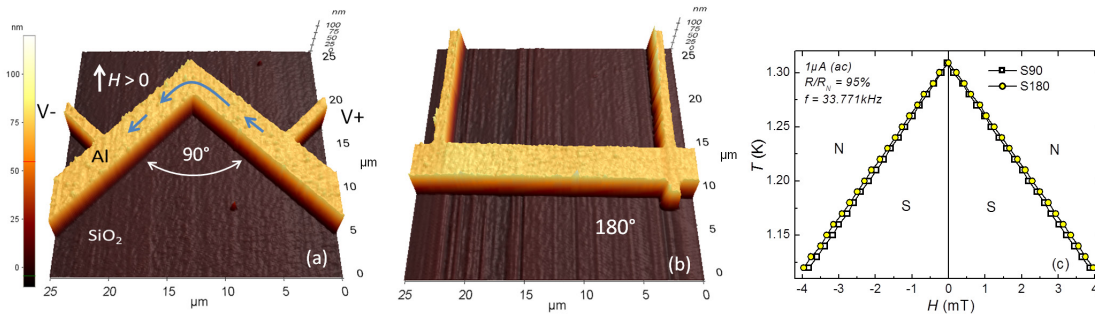


Figure B.1: Atomic force microscopy images of the two superconducting Al bridges studied: (a) S90, and (b) S180. Panel (c) shows the superconducting(S)-normal(N) HT phase diagrams for both samples

independence on the direction of the current persists at all fields for the S180 sample, but does not hold for the S90 sample. Indeed, on the one hand, the outer angle of the sharp corner has a larger surface nucleation critical field H_{c3} (a factor ~ 1.16 higher for the S90) when compared to the critical field at the inner corner [236] thus making the outer corner a point of enhanced superconductivity [228, 229]. On the other hand, stream-lines of the applied current tend to conglomerate at the inner corner [230], depleting the order parameter at that place. Notice that both effects, larger surface nucleation field and lower applied current density at the sharper corner, share the same origin in the impossibility of both, screening or applied currents, to reach the tip of the bend. It is worth mentioning that the analysis by Clem and Berggren [222] based on London equations, i.e., neglecting the depletion of the order parameter, also leads to asymmetric vortex penetration. This shows that the key ingredient for observing this effect is the current crowding at the inner corner of the bend and the consequent reduction of the Gibbs free-energy barrier against nucleation of a vortex.

The reduction of the surface barrier for vortex penetration [222, 235] together with an applied current such that the Lorentz force pushes vortices from the inner towards the outer corner, corresponds to the onset of dissipation. However, if the current is reversed, vortices will not penetrate from the outer corner (where total current is nearly zero) but rather symmetrically from the straight legs of the bridge [235]. As a consequence of this different nucleation position and nucleation condition for the two opposite current directions, it is predicted that such a simple corner shape wire will give rise to asymmetric $V(I)$ characteristics and therefore to a vortex ratchet effect.

In order to demonstrate the existence of vortex motion rectification we submitted the samples to an ac current excitation of zero mean, I_{ac} , while measuring simultaneously the dc drop of voltage V_{dc} . The results of these measurements $V_{dc}(I_{ac})$ are presented in Fig. B.2 for both samples. The chosen temperature $T = 1.22$ K is such that $4.4\xi = 1.9 \mu\text{m}$

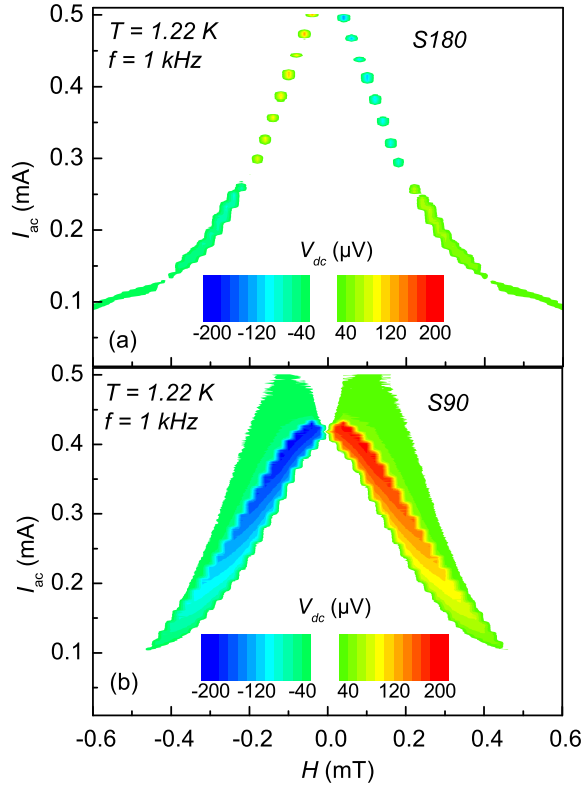


Figure B.2: Contour plot of the dc voltage $V(dc)$ as a function of magnetic field and ac current amplitude at $T = 1.220 \text{ K}$, and frequency of 1 kHz for sample S180 (a) and sample S90 (b).

$\langle w = 3 \mu\text{m} < \Lambda = 8.3 \mu\text{m}$ ensuring the existence of vortices within the superconductor. There are several points that deserve to be highlighted here, (i) rectification effects are almost completely absent in the S180 sample, (ii) there is a very strong ratchet signal for the S90 sample, (iii) the ratchet signal changes polarity at zero field. Ideally, we expect no ratchet effect at all from the S180 sample, however, the fact that both voltage contacts are on the same side of the strip already impose a weak asymmetry in the system which can lead to asymmetric vortex penetration [237, 238]. In any case, the rectification signal obtained in the S180 sample is negligible in comparison to that observed in the sample with the sharp turn. The fact that the rectification signal is positive at positive fields for the S90 sample, and according to the sign convention depicted in Fig. B.1a, we conclude that the easy direction of vortex flow is from the inner corner towards the outer corner, in agreement with the theoretical findings [235]. In Fig. B.3 we show how the ratchet signal progressively disappears as the temperature approaches 1.280 K . For temperatures above this value vortices cannot fit anymore in the bridge and consequently the difference between the two corners vanishes. Similar ratchet effects due to surface barrier asymmetry, have been recently reported [239] in high- T_c superconducting asymmetric nanobridges,

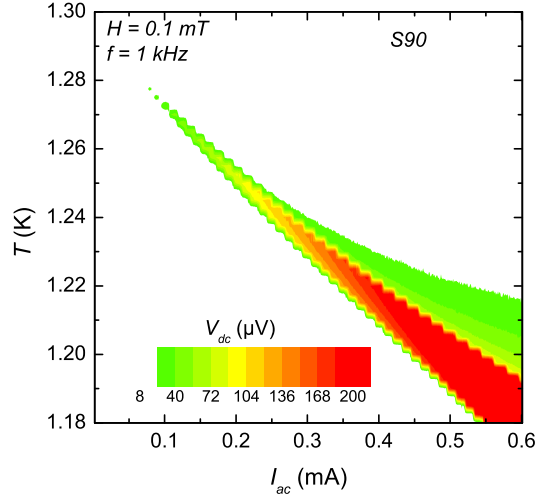


Figure B.3: Contour plot of the dc voltage $V(dc)$ as a function of temperature and ac current amplitude at $H = 0.1$ mT, and frequency of 1 kHz for the sample S90.

with one side straight and the other having a constriction with an angle of 90° .

Notice that the ratchet effect here described results from the crowding of the applied current at the inner corner, and it would exist even if no screening currents were present. Let us now consider the additional effect of the screening currents. As it has been pointed out in Ref. [235] based on both, London and Ginzburg-Landau theories, for a given direction of the applied current (as indicated in Fig. B.1a) a positive magnetic field will reinforce the total current (i.e., applied plus screening) at the inner corner and therefore the critical current will decrease as the field intensity increases. On the contrary, a negative applied magnetic field will induce a screening current which partially compensates the applied current at the inner corner and a field dependent increase of the critical current is expected [235]. We have experimentally confirmed this prediction by measuring the critical current using a voltage criterion of $1 \mu\text{V}$ as a function of field and current orientation. The results are presented in Fig. B.4a for three different temperatures and for the case where $\xi < w < \Lambda$. For positive current and field (as defined in Fig. B.1a), we observe a monotonous decrease of I_c . In contrast to that, for positive current and negative field, a clear enhancement of I_c with field is observed for $H < H_{max}$, whereas for $H > H_{max}$ a monotonous decrease of I_c is recovered as a consequence of antivortices induced by the magnetic field [235] that start to penetrate the sample. Reversing the applied current should lead to the opposite behavior, as indeed observed in Fig. B.4a. This double test for all polarities of current and field also permits us to accurately determine the value of zero external field at the point where

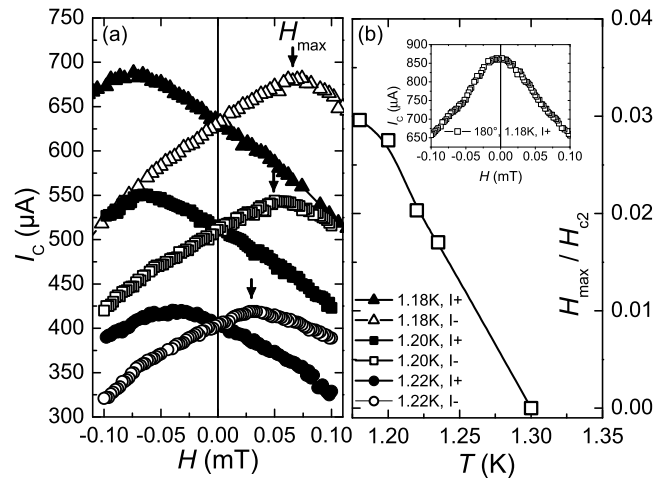


Figure B.4: The critical current I_c of sample S90 as a function of applied magnetic field for both polarities of the applied current (a). Panel (b) shows the maximum field H_{max} (normalized to the critical magnetic field H_{c2}) as a function of temperature. The inset in (b) shows for comparison the critical current of sample S180 versus magnetic field at positive applied currents.

both curves cross each other. This has been convincingly confirmed by independent measurement of the remanent field in the S180 sample. For the sake of comparison, in the inset of Fig. B.4b we show the critical current for the S180 sample as a function of field. Notice that for this sample, the peak of maximum critical current is located at $H = 0$, in contrast to the behavior observed in sample S90. It is important to point out that in Ref. [235] the theoretical prediction of the curves in Fig. B.4a corresponds to a sharp inverted-V shape according to the London model, whereas the Ginzburg-Landau calculations yield a rounded top, which becomes sharper the smaller the ratio of ξ to w . This effect appears to be confirmed, at least qualitatively, in Fig. B.4a, in which the peaks become more rounded as the temperature increases and ξ increases.

The compensation field H_{max} is expected to depend on temperature since it is determined by the screening currents. In Fig. B.4b we plot the temperature dependence of $H_{max}/H_{c2}(T)$ where it can be noticed that this compensation field H_{max} is a small fraction of the upper critical field $H_{c2}(T)$ in agreement with the theoretical calculations [235].

B.4 Conclusions

To summarize, the superconducting properties of corner-shaped Al microstrips have been investigated. We show that sharp 90 degrees turns lead to asymmetric vortex

penetration, being easier for vortices to penetrate from the inner side than from the outer side of the angle. We provide experimental confirmation of the predicted [235] competing interplay of superconducting screening currents and applied currents at the inner side of the turn. We prove that current crowding leads to a distinctly different superconducting responses for positive and negative fields (or currents). These effects are evidenced also by a field dependent critical current enhancement and also by a strong rectification of the voltage signal, thus making these asymmetric superconducting nanocircuits to act as voltage rectifiers. Complementary measurements done in samples with 30° and 60° corners (not shown) reproduce the results presented here, i.e., ratchet signal and field-induced increase of critical current.

A substantial part of the technological implications of our observations, directly concerning the architecture used in superconducting single photon detectors, has been already pointed out in the discussions of Ref. [235]. However, there are at least two more important consequences that we should mention. Firstly, the rectification effect resulting from the reduction of the energy barrier for vortex entrance implies that the commonly used transport bridge geometry with two voltage probes on one side will give rise to (unwanted) rectification signals. This effect has been largely ignored in most of the reports concerning vortex ratchet, and deserves a more in-depth experimental study. Secondly, the current crowding effects likely play a key role in understanding the puzzling morphology of flux avalanches in nanostructured superconducting films as reported in Ref. [212, 221, 240].

List of Publications

- M. Motta, F. Colauto, R. Zadorosny, T. H. Johansen, R. Dinner, M. G. Blamire, G. Ataklti, V. V. Moshchalkov, A. V. Silhanek, and W. A. Ortiz, *Visualizing the ac magnetic susceptibility of superconducting films via magneto-optical imaging*, Phys. Rev. B **84**, 214529 (2011).
- M. Motta, F. Colauto, W. A. Ortiz, J. I. Vestgård, T. H. Johansen, J. Cuppens, V. V. Moshchalkov, and A. V. Silhanek, *Anomalous flux avalanche morphology in a-MoGe superconducting film with a square antidot lattice - experiment and simulation*, arXiv:1109.2532 (2011).
- M. Motta, F. Colauto, T. H. Johansen, R. Dinner, M. G. Blamire, G. Ataklti, V. V. Moshchalkov, A. V. Silhanek, and W. A. Ortiz, *Flux avalanches triggered by AC magnetic fields in superconducting thin films*, Physica C **479**, 134 (2012).
- R. Zadorosny, F. Colauto, M. Motta, T. H. Johansen, R. Dinner, M. G. Blamire, G. Ataklti, V. V. Moshchalkov, A. V. Silhanek, and W. A. Ortiz, *Morphology of Flux Avalanches in Patterned Superconducting Films*, J. Supercond. Nov. Magn. **26**, 2285 (2013).
- O.-A. Adami, D. Cerbu, D. Cobosart, M. Motta, J. Cuppens, W. A. Ortiz, V. V. Moshchalkov, B. Hackens, R. Delamare, J. Van de Vondel, A. V. Silhanek, *Current crowding effects in superconducting corner-shaped Al microstrips*, Appl. Phys. Lett. **102**, 052603 (2013).
- M. Motta, F. Colauto, W. A. Ortiz, J. Fritzsche, J. Cuppens, W. Gillijns, V. V. Moshchalkov, T. H. Johansen, A. Sanchez, A. V. Silhanek, *Enhanced pinning in superconducting thin films with graded pinning landscapes*, Appl. Phys. Lett. **102** 212601 (2013); and at arXiv: <http://arxiv.org/abs/1301.6283v1> (Title: *Enhancement of pinning properties of superconducting thin films by graded pinning landscapes*).
- M. Motta, F. Colauto, J. I. Vestgård, J. Cuppens, T. H. Johansen, V. V. Moshchalkov, A. V. Silhanek, and W. A. Ortiz *Guidance and morphology of flux*

avalanches in superconducting films decorated with lattices of antidots, to be submitted to Physical Review X.

- M. Motta, F. Colauto, J. I. Vestgård, T. H. Johansen, R. Dinner, M. G. Blamire, G. Ataklti, V. V. Moshchalkov, A. V. Silhanek, and W. A. Ortiz, *Threshold critical current densities to trigger flux avalanches in superconducting thin films*, to be submitted to Superconductor Science and Technology.

Printed version on June 11th, 2013.

References

- [1] NOBELPRIZE.ORG. *All Nobel Prizes in Physics*. 2012. Disponível em: <http://www.nobelprize.org/nobel_prizes/physics/laureates/>. Acesso em: 14 Nov. 2012.
- [2] ABRIKOSOV, A. A. On the Magnetic Properties of Superconductor of the Second Group. *Soviet Physics JETP*, v. 5, p. 1174–1182, Dec 1957.
- [3] GINZBURG, V.; LANDAU, L. To the Theory of Superconductivity. *Zh. Eksp. Teor. Fiz.*, v. 20, p. 1064, 1950. English version: L. D. Landau, *Collected papers*, Oxford: Pergamon Press, 1965.
- [4] BEDNORZ, J. G.; MÜLLER, K. A. Possible high T_c superconductivity in the Ba-La-Cu-O system. *Zeitschrift für Physik B Condensed Matter*, Springer Berlin / Heidelberg, v. 64, p. 189–193, 1986. ISSN 0722-3277. Disponível em: <<http://dx.doi.org/10.1007/BF01303701>>.
- [5] SARRAO, J. *Basic research need for superconductivity*. Argonne National Laboratory, Lemont, IL (USA), 2006. Office of Science, U. S. Department of Energy (Technical Report). Disponível em: <http://www.sc.doe.gov/bes/reports/files/SC_rpt.pdf>.
- [6] COLAUTO, F. *Estudos de avalanches de vórtices em filmes supercondutores de Nb e MgB₂*. Tese (Doutorado) — Universidade Federal de São Carlos, 2008. Orientador: Prof. Dr. Wilson Aires Ortiz.
- [7] ZADOROSNY, R. *Interação da matéria de vórtices com estruturas de defeitos: detecção das primeiras penetrações*. Tese (Doutorado) — Universidade Federal de São Carlos, São Carlos, 2009. Orientador: Prof. Dr. Wilson Aires Ortiz.
- [8] OLIVEIRA, A. A. M. de. *Transição ordem-desordem da matéria de vórtices em supercondutores detectada através do terceiro harmônico da suscetibilidade ac*. Tese (Doutorado) — Universidade Federal de São Carlos, São Carlos, 2008. Orientador: Prof. Dr. Wilson Aires Ortiz.
- [9] ONNES, H. K. Sur les résistances électricitriques. *Communication from the Physical Laboratory of the University of Leiden*, Supplement 29, p. 1–11, 1911.
- [10] DELFT, D. van. *Freezing physics, Heike Kamerlingh Onnes and the quest for cold*. Amsterdam: Editora Kluwer, 2007.
- [11] MEISSNER, W.; OCHSHENFELD, R. Ein neuer Effekt bei Eintritt der Supraleitfähigkeit. *Naturwissenschaften*, v. 21, n. 44, p. 787–788, 1933. Disponível em: <<http://www.springerlink.com/content/169w054091n24j14/>>.
- [12] FORREST, A. M. Meissner and Ochsenfeld revisited. *European Journal of Physics*, v. 4, p. 117–120, 1983. Disponível em: <http://iopscience.iop.org/0143-0807/4/2/011/pdf/0143-0807_4_2_011.pdf>.

- [13] LONDON, F.; LONDON, H. The Electromagnetic Equations of the Supraconductor. *Proceedings of the Royal Society of London. Series A, Mathematical and Physical Sciences.*, v. 149, p. 71–88, 1935. Disponível em: <<http://rspa.royalsocietypublishing.org/content/149/866/71.full.pdf>>.
- [14] BARDEEN, J.; COOPER, L. N.; SCHRIEFFER, J. R. Microscopic Theory of Superconductivity. *Physical Review*, v. 108, p. 1175, 1957.
- [15] MAXWELL, E. Isotope Effect in the Superconductivity of Mercury. *Physical Review*, American Physical Society, v. 78, p. 477–477, May 1950. Disponível em: <<http://link.aps.org/doi/10.1103/PhysRev.78.477>>.
- [16] REYNOLDS, C. A.; SERIN, B.; WRIGHT, W. H.; NESBITT, L. B. Superconductivity of Isotopes of Mercury. *Physical Review*, American Physical Society, v. 78, p. 487–487, May 1950. Disponível em: <<http://link.aps.org/doi/10.1103/PhysRev.78.487>>.
- [17] POOLE-JR., C. P.; FARACH, H. A.; CRESWICK, R. J.; PROZOROV, R. *Superconductivity*. Second edition. The Netherlands: Academic Press, 2007. 646 p.
- [18] NORMAN, M. R. The Challenge of Unconventional Superconductivity. *Science*, v. 332, n. 6026, p. 196–200, 2011. Disponível em: <<http://www.sciencemag.org/content/332/6026/196.abstract>>.
- [19] STEWART, G. R. Superconductivity in iron compounds. *Rev. Mod. Phys.*, American Physical Society, v. 83, p. 1589–1652, Dec 2011. Disponível em: <<http://link.aps.org/doi/10.1103/RevModPhys.83.1589>>.
- [20] WU, M. K.; ASHBURN, J. R.; TORNG, C. J.; HOR, P. H.; MENG, R. L.; GAO, L.; HUANG, Z. J.; WANG, Y. Q.; CHU, C. W. Superconductivity at 93 K in a new mixed-phase Y-Ba-Cu-O compound system at ambient pressure. *Physical Review Letters*, American Physical Society, v. 58, p. 908–910, Mar 1987. Disponível em: <<http://link.aps.org/doi/10.1103/PhysRevLett.58.908>>.
- [21] GORTER, C. J.; CASIMIR, H. On Supraconductivity I. *Phys. Z.*, v. 35, p. 963, 1934.
- [22] ASHCROFT, N. W.; MERMIN, M. D. *Solid State Physics*. [S.l.]: Holt, Rinehart and Winston, 1970.
- [23] PIPPARD, A. B. An Experimental and Theoretical Study of the Relation between Magnetic Field and Current in a Superconductor. *Proceedings of the Royal Society of London. Series A. Mathematical and Physical Sciences*, v. 216, n. 1127, p. 547–568, 1953. Disponível em: <<http://rspa.royalsocietypublishing.org/content/216/1127/547.abstract>>.
- [24] LANDAU, L. D. *Physikalische Zeitschrift der Sowjetunion*, v. 11, p. 26–47/545–555, 1937. English Translation Collected Papers of L. D. Landau D. ter Haar, ed., pp. 193–215. Pergamon Press, Oxford, (1965).
- [25] TOLEDANO, J. C.; TOLEDANO., P. *The Landau Theory of Phase Transitions*. New York: World Scientific, 1987.

- [26] GOR'KOV, L. P. Microscopic derivation of the Ginzburg-Landau equations in the theory of superconductivity. *Soviet Physics JETP*, v. 36, n. 6, p. 1364–1367, Dez 1959.
- [27] TINKHAM, M. *Introduction to superconductivity*. Second edition. New York: McGraw-Hill, 1996. 454 p.
- [28] CYROT, M.; PAVUNA, D. *Introduction to superconductivity and high T_c materials*. Singapore: World Scientific Publishing, 1992. 249 p. (1, 1).
- [29] DORIA, M. *Supercondutividade - O mundo quântico veio do frio*. 2007. Disponível em: <<http://omnis.if.ufrj.br/~mmd/pesquisa/supercondutividade.htm>>. Acesso em: 25 Out. 2007.
- [30] DEEVER, B. S.; FAIRBANK, W. M. Experimental Evidence for Quantized Flux in Superconducting Cylinders. *Phys. Rev. Lett.*, American Physical Society, v. 7, p. 43–46, Jul 1961. Disponível em: <<http://link.aps.org/doi/10.1103/PhysRevLett.7.43>>.
- [31] DOLL, R.; NÄBAUER, M. Experimental Proof of Magnetic Flux Quantization in a Superconducting Ring. *Phys. Rev. Lett.*, American Physical Society, v. 7, p. 51–52, Jul 1961. Disponível em: <<http://link.aps.org/doi/10.1103/PhysRevLett.7.51>>.
- [32] SILHANEK, A. V. *Nanostructured Superconductors*. Belgium, Maio 2010. Presentation. Lecture 1.
- [33] GENNES, P. de. *Superconductivity of metals and alloys*. Paris: W.A. Benjamin, 1966. (Frontiers in physics). Disponível em: <<http://books.google.com.br/books?id=M8A8AAAAIAAJ>>.
- [34] FINK, H. J.; PRESSON, A. G. Magnetic Irreversible Solution of the Ginzburg-Landau Equations. *Phys. Rev.*, American Physical Society, v. 151, p. 219–228, Nov 1966. Disponível em: <<http://link.aps.org/doi/10.1103/PhysRev.151.219>>.
- [35] MOSHCHALCOV, V. V.; GIELEN, L.; STRUNK, C.; JONCKHEERE, R.; QIU, X.; HAESSENDONCK, C. V.; BRUYNSERAEDE, Y. Effect of sample topology on the critical fields of mesoscopic superconductors. *Nature*, v. 373, p. 319–322, Jan 1995. Disponível em: <<http://www.nature.com/nature/journal/v373/n6512/pdf/373319a0.pdf>>.
- [36] BLATTER, G.; FEIGEL'MAN, M. V.; GESHKENBEIN, V. B.; LARKIN, A. I.; VINOKUR, V. M. Vortices in high-temperature superconductors. *Rev. Mod. Phys.*, American Physical Society, v. 66, p. 1125–1388, Oct 1994. Disponível em: <<http://link.aps.org/doi/10.1103/RevModPhys.66.1125>>.
- [37] KLEINER, W. H.; ROTH, L. M.; AUTLER, S. H. Bulk Solution of Ginzburg-Landau Equations for Type II Superconductors: Upper Critical Field Region. *Phys. Rev.*, American Physical Society, v. 133, p. A1226–A1227, Mar 1964. Disponível em: <<http://link.aps.org/doi/10.1103/PhysRev.133.A1226>>.
- [38] ESSMANN, U.; TRÄUBLE, H. The direct observation of individual flux lines in type II superconductors. *Physics Letters*, v. 24A, p. 526–527, May 1967.
- [39] BAARLE, G. J. C. van; TROIANOVSKI, A. M.; NISHIZAKI, T.; KES, P. H.; AARTS, J. Imaging of vortex configurations in thin films by scanning-tunneling microscopy. *Applied Physics Letters*, v. 82, p. 1081–1083, Fev 2003.

- [40] GRIGORENKO, A.; BENDING, S.; TAMEGAI, T.; OOI, S.; HENINI, M. A one-dimensional chain state of vortex matter. *Nature*, v. 414, p. 728–731, Dec 2001.
- [41] ESKILDSEN, M. R.; KUGLER, M.; TANAKA, S.; JUN, J.; KAZAKOV, S. M.; KARPINSKI, J.; FISCHER, O. Vortex Imaging in the π Band of Magnesium Diboride. *Phys. Rev. Lett.*, American Physical Society, v. 89, p. 187003, Oct 2002. Disponível em: <<http://link.aps.org/doi/10.1103/PhysRevLett.89.187003>>.
- [42] VOLODIN, A.; TEMST, K.; HAESSENDONCK, C. V.; BRUYNSEAEDE, Y.; MONTERO, M. I.; SCHULLER, I. K. Magnetic-force microscopy of vortices in thin niobium films: Correlation between the vortex distribution and the thickness-dependent film morphology. *Europhys. Lett.*, v. 58, n. 4, p. 582–588, 2002. Disponível em: <<http://dx.doi.org/10.1209/epl/i2002-00435-1>>.
- [43] GOA, P. E.; HAUGLIN, H.; BAZILJEVICH, M.; IL'YASHENKO, E.; GAMMEL, P. L.; JOHANSEN, T. H. Real-time magneto-optical imaging of vortices in superconducting NbSe₂. *Superconductor Science and Technology*, v. 14, n. 9, p. 729, 2001. Disponível em: <<http://stacks.iop.org/0953-2048/14/i=9/a=320>>.
- [44] ANDERSON, P. W. Theory of Flux Creep in Hard Superconductors. *Phys. Rev. Lett.*, American Physical Society, v. 9, p. 309–311, Oct 1962. Disponível em: <<http://link.aps.org/doi/10.1103/PhysRevLett.9.309>>.
- [45] CIVALE, L.; MARWICK, A. D.; WORTHINGTON, T. K.; KIRK, M. A.; THOMPSON, J. R.; KRUSIN-ELBAUM, L.; SUN, Y.; CLEM, J. R.; HOLTZBERG, F. Vortex confinement by columnar defects in YBa₂Cu₃O₇ crystals: Enhanced pinning at high fields and temperatures. *Phys. Rev. Lett.*, American Physical Society, v. 67, p. 648–651, Jul 1991. Disponível em: <<http://link.aps.org/doi/10.1103/PhysRevLett.67.648>>.
- [46] BANERJEE, S. S.; SOIBEL, A.; MYASOEDOV, Y.; RAPPAPORT, M.; ZELDOV, E.; MENGHINI, M.; FASANO, Y.; CRUZ, F. de la; BEEK, C. J. van der; KONCZYKOWSKI, M.; TAMEGAI, T. Melting of “Porous” Vortex Matter. *Phys. Rev. Lett.*, American Physical Society, v. 90, p. 087004, Feb 2003. Disponível em: <<http://link.aps.org/doi/10.1103/PhysRevLett.90.087004>>.
- [47] NUNES-KAPP, J.; ZADOROSNY, R.; OLIVEIRA, A.; VAZ, A.; MOSHKALEV, S.; LEPIENSKI, M.; ORTIZ, W. Vortices trapped in the damaged surroundings of antidots in Nb films - Depinning transition. *Physica C: Superconductivity*, v. 470, n. 19, p. 960 – 962, 2010. ISSN 0921-4534. Vortex Matter in Nanostructured Superconductors. Disponível em: <<http://www.sciencedirect.com/science/article/pii/S092145341000167X>>.
- [48] MOSHCHALKOV, V. V.; BAERT, M.; METLUSHKO, V. V.; ROSSEEL, E.; BAEL, M. J. V.; TEMST, K.; JONCKHEERE, R.; BRUYNSEAEDE, Y. Magnetization of multiple-quantum vortex lattices. *Phys. Rev. B*, American Physical Society, v. 54, p. 7385–7393, Sep 1996. Disponível em: <<http://link.aps.org/doi/10.1103/PhysRevB.54.7385>>.
- [49] BAERT, M.; METLUSHKO, V. V.; JONCKHEERE, R.; MOSHCHALKOV, V. V.; BRUYNSEAEDE, Y. Composite Flux-Line Lattices Stabilized in Superconducting Films by a Regular Array of Artificial Defects. *Phys. Rev. Lett.*, American Physical Society, v. 74, p. 3269–3272, Apr 1995. Disponível em: <<http://link.aps.org/doi/10.1103/PhysRevLett.74.3269>>.

- [50] BRUYNSEAEDE, Y.; BAERT, M.; BRUYNDONCX, V.; CHIEN, C. J.; EOM, J.; METLUSHKO, V. V.; NEUTTIENS, G.; PUIG, T.; ROSSEEL, E.; STRUNK, C.; TEMST, K.; BAEL, M. J. van; CHANDRASEKHAR, V.; HAESSENDONCK, C. van; MOSHCHALKOV, V. V. New phenomena in nanostructured materials. *Physica Scripta*, v. 1996, n. T66, p. 16, 1996. Disponível em: <<http://stacks.iop.org/1402-4896/1996/i=T66/a=002>>.
- [51] RAEDTS, S.; SILHANEK, A.; BAEL, M. V.; JONCKHEERE, R.; MOSHCHALKOV, V. Flux pinning properties of holes and blind holes arranged periodically in a superconductor. *Physica C: Superconductivity*, v. 404, n. 1-4, p. 298 – 301, 2004. ISSN 0921-4534. Proceedings of the Third European Conference on Vortex Matter in Superconductors at Extreme Scales and Conditions. Disponível em: <<http://www.sciencedirect.com/science/article/pii/S0921453404000966>>.
- [52] BEZRYADIN, A.; OVCHINNIKOV, Y. N.; PANNETIER, B. Nucleation of vortices inside open and blind microholes. *Phys. Rev. B*, American Physical Society, v. 53, p. 8553–8560, Apr 1996. Disponível em: <<http://link.aps.org/doi/10.1103/PhysRevB.53.8553>>.
- [53] BAEL, M. J. V.; BEKAERT, J.; TEMST, K.; LOOK, L. V.; MOSHCHALKOV, V. V.; BRUYNSEAEDE, Y.; HOWELLS, G. D.; GRIGORENKO, A. N.; BENDING, S. J.; BORGHS, G. Local Observation of Field Polarity Dependent Flux Pinning by Magnetic Dipoles. *Phys. Rev. Lett.*, American Physical Society, v. 86, p. 155–158, Jan 2001. Disponível em: <<http://link.aps.org/doi/10.1103/PhysRevLett.86.155>>.
- [54] MARTÍN, J. I.; VÉLEZ, M.; NOGUÉS, J.; SCHULLER, I. K. Flux Pinning in a Superconductor by an Array of Submicrometer Magnetic Dots. *Phys. Rev. Lett.*, American Physical Society, v. 79, p. 1929–1932, Sep 1997. Disponível em: <<http://link.aps.org/doi/10.1103/PhysRevLett.79.1929>>.
- [55] BUZDIN, A.; FEINBERG, D. On the theory of electromagnetic pinning of vortices. *Physica C: Superconductivity*, v. 235240, Part 4, n. 0, p. 2755 – 2756, 1994. ISSN 0921-4534. Disponível em: <<http://www.sciencedirect.com/science/article/pii/0921453494925984>>.
- [56] MKRTCHYAN, G. S.; SHMIDT, V. V. Interaction between a cavity and a vortex in a superconductor of second kind. *Soviet Physics JETP-USSR*, v. 34, p. 195–197, 1972.
- [57] DORIA, M.; ANDRADE, S. de; SARDELLA, E. Maximum number of flux lines inside columnar defects. *Physica C: Superconductivity*, v. 341-348, Part 2, n. 0, p. 1199 – 1200, 2000. ISSN 0921-4534. Disponível em: <<http://www.sciencedirect.com/science/article/pii/S0921453400008583>>.
- [58] DORIA, M. M.; ZEBENDE, G. F. Multiple trapping of vortex lines by a regular array of pinning centers. *Phys. Rev. B*, American Physical Society, v. 66, p. 064519, Aug 2002. Disponível em: <<http://link.aps.org/doi/10.1103/PhysRevB.66.064519>>.
- [59] DALDINI, O.; MARTINOLI, P.; OLSEN, J. L.; BERNER, G. Vortex-Line Pinning by Thickness Modulation of Superconducting Films. *Phys. Rev. Lett.*, American Physical Society, v. 32, p. 218–221, Feb 1974. Disponível em: <<http://link.aps.org/doi/10.1103/PhysRevLett.32.218>>.

- [60] KIM, Y. B.; HEMPSTEAD, C. F.; STRNAD, A. R. Magnetization and Critical Supercurrents. *Phys. Rev.*, American Physical Society, v. 129, p. 528–535, Jan 1963. Disponível em: <<http://link.aps.org/doi/10.1103/PhysRev.129.528>>.
- [61] ALTSHULER, E.; JOHANSEN, T. H. *Colloquium* : Experiments in vortex avalanches. *Rev. Mod. Phys.*, American Physical Society, v. 76, p. 471–487, Apr 2004. Disponível em: <<http://link.aps.org/doi/10.1103/RevModPhys.76.471>>.
- [62] ZELDOV, E.; CLEM, J. R.; MCELFFRESH, M.; DARWIN, M. Magnetization and transport currents in thin superconducting films. *Phys. Rev. B*, American Physical Society, v. 49, p. 9802–9822, Apr 1994. Disponível em: <<http://link.aps.org/doi/10.1103/PhysRevB.49.9802>>.
- [63] BEAN, C. P. Magnetization of Hard Superconductors. *Phys. Rev. Lett.*, American Physical Society, v. 8, p. 250–253, Mar 1962. Disponível em: <<http://link.aps.org/doi/10.1103/PhysRevLett.8.250>>.
- [64] BEAN, C. P. Magnetization of High-Field Superconductors. *Rev. Mod. Phys.*, American Physical Society, v. 36, p. 31–39, Jan 1964. Disponível em: <<http://link.aps.org/doi/10.1103/RevModPhys.36.31>>.
- [65] FIETZ, W. A.; BEASLEY, M. R.; SILCOX, J.; WEBB, W. W. Magnetization of Superconducting Nb-25%Zr Wire. *Phys. Rev.*, American Physical Society, v. 136, p. A335–A345, Oct 1964. Disponível em: <<http://link.aps.org/doi/10.1103/PhysRev.136.A335>>.
- [66] PEARL, J. Current distribution in superconducting films carrying quantized fluxoids. *Applied Physics Letters*, v. 5, p. 65–66, 1964.
- [67] DOLAN, G. J.; SILCOX, J. Critical Thicknesses in Superconducting Thin Films. *Phys. Rev. Lett.*, American Physical Society, v. 30, p. 603–606, Mar 1973. Disponível em: <<http://link.aps.org/doi/10.1103/PhysRevLett.30.603>>.
- [68] GOLDFARB, R. B.; LELENTAL, M.; THOMPSON, C. A. Magnetic susceptibility of superconductors and other spin systems. In: _____. New York: Plenum Press, 1991. cap. Alternating-field susceptometry and magnetic susceptibility of superconductors, p. 49–80.
- [69] BRANDT, E. H.; INDENBOM, M. V.; FORKL, A. Type-II Superconducting Strip in Perpendicular Magnetic Field. *Europysics Letters*, v. 22, p. 735–740, 1993.
- [70] CLEM, J. R.; SANCHEZ, A. Hysteretic ac losses and susceptibility of thin superconducting disks. *Phys. Rev. B*, American Physical Society, v. 50, p. 9355–9362, Oct 1994. Disponível em: <<http://link.aps.org/doi/10.1103/PhysRevB.50.9355>>.
- [71] BRANDT, E. H. The flux-line lattice in superconductors. *Reports on Progress in Physics*, v. 58, n. 11, p. 1465, 1995. Disponível em: <<http://stacks.iop.org/0034-4885/58/i=11/a=003>>.
- [72] JOHANSEN, T.; BAZILJEVICH, M.; BRATSBERG, H.; SHEN, Y.; VASE, P.; GAEVSKI, M. Direct observation of current distributions in thin superconductors using magneto-optic imaging. In: BALACHANDRAN, U.; MCGINN, P. (Ed.). *High-temperature superconductors: synthesis, processing, and applications II*. Warrendale,

PA: USA: Minerals, Metals & Materials Soc, 1996. p. 99–108. Symposium on High-Temperature Superconductors - Synthesis, Processing, and Applications, at the 126th Minerals-Metals-and-Materials-Society Annual Meeting, ORLANDO, FL, FEB 09-13, 1997.

[73] BRANDT, E. H. Tilted and curved vortices in anisotropic superconducting films. *Phys. Rev. B*, American Physical Society, v. 48, p. 6699–6702, Sep 1993. Disponível em: <<http://link.aps.org/doi/10.1103/PhysRevB.48.6699>>.

[74] FIELD, S.; WITT, J.; NORI, F.; LING, X. Superconducting Vortex Avalanches. *Phys. Rev. Lett.*, American Physical Society, v. 74, p. 1206–1209, Feb 1995. Disponível em: <<http://link.aps.org/doi/10.1103/PhysRevLett.74.1206>>.

[75] AEGERTER, C. M. Evidence for self-organized criticality in the Bean critical state in superconductors. *Phys. Rev. E*, American Physical Society, v. 58, p. 1438–1441, Aug 1998. Disponível em: <<http://link.aps.org/doi/10.1103/PhysRevE.58.1438>>.

[76] WIJNGAARDEN, R. J.; WELLING, M. S.; AEGERTER, C. M.; MENGHINI, M. Avalanches and Self-Organized Criticality in superconductors. *The European Physical Journal B - Condensed Matter and Complex Systems*, EDP Sciences, v. 50, p. 117–122, 2006. ISSN 1434-6028. Disponível em: <<http://dx.doi.org/10.1140/epjb/e2006-00063-7>>.

[77] ALTSHULER, E.; JOHANSEN, T. H.; PALTIEL, Y.; JIN, P.; BASSLER, K. E.; RAMOS, O.; CHEN, Q. Y.; REITER, G. F.; ZELDOV, E.; CHU, C. W. Vortex avalanches with robust statistics observed in superconducting niobium. *Phys. Rev. B*, American Physical Society, v. 70, p. 140505, Oct 2004. Disponível em: <<http://link.aps.org/doi/10.1103/PhysRevB.70.140505>>.

[78] SCHAWLOW, A. L. Structure of the Intermediate State in Superconductors. *Phys. Rev.*, American Physical Society, v. 101, p. 573–579, Jan 1956. Disponível em: <<http://link.aps.org/doi/10.1103/PhysRev.101.573>>.

[79] BITTER, F. Experiments on the Nature of Ferromagnetism. *Phys. Rev.*, American Physical Society, v. 41, p. 507–515, Aug 1932. Disponível em: <<http://link.aps.org/doi/10.1103/PhysRev.41.507>>.

[80] WERTHEIMER, M.; GILCHRIST, J. le G. Flux jumps in type II superconductors. *Journal of Physics and Chemistry of Solids*, v. 28, n. 12, p. 2509 – 2524, 1967. ISSN 0022-3697. Disponível em: <<http://www.sciencedirect.com/science/article/pii/0022369767900388>>.

[81] WIKTIONARY. *dendritic* — *Wiktionary, The Free Dictionary*. 2012. [Online; accessed 7-February-2013]. Disponível em: <<http://en.wiktionary.org/w/index.php?title=dendritic>>.

[82] VESTGÅRDEN, J. I.; SHANTSEV, D. V.; GALPERIN, Y. M.; JOHANSEN, T. H. Dynamics and morphology of dendritic flux avalanches in superconducting films. *Phys. Rev. B*, American Physical Society, v. 84, p. 054537, Aug 2011. Disponível em: <<http://link.aps.org/doi/10.1103/PhysRevB.84.054537>>.

- [83] VESTGÅRDEN, J. I.; SHANTSEV, D. V.; GALPERIN, Y. M.; JOHANSEN, T. H. Lightning in superconductors. *Scientific Reports*, v. 2, p. 886, 2012. Disponível em: <<http://dx.doi.org/10.1038/srep00886>>.
- [84] SWARTZ, P. S.; BEAN, C. P. A Model for Magnetic Instabilities in Hard Superconductors: The Adiabatic Critical State. *Journal of Applied Physics*, AIP, v. 39, n. 11, p. 4991–4998, 1968. Disponível em: <<http://link.aip.org/link/?JAP/39/4991/1>>.
- [85] MINTS, R. G.; RAKHMANOV, A. L. Critical state stability in type-II superconductors and superconducting-normal-metal composites. *Rev. Mod. Phys.*, American Physical Society, v. 53, p. 551–592, Jul 1981. Disponível em: <<http://link.aps.org/doi/10.1103/RevModPhys.53.551>>.
- [86] WIPF, S. Review of stability in high temperature superconductors with emphasis on flux jumping. *Cryogenics*, v. 31, n. 11, p. 936 – 948, 1991. ISSN 0011-2275. Disponível em: <<http://www.sciencedirect.com/science/article/pii/001122759190217K>>.
- [87] ARANSON, I.; GUREVICH, A.; VINOKUR, V. Vortex Avalanches and Magnetic Flux Fragmentation in Superconductors. *Phys. Rev. Lett.*, American Physical Society, v. 87, p. 067003, Jul 2001. Disponível em: <<http://link.aps.org/doi/10.1103/PhysRevLett.87.067003>>.
- [88] DENISOV, D. V.; SHANTSEV, D. V.; GALPERIN, Y. M.; CHOI, E.-M.; LEE, H.-S.; LEE, S.-I.; BOBYL, A. V.; GOA, P. E.; OLSEN, A. A. F.; JOHANSEN, T. H. Onset of Dendritic Flux Avalanches in Superconducting Films. *Phys. Rev. Lett.*, American Physical Society, v. 97, p. 077002, Aug 2006. Disponível em: <<http://link.aps.org/doi/10.1103/PhysRevLett.97.077002>>.
- [89] LEIDERER, P.; BONEBERG, J.; BRÜLL, P.; BUJOK, V.; HERMINGHAUS, S. Nucleation and growth of a flux instability in superconducting $\text{YBa}_2\text{Cu}_3\text{O}_{7-\delta}$ films. *Phys. Rev. Lett.*, American Physical Society, v. 71, p. 2646–2649, Oct 1993. Disponível em: <<http://link.aps.org/doi/10.1103/PhysRevLett.71.2646>>.
- [90] BOLZ, U.; BIEHLER, B.; SCHMIDT, D.; RUNGE, B.-U.; LEIDERER, P. Dynamics of the dendritic flux instability in $\text{YBa}_2\text{Cu}_3\text{O}_{7-\delta}$ films. *Europhysics Letters*, v. 64, n. 4, p. 517, 2003. Disponível em: <<http://stacks.iop.org/0295-5075/64/i=4/a=517>>.
- [91] DURÁN, C. A.; GAMMEL, P. L.; MILLER, R. E.; BISHOP, D. J. Observation of magnetic-field penetration via dendritic growth in superconducting niobium films. *Phys. Rev. B*, American Physical Society, v. 52, p. 75–78, Jul 1995. Disponível em: <<http://link.aps.org/doi/10.1103/PhysRevB.52.75>>.
- [92] JOHANSEN, T. H.; BAZILJEVICH, M.; SHANTSEV, D. V.; GOA, P. E.; GALPERIN, Y. M.; KANG, W. N.; KIM, H. J.; CHOI, E. M.; KIM, M.-S.; LEE, S. I. Dendritic flux patterns in MgB_2 films. *Superconductor Science and Technology*, v. 14, n. 9, p. 726, 2001. Disponível em: <<http://stacks.iop.org/0953-2048/14/i=9/a=319>>.
- [93] JOHANSEN, T. H.; BAZILJEVICH, M.; SHANTSEV, D. V.; GOA, P. E.; GALPERIN, Y. M.; KANG, W. N.; KIM, H. J.; CHOI, E. M.; KIM, M.-S.; LEE, S. I. Dendritic magnetic instability in superconducting MgB_2 films. *EPL (Europhysics*

Letters), v. 59, n. 4, p. 599, 2002. Disponível em: <<http://stacks.iop.org/0295-5075/59/i=4/a=599>>.

- [94] RUDNEV, I.; ANTONENKO, S.; SHANTSEV, D.; JOHANSEN, T.; PRIMENKO, A. Dendritic flux avalanches in superconducting Nb₃Sn films. *Cryogenics*, v. 43, n. 12, p. 663 – 666, 2003. ISSN 0011-2275. Disponível em: <<http://www.sciencedirect.com/science/article/pii/S0011227503001577>>.
- [95] WIMBUSH, S. C.; HOLZAPFEL, B.; JOOSS, C. Observation of dendritic flux instabilities in YNi₂B₂C thin films. *Journal of Applied Physics*, AIP, v. 96, n. 6, p. 3589–3591, 2004. Disponível em: <<http://link.aip.org/link/?JAP/96/3589/1>>.
- [96] RUDNEV, I. A.; SHANTSEV, D. V.; JOHANSEN, T. H.; PRIMENKO, A. E. Avalanche-driven fractal flux distributions in NbN superconducting films. *Applied Physics Letters*, AIP, v. 87, n. 4, p. 042502, 2005. Disponível em: <<http://link.aip.org/link/?APL/87/042502/1>>.
- [97] WELLING, M.; WESTERWAAL, R.; LOHSTROH, W.; WIJNGAARDEN, R. Huge compact flux avalanches in superconducting Nb thin films. *Physica C: Superconductivity*, v. 411, n. 1-2, p. 11–17, set. 2004. ISSN 09214534. Disponível em: <<http://linkinghub.elsevier.com/retrieve/pii/S0921453404010482>>.
- [98] JAMES, S.; FIELD, S.; SEIGEL, J.; SHTRIKMAN, H. Scanning Hall probe microscope images of field penetration into niobium films. *Physica C: Superconductivity*, v. 332, n. 1–4, p. 445 – 449, 2000. ISSN 0921-4534. Disponível em: <<http://www.sciencedirect.com/science/article/pii/S0921453499007212>>.
- [99] BAGGIO, C.; GOLDSTEIN, R. E.; PESCI, A. I.; SAARLOOS, W. van. Boundary layer model for vortex fingers in type-II superconductors. *Phys. Rev. B*, American Physical Society, v. 72, p. 060503, Aug 2005. Disponível em: <<http://link.aps.org/doi/10.1103/PhysRevB.72.060503>>.
- [100] MAKSIMOV, I. On the magnetic flux branching instability in superconductors. *Physica C: Superconductivity*, v. 235240, Part 5, n. 0, p. 3017 – 3018, 1994. ISSN 0921-4534. Disponível em: <<http://www.sciencedirect.com/science/article/pii/0921453494910359>>.
- [101] ROSENSTEIN, B.; SHAPIRO, B.; SHAPIRO, I. Shock waves and avalanches in type-II superconductor. *Europhysics Letters*, v. 70, n. 4, p. 506–512, 2005. Disponível em: <<http://dx.doi.org/10.1209/epl/i2005-10019-1>>.
- [102] DENISOV, D. V.; RAKHMANOV, A. L.; SHANTSEV, D. V.; GALPERIN, Y. M.; JOHANSEN, T. H. Dendritic and uniform flux jumps in superconducting films. *Phys. Rev. B*, American Physical Society, v. 73, p. 014512, Jan 2006. Disponível em: <<http://link.aps.org/doi/10.1103/PhysRevB.73.014512>>.
- [103] ALBRECHT, J.; MATVEEV, A. T.; STREMPFER, J.; HABERMEIER, H.-U.; SHANTSEV, D. V.; GALPERIN, Y. M.; JOHANSEN, T. H. Dramatic Role of Critical Current Anisotropy on Flux Avalanches in MgB₂ Films. *Phys. Rev. Lett.*, American Physical Society, v. 98, p. 117001, Mar 2007. Disponível em: <<http://link.aps.org/doi/10.1103/PhysRevLett.98.117001>>.

- [104] YURCHENKO, V. V.; SHANTSEV, D. V.; JOHANSEN, T. H.; NEVALA, M. R.; MAASILTA, I. J.; SENAPATI, K.; BUDHANI, R. C. Reentrant stability of superconducting films and the vanishing of dendritic flux instability. *Phys. Rev. B*, American Physical Society, v. 76, p. 092504, Sep 2007. Disponível em: <<http://link.aps.org/doi/10.1103/PhysRevB.76.092504>>.
- [105] LAVIANO, F.; BOTTA, D.; FERDEGHINI, C.; FERRANDO, V.; GOZZELINO, L.; MEZZETTI, E. Magneto-optical imaging. In: _____. Dodrecht, The Netherlands: Kluwer Academic Publishers, 2004. cap. Thermomagnetic instability as limiting mechanism for electrical current density in MgB₂ thin films, p. 237–242.
- [106] RUNGE, B.-U.; BOLZ, U.; EISENMENGER, J.; LEIDERER, P. Ultrafast magneto-optical study of flux avalanches in high-T_c superconductors. *Physica C: Superconductivity*, v. 341-348, Part 3, n. 0, p. 2029 – 2030, 2000. ISSN 0921-4534. Disponível em: <<http://www.sciencedirect.com/science/article/pii/S0921453400012326>>.
- [107] MIKHEENKO, P.; QVILLER, A. J.; VESTGÅRDEN, J. I.; CHAUDHURI, S.; MAASILTA, I. J.; GALPERIN, Y. M.; JOHANSEN, T. H. Nanosecond voltage pulses from dendritic flux avalanches in superconducting NbN films. *Applied Physics Letters*, AIP, v. 102, n. 2, p. 022601, 2013. Disponível em: <<http://link.aip.org/link/?APL/102/022601/1>>.
- [108] MINTS, R. G.; BRANDT, E. H. Flux jumping in thin films. *Phys. Rev. B*, American Physical Society, v. 54, p. 12421–12426, Nov 1996. Disponível em: <<http://link.aps.org/doi/10.1103/PhysRevB.54.12421>>.
- [109] SILHANEK, A. V.; RAEDTS, S.; MOSHCHALKOV, V. V. Paramagnetic reentrance of ac screening: Evidence of vortex avalanches in Pb thin films. *Phys. Rev. B*, American Physical Society, v. 70, p. 144504, Oct 2004. Disponível em: <<http://link.aps.org/doi/10.1103/PhysRevB.70.144504>>.
- [110] MENGHINI, M.; WIJNGAARDEN, R. J.; SILHANEK, A. V.; RAEDTS, S.; MOSHCHALKOV, V. V. Dendritic flux penetration in Pb films with a periodic array of antidots. *Phys. Rev. B*, American Physical Society, v. 71, p. 104506, Mar 2005. Disponível em: <<http://link.aps.org/doi/10.1103/PhysRevB.71.104506>>.
- [111] YURCHENKO, V.; QVILLER, A.; MOZHAEV, P.; MOZHAEVA, J.; HANSEN, J.; JACOBSEN, C.; KOTELYANSKII, I.; PAN, A.; JOHANSEN, T. Anisotropic currents and flux jumps in high- superconducting films with self-organized arrays of planar defects. *Physica C: Superconductivity*, v. 470, n. 19, p. 799 – 802, 2010. ISSN 0921-4534. Vortex Matter in Nanostructured Superconductors. Disponível em: <<http://www.sciencedirect.com/science/article/pii/S0921453410001929>>.
- [112] VLASKO-VLASOV, V.; WELP, U.; METLUSHKO, V.; CRABTREE, G. Flux avalanches in superconducting films with periodic arrays of holes. *Physica C: Superconductivity*, v. 341348, Part 2, n. 0, p. 1281 – 1282, 2000. ISSN 0921-4534. Disponível em: <<http://www.sciencedirect.com/science/article/pii/S0921453400008959>>.
- [113] GHIGO, G.; LAVIANO, F.; GOZZELINO, L.; GERBALDO, R.; MEZZETTI, E.; MONTICONE, E.; PORTESI, C. Evidence of rf-driven dendritic vortex avalanches in MgB₂ microwave resonators. *Journal of Applied Physics*, v. 102, p. 113901, 2007.

- [114] COLAUTO, F.; CHOI, E. M.; LEE, J. Y.; LEE, S. I.; YURCHENKO, V. V.; JOHANSEN, T. H.; ORTIZ, W. A. Mapping flux avalanches in MgB₂ films: equivalence between magneto-optical imaging and magnetic measurements. *Superconductor Science and Technology*, v. 20, n. 8, p. L48, 2007. Disponível em: <<http://stacks.iop.org/0953-2048/20/i=8/a=L02>>.
- [115] BAZILJEVICH, M.; BOBYL, A.; SHANTSEV, D.; ALTSHULER, E.; JOHANSEN, T.; LEE, S. Origin of dendritic flux patterns in MgB₂ films. *Physica C: Superconductivity*, v. 369, n. 14, p. 93 – 96, 2002. ISSN 0921-4534. Disponível em: <<http://www.sciencedirect.com/science/article/pii/S0921453401012266>>.
- [116] COLAUTO, F.; CHOI, E.; LEE, J. Y.; LEE, S. I.; NO, E. J. P.; BLAMIRE, M. G.; JOHANSEN, T. H.; ORTIZ, W. A. Suppression of flux avalanches in superconducting films by electromagnetic braking. *Applied Physics Letters*, AIP, v. 96, n. 9, p. 092512, 2010. Disponível em: <<http://link.aip.org/link/?APL/96/092512/1>>.
- [117] VIEU, C.; CARCENAC, F.; PÉPIN, A.; CHEN, Y.; MEJIAS, M.; LEBIB, A.; MANIN-FERLAZZO, L.; COURAUD, L.; LAUNOIS, H. Electron beam lithography: resolution limits and applications. *Applied Surface Science*, v. 164, n. 14, p. 111 – 117, 2000. ISSN 0169-4332. Surface Science in Micro & Nanotechnology. Disponível em: <<http://www.sciencedirect.com/science/article/pii/S0169433200003524>>.
- [118] MARTÍN, J.; NOGUÉS, J.; LIU, K.; VICENT, J.; SCHULLER, I. K. Ordered magnetic nanostructures: fabrication and properties. *Journal of Magnetism and Magnetic Materials*, v. 256, n. 13, p. 449 – 501, 2003. ISSN 0304-8853. Disponível em: <<http://www.sciencedirect.com/science/article/pii/S0304885302008983>>.
- [119] EGERTON, R. *Physical Principles of Electron Microscopy: An Introduction to TEM, SEM, and AEM*. Springer, 2005. ISBN 9780387258003. Disponível em: <<http://books.google.com.br/books?id=t6TTgqp3O5MC>>.
- [120] GOLUBOVIĆ, D. *Nucleation of superconductivity and vortex matter in superconductor/ferromagnet structures*. Tese (Doutorado) — Katholieke Universiteit Leuven, Leuven, Belgium, 2005. Orientador: Prof. Dr. Victor V. Moshchalkov.
- [121] MARTIN, L.; CHU, Y.-H.; RAMESH, R. Advances in the growth and characterization of magnetic, ferroelectric, and multiferroic oxide thin films. *Materials Science and Engineering: R: Reports*, v. 68, n. 46, p. 89 – 133, 2010. ISSN 0927-796X. Disponível em: <<http://www.sciencedirect.com/science/article/pii/S0927796X1000032X>>.
- [122] MARLA, D.; BHANDARKAR, U. V.; JOSHI, S. S. Critical assessment of the issues in the modeling of ablation and plasma expansion processes in the pulsed laser deposition of metals. *Journal of Applied Physics*, AIP, v. 109, n. 2, p. 021101, 2011. Disponível em: <<http://link.aip.org/link/?JAP/109/021101/1>>.
- [123] DIJKKAMP, D.; VENKATESAN, T.; WU, X. D.; SHAHEEN, S. A.; JISRRAWI, N.; MIN-LEE, Y. H.; MCLEAN, W. L.; CROFT, M. Preparation of Y-Ba-Cu oxide superconductor thin films using pulsed laser evaporation from high T_c bulk material. *Applied Physics Letters*, AIP, v. 51, n. 8, p. 619–621, 1987. Disponível em: <<http://link.aip.org/link/?APL/51/619/1>>.

- [124] WILLMOTT, P. Deposition of complex multielemental thin films. *Progress in Surface Science*, v. 76, n. 68, p. 163 – 217, 2004. ISSN 0079-6816. Disponível em: <<http://www.sciencedirect.com/science/article/pii/S0079681604000371>>.
- [125] LEHMANN, M.; SAEMANN-LSCHENKO, G.; ADRIAN, H.; NÖLSCHER, C. Disordered A15 compounds from the Matthias-valley: Mo₃Ge and Mo₃Si. *Physica*, v. 107B, p. 473–474, 1981.
- [126] ROSSNAGEL, S. Handbook of thin film deposition processes and techniques: Principles, methods, equipment, and applications. In: _____. Norwich, New York, USA: Noyes Publication / William Andrews Publishing, 2002. cap. Sputtering and sputter deposition, p. 319–348.
- [127] CULLITY, B. *Elements of X-ray diffraction*. Addison-Wesley Pub. Co., 1956. (Addison-Wesley metallurgy series). Disponível em: <<http://books.google.com.br/books?id=XJVCgGFTODMC>>.
- [128] MARKOWICZ, A. A. Handbook of x-ray spectroscopy. In: _____. New York: Marcel Dekker, 2002. cap. X-ray Physics, p. 1–94.
- [129] BINNING, G.; QUATE, C. F.; GERBER, C. Atomic force microscope. *Physical Review Letters*, v. 56, p. 930–933, 1986.
- [130] HELM, C. A. *Atomic Force Microscope*. Jan 2013. Disponível em: <<http://www3.physik.uni-greifswald.de/method/afm/eafm.htm>>.
- [131] WILLIAMS, D. B.; CARTER, C. B. *Transmission Electron Microscopy: A Textbook for Materials Science*. 2a. edition. ed. New York: Springer, 2009.
- [132] BENDING, S. J.; BROOK, A.; GREGORY, J. K.; CRISAN, I. A.; PROSS, A.; GRIGORENKO, A. N.; ORAL, A.; LAVIANO, F.; MEZZETTI, E. Magneto-optical imaging. In: _____. Dodrecht, The Netherlands: Kluwer Academic Publishers, 2004. cap. Comparison of magneto-optical imaging with other local magnetic probes, p. 11–18.
- [133] JOOSS, C.; ALBRECHT, J.; KUHN, H.; LEONHARDT, S.; KRONMÜLLER, H. Magneto-optical studies of current distributions in high- T_c superconductors. *Reports on Progress in Physics*, v. 65, n. 5, p. 651, 2002. Disponível em: <<http://stacks.iop.org/0034-4885/65/i=5/a=202>>.
- [134] ALERS, P. B. Structure of the Intermediate State in Superconducting Lead. *Phys. Rev.*, American Physical Society, v. 105, p. 104–108, Jan 1957. Disponível em: <<http://link.aps.org/doi/10.1103/PhysRev.105.104>>.
- [135] DESORBO, W. Study of the Intermediate State in Superconductors using Cerium Phosphate Glass. *Phys. Rev. Lett.*, American Physical Society, v. 4, p. 406–408, Apr 1960. Disponível em: <<http://link.aps.org/doi/10.1103/PhysRevLett.4.406>>.
- [136] KIRCHNER, H. High-resolution magneto-optical observation of magnetic structures in superconductors. *Physics Letters A*, v. 26, n. 12, p. 651 – 652, 1968. ISSN 0375-9601. Disponível em: <<http://www.sciencedirect.com/science/article/pii/0375960168901783>>.

- [137] HÜEBENER, R. P.; ROWE, V. A.; KAMPWIRTH, R. T. Magneto-Optical Observation of the Magnetic Flux Structure in Superconducting Niobium. *Journal of Applied Physics*, AIP, v. 41, n. 7, p. 2963–2967, 1970. Disponível em: <<http://link.aip.org/link/?JAP/41/2963/1>>.
- [138] HABERMEIER, H.-U. Magneto-optical imaging. In: _____. Dodrecht, The Netherlands: Kluwer Academic Publishers, 2004. cap. Paving the way for the success of magneto-optics, p. 1–11.
- [139] JOHANSEN, T. H. *Magneto-optical imaging of superconductors - Department of Physics*. 2012. Disponível em: <<http://www.mn.uio.no/fysikk/english/research/groups/amks/superconductivity/mo/>>. Acesso em: 14 Nov. 2012.
- [140] POLYANSKII, A.; DOROSINSKII, L.; INDENBOM, M.; NIKITENKO, V.; OSSIPYAN, Y.; VLASKO-VLASOV, V. *Sov. Tech. Phys. Lett.*, v. 15, p. 872, 1989.
- [141] POLYANSKII, A.; DOROSINSKII, L.; INDENBOM, M.; NIKITENKO, V.; OSSIPYAN, Y.; VLASKO-VLASOV, V. Direct study of the pinning anisotropy in HTSC. *Journal of the Less Common Metals*, v. 164165, Part 2, n. 0, p. 1300 – 1307, 1990. ISSN 0022-5088. Disponível em: <<http://www.sciencedirect.com/science/article/pii/002250889090549Y>>.
- [142] KIRTLEY, J. R. Fundamental studies of superconductors using scanning magnetic imaging. *Reports on Progress in Physics*, v. 73, n. 12, p. 126501, 2010. Disponível em: <<http://stacks.iop.org/0034-4885/73/i=12/a=126501>>.
- [143] VINNIKOV, L.; KARPINSKI, J.; KAZAKOV, S.; JUN, J.; ANDEREGG, J.; BUDKO, S.; CANFIELD, P. Bitter decoration of vortex structure in MgB₂ single crystals. *Physica C: Superconductivity*, v. 385, n. 12, p. 177 – 179, 2003. ISSN 0921-4534. Disponível em: <<http://www.sciencedirect.com/science/article/pii/S0921453402023249>>.
- [144] LOUDON, J.; MIDGLEY, P. Imaging Flux Vortices in Type II Superconductors with a Commercial Transmission Electron Microscope. *arXiv.org: Condensed Matter*, p. 0807.2401, 2008. Disponível em: <<http://arxiv.org/ftp/arxiv/papers/0807/0807.2401.pdf>>.
- [145] GHEORGHE, D. G. *Magneto-optics of superconductors with nanotailored pinning and with ferromagnetic layers*. Tese (Doutorado) — Vrije Universiteit, Amsterdam, The Netherlands, 2008. Orientador: Prof. Dr. R. P. Griessen.
- [146] HARLINGEN, D. van. *Magnetic field sensitivity versus spatial resolution*. 2012. Disponível em: <<http://groups.mrl.uiuc.edu/dvh/ssm/image006.gif>>. Acesso em: 14 Nov. 2012.
- [147] RASBAND, W. *ImageJ*. Jan 2013. Domínio Público. Disponível em: <<http://rsbweb.nih.gov/ij/index.html>>.
- [148] DESIGN, Q. *MPMS: Hardware & Software (Manual)*. [S.l.], 1996. Disponível em: <<http://www.qdusa.com/products/mpms.html>>.

- [149] JOSEPHSON, B. Possible new effects in superconductive tunnelling. *Physics Letters*, v. 1, n. 7, p. 251 – 253, 1962. ISSN 0031-9163. Disponível em: <<http://www.sciencedirect.com/science/article/pii/0031916362913690>>.
- [150] JOSEPHSON, B. D. The discovery of tunnelling supercurrents. *Rev. Mod. Phys.*, American Physical Society, v. 46, p. 251–254, Apr 1974. Disponível em: <<http://link.aps.org/doi/10.1103/RevModPhys.46.251>>.
- [151] FAGALY, R. L. Superconducting quantum interference device instruments and applications. *Review of Scientific Instruments*, AIP, v. 77, n. 10, p. 101101, 2006. Disponível em: <<http://link.aip.org/link/?RSI/77/101101/1>>.
- [152] MCELFRISH, M.; LI, S.; SAGER, R. *Effects of Magnetic Field Uniformity on the Measurement of Superconducting Samples*. San Diego, CA, USA, 1997. Disponível em: <<http://www.qdusa.com/sitedocs/appNotes/mpms/effects.pdf>>.
- [153] DESIGN, Q. *PPMS: Hardware & Option Manuals*. [S.l.], 2000. Disponível em: <<http://www.qdusa.com/products/ppms.html>>.
- [154] DESIGN, Q. *Application note: Magnetometry*. 3.07. ed. [S.l.], 2000. Disponível em: <<http://www.qdusa.com/sitedocs/productBrochures/mag3-07.pdf>>.
- [155] GÖMÖRY, F. Characterization of high-temperature superconductors by AC susceptibility measurements. *Superconductor Science and Technology*, v. 10, n. 8, p. 523, 1997. Disponível em: <<http://stacks.iop.org/0953-2048/10/i=8/a=001>>.
- [156] BRANDT, E. H. Ac response of thin-film superconductors at various temperatures and magnetic fields. *Philosophical Magazine B*, v. 80, n. 5, p. 835–845, 2000. Disponível em: <<http://www.ingentaconnect.com/content/tandf/tphb/2000/00000080/00000005/art00003>>.
- [157] CHEN, Q. Y. Magnetic susceptibility of superconductors and other spin systems. In: _____. New York: Plenum Press, 1991. cap. Ac inductive measurement: its application to the studies of High T_c superconductivity, p. 81–105.
- [158] ISHIDA, T.; GOLDFARB, R. B. Fundamental and harmonic susceptibilities of $\text{YBa}_2\text{Cu}_3\text{O}_{7-\delta}$. *Phys. Rev. B*, American Physical Society, v. 41, p. 8937–8948, May 1990. Disponível em: <<http://link.aps.org/doi/10.1103/PhysRevB.41.8937>>.
- [159] CLEM, J. R. Magnetic susceptibility of superconductors and other spin systems. In: _____. New York: Plenum Press, 1991. cap. Ac losses in type II superconductor, p. 177–211.
- [160] SHANTSEV, D. V.; GALPERIN, Y. M.; JOHANSEN, T. H. Thin superconducting disk with field-dependent critical current: Magnetization and ac susceptibilities. *Phys. Rev. B*, American Physical Society, v. 61, p. 9699–9706, Apr 2000. Disponível em: <<http://link.aps.org/doi/10.1103/PhysRevB.61.9699>>.
- [161] HERZOG, T.; RADOVAN, H. A.; ZIEMANN, P.; BRANDT, E. H. Experimental test of theories describing the magnetic ac susceptibility of differently shaped superconducting films: Rectangles, squares, disks, and rings patterned from $\text{YBa}_2\text{Cu}_3\text{O}_{7-\delta}$ films. *Phys. Rev. B*, American Physical Society, v. 56, p. 2871–2881, Aug 1997. Disponível em: <<http://link.aps.org/doi/10.1103/PhysRevB.56.2871>>.

- [162] SILHANEK, A.; RAEDTS, S.; BAEL, M.; MOSHCHALKOV, V. Dynamic regimes in films with a periodic array of antidots. *The European Physical Journal B - Condensed Matter and Complex Systems*, Springer-Verlag, v. 37, p. 19–24, 2003. ISSN 1434-6028. Disponível em: <<http://dx.doi.org/10.1140/epjb/e2004-00026-0>>.
- [163] RAEDTS, S. *Vortex dynamics in type-II superconductors with a periodic pinning array*. Tese (Doutorado) — Katholieke Universiteit Leuven, Leuven, Belgium, 2004. Orientador: Prof. Dr. Victor V. Moshchalkov.
- [164] COLE, K. S.; COLE, R. H. Dispersion and Absorption in Dielectrics I. Alternating Current Characteristics. *The Journal of Chemical Physics*, AIP, v. 9, n. 4, p. 341–351, 1941. Disponível em: <<http://link.aip.org/link/?JCP/9/341/1>>.
- [165] CHEN, D.-X.; PARDO, E.; GU, C. Critical-state and eddy-current ac susceptibilities of conducting cylinders. *Superconductor Science and Technology*, v. 18, n. 10, p. 1280, 2005. Disponível em: <<http://stacks.iop.org/0953-2048/18/i=10/a=006>>.
- [166] CHEN, D.-X.; NAVAU, C.; DEL-VALLE, N.; SANCHEZ, A. Analytic expressions for critical-state ac susceptibility of rectangular superconducting films in perpendicular magnetic field. *Physica C: Superconductivity*, v. 470, n. 1, p. 89 – 94, 2010. ISSN 0921-4534. Disponível em: <<http://www.sciencedirect.com/science/article/pii/S092145340900570X>>.
- [167] ULLMAIER, H. A. AC Measurements on Hard Superconductors. *Physica Status Solidi (b)*, WILEY-VCH Verlag, v. 17, n. 2, p. 631–643, 1966. ISSN 1521-3951. Disponível em: <<http://dx.doi.org/10.1002/pssb.19660170220>>.
- [168] CLEM, J. R. Theory of ac losses in type-II superconductors with a field-dependent surface barrier. *Journal of Applied Physics*, AIP, v. 50, n. 5, p. 3518–3530, 1979. Disponível em: <<http://link.aip.org/link/?JAP/50/3518/1>>.
- [169] INDENBOM, M. V.; SCHUSTER, T.; KUHN, H.; KRONMÜLLER, H.; LI, T. W.; MENOVSKY, A. A. Observation of current strings in $\text{Bi}_2\text{Sr}_2\text{CaCu}_2\text{O}_8$ single crystals. *Phys. Rev. B*, American Physical Society, v. 51, p. 15484–15491, Jun 1995. Disponível em: <<http://link.aps.org/doi/10.1103/PhysRevB.51.15484>>.
- [170] SILHANEK, A. V.; GUTIERREZ, J.; KRAMER, R. B. G.; ATAKLTI, G. W.; VONDEL, J. Van de; MOSHCHALKOV, V. V.; SANCHEZ, A. Microscopic picture of the critical state in a superconductor with a periodic array of antidots. *Phys. Rev. B*, American Physical Society, v. 83, p. 024509, Jan 2011. Disponível em: <<http://link.aps.org/doi/10.1103/PhysRevB.83.024509>>.
- [171] HÉBERT, S.; LOOK, L. V.; WECKHUYSEN, L.; MOSHCHALKOV, V. V. Vortex avalanches in a Pb film with a square antidot array. *Phys. Rev. B*, American Physical Society, v. 67, p. 224510, Jun 2003. Disponível em: <<http://link.aps.org/doi/10.1103/PhysRevB.67.224510>>.
- [172] COLAUTO, F.; NO, E. J. P.; BLAMIRE, M. G.; ORTIZ, W. A. Boundaries of the instability region on the HT diagram of Nb thin films. *Superconductor Science and Technology*, v. 21, n. 4, p. 045018, 2008. Disponível em: <<http://stacks.iop.org/0953-2048/21/i=4/a=045018>>.

[173] HELSETH, L. E.; HANSEN, R. W.; IL'YASHENKO, E. I.; BAZILJEVICH, M.; JOHANSEN, T. H. Faraday rotation spectra of bismuth-substituted ferrite garnet films with in-plane magnetization. *Phys. Rev. B*, American Physical Society, v. 64, p. 174406, Oct 2001. Disponível em: <<http://link.aps.org/doi/10.1103/PhysRevB.64.174406>>.

[174] BOBYL, A. V.; SHANTSEV, D. V.; JOHANSEN, T. H.; KANG, W. N.; KIM, H. J.; CHOI, E. M.; LEE, S. I. Current-induced dendritic magnetic instability in superconducting MgB₂ films. *Applied Physics Letters*, AIP, v. 80, n. 24, p. 4588–4590, 2002. Disponível em: <<http://link.aip.org/link/?APL/80/4588/1>>.

[175] KOLEŠNIK, S.; VLASKO-VLASOV, V.; WELP, U.; CRABTREE, G.; PIOTROWSKI, T.; WRÓBEL, J.; KLIMOV, A.; PRZYSTUPSKI, P.; SKOŚKIEWICZ, T.; DABROWSKI, B. Flux pinning by anisotropic arrays of antidots in superconducting thin films. *Physica C: Superconductivity*, v. 341348, Part 2, n. 0, p. 1093 – 1094, 2000. ISSN 0921-4534. Disponível em: <<http://www.sciencedirect.com/science/article/pii/S0921453400007991>>.

[176] MOSHCHALCOV, V. V.; BAERT, M.; METLUSHKO, V. V.; ROSSEEL, E.; BAEL, M. J. V.; TEMST, K.; BRUYNSERAEDE, Y.; JONCKHEERE, R. Pinning by an antidot lattice: The problem of the optimum antidot size. *Phys. Rev. B*, American Physical Society, v. 57, p. 3615–3622, Feb 1998. Disponível em: <<http://link.aps.org/doi/10.1103/PhysRevB.57.3615>>.

[177] BRANDT, E. H. Susceptibility of superconductor disks and rings with and without flux creep. *Phys. Rev. B*, American Physical Society, v. 55, p. 14513–14526, Jun 1997. Disponível em: <<http://link.aps.org/doi/10.1103/PhysRevB.55.14513>>.

[178] BRANDT, E. H. Superconductor disks and cylinders in an axial magnetic field: II. Nonlinear and linear ac susceptibilities. *Phys. Rev. B*, American Physical Society, v. 58, p. 6523–6533, Sep 1998. Disponível em: <<http://link.aps.org/doi/10.1103/PhysRevB.58.6523>>.

[179] GOLDFARB, R.; CLARK, A. Magnetic hysteresis and complex susceptibility as measures of ac losses in a multifilamentary NbTi superconductor. *Magnetics, IEEE Transactions on*, v. 21, n. 2, p. 332 – 335, mar 1985. ISSN 0018-9464.

[180] WELLING, M. S.; WIJNGAARDEN, R. J.; AEGERTER, C. M.; WÖRDENWEBER, R.; LAHL, P. Flux flow anisotropy in superconducting films with a rectangular array of holes. *Physica C: Superconductivity*, v. 404, n. 14, p. 410 – 414, 2004. ISSN 0921-4534. Proceedings of the Third European Conference on Vortex Matter in Superconductors at Extreme Scales and Conditions. Disponível em: <<http://www.sciencedirect.com/science/article/pii/S0921453404001194>>.

[181] JOOSS, C.; WARTHMAN, R.; KRONMÜLLER, H. Pinning mechanism of vortices at antiphase boundaries in YBa₂Cu₃O_{7- δ} . *Phys. Rev. B*, American Physical Society, v. 61, p. 12433–12446, May 2000. Disponível em: <<http://link.aps.org/doi/10.1103/PhysRevB.61.12433>>.

[182] POLYANSKII, A.; EMERGO, R. L. S.; WU, J. Z.; AYTUG, T.; CHRISTEN, D. K.; PERKINS, G. K.; LARBALESTIER, D. Magneto-optical imaging and electromagnetic study of YBa₂Cu₃O_{7- δ} vicinal films of variable thickness. *Phys.*

Rev. B, American Physical Society, v. 72, p. 174509, Nov 2005. Disponível em: <<http://link.aps.org/doi/10.1103/PhysRevB.72.174509>>.

[183] DJUPMYR, M.; CRISTIANI, G.; HABERMEIER, H.-U.; ALBRECHT, J. Anisotropic temperature-dependent current densities in vicinal $\text{YBa}_2\text{Cu}_3\text{O}_{7-\delta}$. *Phys. Rev. B*, American Physical Society, v. 72, p. 220507, Dec 2005. Disponível em: <<http://link.aps.org/doi/10.1103/PhysRevB.72.220507>>.

[184] JIN H. MAVOORI, C. B. R. B. v. D. S. High critical currents in iron-clad superconducting MgB_2 wires. *Nature*, v. 411, p. 563–565, 2001. Disponível em: <<http://dx.doi.org/10.1038/35079030>>.

[185] MOTTA, M.; COLAUTO, F.; ZADOROSNY, R.; JOHANSEN, T. H.; DINNER, R. B.; BLAMIRE, M. G.; ATAKLTI, G. W.; MOSHCHALCOV, V. V.; SILHANEK, A. V.; ORTIZ, W. A. Visualizing the ac magnetic susceptibility of superconducting films via magneto-optical imaging. *Phys. Rev. B*, American Physical Society, v. 84, p. 214529, Dec 2011. Disponível em: <<http://link.aps.org/doi/10.1103/PhysRevB.84.214529>>.

[186] MOTTA, M.; COLAUTO, F.; JOHANSEN, T.; DINNER, R.; BLAMIRE, M.; ATAKLTI, G.; MOSHCHALCOV, V.; SILHANEK, A.; ORTIZ, W. Flux avalanches triggered by AC magnetic fields in superconducting thin films. *Physica C: Superconductivity*, v. 479, n. 0, p. 134 – 136, 2012. ISSN 0921-4534. Proceedings of VORTEX VII Conference. Disponível em: <<http://www.sciencedirect.com/science/article/pii/S0921453411005533>>.

[187] ARANSON, I. S.; GUREVICH, A.; WELLING, M. S.; WIJNGAARDEN, R. J.; VLASKO-VLASOV, V. K.; VINOKUR, V. M.; WELP, U. Dendritic Flux Avalanches and Nonlocal Electrodynamics in Thin Superconducting Films. *Phys. Rev. Lett.*, American Physical Society, v. 94, p. 037002, Jan 2005. Disponível em: <<http://link.aps.org/doi/10.1103/PhysRevLett.94.037002>>.

[188] CHOI, E.-M.; LEE, H.-S.; LEE, J. Y.; LEE, S.-I.; OLSEN, A. A. F.; YURCHENKO, V. V.; SHANTSEV, D. V.; JOHANSEN, T. H.; KIM, H.-J.; CHO, M.-H. Width-dependent upper threshold field for flux noise in MgB_2 strips. *Applied Physics Letters*, AIP, v. 91, n. 4, p. 042507, 2007. Disponível em: <<http://link.aip.org/link/?APL/91/042507/1>>.

[189] ESQUINAZI, P.; SETZER, A.; FUCHS, D.; KOPELEVICH, Y.; ZELDOV, E.; ASSMANN, C. Vortex avalanches in Nb thin films: Global and local magnetization measurements. *Phys. Rev. B*, American Physical Society, v. 60, p. 12454–12461, Nov 1999. Disponível em: <<http://link.aps.org/doi/10.1103/PhysRevB.60.12454>>.

[190] AWAD, A. A.; ALIEV, F. G.; ATAKLTI, G. W.; SILHANEK, A.; MOSHCHALCOV, V. V.; GALPERIN, Y. M.; VINOKUR, V. Flux avalanches triggered by microwave depinning of magnetic vortices in Pb superconducting films. *Phys. Rev. B*, American Physical Society, v. 84, p. 224511, Dec 2011. Disponível em: <<http://link.aps.org/doi/10.1103/PhysRevB.84.224511>>.

[191] JOHANSEN, T. H.; BRATSBERG, H. New critical-state model for magnetization of hard type-II superconductors. *Journal of Applied Physics*, AIP, v. 76, n. 12, p. 8001–8004, 1994. Disponível em: <<http://link.aip.org/link/?JAP/76/8001/1>>.

- [192] CAMPBELL, A. M.; EVETTS, J. E. Flux vortices and transport current in type II superconductors. *Advances in Physics*, v. 21, p. 199–399, 1972.
- [193] HEIN, R. A. Superconductivity - Large-scale applications. *Science*, v. 185, n. 4147, p. 211–222, 1974. Disponível em: <<http://dx.doi.org/10.1126/science.185.4147.211>>.
- [194] MEINGAST, C.; LARBALESTIER, D. C. Quantitative description of a very high critical current density Nb-Ti superconductor during its final optimization strain. II. Flux pinning mechanisms. *Journal of Applied Physics*, AIP, v. 66, n. 12, p. 5971–5983, 1989. Disponível em: <<http://link.aip.org/link/?JAP/66/5971/1>>.
- [195] DAM, B.; HUIJBREGTSE, J.; KLAASSEN, F.; GEEST, R. van der; DOORNBOS, G.; RECTOR, J.; TESTA, A.; FREISEM, S.; MARTINEZ, J.; STAUBLE-PUMPIN, B.; GRIESSEN, R. Origin of high critical currents in $\text{YBa}_2\text{Cu}_3\text{O}_{7-\delta}$ superconducting thin films. *Nature*, v. 399, n. 6735, p. 439–442, JUN 3 1999. Disponível em: <<http://dx.doi.org/10.1038/20880>>.
- [196] KANG, S.; GOYAL, A.; LI, J.; GAPUD, A.; MARTIN, P.; HEATHERLY, L.; THOMPSON, J.; CHRISTEN, D.; LIST, F.; PARANTHAMAN, M.; LEE, D. High-performance high- T_c superconducting wires. *Science*, 311, n. 5769, p. 1911–1914, MAR 31 2006. Disponível em: <<http://dx.doi.org/10.1126/science.1124872>>.
- [197] FOLTYN, S. R.; CIVALE, L.; MACMANUS-DRISCOLL, J. L.; JIA, Q. X.; MAIOROV, B.; WANG, H.; MALEY, M. Materials science challenges for high-temperature superconducting wire. *Nature Materials*, 6, n. 9, p. 631–642, SEP 2007. Disponível em: <<http://dx.doi.org/10.1038/nmat1989>>.
- [198] GUTIERREZ, J.; LLORDES, A.; GAZQUEZ, J.; GIBERT, M.; ROMA, N.; RICART, S.; POMAR, A.; SANDIUMENGE, F.; MESTRES, N.; PUIG, T.; OBRADORS, X. Strong isotropic flux pinning in solution-derived $\text{YBa}_2\text{Cu}_3\text{O}_{7-x}$ nanocomposite superconductor films. *Nature Materials*, 6, n. 5, p. 367–373, MAY 2007. Disponível em: <<http://dx.doi.org/10.1038/nmat1893>>.
- [199] VÉLEZ, M.; MARTÍN, J.; VILLEGAS, J.; HOFFMANN, A.; GONZÁLEZ, E.; VICENT, J.; SCHULLER, I. K. Superconducting vortex pinning with artificial magnetic nanostructures. *Journal of Magnetism and Magnetic Materials*, v. 320, n. 21, p. 2547 – 2562, 2008. ISSN 0304-8853. Disponível em: <<http://www.sciencedirect.com/science/article/pii/S0304885308007014>>.
- [200] KATE, H. H. J. T. ATLAS Superconducting Toroids - The largest ever built. *International Journal of Modern Physics A*, v. 25, n. 15, p. 2933–2954, JUN 20 2010. Disponível em: <<http://dx.doi.org/10.1142/S0217751X10050159>>.
- [201] MAIOROV, B.; BAILY, S. A.; ZHOU, H.; UGURLU, O.; KENNISON, J. A.; DOWDEN, P. C.; HOLESINGER, T. G.; FOLTYN, S. R.; CIVALE, L. Synergetic combination of different types of defect to optimize pinning landscape using BaZrO_3 -doped $\text{YBa}_2\text{Cu}_3\text{O}_7$. *Nature Materials*, v. 8, n. 5, p. 398–404, MAY 2009. Disponível em: <<http://dx.doi.org/10.1038/NMAT2408>>.
- [202] COOTE, R.; CAMPBELL, A.; EVETTS, J. Flux line pinning by large normal particles in type-II superconductors. *Canadian Journal of Physics*, v. 50, n. 5, p. 421–427, 1972. Disponível em: <<http://dx.doi.org/10.1139/p72-062>>.

- [203] RAFFY, H.; RENARD, J.; GUYON, E. Critical currents and pinning effect in superconducting alloy films spatially modulated in concentration. *Solid State Communications*, v. 11, n. 12, p. 1679–1682, 1972. Disponível em: <[http://dx.doi.org/10.1016/0038-1098\(72\)90770-3](http://dx.doi.org/10.1016/0038-1098(72)90770-3)>.
- [204] CHONG, I.; HIROI, Z.; IZUMI, M.; SHIMOYAMA, J.; NAKAYAMA, Y.; KISHIO, K.; TERASHIMA, T.; BANDO, Y.; TAKANO, M. High critical-current density in the heavily Pb-doped $\text{Bi}_2\text{Sr}_2\text{CaCu}_2\text{O}_{8+\delta}$ superconductor: Generation of efficient pinning centers. *Science*, 276, n. 5313, p. 770–773, MAY 2 1997. Disponível em: <<http://dx.doi.org/10.1126/science.276.5313.770>>.
- [205] ZHAO, Y.; FENG, Y.; CHENG, C. H.; ZHOU, L.; WU, Y.; MACHI, T.; FUDAMOTO, Y.; KOSHIZUKA, N.; MURAKAMI, M. High critical current density of MgB_2 bulk superconductor doped with Ti and sintered at ambient pressure. *Applied Physics Letters*, AIP, v. 79, n. 8, p. 1154–1156, 2001. Disponível em: <<http://link.aip.org/link/?APL/79/1154/1>>.
- [206] DOU, S. X.; SOLTANIAN, S.; HORVAT, J.; WANG, X. L.; ZHOU, S. H.; IONESCU, M.; LIU, H. K.; MUNROE, P.; TOMSIC, M. Enhancement of the critical current density and flux pinning of MgB_2 superconductor by nanoparticle SiC doping. *Applied Physics Letters*, AIP, v. 81, n. 18, p. 3419–3421, 2002. Disponível em: <<http://link.aip.org/link/?APL/81/3419/1>>.
- [207] OTANI, Y.; PANNETIER, B.; NOZIERES, J.; GIVORD, D. Magnetostatic interactions between magnetic arrays and superconducting thin films. *Journal of Magnetism and Magnetic Materials*, v. 126, n. 13, p. 622 – 625, 1993. ISSN 0304-8853. Disponível em: <<http://www.sciencedirect.com/science/article/pii/0304885393907057>>.
- [208] FIORY, A. T.; HEBARD, A. F.; SOMEKH, S. Critical currents associated with the interaction of commensurate flux-line sublattices in a perforated Al film. *Applied Physics Letters*, AIP, v. 32, n. 1, p. 73–75, 1978. Disponível em: <<http://link.aip.org/link/?APL/32/73/1>>.
- [209] WELP, U.; XIAO, Z. L.; JIANG, J. S.; VLASKO-VLASOV, V. K.; BADER, S. D.; CRABTREE, G. W.; LIANG, J.; CHIK, H.; XU, J. M. Superconducting transition and vortex pinning in Nb films patterned with nanoscale hole arrays. *Phys. Rev. B*, American Physical Society, v. 66, p. 212507, Dec 2002. Disponível em: <<http://link.aps.org/doi/10.1103/PhysRevB.66.212507>>.
- [210] WELP, U.; XIAO, Z. L.; NOVOSAD, V.; VLASKO-VLASOV, V. K. Commensurability and strong vortex pinning in nanopatterned Nb films. *Phys. Rev. B*, American Physical Society, v. 71, p. 014505, Jan 2005. Disponível em: <<http://link.aps.org/doi/10.1103/PhysRevB.71.014505>>.
- [211] PANNETIER, M.; WIJNGAARDEN, R. J.; FLØAN, I.; RECTOR, J.; DAM, B.; GRIESSEN, R.; LAHL, P.; WÖRDENWEBER, R. Unexpected fourfold symmetry in the resistivity of patterned superconductors. *Phys. Rev. B*, American Physical Society, v. 67, p. 212501, Jun 2003. Disponível em: <<http://link.aps.org/doi/10.1103/PhysRevB.67.212501>>.

- [212] TAMEGAI, T.; TSUCHIYA, Y.; NAKAJIMA, Y.; YAMAMOTO, T.; NAKAMURA, Y.; TSAI, J.; HIDAKA, M.; TERAJ, H.; WANG, Z. Preferential diagonal penetration of vortices into square superconducting networks. *Physica C: Superconductivity*, v. 470, n. 19, p. 734 – 738, 2010. ISSN 0921-4534. Vortex Matter in Nanostructured Superconductors. Disponível em: <<http://www.sciencedirect.com/science/article/pii/S0921453410001826>>.
- [213] KES, P. H.; TSUEI, C. C. Two-dimensional collective flux pinning, defects, and structural relaxation in amorphous superconducting films. *Phys. Rev. B*, American Physical Society, v. 28, p. 5126–5139, Nov 1983. Disponível em: <<http://link.aps.org/doi/10.1103/PhysRevB.28.5126>>.
- [214] MISKO, V. R.; NORI, F. Magnetic flux pinning in superconductors with hyperbolic-tessellation arrays of pinning sites. *Phys. Rev. B*, American Physical Society, v. 85, p. 184506, May 2012. Disponível em: <<http://link.aps.org/doi/10.1103/PhysRevB.85.184506>>.
- [215] RAY, D.; REICHHARDT, C. J. O.; JANKO, B.; REICHHARDT, C. Strongly enhanced vortex pinning by conformal crystal arrays. *arXiv.org: Condensed Matter*, p. 6, Novembro 2012. Disponível em: <<http://arxiv.org/pdf/1210.1229v1.pdf>>.
- [216] CHOI, E.-M.; LEE, H.-S.; KIM, H. J.; KANG, B.; LEE, S.-I.; OLSEN, A. A. F.; SHANTSEV, D. V.; JOHANSEN, T. H. Dendritic magnetic avalanches in carbon-free MgB₂ thin films with and without a deposited Au layer. *Applied Physics Letters*, AIP, v. 87, n. 15, p. 152501, 2005. Disponível em: <<http://link.aip.org/link/?APL/87/152501/1>>.
- [217] CHOI, E.-M.; YURCHENKO, V. V.; JOHANSEN, T. H.; LEE, H.-S.; LEE, J. Y.; KANG, W. N.; LEE, S.-I. Suppression of dendritic flux jumps in MgB₂ films coated with a gold rim. *Superconductor Science and Technology*, v. 22, n. 1, p. 015011, 2009. Disponível em: <<http://stacks.iop.org/0953-2048/22/i=1/a=015011>>.
- [218] CERN. *CERN FAQ LHC the guide*. 2009. Disponível em: <<http://cdsweb.cern.ch/record/1165534/files/CERN-Brochure-2009-003-Eng.pdf>>.
- [219] DELFT, D. van; KES, P.; OVERWEG, J.; ZAAANEN, J. *100 Years of Superconductivity*. 2011. Disponível em: <http://www.ewh.ieee.org/tc/csc/milestones/graphics/Superconductivity/_Booklet/_Leiden/_FINAL.pdf>.
- [220] THOMPSON, J. R.; SUN, Y. R.; KERCHNER, H. R.; CHRISTEN, D. K.; SALES, B. C.; CHAKOUMAKOS, B. C.; MARWICK, A. D.; CIVALE, L.; THOMSON, J. O. Enhanced current density J_c and extended irreversibility in single-crystal Bi₂Sr₂CaCu₂O₈ via linear defects from heavy ion irradiation. *Applied Physics Letters*, AIP, v. 60, n. 18, p. 2306–2308, 1992. Disponível em: <<http://link.aip.org/link/?APL/60/2306/1>>.
- [221] MOTTA, M.; COLAUTO, F.; ORTIZ, W. A.; VESTGÅRDEN, J. I.; JOHANSEN, T. H.; CUPPENS, J.; MOSHCHALOKOV, V. V.; SILHANEK, A. V. Anomalous flux avalanche morphology in a-MoGe superconducting film with a square antidot lattice - experiment and simulation. *arXiv.org: Condensed Matter*, p. 3, 2011. Disponível em: <<http://arxiv.org/abs/1109.2532>>.

- [222] CLEM, J. R.; BERGGREN, K. K. Geometry-dependent critical currents in superconducting nanocircuits. *Phys. Rev. B*, American Physical Society, v. 84, p. 174510, Nov 2011. Disponível em: <<http://link.aps.org/doi/10.1103/PhysRevB.84.174510>>.
- [223] ADAMI, O.-A.; CERBU, D.; CABOSART, D.; MOTTA, M.; CUPPENS, J.; ORTIZ, W. A.; MOSHCHALKOV, V. V.; HACKENS, B.; DELAMARE, R.; VONDEL, J. V. de; SILHANEK, A. V. Current crowding effects in superconducting corner-shaped Al microstrips. *Applied Physics Letters*, AIP, v. 102, n. 5, p. 052603, 2013. Disponível em: <<http://link.aip.org/link/?APL/102/052603/1>>.
- [224] LIKHAREV, K. K. Superconducting weak links. *Rev. Mod. Phys.*, American Physical Society, v. 51, p. 101–159, Jan 1979. Disponível em: <<http://link.aps.org/doi/10.1103/RevModPhys.51.101>>.
- [225] KUPRIYANOV, M. Y.; LUKIEV, V. F. *Sov. J. Low Temp. Phys.*, v. 6, p. 210, 1980.
- [226] ROMIJN, J.; KLAPWIJK, T. M.; RENNE, M. J.; MOOIJ, J. E. Critical pair-breaking current in superconducting aluminum strips far below T_c . *Phys. Rev. B*, American Physical Society, v. 26, p. 3648–3655, Oct 1982. Disponível em: <<http://link.aps.org/doi/10.1103/PhysRevB.26.3648>>.
- [227] BULAEVSKII, L. N.; GRAF, M. J.; KOGAN, V. G. Vortex-assisted photon counts and their magnetic field dependence in single-photon superconducting detectors. *Phys. Rev. B*, American Physical Society, v. 85, p. 014505, Jan 2012. Disponível em: <<http://link.aps.org/doi/10.1103/PhysRevB.85.014505>>.
- [228] KLIMIN, S.; FOMIN, V.; DEVREESE, J.; MOSHCHALKOV, V. Superconductivity in a wedge with a small angle: an analytical treatment. *Solid State Communications*, v. 111, n. 10, p. 589 – 594, 1999. ISSN 0038-1098. Disponível em: <<http://www.sciencedirect.com/science/article/pii/S0038109899002264>>.
- [229] BROSENS, F.; FOMIN, V.; DEVREESE, J.; MOSHCHALKOV, V. Superconductivity in a wedge: Analytical variational results II. *Solid State Communications*, v. 144, n. 1011, p. 494 – 497, 2007. ISSN 0038-1098. Disponível em: <<http://www.sciencedirect.com/science/article/pii/S0038109807006692>>.
- [230] HAGEDORN, F. B.; HALL, P. M. Right-Angle Bends in Thin Strip Conductors. *Journal of Applied Physics*, AIP, v. 34, n. 1, p. 128–133, 1963. Disponível em: <<http://link.aip.org/link/?JAP/34/128/1>>.
- [231] SILHANEK, A. V.; VONDEL, J. V. de; MOSHCHALKOV, V. V.; LEO, A.; METLUSHKO, V.; ILIC, B.; MISKO, V. R.; PEETERS, F. M. Comment on “Transverse rectification in superconducting thin films with arrays of asymmetric defects” [Appl. Phys. Lett. **91**, 062505 (2007)]. *Applied Physics Letters*, AIP, v. 92, n. 17, p. 176101, 2008. Disponível em: <<http://link.aip.org/link/?APL/92/176101/1>>.
- [232] HORTENSIUS, H. L.; DRIESSEN, E. F. C.; KLAPWIJK, T. M.; BERGGREN, K. K.; CLEM, J. R. Critical-current reduction in thin superconducting wires due to current crowding. *Applied Physics Letters*, AIP, v. 100, n. 18, p. 182602, 2012. Disponível em: <<http://link.aip.org/link/?APL/100/182602/1>>.

- [233] HENRICH, D.; REICHENSPERGER, P.; HOFHERR, M.; MECKBACH, J. M.; IL'IN, K.; SIEGEL, M.; SEMENOV, A.; ZOTOVA, A.; VODOLAZOV, D. Y. Geometry-induced reduction of the critical current in superconducting nanowires. *Phys. Rev. B*, v. 14, p. 144504, Oct 2012. Disponível em: <<http://link.aps.org/doi/10.1103/PhysRevB.86.144504>>.
- [234] VESTGÅRDEN, J. I.; JOHANSEN, T. H. Modeling non-local electrodynamics in superconducting films: the case of a right angle corner. *Superconductor Science and Technology*, v. 25, n. 10, p. 104001, 2012. Disponível em: <<http://stacks.iop.org/0953-2048/25/i=10/a=104001>>.
- [235] CLEM, J. R.; MAWATARI, Y.; BERDIYOROV, G. R.; PEETERS, F. M. Predicted field-dependent increase of critical currents in asymmetric superconducting nanocircuits. *Phys. Rev. B*, American Physical Society, v. 85, p. 144511, Apr 2012. Disponível em: <<http://link.aps.org/doi/10.1103/PhysRevB.85.144511>>.
- [236] SCHWEIGERT, V. A.; PEETERS, F. M. Influence of the confinement geometry on surface superconductivity. *Phys. Rev. B*, American Physical Society, v. 60, p. 3084–3087, Aug 1999. Disponível em: <<http://link.aps.org/doi/10.1103/PhysRevB.60.3084>>.
- [237] VODOLAZOV, D. Y.; PEETERS, F. M. Superconducting rectifier based on the asymmetric surface barrier effect. *Phys. Rev. B*, American Physical Society, v. 72, p. 172508, Nov 2005. Disponível em: <<http://link.aps.org/doi/10.1103/PhysRevB.72.172508>>.
- [238] CERBU, D.; GLADILIN, V.; CUPPENS, J.; FRITZSCHE, J.; SILHANEK, A. V.; TEMPERE, J.; DEVREESE, J. T.; MOSHCHALOV, V. V.; VONDEL, J. V. de. Vortex ratchet induced by controlled difference between the surface barrier. Unpublished.
- [239] KAJINO, K.; FUJITA, K.; AN, B.; INOUE, M.; FUJIMAKI, A. Ratchet Effect of Single Vortex Motion in Superconducting Asymmetrical Nanobridges. *Japanese Journal of Applied Physics*, The Japan Society of Applied Physics, v. 51, p. 053101, 2012. Disponível em: <<http://jjap.jsap.jp/link?JJAP/51/053101/>>.
- [240] NAKAI, N.; MACHIDA, M. Simulation study on the vortex penetration in the presence of the square antidot array. *Physica C: Superconductivity*, v. 470, n. 20, p. 1148 – 1150, 2010. ISSN 0921-4534. Proceedings of the 22nd International Symposium on Superconductivity (ISS 2009). Disponível em: <<http://www.sciencedirect.com/science/article/pii/S0921453410003163>>.